Loughborough University

Modelling CO_2 Sequestration in Deep Saline Aquifers

by

Kamal Jawher Khudaida

A thesis submitted in fulfilment of the
requirements for the degree of Doctor of Philosophy (PhD)

October 2015

DEDICATION

This thesis is dedicated to the soul of my late father,

Jawher Khudaida

And

My Beloved Mum in Heaven

who would have wanted to be a part of this achievement.
I know this would have been a proud moment for them.

Abstract

In spite of the large number of research works on carbon capture and sequestration (CCS), the migration and behaviour of CO_2 in the subsurface (i. e. strata below the earth's surface) still needs further understanding and investigations with the aim of encouraging the governmental policy makers to adopt CCS technology as one of the most viable means to tackle the global warming threats.

In this research work, a series of numerical simulations has been carried out using STOMP-CO_2 simulation code to determine the flow behaviour and ultimate fate of the injected supercritical carbon dioxide ($scCO_2$) into saline aquifers in medium terms of storage (i. e. few thousand years). The characteristics of the employed simulator, including the mathematical algorithm, governing equations, equations of states and phase equilibria calculations are explained in details.

The numerical results have been validated against experimental ones from the literature to quantify the credibility and integrity of the employed simulation code. The experimental and numerically predicted results demonstrated good agreement, which has established a robust credibility of the computer code in modelling the injection of CO_2 into geological formation and assess the storage efficiency and ultimate fate of the injected gas.

The significance of the dynamic capillary pressure effects and the time required to capillary equilibrium during geological sequestration of CO_2, have been investigated for $scCO_2$-water flow in a lab-scale porous media including the influence of temperature, injection pressure and porosity on the estimation of the dynamic coefficient (τ). This is an important factor in determining the storage capacity and efficiency of geological formations to sequester CO_2. The findings from this study show that the dynamic effect is significantly influenced by and increases as water saturation decreases in the domain.

A number of numerical simulation runs have been conducted in this work to identify the possible implications of permeability, heterogeneity, injection pressure and temperature on the capillary pressure – saturation relationship for $scCO_2$ in deep saline aquifers at core, large and field-scale domains. Additionally, the dynamic effect in water-CO_2 multi-phase flow system and consequently its impact on the solubility and residual trapping mechanisms of $scCO_2$ has been quantified in this research work. The value of the dynamic coefficient (τ) was found to

increase as the aqueous desaturation rate ($\partial S/\partial t$) decreases. Moreover, the results indicated that warm aquifers are more efficient in sequestering CO_2 compared to cold ones.

This work aims at evaluating the applicability of different injection techniques in terms of orientation and continuity to enhance the capacity and efficiency of CO_2 sequestration in saline aquifers. Moreover, it provides further understanding on how to assess the feasibility of any potential storage site to safely store CO_2 by investigating the behaviour and migration of CO_2-brine as a two-phase flow system in porous geological formations under various injection conditions and scenarios. It also demonstrates the effect of various site characteristics like heterogeneity and anisotropy on the injectivity and the ultimate fate of the injected CO_2.

Based on the geological settings for Sleipner Vest Field as one of the typical known CCS project sites, which is located in the Norwegian part of the North Sea, the simulation results from this work further revealed that the injection scenario and methodology, heterogeneity and permeability isotropy have significant impact on capillary-saturation relationships and the amounts of integrated CO_2 throughout the timeline of the simulation via different trapping mechanisms. Furthermore, the outcomes from this work illustrate that CO_2 dissolution is more competent in homogeneous formations compared to heterogeneous ones that are found to be more effective in storing CO_2 safely over long-time frames.

Keywords: CO_2 geological storage, Numerical modelling, Two-phase flow, Dynamic capillary pressure effect, CO_2 injection into the subsurface, Carbon Storage, CO_2 storage in deep saline aquifers

ACKNOWLEDGEMENTS

I would like to express my gratitude to everyone who has contributed in one way or the other during the time of preparing this research project including Loughborough University Graduate School for their outstanding effort in providing an excellent program for researcher skills development all the way through the timeline of this project.

I gratefully acknowledge the enormous efforts of my supervisor, Dr Diganta B. Das, who has been providing superb support through the timeline of this study with his extremely obliging comments and proficient guidelines to achieve the objectives of this project. My deep gratefulness is also expressed to Professor VM Starov for his thoughtful advice throughout the preparation and completion of this research programme.

The collaborative contribution of my colleague Luqman K. Abidoye is greatly appreciated and acknowledged. My deep acknowledgement goes to the entire staff and colleagues in the Chemical Engineering Department for their continuous and unlimited support in developing and completing this dissertation.

I am also thankful to Dr Mark White from Pacific Northwest National Laboratory (PNNL) for his tremendous help in employing STOMP simulation code in this project.

I am extremely grateful to my whole family for their patience, encouragement and continuous support throughout the timeline of preparing this research work.

Finally yet importantly, I would like to acknowledge all my friends specifically Professor Hamid Al-raweshidy from Brunel University for his continuous support and Mr Rabie Dean for his intimate encouragement during the years of this research making it possible for me to finish it.

TABLE OF CONTENTS

LIST OF FIGURES

LIST OF TABLES

LIST OF PUBLICATIONS

The publications as a result of this research are:

PUBLISHED JOURNAL ARTICLES

1. **Khudaida, K. J.**, & Das, D. B. (2014). A numerical study of capillary pressure–saturation relationship for supercritical carbon dioxide (CO_2) injection in deep saline aquifer. *Chemical Engineering Research and Design*, *92*(12), 3017-3030.
2. Das, D. B., Gill, B. S., Abidoye, L. K., & **Khudaida, K. J.** (2014). A numerical study of dynamic capillary pressure effect for supercritical carbon dioxide-water flow in porous domain. *AIChE Journal*, *60*(12), 4266-4278.
3. Abidoye, L. K., **Khudaida, K. J.**, & Das, D. B. (2015). Geological carbon sequestration in the context of two-phase flow in porous media: A review. *Critical Reviews in Environmental Science and Technology*, *45*(11), 1105-1147.

ARTICLE UNDER PREPARATION

1. **Khudaida, K. J.**, & Das, D. B. (2015). Scenario analysis of supercritical CO_2 injection into geological formations.

CONFERENCES / SEMINARS

PRESENTATIONS

1. **Khudaida, K. J.**, Diganta B. Das, (2015). A numerical analysis of supercritical CO_2 injection into geological formations. In *Proceedings* of the Industrial Simulation Conference, Universitat Politecnica, Valencia, Spain, 1-3 June 2015.

2. **Khudaida, K. J.** and DAS, D.S., 2013. Modelling CO_2 sequestration in deep saline aquifers. IN: The 3rd UKCCSRC Early Career Researcher Winter School, the University of Edinburgh, Scotland, 8 - 11 January 2013.

3. **Khudaida, K. J., and** Das, D.B., (2013). Modelling CO_2 sequestration in deep saline aquifers: PhD Group Seminar at Loughborough University, June 1st, 2012.

IN ATTENDANCE

1. The 7th Dutch CCS conference - By CATO-2 (The National Dutch CCS Research Programme), *Amsterdam RAI, Europaplein*, 1078 GZ in Amsterdam, the Netherlands, 19-20 June 2014.

2. First North Sea Young CCS Researchers Meeting - By CATO-2 (The National Dutch CCS Research Programme), *Rotterdam Harbour Area*, the Netherlands, 17-18th June 2014.

3. Carbon Capture and Storage Conference, by the American Association of Petroleum Geologists (AAPG). *The Geological Society*, Burlington House, in London W1J 0BG, UK, 14-15 January 2013.

4. UKCCSC Biannual Meeting London - *University College London.* To start a CCS Research and Pathways to Impact Delivery (RAPID), 2nd April 2012

5. Potential environmental effects of CO_2 leakage in the marine and terrestrial environment: Understanding, monitoring, mitigation workshop, Nottingham Centre for Carbon Capture and Storage, *University of Nottingham, Nottingham*, UK, 21st Feb. 2012.

6. Carbon Capture and Storage, A joint meeting between the Geological Society and AAPG, November 22nd -23rd , 2011, *The Geological Society*, Burlington House, in London W1J 0BG, UK.

7. UK Carbon Capture and Sequestration Consortium's first annual winter school from 8-11 February 2011 hosted by *Imperial College London*.

LIST OF ACRONYMS

BGS	British Geological Survey
CCS	Carbon-Dioxide Capture and Storage
CS	Carbon Storage
DCPE	Dynamic Capillary Pressure Effect
DSA	Deep Saline Aquifer
EOR	Enhanced Oil Recovery
EOS	Equation of State
FDM	Finite Difference Method
FVM	Finite Volume Method
GHG	Greenhouse Gases
IPCC	Intergovernmental Panel on Climate Change
MMT	Million Metric Ton
PDE	Partial Differential Equation
PNNL	Pacific Northwest National Laboratory
SC	Super Critical
STOMP	Subsurface Transport Over Multiple Phases
TCE	the Crown of State
VTF	Vogel-Tammann-Fulcher
US-DOE	United State Department of Energy

NOMENCLATURE

Symbol	Definition	Dimension
$\frac{2}{\varepsilon_T}$	storage efficiency factor	[-]
α^{VG}	Van Genuchten parameter	[1/Pa]
α_S	Stauffer scaling parameter	[-]
α_L	longitudinal dispersivity	[m]
α_T	transverse dispersivity	[m]
Γ	boundary	[-]
σ'_v	effective vertical stress for deep aquifers	[Kg/m^2]
$\partial S/\partial t$	desaturation rate	[s^{-1}]
Δt	time step	[s]
ε	residuum	[-]
ε_S	equilibrium criterion for saturation	[-]
ε_P	equilibrium criterion for pressure	[Pa]
η_i	set of all neighbouring nodes of node *i*	[-]
θ_e	static contact angle	[°]
θ_d	dynamic contact angle	[°]
ι	Mualem parameter in *k*rα(*S*α)	[-]
$\lambda\alpha$	mobility of phase α	[m s/kg]
μ_b	bulk viscosity	[Pa s]
ρ_b	bulk and brine densities	[kg/m^3]
ρ_r	rock density	[kg/m^3]
ρ_w	brine density	[kg/m^3]
$\overline{\rho_w}$	average density of brine	[kg/m^3]
τ_B	coefficient after Barenblatt	[s]
τ_*	coefficient after Bourgeat & Panfilow	[-]
τ_{HG}	coefficient after Hassanizadeh & Gray	[Pa s]
τ_K	coefficient after Kalaydjian	[Pa s]
τ_S	coefficient after Stauffer	[Pa s]

$\psi_{\alpha i}$	total potential of phase a at node *i*	[-]
A	surface area	[m^2]
C	compressibility of the formation	[-]
C_p	CO_2 mass for the pressure-limited systems	[m]
C_t	CO_2 mass for the open systems	[m]
C_v	coefficient of variation	[-]
D	depth to the top of the aquifer	[m]
D	diffusion coefficient	[m^2/s]
E_{aq}	aquifer storage efficiency	[-]
G_{CO_2}	CO_2 mass storage capacity	[Kg]
G	geothermal gradients	[K]
g	vector of gravitational acceleration $(0,0,-g)^T$	[m/s^2]
g	scalar gravitational acceleration	[m/s^2]
h	piezometric head	[m]
H	thickness of the aquifer	[m]
J	diffusive flux rate	[kg/m^2 s]
K	hydraulic conductivity	[m/s]
k	absolute (intrinsic) permeability	[m^2]
k_{aq}	permeability of the aquifer	[m^2]
k_e	effective permeability	[m^2]
k_r	relative permeability	[-]
k	water saturation line constant	[-]
L_c	Lorenz coefficient	[-]
L_t	total length of the aquifer	[m]
m	mass rate density	[kg/ s m^3]
M	molecular weight	[kg/ kmol]
M_p	pressure-limited storage capacity	[-]
MMT	million metric ton	[10^9 Kg]
P	pressure	[Pa]
P_c	capillary pressure	[Pa]
P_c^{dyn}	dynamic capillary pressure	[Pa]

P_c^{stat}	static (equilibrium) capillary pressure	[Pa]
P_d	entry pressure for the $P_c(S_w)$ relationship	[Pa]
P_{fraq}	fracture pressure of the rock	[Pa]
$\tilde{p}_{max}$	maximum dimensionless pressure	[Pa]
q	fluid flow velocity (source or sink)	[m/s]
Q	volumetric flux	[m^3/s]
r	meniscus radius	[m]
R	gas constant	[-]
r	radius	[m]
s	sensitivity	
S	saturation	[-]
$S\alpha_r$	residual saturation of phase a	[-]
$\hat{S}_{gt}^{potential}$	potential effective trapped gas	[-]
S_{gr}^{max}	maximum trapped gas saturation	[-]
S_e	effective saturation of the wetting phase	[-]
$\bar{S}_l$	effective aqueous saturation	[-]
$\bar{\bar{S}}_l$	apparent aqueous saturation	[-]
$\hat{S}_l^{min}$	minimum aqueous saturation	[-]
S_w	wetting phase (water) saturation	[-]
S_{nw}	non-wetting phase (brine) saturation	[-]
S_{wc}	connate water saturation	[-]
t	time	[s]
T	temperature	[K]
v	vector of Darcy velocity	[m/s]
v	Darcy velocity	[m/s]
v_s	seepage velocity	[m/s]
V	volume	[m^3]
V	Darcy velocity vector	[m/s]
$V_\emptyset$	volume of the pores	[m^3]
$V_\emptyset$	volume of the pores	[m^3]

z_i	geodetic height of node *i*	[m]

Greek Symbols:

β	scaling factor	[-]
γ	interfacial tension	[Nm]
λ	Brooks-Corey parameter for pore size index	[-]
θ	contact angle	[°]
∇	defferential	[-]
μ	dynamic fluid viscosity	[Pa s]
ρ	density	[kg/m^3]
δ	capillary tube diameter	[m]
σ	interfacial (surface) tension	[kg/s^2]
τ	dynamic (damping) coefficient	[Pa s]
τ	tortuousity factor	[-]
~	tilde symbol (preceding card title in STOMP input files	[-]
ϕ	porosity	[-]
ϕ	fugacity coefficient	[-]
x	mass fraction	[-]
ω	mass fraction	[-]

Subscripts:

aq	aqueous
e	effective
g	gas
gf	free gas
gt	trapped gas
h	horizontal
s	solid phase
l	liquid
v	vertical

w	wetting phase
nw	non-wetting

Superscripts:

˜	approximation
d	dynamic
equ	equilibrium
stat	static
n	time step
B	boundary
L	lower
S	grid-volume weighted average
T	top
V	phase-volume weighted average

Chapter 1

Introduction

1.1. Background

Carbon capture and sequestration (CCS) refers to reducing the effects of global warming by capturing the emitted carbon dioxide (CO_2) from the releasing sources which are mainly presented by power generation plants, and then storing and isolating it from the atmosphere using specific technologies. Though applying CCS technologies to modern power generation plants could decrease CO_2 release to the environment by approximately 80-90% (IPPC 2005), it may increase operational costs which vary depending on the location of the source and storage area. It is believed that the increased anthropogenic CO_2 is greatly attributed to fossil fuel combustion. Therefore, industries that involve fossil fuel combustion such as cement manufacturing, power generation, iron and steel manufacture and oil refinery are amongst the main sources of CO_2 emissions. Of all these sources, power generation has been found to be the largest source of these emissions and accounts for almost one third of global CO_2 emissions. Researches imply that the increasing levels of CO_2 emitted into the ambience are heightening the natural greenhouse effect, which raises concerns about trapping the solar heat, causing an increase in the Earth surface temperature that is claimed to harmfully distress life on Earth (Allen and Stocker 2014).

Different means have been developed to moderate CO_2 emissions including CO_2 sequestration in geological formations, which is a relatively new concept that had been developed to address the problem of global warming that is attributed to high levels of atmospheric CO_2. In principle, CO_2 sequestration involves capturing CO_2 that would otherwise be emitted into the atmosphere, and storing it. The main options available to this method include sequestration in declining gas and oil fields, brine aquifers and unminable coal veins (Fujii et al. 2007). The oil and gas fields are the favourite places for CO_2 sequestration due to the cost effectiveness as a result of using the same infrastructure used for gas and oil production for the injection of CO_2. In spite of their enormous capacity, these depleted fields' storage capacity is not sufficient for long-term needs.

According to the UK's Storage Atlas developed in partnership by The Crown Estate (TCE) and the British Geological Survey (BGS), the total estimated theoretical storage capacity for the UK carbon storage is 78 Gt from which 60 Gt (equivalent to about 500 years of CO_2 emissions in the UK) could potentially be stored in saline aquifers. Besides that, there is the potential to store 8 Gt (equivalent to 10 years of CO_2 emissions in the UK) in depleted and depleting oil and gas fields in addition to the extra storage potential which may be available through enhanced oil recovery

using CO_2 (Bentham et al. 2014). In the United states, saline aquifers have even larger potential to store up to 500Gt CO_2 (Bergman and Winter, 1995)

Stauffer et al. (2008) explain that while injecting CO_2 into saline aquifers is a clean type of storage, injection of the gas into currently producing oil and gas reservoirs enhances their recovery and helps achieve an economic benefit that could somehow reduce the cost of gas storage. Sedimentary basin aquifers provide the largest potential for CO_2 sequestration particularly for regions in the world that are landlocked like the United Kingdom (Fujii et al. 2007). According to these authors, injecting CO_2 into a geological reservoir requires ascertaining its potential to store the gas in order to avoid leakage back into the atmosphere. They explain that the potential of geological reservoir for sequestration of CO_2 has been evaluated with regard to several criterions including;

- The reservoir's tectonic setting and its geology
- The reservoir's hydrocarbon potential and maturity of the basin
- The hydrodynamic system of water formation
- Economic factors relating to infrastructure as well as access, and
- Social and political factors

Interest in this technology as a powerful mean for considerably reducing CO_2 is high in developed countries because the technology is expected to be instantly available and technologically feasible for decreasing CO_2 emissions in quantity as well as economy. In discussion of modelling CO_2 sequestration, this study aims at investigating the influential parameters on the storage of carbon dioxide in briny aquifers including the injection methodology that are fundamental for assessing the storage efficiency of any potential site. The present work also focuses on modelling CO_2 and water systems under static and dynamic multiphase flow conditions in porous media to quantify the dynamic flow effect represented by the dynamic coefficient (τ) on capillary pressure-saturation relationship.

1.2. Aims and Objectives

1.2.1. Overall Project Aims

The overall goal of this study is to evaluate the static and dynamic capillary pressures for CO_2-water system as a function of saturation, permeability and heterogeneity at various time scales, temperature and pressure conditions in order to evaluate injection strategy and storage capacity of CO_2 in brine aquifers. The modelling attempts to determine the significance of the dynamic capillary pressure effects for scCO_2-water flow as discussed later. Additionally, the effect of various injection schemes/scenarios (i.e. injection orientation, scope of injection and cyclic injection schemes) and aquifer characteristics on enhancing the two permanent sequestration mechanisms namely residual and solubility trapping of CO_2 is to be examined in this work.

For the purpose of this work, a series of simulations is to be carried out under various pressure, temperature, heterogeneity and injection rate conditions. This helps the prediction of the optimized gas injection process and CO_2 behaviour within the aquifer formation during the sequestration lifetime, which has a vast impact on the energy cost and storage process safety. It is believed that this research study will provide important insights on how to assess the feasibility of any potential storage site by investigating the behaviour and migration of CO_2-brine as a two-phase flow system in porous geological formations under various injection conditions and scenarios. It further correlates how increase in the mean permeability of the geological formation allows greater injectivity and mobility of CO_2 that should lead to increase in CO_2 dissolution into the resident brine in the subsurface.

1.2.2. Specific Project Objectives

The specific objectives of this research work are:

- To carry out a comprehensive *literature survey on* different factors that influence the success of CO_2 sequestration in deep saline aquifers to the traditional theories of multiphase flow in permeable media that rely on the extended version of Darcy's law and the correlations of capillary pressure (P_c), saturation (S), and relative permeability (k_r).
- Thoroughly investigate behaviour of injected carbon dioxide focussing on capillary trapping of CO_2.

- To address and comprehensively study a combination of most salient hydrogeological and multiphase flow parameters to predict the behaviour of CO_2 within an aquifer after an injection process.
- To determine the effects of heterogeneity and injection conditions on saturation and capillary pressure at field-scale domains from the locally calculated values using a series of numerical simulations and implement them in plotting $P_c - S$ curves at different time scales.
- To establish a robust credibility of our simulation results prior to upscaling them for deployment on practical field-scale projects, a reasonable mapping with a lab-scale setup results is significantly important. This study aims at assessing the reliability of the obtained numerical results in terms of investigating P_c-S relations and the dynamic effects in CO_2-water flow system.
- To quantify the significance of the dynamic capillary pressure effects for supercritical carbon dioxide-water flow in terms of dynamic coefficient (τ) through a comparison between dynamic and static capillary pressure – saturation relation. Additionally, the influence of temperature, injection pressure and permeability on the P_c-S is to be determined.
- To evaluate the capacity of different sequestration mechanisms within large time scales of numerical and reactive transport simulation results.

1.3. Outline of the Thesis

This thesis embraces of six chapters explained as follows:

Chapter one is an introduction to describe the concept of carbon capture and sequestration (CCS) with an explanation of the feasibility of this new technology as a means of tackling the issue of global warming and climate change. It is followed by clarifying the overall aims and specific objectives of the project. Furthermore, the outline of the thesis has been set out clearly in this chapter.

Chapter two presents the perception of CO_2 storage in deep saline aquifers (DSAs) and description of multi-phase fluid flow in porous media and the dependant parameters. It also demonstrates the characterization of potential sites for sequestering CO_2 and methodologies used to assess their suitability for keeping the gas safely contained after injection. Various effective

parameters on modelling CO_2 injection are explained with their influence on the fate of the injected gas at different time scales. Additionally this chapter explores several previous works related to modelling CO_2 sequestration in geological formations and the employed simulation codes.

Chapter three briefly reviews the characteristics of the employed simulator (STOMP-CO_2) including the mathematical algorithm, the governing equations and correlations for CO_2-water flow system and the equations of state (EOS) that are built-in the simulation code along with the phase equilibria calculations. Additionally, it describes the methodology of conducting the simulation cases in different chapters of this study. The achieved numerical results are verified and validated with experimental results from literature for the sake of establishing robust credibility on their accuracy. Moreover, the simulation results from a 2D model are validated against a 3D model to avoid using time-expensive 3D modelling runs.

Chapter four compares the dynamic and quasi-static flow conditions on P_c-S relationship at temperature ranges between 35-65 ℃ at core-scale. In this chapter, the dynamic coefficient (τ) for CO_2-Water flow system is determined and the values are compared with those for Oil-Water system. Additionally it underlines the CO_2 and water densities, viscosities and interfacial tension dependency on various simulation conditions and investigates their effects on P_c-S relationship. The simulations carried out for 3D cylindrical porous domains measuring 10 cm in diameter and 12 cm in height are illustrated in this chapter. The governing model equations for two-phase flow in porous media are explained beside the temperature dependency of CO_2 thermodynamic properties.

Chapter five investigates modelling the injection and transport behaviour of supercritical CO_2 in DSAs as a multi-phase flow (H_2O-CO_2-NaCl) in a porous media and examines the governing equations and other related constitutive correlations. Additionally, it highlights the influence of different parameters such as time scale, temperature, pressure, permeability and geochemical conditions on the scCO_2 injection into underground formations at large-scale domains. This chapter concerns also about utilizing the dedicated mode of STOMP (*subsurface transport over multiple phases*) simulation code (STOMP-CO_2) to conduct a series of numerical simulations to determine CO_2 saturation at various time scales, temperatures and pressure conditions taking into consideration the effects of porosity/permeability, heterogeneity and capillarity for CO_2-water flow system.

Chapter six illustrates different scenarios of injecting supercritical CO_2 into heterogeneous porous media at field-scale domain and highlights their effects on storage efficiency. The influences of grid resolution and aquifer characteristics including anisotropy, injection scope and injection methodology on the two permanent sequestration mechanisms (residual and solubility) are also investigated thoroughly in this chapter.

Chapter seven summarizes the main features of this work and demonstrates a list of further recommended investigations and knowledge gaps for future research.

Chapter 2

CO_2 Storage in Geological Medium: A Review

2.1. The Concept of CO_2 Storage

The increased anthropogenic carbon dioxide is greatly attributed to fossil fuel combustion and industries that involve this fuel combustion such as cement manufacturing, power generation, iron and steel manufacture and oil refineries are amongst the main sources of carbon dioxide emissions. Of all these sources, power generation has been found to be the largest source of these emissions and accounts for almost one third of global carbon dioxide emissions. Researches imply that the increasing levels of carbon dioxide emitted into the ambience are heightening the natural greenhouse effect, which raises concerns about trapping the solar heat, causing an increase in the Earth surface temperature that is claimed to harmfully distress life on Earth (IPCC 2001).

According to the IPCC's fifth assessment report (2013), there has been a significant rise in annual greenhouse gas (GHG) emissions that grew on average by 1.0 gigatonne carbon dioxide equivalent ($GtCO_2eq$) (2.2 %) per year from 2000 to 2010 compared to 0.4 $GtCO_2eq$ (1.3 %) per year from 1970 to 2000. This report further adds that Fossil fuel-related CO_2 emissions reached 32 $GtCO_2/yr.$, in 2010, and grew further by about 3 % between 2010 and 2011 and by about 1 – 2 % between 2011 and 2012. It concluded that of the 49 $GtCO_2eq$/year in total anthropogenic GHG emissions in 2010, CO_2 remains the major anthropogenic GHG accounting for 76 % $GtCO_2eq$/year of total anthropogenic GHG emissions in 2010 (Edenhofer et al. 2014).

In response to these serious threats, numerous studies and researches have been conducted since early 1990s, to highlight the viability of carbon capture and sequestration (CCS) as an immediate technology to mitigate CO_2 concentration in the atmosphere and assess the feasibility of potential storage areas including saline aquifers to dispose the captured gas. Carbon storage (CS) represents the last step in the chain of CCS technology following capturing the emitted CO_2 from the emission sources and transmitting it to the storage site locale where it is planned to dispose. The concept of geological CS dwells in injecting CO_2 into geological porous formations to either keep it underground safely for a specific period of time (storage) or permanently over long periods of time that extend to thousands of years (sequestration), (IPCC 2005; Bachu 2008). Deep saline aquifers (DSAs) are considered the most favourite means of geological storage owing to their largest potential capacity, constancy and being widely spread worldwide (Fujii et al. 2010; Zahid et al. 2011; Metz et al. 2005). $ScCO_2$ can be stored or sequestered in DSAs

through four trapping mechanisms; 1) structural trapping where the injected gas is trapped under the impervious caprock overlaying the aquifer, 2) residual trapping where the gas is immobilized in the pore spaces due to the capillarity, 3) solubility trapping which is represented by CO_2 dissolution in the hosted brine, and finally, 4) mineral trapping where the dissolved gas tends to form a weak carbonic acid which reacts with the dissolved ions and rock minerals leading to precipitated solid minerals. These mechanisms were discussed in details in a peer-reviewed preceding paper (Abidoye et al. 2015).

A growing number of studies and research works have been conducted in the CCS area since early 1990s to assess the feasibility and applicability of injecting the gas into geological formations including DSAs (see Table 2.1). These studies have revealed that CCS can play a major part in reducing CO_2 emissions using technologies, which are commercially available. However, there is a need to adapt and optimise these technologies for cost effectiveness because up to date, only few commercial projects have been brought into operation (Lokhorst and Wildenborg 2005). Such developed projects include Sleipner in Norway, operating at a rate of 1 Mt/year; Weyburn and Midale field in Canada, operating at 1 Mt/year; In Salah in Algeria operating at 1.2 Mt/year; the Snøhvit field in Norway operating at rate of 0.7 Mt/year CO_2 injected into saline aquifers. These are in addition to tens of pilot projects in the US, UK and other EU countries, currently exploit saline aquifers to assess their performance in storing CO_2, (Smith et al. 2011). This imposes further research work and technology development to eliminate the knowledge gaps in geological sequestration of CO_2 in DSAs.

Table 2.1, Overview of related previous works to modelling CO_2 sequestration in geological formations.

Author	Simulation Code	Studied Factors	Results
Orsini et al., (2014)	PFLOTRAN (Hammond et al. 2012)	- CO_2 plume extension. - Pressure build-up. - Solubility and residual trapping mechanisms	- CO_2 plume was estimated to extend radially up to about 1.75 km. - Maximum pressure build-up of about 38 bars was quantified. - 69% and 79% of the total amount of injected CO_2 was dissolved in brine after 1000 and 2000 years respectively. - 9% and 6% of the total amount of injected CO_2 was residually trapped in the formation pores after 1000 and 2000 years respectively.
Mehnert et al., (2013)	TOUGH2-MP (Zhang et al. 2008) And module ECO2N (Pruess, 2011)	- Porosity and permeability. - Permeability anisotropy (vertical to horizontal permeability ratio).	- The highest pressure build-up was observed in the top injection zones while the lowest value was observed in the bottom injection zones. - Lower permeabilities resulted in higher pressures near the injection wells. - >90% of the injected CO_2 remains as free phase gas in the injection zone and solubility trapping retained <10% of it. - Reduction in anisotropy ratio resulted in less CO_2 dissolved in brine. - The amount of CO_2 retained by residual trapping was unknown.
Wang et al., (2013)	TOUGH2-MP (Zhang et al. 2008)	- Domain size - Heterogeneity and permeability - Different injection schemes - Porosity and compressibility. - Number of injection wells.	- Heterogeneous formations have lower storage efficiency than homogeneous ones. - Large compressibility can improve CO_2 storage efficiency. - Large porosity reduces CO_2 storage efficiency. - The storage efficiency factor decreases almost linearly with domain size. - The larger number of injection wells, the more CO_2 can be stored in the formation. - Short period pause of injection shows very limited improvement on CO_2 storage efficiency.

Gonzalez-Nicolas et al., (2011)	MFLOW3D (Comerlati et al. 2005)	- Domain size. - Grid resolution. - Boundary conditions. - Heterogeneity.	- Mesh refinement increases simulation execution time but gives more accurate results. - MFLOW3D model is unable to handle large element size variations. - Lateral boundary distance must be larger than the CO_2 plume extent. - Non-regular grids are more effective in reducing computational time.
Ranganathan et al., (2011)	CMG-GEM (Computer Modeling Group, 2012)	- Effects of permeability and residual gas saturation on CO_2 storage capacity. - Storage efficiency in terms of CO_2 dissolution and entrapment. - The effect of mineralisation on permanent sequestration.	- During the injection process of 16 years, up to 90% of the injected CO_2 was trapped as a free gas while about 10% of it dissolved in the brine. - Most of the dissolved CO_2 was observed close to the injection well and in the upper layers of the reservoir. - After the injection stopped, more CO_2 dissolved in the aqueous phase due to gravity effects and concentration gradients. - CO_2 sequestration in saline aquifers by means of mineralisation is limited and doesn't start before about 200 years. - After 10,000 years, up to 90% of the injected CO_2 was dissolved in the brine and about 30% was detained as a free gas while mineral trapping played an insignificant role (about 10%). - A random permeability field increases CO_2 dissolution, while a higher residual gas saturation enhances the CO_2 spatial distribution.
Hassanzadeh et al., (2009)	ECLIPSE 100 (GeoQuest, 2003)	- Formation thickness and layering heterogeneity. - Heterogeneity anisotropic ratio. - The effect of discretization on solution accuracy. - The influence of	- Lesser formation thickness showed higher dissolution during the CO_2 injection period however, it leads to less dissolution in the post-injection period. - Splitting the CO_2 plume by intermingled shale layers into several fronts (i. e. multi-layering) enhances the solubility trapping mechanism of CO_2. - Lower anisotropic ratios (vertical/horizontal permeability) significantly increase CO_2 dissolution. - Coarse grids overestimate CO_2 dissolution over long periods of times (i. e. after 150 years).

		brine injection.	- Injecting brine on top of CO_2 may increase dissolution by about 40%.
Mirzaei and Das, (2007)	STOMP (water-oil) mode (White and Oostrom, 2006)	- Micro-scale heterogeneities effect on the dynamics of multi-phase flow in porous media represented by the dynamic coefficient (τ). - Domain shape, dimensionality and length to diameter (L/D) aspect ratio.. - Permeability anisotropy.	- The dynamics of the flow depend on the geometry of the simulated domain. - *Pc -S* relationship is subjected to greater dynamic effects in heterogeneous domains compared to homogeneous ones. - The dynamic coefficient (τ) increases with the intensity of heterogeneity. - A polynomial function relationship for dynamic capillary pressure may be more applicable at higher water saturation when the desaturation rate is higher. - The higher the aspect ratio of the domain, the higher the dynamic coefficient for both homogeneous and heterogeneous domains at the same water saturation. - At any given water saturation value, higher values of (τ) were observed for lower vertical/horizontal permeability ratios.
Zerai et al., (2006)	Geochemist's Workbench (GWBTM) version 3.2.2 (Bethke, 1996)	- The impact of temperature, pressure, mineralogy, brine composition and CO_2 fugacity on mineral dissolution and precipitation. - To evaluate the intermediate products from mineral-CO_2 enriched brine reactions.	- The mass of dawsonite and siderite precipitated depends on mineral and brine compositions, temperature, and initial CO_2 fugacity. - The brine-to-rock ratio, the kinetic rate of reaction also has a strong impact on the pH and saturation index of the precipitated/dissolved minerals. - The time scale of the chemical reaction is very sensitive to the rate constants. - High CO_2 fugacity is needed for mineral trapping and consequently reactions must be fast enough to reach carbonate phase saturation before the CO_2 is overly diluted by outward radial flow and diffusion.

		- Modelling sensitivity to the reaction rate constant.	
Jikich et al., (2003)	Modified model of UTCOMP Compositional simulator (Chang, 1990)	- The impact of vertical and horizontal injection on CO_2 injectivity into low permeability formations. - The effect of the horizontal injection well length and location on the injectivity of CO_2.	- Horizontal injection can be a way to improve CO2 injection rate. - Horizontal injectors placed at the middle depth offer the best injectivity. - Injectivity increases linearly with the length of the injector. - Heterogeneous formations exhibit lower injectivities than homogeneous ones at same simulation conditions. - One horizontal well with a length of about 1000 m can handle up to 1.5 MMT of CO_2. - It is crucial to consider the fracture pressure when determining the allowable rates and pressures of injection.
Law and Bachu, (1996)	STARS Multiphase, multicomponent numerical model (CMG, 1990)	- The impact of depth, thickness, porosity and permeability on CO_2 injectivity in briny aquifers. - The effects of injection pressure. - The influence of permeability heterogeneity.	- Aquifer thickness plays a moderate role in CO_2 injectivity. - $scCO_2$ density increases with depth, however, mobility ratio decreases, which leads to larger CO_2-brine area and consequently more gas dissolution. - Porosity was found to have only a little effect on the CO_2 injectivity , however, has an important influence on aquifer storage capacity. - The injected CO_2 amount increases nearly linearly with permeability regardless of porosity. - Increasing the injection pressure was found to significantly increase the amount of injected CO_2 under same aquifer characteristics and hydrostatic conditions. - Heterogeneous permeability with zones of high permeability around the injection well, significantly increases the CO_2 injectivity.

2.2. Mathematical Description of Porous Media

Studying and modelling CO_2 sequestration in geological formation needs a clear understanding of multiphase flow characteristics and behaviour in porous media. The related bulk flow properties to pore description include porosity, permeability, dispersion coefficient, tortuosity, capillarity, connectivity, relative permeability, adsorption, and wettability.

2.2.1. Pore Size Distribution

Due to the enormous complexity of the pore structure of any porous media in terms of the number of pores, their size, shape, orientation, and manner of interconnection of the pores, different methods have been considered to describe pore size distributions.

The pore size distribution is defined as a fraction of total pore spaces within a range of pore diameter δ and δ+dδ as shown in the following probability density and distribution functions.

$$\int_0^\infty f(\delta)\ \mathrm{d}\delta = 1 \tag{2.1}$$

$$F(\delta) = \int_\delta^\infty f(\delta)\,\mathrm{d}\delta \tag{2.2}$$

Pore size distribution is measured by one of the following methods:

1. Modelling the porous medium as a bundle of cylindrical capillaries and defining the size distribution as a function of lengths and diameters of the capillaries for consolidated media or giving the capillaries a length to match the pore volume based on the average diameter, for interpreting capillary pressure measurements in terms of pore size.
2. Photomicrographic methods used by Dullien and Mehta (1971-1972), and Dullien and Dhawan (1973) to determine pore size distribution based on calculating the arithmetic average of all chords obtained by intersecting the pores in a photomicrograph with parallel straight lines in all directions. According to Greenkorn (1983), the mean intercept of a bundle of capillaries is equal to four times the ratio of the volume to the surface area, which is four times the hydraulic radius.
3. Using measurements of capillary pressure that is a multi-fluid function property related to the specific free energies of the interfaces between the fluids, and fluids and pore walls. It is also an equilibrium property, directly related to the interfacial tension as explained by

Morrow (1970). Laplace equation expresses the equilibrium condition at which the surface free energy between the fluids is a minimum

$$P_c = \gamma_{12}(\frac{1}{r_1} + \frac{1}{r_2}) \quad (2.3)$$

where P_c = capillary pressure, γ_{12} = specific free energy interface between fluid 1 and 2, which is equivalent to the interfacial tension between them, r_1 *and* r_2 , are the two radii of curvature of the interface at any point.

For a straight cylindrical capillary, the above equation can be simplified to

$$P_c = \frac{2\gamma_{12}}{r} \quad (2.4)$$

where (r) is the average of the two radii

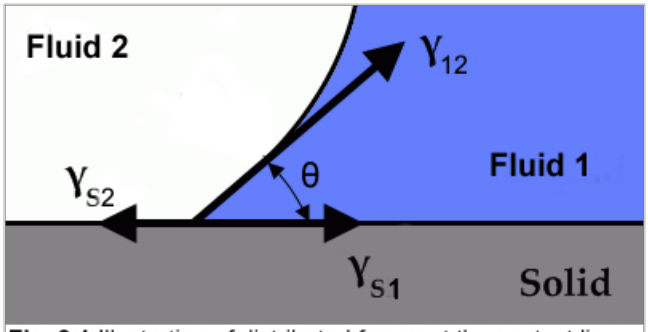

Fig. 2.1 Illustration of distributed forces at the contact line. https://en.wikipedia.org/wiki/Capillary_surface (accessed September, 2012)

The angle at which the fluid-fluid interface and the solid surface can be found from this equation;

$$\cos\theta = \frac{\gamma_{s1} - \gamma_{s2}}{\gamma_{12}} \quad (2.5)$$

where $\gamma_{s1} and\ \gamma_{s2}$ are the free energy of the interface between the solid and fluid 1 and 2 respectively.

The radius of curvature of the meniscus is determined by

$$r = \frac{\sigma}{2\cos\theta} \quad (2.6)$$

Relating this equation to equation (2.4), the capillary pressure for a tube is

$$P_c = \frac{\gamma_{12}\cos\theta}{\delta} = \frac{2\sigma\cos\theta}{\delta} \quad (2.7)$$

where δ is the capillary tube diameter (=2r). For capillary tube it is assumed that $\gamma_{12} = \sigma$ (the interfacial tension between the two fluids).

For fluid surrounding a bundle of rods $\gamma_{s2} = 0$ and $\gamma_{s1} = \gamma_{12} = \sigma$, then $\cos\theta = 1$ and

$$P_c = \frac{\sigma}{\delta} = \frac{2\sigma}{\mathrm{r}} \quad (2.8)$$

Applying a specific pressure to a fluid-filled porous medium, the saturation can be calculated by;

$$S = \int_{\delta_c}^{\infty} f(\delta)\,\mathrm{d}\delta \quad (2.9)$$

where δ_c is the capillary tube diameter at the specific applied pressure.

According to Corey (1977), the relationship between capillary pressure and the saturation of water as a wetting fluid with oil as a non-wetting one, determined in a porous sandstone rock, creates hysteresis as shown in Figure 2.2.

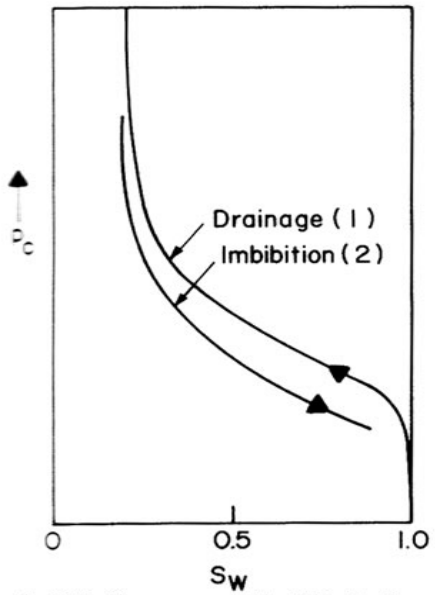

Fig. 2.2 Capillary pressure-wetting fluid saturation for a porous rock. (after Core, 1977.)

Pore size distribution can be determined through measuring the capillary pressure as a function of saturation by injecting a non-wetting fluid into a saturated porous media and integrating collected data in terms of equations 2.2 and 2.7 to obtain pore size distribution as a function of the effective radius of the capillary and as a function of the volume of the injected fluid.

4. Using a nuclear magnetic resonance spectrometry technique, the method that was developed by Lauffer (1981). In this method, a sample of a porous media saturated with brine was placed in a static magnetic field and the resultant spin echo was utilized to determine the pore size distribution in the porous medium from the maximum amplitude spin echo expression. According to the inventor, same technique can be used to determine fluid distribution in a porous medium saturated with mixture of water and hydrocarbon-containing fluids.
5. X-ray computed tomography (XRCT) is a commonly used as a non-destructive methodology to determine porosity and pore size distribution in porous rocks by measuring variations in material density (Farber et al. 2003). This technique uses a set of 2D X-ray images to recreate a 3D structure of an object using a digital geometry processing and mathematical algorithm (Cormack 1963; Cormack 1964; Wellington and Vinegar 1987; Flannery et al. 1987).

There are many more methods used to determine a pore size distribution in porous mediums, like direct measurement of the pores on a set of photomicrographs, and particle size and packing about which are not detailed here.

2.2.2. Effective and Relative Permeability

The relative permeability of a phase in a multi-fluid flow in a porous media is a dimensionless measure of the ratio of the effective permeability of that phase to the absolute permeability which is the “Klinkenberg” or theoretical “air” permeability, that can be determined by cleaning and completely drying a core sample of a porous media before passing air for which the effective permeability represents the absolute permeability of the porous medium.

$$k_{r\alpha} = \frac{k_\alpha}{k} \tag{2.10}$$

Where $k_{r\alpha}$ and k_α are the relative and effective permeabilities of the phase α respectively and k is the absolute permeability of the porous medium in single-phase flow (usually air) which can be determined from the hydraulic conductivity (K) that describes the ease with which water can move through pore spaces or fractures in a porous medium. Permeability (k) is a portion of the Hydraulic conductivity, which depends on the fluid properties (density and viscosity) and can be calculated by equation 2.11 (Domenico and Schwartz 1998).

$$k = \mathrm{K}\frac{\mu}{\rho g} \tag{2.11}$$

2.2.3. Wettability

Wettability is the ability of a liquid to adhere to a solid surface due to their intermolecular interactions. In connection with heterogeneity, wettability has a significant impact on the relative permeability-saturation relationship and can be determined from the combination of cohesion forces, which cause the drop to prevent contact with the solid surface, and adhesion forces that try to spread the liquid across the solid surface in a flow system.

Wetting is also related to capillary effects and occurs at different degrees according to the angle at which fluid1-fluid2 interface meets fluid1-solid interface and called contact angle, which provides an inverse measure of wettability as seen in Figure 2.3 (Shafrin and Zisman 1960). Relative permeability-saturation relationships usually show curve shapes due to the interfacial tension between the fluid phases.

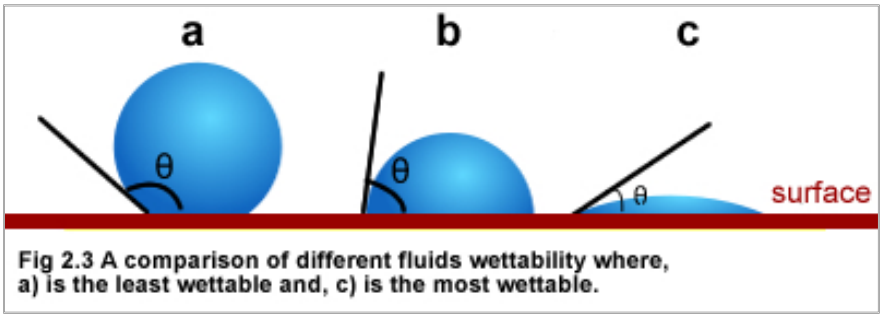

Fig 2.3 A comparison of different fluids wettability where, a) is the least wettable and, c) is the most wettable.

2.2.4. Capillarity

Generally capillarity is known as the ability of a liquid to flow against the gravity in a narrow space such as a thin tube or a porous media due to the combination of surface tension between the liquid molecules which is called cohesion force and force of adhesion between the liquid and the solid surface of the tube or pores wall in a porous medium. In hydrology, capillarity is shown to be important where the capillary action causes groundwater moving from wet areas of a soil to dry ones. It is experimentally approved that the contact length between the top of a liquid column and the tube is proportional to the diameter of the tube, while the weight of the liquid column is proportional to the square of the diameter, so a narrow tube will draw a liquid column higher than a wide tube which is reflected also to porous mediums as low porosity mediums have more

ability to pass fluids by capillary action than those of higher porosity. In CO_2 sequestration reservoirs, capillary forces cause some of the moving CO_2 to coat the solid surface of the rock pores and remain trapped and may dissolve into formation water at later stages. This mechanism is called residual trapping which according to Gough et al., (2006) may trap about 5-30% of the total injected CO_2 into the reservoir.

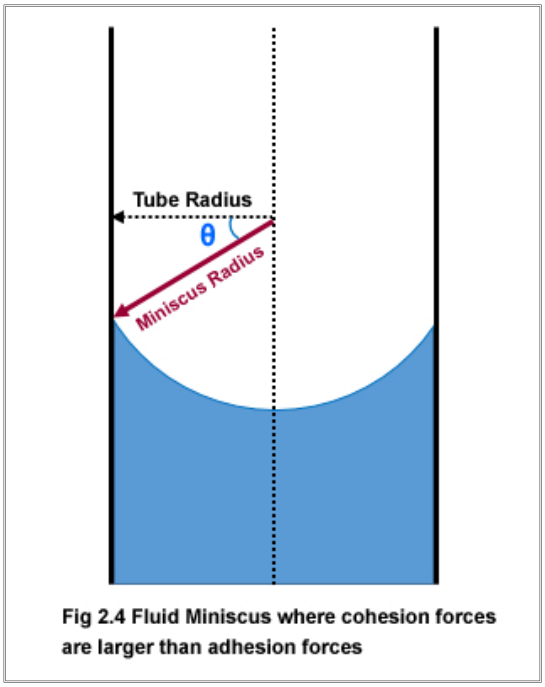

Fig 2.4 Fluid Miniscus where cohesion forces are larger than adhesion forces

In a narrow tube of radius (r), the interface between two fluids forms a concave or convex meniscus of radius (R) depending on their properties and the solids they are in contact with, as illustrated in Figure 2.4. The meniscus radius (R) is a function of the contact angle (θ) and can be easily calculated.

The pressure difference can be found out using the Young–Laplace equation

$$\Delta p = \frac{2\gamma cos\theta}{r} \tag{2.12}$$

In addition, the height of the liquid in the tube can be calculated by

$$h = \frac{2\gamma cos\theta}{\rho g r} \tag{2.13}$$

where r is the capillary radius, R is the meniscus radius, γ is the interfacial tension between the two fluids, θ is the contact angle and, ρ and g are the liquid density and the gravitational acceleration respectively.

2.3. CO_2 Geological Sequestration

Various measures have been developed to mitigate CO_2 emissions including, carbon dioxide sequestration in geological media (Fujii et al. 2007). Carbon sequestration is a technique for managing CO_2 that has been emitted into the atmosphere by combustion of carbon-based fuels.

It is a relatively new concept that had been developed to address the problem of global warming that is attributed to high levels of atmospheric carbon dioxide. In principle, CO_2 sequestration involves capturing carbon that would otherwise be emitted into the atmosphere and storing it safely in the subsurface.

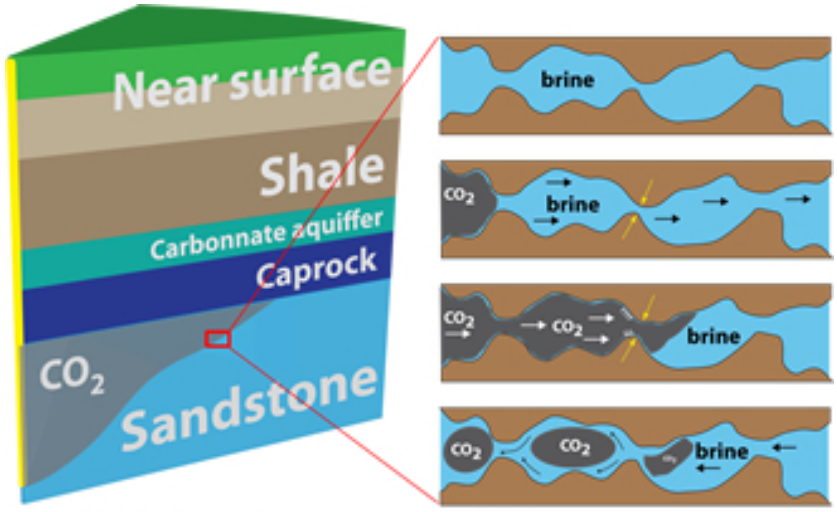

Fig. 2.5 Geological sequestration of CO_2.
(source: www.http://chaire-gaz-naturel.epfl.ch/skills, last visited 27/04/2016)

Formerly, CCS technology included ocean storage, geological storage and surface mineral carbonation (IPCC 2005), however, nowadays it refers only to CO_2 capture, transportation and storage in geological formations (Bachu 2015). According to a survey by the Global CCS Institute in 2010, 80 largescale integrated projects at various stages of development had been identified around the world and further 19-43 large-scale integrated projects to be launched before 2020 (Zahid et al. 2011).

Fujii et al. (2007) explain that the main options available to this method include sequestration in declining gas and oil fields, briny aquifers and unminable coal veins. The oil and gas fields are the favourite places for CO_2 sequestration due to the cost effectiveness as a result of using the same infrastructure used for gas and oil production for the injection of CO_2. In spite of their enormous capacity theses depleted fields' storage capacity is not sufficient for long-term needs.

According to the Intergovernmental Panel on Climate Change (IPCC) Special Report, depleted oil and gas reservoirs are estimated to have a storage capacity of 675–900 $GtCO_2$ and deep saline formations are very likely to have a storage capacity of at least 1000 $GtCO_2$ and some studies suggest it may be an order of magnitude greater than this (IPCC 2005).

While injecting CO_2 into saline aquifers is a clean type of storage, injection of the gas into currently producing oil and gas reservoirs enhances their recovery and helps achieve an economic benefit that could somehow reduce the cost of gas storage (Stauffer et al. 2008). Sedimentary basin aquifers provide the largest potential for carbon dioxide sequestration particularly for regions in the world that are landlocked like United Kingdom (Fujii et al. 2007). According to the authors, injecting carbon dioxide into a geological reservoir requires ascertaining its potential to store the gas in order to avoid leakage back into the atmosphere. They explain that the potential of geological reservoir for sequestration of carbon dioxide has been evaluated with respect regard to several criterions including

- The reservoir's tectonic setting and its geology
- The reservoir's hydrocarbon potential and maturity of the basin
- The hydrodynamic system of water formation
- Economic factors relating to infrastructure as well as access, and
- Social and political factors

Interest in this technology as a powerful means for considerably reducing carbon dioxide is high in developed countries. The technology is expected to be instantly available and technologically feasible for decreasing carbon dioxide emissions in quantity as well as economy. In discussion of modelling CO_2 sequestration, this study will focus on sequestration of carbon dioxide in briny aquifers, how it is injected, the processes that are fundamental and all other important parameters,

which affect the process. The present work also focuses on modelling carbon dioxide and water systems under dynamic multiphase flow conditions in porous media.

2.3.1. Deep Saline Aquifers

Injecting supercritical CO_2 into geological formations represents a multiphase flow in a porous medium because the gas and existing fluid flow as two immiscible fluids. It differs from the conventional waste disposal, which entails a single-phase flow because both the present and disposed fluids are aqueous though with different densities.

To stay in supercritical state carbon dioxide has to be injected at high pressure and maintain high temperature the conditions that are employed in deep underground. Supercritical CO_2 is considerably heavier than the gaseous phase but lighter than the occupant formation brine, which has higher viscosity than the CO_2. As a result of that difference, CO_2 migrates buoyantly away from the injection well overcoming gravity forces with the consideration of the fingering viscosity forces.

In their study, Nordbotten et al., (2004b) analytically described the time evolution of the CO_2 plume based on a simplified form of Buckley-Leverett equation dominated by viscous forces with irrelevant effect of the CO_2 buoyancy forces that can be included to identify when this form of solution is applicable. Comparing their analytical solution results with similar numerical ones they demonstrate that the simplified viscous-dominant analytical solution applicable for a wide range of injection situations. They utilized their modelling results to inspect the accuracy of assuming constant properties for the present fluids in the storage formation specifically their compressibility. They also discussed some cases where buoyancy and nonzero residual saturations has more influence on the mobility of CO_2 plume in addition to the effects of CO_2 dissolution into water and water desertion of the CO_2.

One of the limiting factors in employing geological sequestration of CO_2 is the accurate estimation of the storage capacity of the potential site, which is limited by pressure build up as a result of the applied injection rate, permeability reduction due to the salt precipitation and hydrostatic conditions. Estimating CO_2 storage in deep saline aquifers has been a challenge because of their continuous nature, different concepts used in estimating storage capacity and the

various trapping mechanisms in deep saline aquifers that operate in different time scales (Michael et al. 2010; IPCC 2005).

2.3.2. CO_2 and Brine Properties

Carbon dioxide is a colourless chemical compound with insignificant irritating odour. At atmospheric temperature and pressure, carbon dioxide is in the gas phase up to temperature ranges between -56.5 and 31.1 ℃ however, at temperatures below -78 ℃, it is a solid. At temperatures and pressures higher than critical values (31.1 ℃, 7.38 MPa), CO_2 is in supercritical state with large gradients in properties such as density, viscosity and solvent strength occurring at conditions near the phase boundary (Shukla et al., 2010). The solubility of CO_2 in water decreases with increasing temperature and salinity, and increases with increasing pressure as exposed in Fig. 2.6 (IPCC 2005).

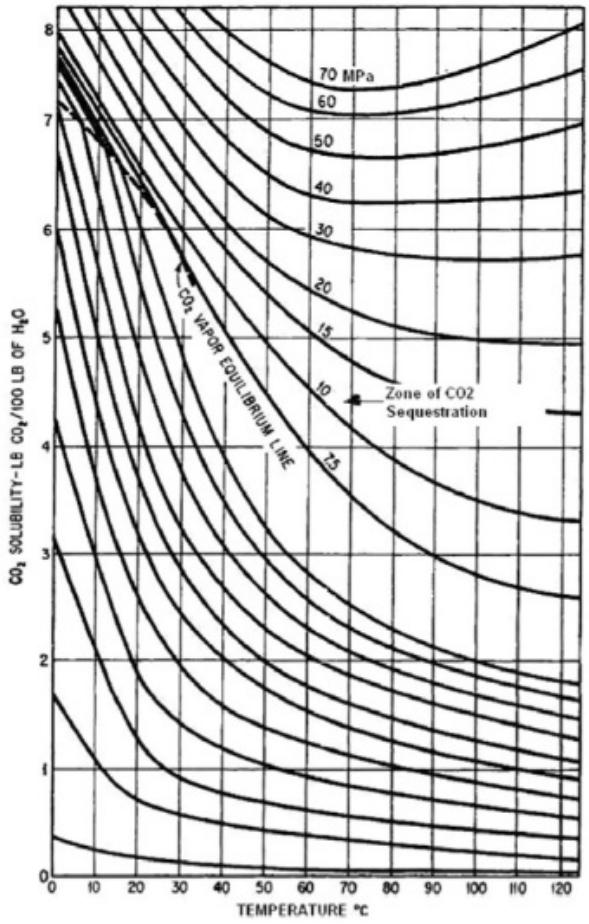

Figure 2.6. Solubility of CO_2 in water (after Shukla et al. 2010, reused with permission from the publisher “Elsevier Limited”, License no. 3856750944318 on Apr 26, 2016).

In an aqueous solution, CO_2 forms carbonic acid, which is too unstable to be easily isolated. CO_2 solubility in brine can be estimated by the following empirical relation (Enick and Klara, 1990):

$$w_{CO_2,b} = w_{CO_2,w} \cdot (1.0 - 4.893414 \cdot 10^{-2} \cdot S + 0.1302838 \cdot 10^{-2} \cdot S^2 - 0.1871199 \cdot 10^{-4} \cdot S^3) \quad (2.14)$$

where $w_{CO_2,b}$ is CO_2 solubility, S is water salinity and the subscripts w and b stand for pure water and brine, respectively.

CO_2 is considerably stable at standard conditions and has a density of 1.872 kg/m^3, which is higher than air. At values higher than critical point (31.1 ℃, 7.38 MPa), CO_2 transits into a supercritical fluid with density that is significantly dependant on pressure and temperature and may vary in a range of 150 to 800 kg/m^3 which are similar to the hydrostatic conditions found in sedimentary basins (Bachu 2003). Figure 2.7 shows the profiles of density and viscosity as functions of temperature and pressure.

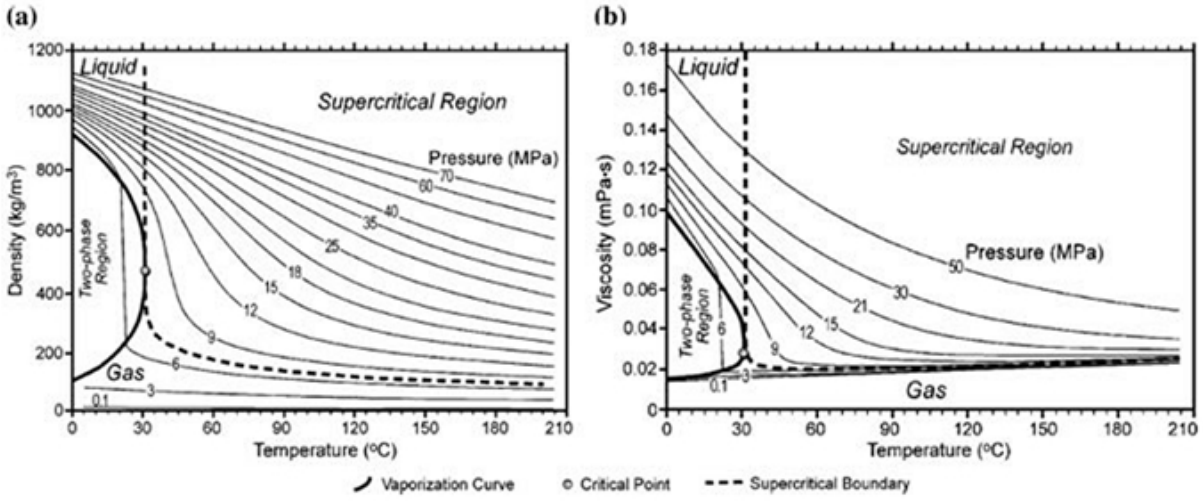

Fig. 2.7 Density and viscosity values for CO_2. (After Nordbotten et al. 2005, reused with permission from the publisher "Springer", License no. 3856770331702 on Apr 26, 2016)

To assure successful injection of carbon dioxide into porous formations, it is crucial to determine the expected properties of the gas at the characteristic injection process conditions. The gas-phase density and viscosity are significantly influenced by the geothermal system in the sedimentary sink. According to that, different basins had been identified by Bachu (2003) based on their depth from the surface, surface temperature and geothermal gradient. Shallow basins are

about 1000 m whilst deep ones are around 3000 m below ground surface. The author further demonstrates that for the cold basins that have a surface temperature about 10 ℃, the temperature gradient is nearly 25℃/km while the warm basins with surface temperature around 20 ℃ represent a gradient of 45℃/km. These figures control the optimal depth at which CO_2 injection should occur to preserve the CO_2 in a supercritical state. The typical hydrostatic pressure gradient is estimated to be 10.5 MPa/km in saline aquifers. Therefore, assuming that and combining the types of basins above, CO_2 density and viscosity can be determined. CO_2 and water (brine) properties are detailed in Table 2.2 taking into account the salinity of brine in the simulated aquifer.

Table 2.2. Fluids properties, after Wagner et al. (2000).

Property	CO_2	Water (Brine)
Critical temperature, ^oC	30.98	652.68
Critical pressure, MPa	7.38	23.22
Critical volume, l/gmole	0.94	0.053
Critical density, kg/m^3	468.2	334.64
Salt mass fraction	-	0.20
Molecular weight, g/gmole	44.01	18.015
Acentric factor	0.22394	0.344
Gas constant (R), J/kg k	188.9241	461.526
Coefficient of compressibility (at 65 ^oC and 16 Pa)	0.4332	-
Density, kg/m^3 (at 65 ^oC and 16 MPa)	585.975	987.4
Dynamic viscosity, Pa. s (at 65 ^oC and 16 MPa)	45.4595e-6	4.371e-4

It is proven that formation brine density and viscosity decrease with temperature rise but weakly increase with pressure, which increases with aquifer depth. This applies to the case of this study as the density and viscosity of the brine occupied in geological formations are mostly affected by salinity and temperature but least affected by pressure because water is almost considered to be incompressible.

In addition to Adams and Bachu (2002) who claim that density values may reach 1300 kg/m3 and viscosity values in saline aquifers can be around 1.3 MPa.s, a series of formulas (McCain, 1991; Rowe et al. 1970; Mercer et al. 1975; Kestin et al. 1981; Batzle and Wand, 1992; Phillips

et al. 1981) have been developed aiming to determine the effects of temperature, pressure and salinity on the density and viscosity of water (brine).

A comparison study carried out by Adams and Bachu (2002) demonstrates that for a salinity of 0.4, the difference in estimated values of densities and viscosities using various algorithms reaches 20% and 50% respectively. Hydrostatic conditions in aquifers involve a wide range of pressure and temperature values and according to Adam and Bachu's study, the Batzle and Wang (1992) correlation is the most applicable to estimate values of fluid density in sedimentary basins however, for viscosity estimation, the formula developed by Kestin et al. (1981) better fits. Formulations developed by Adams and Bachu (2002) are applicable for calculating fluid properties in basins with salinity ranges from 0.02 to 0.3 for different injection depth scenarios and based on determining the ratios of the fluids density, ρ_c/ρ_w and viscosity μ_c / μ_w that vary for each type of basins described earlier in this section showing lower values for higher temperatures, lower depths and greater salinities. These variations signify that buoyancy-driving forces proportionally varies with viscosity forces and should be critically considered in describing CO_2 injection into deep saline aquifers and other geological formations. In their published work, Adams and Bachu (2002) used their correlations in different numerical simulations and compared the results to the derived analytical solution to determine the accuracy of their algorithms.

2.4. Modelling CO_2 injection: Effective Parameters

Sensitivity analysis of the applicable model parameters is critical in modelling, and gaining useful understanding of the involved processes. Therefore, an analysis is needed to assess the effects of the system attributes on the trapping and migration of carbon dioxide (CO_2) by successively varying one parameter while the rest are held at constant values. In this case, the modelling parameter that greatly influences the migration of the CO_2 is noted. This gives guidance in the subsequent modelling of injection sites. However, it is worthy to note that the different responses obtained as a result of varying the model parameters will be dependent on the applicable site and system.

2.4.1. Injection Rate

The capacity and efficiency of geological formations to store CO_2 depends on the maximum injection rate it can hold without reaching the maximum pressure build-up (MPB), which is of more concern in confined formations. Therefore, care must be taken when setting the injection rate, which is controlled by the injection pressure, for any CO_2 sequestration project to avoid any damage to the overlaying caprock that might lead to gas leakage.

Increasing the injection rate increases CO_2 migration and consequently increases the residual trapping of the gas by capillary forces as a result of CO_2 invasion into an expansive area of the pore sizes. However, further increase in the rate of injection causes a decrease in the migration of the cumulative CO_2 because the increased mass is halted by the capillary forces (Schnaar and Digiulio, 2009).

Continuous injection of CO_2 into closed or semi-closed systems causes pressure build-up, which may lead to geomechanical damage in the overlaying caprock by reaching maximum sustainable pressure that should be avoided in all CO_2 sequestration processes. The analytical method modified by Zhou et al. (2008) to quickly weigh up the aptitude of CO_2 storage in closed and semi-closed systems is based on the fact that as a result of pressure build-up, additional amount of CO_2 may displace the resident brine within the storage media. To validate their method they compared their results with the ones from a true numerical model and achieved good agreement with them in regards to the pressure raise history and the efficiency factor of storage. Moreover, the results by Zhou et al. (2008), depicted that the cap-rock permeability has important effect on pressure increase in the storage formation. They show that seal permeability varying from 10^{-19} to 10^{-17} m^2, causes brine leakage and consequently reduces pressure rise in the storage formation, which in turn significantly enhances CO_2 storage efficiency and ensures safe entrapment (Zhou et al., 2008). The results demonstrated almost no effects of permeability on the average pressure change through the whole domain however pore compressibility, has a significant influence on the average pressure increase as a result of CO_2 injection.

It is important to continuously monitor the condition of injection wells at any CO_2 storage site by measuring the injection rate and resulted pressure rise using gauges either at the well-head or across the gas distribution area. Typically, devices that relate pressure drop to the flow rate like orifice meters, are used to measure CO_2 injection rates. Various pressure sensors are used at the

well-head or across the storage site to monitor injection pressures to avoid exceeding the safe threshold or to detect any pressure drop as a result of CO_2 leakage. Increasing the injection rate can slightly improve the gas injectivity and tends to limit the loss of permeability caused by salt precipitation in the near-wellbore region (Giorgis et al., 2007). Well injectivity is also influenced by the surrounding strata as higher permeability of the adjacent layers promotes the migration of the displaced brine through the multilayered system, thereby attenuating pressure build-up in the aquifer and improving gas injectivity (Birkholzer et al., 2009; Chasset et al., 2011).

2.4.2. Formation Permeability and Heterogeneity

Permeability is a measure of how easily and efficiently fluids can flow in a porous medias depending on the pore size and the way they are connected. Permeability is a dynamic property that depends on the cross-sectional area as well as pressure changes and viscosities of the fluids involved according to Darcy's law (Kovscek, 2002; Flett et al., 2005; Fitch, 2011). Permeability plays a key role in geological sequestration of CO_2 because it controls the injectivity and mobility of the injected gas. It is closely related and dependent on porosity, which refers to the volume percentage of pore space in the formation rock and depends on the grain size and shape of the solid partices, and the distribution of grain sizes. Porosity ($\emptyset$) and permeability (k) are related by the following regression equation (Chasset et al., 2011);

$$log_{10}k = 15.58\emptyset - 16.57 \tag{2.15}$$

where k is measured in m^2.

The mobility of the injected CO_2 in homogeneous formations increases with an increase in permeability while comparing layered heterogeneities, the sweep and CO_2 dissolution rates in the resident brine are increased by the availability of shale layers along with sand or carbonate layers in the formation rock because they retard the upward progression of the CO_2-rich phase (Bachu and Bennion, 2008). The same results were achieved by Law and Bachu (1996) who further used regression analysis and a simple steady-state radial outflow model to generalize their numerical results and formulate the following relationship between the CO_2 injectivity ($Q/[D(p_i - p_a)]$) and its mobility (kk_r/μ) ;

$$Q/[D(p_i - p_a)] = 0.000538\,\rho\ (kk_r/\mu)/ln(r_e/r_w) \quad (2.16)$$

where Q represents the CO_2 mass rate in tonnes/day ; D is the aquifer thickness (m), p_i and p_a define the injection and aquifer pressures in MPa, respectively; k and k_r are the absolute permeability of the aquifer ($10^{-15}m^2$) and CO_2 relative permeability, respectively; ρ and μ are CO_2 density (kg/m^3) and dynamic viscosity (mPa.s) respectively; and r_w and r_e are the radii of the injection well and injection influence, respectively. The authors assumed well completion for the whole thickness of the aquifer and determined the absolute permeability k for anisotropic aquifers as;

$$k = (k_h k_v)^{0.5} \quad (2.17)$$

where k_h and k_v are the horizontal and vertical permeability respectively.

For constant CO_2 properties and the radius of injection influence, equation (2.16) can be simplified to equation (2.18) to calculate the CO_2 injection rate into homogeneous aquifers (Law and Bachu,1996).

$$Q = 0.0208(k_h k_v)^{0.5} D\,(p_i - p_a)/\mu \quad (2.18)$$

Furthermore, increased heterogeneity enhances lateral migration and as a result, the rate of dissolution increases (Law and Bachu, 1996; Schnaar and Digiulio, 2009). Pruess and Garcia (2002) demonstrated that in the case of discharge simulations through faulty areas, reduced permeability of the fault resulted in slow leakage to the surface and an enhanced maximum rate of leakage.

Investigating the difference in the flow rate of fluid in homogeneous media and different types of heterogeneous media, Alabi (2011) found out that the permeabilities of heterogeneous media are lower than the permeabilities of homogeneous media and that mixed heterogeneous domain has the highest permeability which means that fluid flow faster in mixed heterogeneous than layered heterogeneous media. This is because of non-uniform grain distribution with large pore size interconnectivity. Numerical simulation results by Law and Bachu, (1996) showed that the existence of high permeability zones around the injection well in low-permeability aquifers in addition to the contrast between the local and regional permeability values, significantly enhances the injectivity of CO_2 and consequently increases the cumulative injected amount.

2.4.3. Relative Permeability and Saturation Relationships

Generally, permeability represents the capacity for a fluid to flow through interconnected pores within a porous media. The SI unit for permeability is m^2 and practically it is also measured by darcy (d) or millidarcy (md) where (1 darcy ≈ 10^{-12} m^2). Permeability (*k*) is part of the hydraulic conductivity (K) of the porous media, which describes the affluence with which a fluid can move through any available voids with in the medium. It is influenced by the degree of saturation, density and viscosity of the flowing fluid in addition to the intrinsic permeability (*k*) of the medium material. Intrinsic (absolute) permeability is a bulk (physical) property (i.e. does not depend on the media size or amount of material in the system), which represents the aptitude of the porous media to permit fluids to flow through.

The term of effective permeability ($k_{e\propto}$) refers to the permeability of each phase in a multi-phase flow system and it is a function of effective saturation ($S_{e\propto}$) that can be calculated by:

$$S_{e\propto} = \left(\frac{S_\propto - S_{r\propto}}{1 - S_{r\propto}}\right) \tag{2.15}$$

where, $S_{r\propto} \equiv$ irreducible saturation for the wetting or nonwetting phase $[-]$

Relative permeability for CO_2-water flow in porous formations as a two-phase flow system is defined as the portion of permeability of each phase depending on the saturation of that fluid within the domain and can be calculated through a variety of correlations and functions (Brooks and Corey 1964; Van Genuchten 1980; Mualem 1976; Land 1968). It can be calculated from effective saturation:

$$k_{r\propto} = S_{e\propto}^{(2+\lambda)/\lambda} \tag{2.16}$$

where, λ is the pore size distribution.

And accordingly the effective permeability ($k_{e\propto}$) of any phase can be calculated through;

$$k_{e\propto} = k_{r\propto}\, k \tag{2.17}$$

where,

$k_{r\propto} \equiv$ relative permeability of the wetting or nonwetting phase $[-]$

$k \equiv$ interinsic permeability of the porous media [–]

Benson et al. (2012) describe relative permeability as one of the most important properties influencing the behaviour and transport of CO_2 in the subsurface because it affects almost all important aspects of the storage process including, the spatial extent of the CO_2 plume, the injectivity of a well, the extent of capillary trapping, and the gas leakage through the seal.

Relative permeability (k_r) - saturation (S) relationships are characteristic curves that describe the relative permeability of water and CO_2 based on their relative saturation within a given point or location as shown in Figure 2.8. In addition to the dependency of the relative permeability on the residual saturation, it also depends on the direction of the saturation change.

This direction change is referred to by hysteresis, which indicates the irreversibility of multiphase flow when it transits from drainage (when the non-wetting phase replaces the wetting phase at the front end of the plume) to imbibition (when the wetting phase invades back the domain to replace the non-wetting phase at the trailing end of the plume).

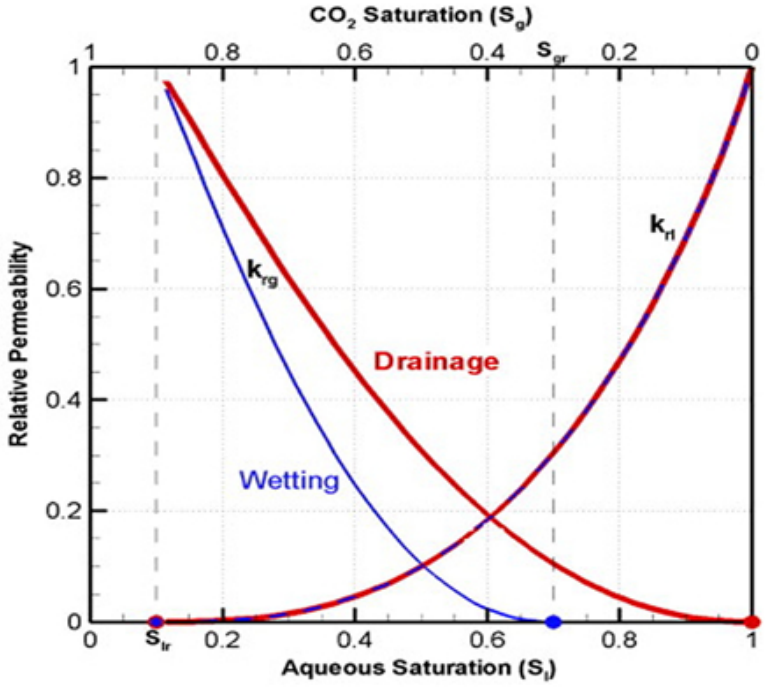

Fig. 2.8 Typical non-hysteretic characteristic curves. (after Doughty 2007, reused with permission from the publisher "Elsevier Limited", License no. 3857150156755 on Apr 27, 2016)

The advantage of this process in the context of the CO_2 storage is that a significant amount of the injected gas is residually trapped in some pore spaces to be dissolved at later stages of the

storage process. elative permeabilities and capillary pressure are complex functions of the structure and chemistry of the fluids and solids in a reservoir and as a result, they are spatial dependent. Predominantly, k_r-S relationships are experimentally measured but a network of developed models have been used to estimate such functions (Fanchi and Christiansen, 2015).

According to Doughty (2007) choosing these curves has essential power on the shape and size of the plume and its progress. They also pointed out that the results obtained from different models were highly sensitive to the parameters of the characteristic curve. Neufeld and Huppert (2009) clarified that the consideration of capillary trapping as well as hysteresis led to a CO_2 distribution that was highly spread out as well as with low caprock accumulation.

2.4.4. Mineral Precipitation and Dissolution Kinetics

Mineral trapping (also named mineral carbonation) is a permanent sequestration mechanism that governs the ultimate fate of the injected CO_2. It refers to the reaction of metal bearing oxides with CO_2 via a series of chemical reactions to form insoluble solid carbonates that are environmentally stable due to their low energy state (60-180 kJ/mol) compared to that of CO_2, which is 400 kJ/mol (Azdarpour et al. 2015). Mineral carbonation consists of two different methods; in situ, which involves production of carbonates by injecting CO_2 into geological formations and ex situ that can ensue either directly through gas/aqueous-solid-mineral carbonation in a single step or indirectly through several stages using different technologies, like acid extractions, bioleaching, pH swing process, the molten salt process, ammonia and caustic extraction (Sipilä et al., 2008; Bobicki et al., 2012).

Mineral carbonation in briny aquifers (in situ carbonation) takes place when part of the injected CO_2 dissolves in the resident brine to form carbonic acid that decomposes into H^+ and HCO_3^- ions and increases the acidity of the solution (i. e. lower pH). The dissolution of CO_2 can be presented by the following reactions (Rochelle et al. 2004);

$$CO_2 + H_2O \ <==> \ H_2CO_3 \tag{2.18}$$

$$H_2CO_3 \ <==> \ H^+ + HCO_3^- \tag{2.19}$$

$$HCO_3^- \ <==> \ H^+ + CO_3^{--} \tag{2.20}$$

The chemical reactions involved in mineralization depend on the mineralogy of the formation rock. Most sandstone formations consist of quartz and minor amounts of K-feldspar, Calcite , Kaolinite, Illite and chlorite (Beni et al., 2012). The increased acidity of the solution in the aquifer results in the dissolution of many of the primary minerals of the rock matrix (e. g. calcite, Kaolinite and Illite) releasing divalent cations that induce the precipitation of secondary carbonates such as Dolomite, Dawsonite and Siderite. The most important primary minerals that contribute in carbonate precipitation, are those mainly containing divalent cations (M^{++}) including; Ca^{++}, Mg^{++} and Fe^{++} (Soldal, 2008).

Soon after the injection of $scCO_2$, the pH sharply declines (acidity increases) as a result of chemical reactions inducing; the dissolution of calcite (the main primary minerals of the carbonate formations) and precipitation of dolomite in the short-time frames of geological sequestration according to the following equations (Beni et al., 2012);

$$CaCO_3\,(\text{Calcite}) <==> Ca^{++} + CO_3{}^{--} \quad (2.21)$$

$$Ca^{++} + Mg^{++} + (CO_3)^{--} <==> CaMg\,(CO_3)_2\ (\text{Dolomite}) \quad (2.22)$$

After few hundred years, albite alteration starts forming kaolinite and calcite followed by dawsonite when Ca^{++}cations decrease according to the following reactions (Beni et al. 2012);

$$2NaAlSi_3O_8\,(\text{Albite}) + CO_2 + 2H_2O + Ca^{++} <==> 4SiO_2 + CaCO_3(\text{Calcite}) + Al_2Si_2O_5\,(OH)_4\,(\text{Kaolinite}) + 2Na^+ \quad (2.23)$$

$$2NaAlSi_3O_8\,(\text{Albite}) + CO_2 + H_2O <==> NaAlCO_3\,(OH)_2\,(\text{Dawsonite}) + 3SiO_2 \quad (2.24)$$

Siderite may also be formed by the alteration of chlorite:

$$2Na_{2.5}Mg_{2.5}AlSi_3O_{10}(OH)_8\,(\text{chloite}) + 2.5CaCO_3\,(\text{calcite}) + 5CO_2 <==> 2.5FeCO_3\,(\text{sidirite}) + CaMg\,(CO3)2\ (\text{Dolomite}) + SiO_2 + 2H_2O \quad (2.25)$$

The rate of mineralization reactions is affected by the formation mineral and the hosted brine composition, salinity, temperature and the geochemical interaction surface area between the fluids and rock matrix. Increased salinity and temperature reduces the solubility of CO_2 in water while lower temperatures greatly decelerate the rate of chemical reactions (Rosenbauer et al.,

2005). The capacity of storage reservoirs depends on the geochemical reactions involved and the produced chemical complexes during these reactions.

Siliciclastic aquifers demonstrate better "mineral trapping" characteristics for CO_2, because the injection of CO_2 takes much longer (hundreds of years) to reach equilibrium compared to the case of carbonate aquifers and the availability of hydroxide components such as $Mg(OH)_2$, $Ca(OH)_2$ and $Fe(OH)_2$ that are less abundant in carbonates (Gunter et al., 2000). The geochemical interaction between the CO_2–brine–rock is likely to result in acid hydrolysis of the rock minerals and can have several different effects on the caprock and the overall migration of the injected CO_2 (Shukla et al. 2010). Precipitation of the carbonate minerals as a result of geochemical reactions may enhance storage safety through increasing the integrity of the caprock by sealing the existed fractures and reducing the permeability of it that leads to enhanced isolation of the CO_2-saturated water as experimentally and analytically presented by (Rosenbauer et al., 2005).

Mineral reactions are either controlled by the local equilibrium or kinetic conditions and the rate of these reactions (r_m) can be determined by a general equation (Lasaga, 1984; Steefel and Lasaga, 1994);

$$r_m = -sgn\left[log\left(\frac{Q_m}{K_m}\right)\right] k_m A_m \left|\left[\left(\frac{Q_m}{K_m}\right)^{\mu} - 1\right]\right|^{n} \quad (2.26)$$

Where r_m is the mineral dissolution/precipitation rate, A_m is the specific reactive surface area per kg of water, k_m is the rate constant , K_m is the equilibrium constant , Q_m defines the ion activity product, μ and n are positive numbers determined experimentally.

$-sgn\left[log\left(\frac{Q_m}{K_m}\right)\right]$ ensures that the correct sign is enforced when the exponents μ and n are not equal to one (Xu et al., 2004).

The reaction rate constant is temperature dependent and can be calculated by the following equation (Lasaga, 1984; Steefel and Lasaga, 1994);

$$k = k_{25} exp\left[\frac{-E_a}{R}\left(\frac{1}{T} - \frac{1}{298.15}\right)\right] \quad (2.27)$$

Where E_a is the activation energy and k_{25} is the rate constant at 25 ℃, which are kinetic properties of the minerals. R is the gas constant and T is the absolute temperature.

Mineral reactive surface areas are calculated using the geometric area of a cubic array of truncated spheres that make up the framework of the rock (Sonnenthale, 2001).

Under favourable conditions the amount of CO_2 that may be sequestered by precipitation of secondary carbonates is significantly dependent on the minerology of the rock. It is comparable with and can be larger than the solubility trapping and ranges between 17 – 100 kg per m^3 (Xu et al., 2004). However, mineral trapping is a very slow process at geological formation conditions and it is difficult to experimentally represent scenarios of deep geological reservoir under high temperature and pressure conditions, therefore numerical modelling of geochemical reactions involved in geological sequestration of CO_2 is crucial to investigate the ultimate fate of the injected supercritical gas after long-time frames of storage (hundreds of thousands of years) (Xu et al., 2004; IPCC, 2005). Since early 1990s, several empirical and modelling studies at different scales have been carried out to assess the feasibility of geological sequestration of CO_2 (Gunter et al., 1993, 1996, 1997; Bachu et al., 1994, 2003, 2007; Law and Bachu, 1996; Doughty and Pruess, 2004; Bottero et al., 2006; Das et al., 2006, 2007; Das and Merzaei, 2012, 2013; Bickle at al., 2007; Birkholzer et al., 2007, 2009; Bielinski, 2007; Plug and Bruining, 2007; Bachu, 2008; Frailey, 2009; Szulczewski, 2009, 2013; Szulczewski et al., 2011; Spycher and Pruess, 2010; Beni et al., 2012; Hanspal and Das, 2012; Mehnert et al., 2013; Mirzaei, and Das, 2007, 2013; Vilarrasa, 2014; Zhao et al., 2014; Khudaida and das, 2014).

The amount of mineral trapping of CO_2 is mainly responsive to the fugacity of the initial injected CO_2 and the initial composition of the hosted brine as they have a great influence on the mass of precipitated siderite ($FeCO_3$) and dawsonite ($NaAlCO_3(OH)_2$) carbonates which show more stability at low pH values and tend to be crucial in mineral trapping mechanism. In a reaction and kinetic modelling study of CO_2-brine-mineral reactions in a sandstone and carbonate saline aquifer by Zerai et al. (2006), it was demonstrated that “dissolution of albite, K-feldspar, and glauconite is potentially very important for mineral trapping of CO_2 and that a high CO_2 fugacity is needed for mineral trapping and consequently, reactions must be fast enough to reach carbonate phase saturation before the CO_2 is overly diluted by radial flow and diffusion”. Results from their kinetic modelling indicated that up to first few hundred years the solubility trapping is the most governing mechanism in CO_2 sequestration process while after that, the mineral trapping may take an important role.

Another numerical study by Beni et al. (2012) evidenced that after 10,000 years, more than 80% of the injected CO_2 was precipitated as mineral carbonates reducing the risk of any future leakage to the surface however, the mineral reactions resulted in decreased porosity and consequently reduced permeability by about 90%. In agreement with other works (Zerai et al., 2006; Mitiku et al., 2013), the authors found out that during the injection period, mineral trapping is not significant but after 200 years it starts to contribute. Additionally they concluded that CO_2 dissolution into brine does not significantly affect the pressure build-up however, it reduces the pressure in the reservoir due to the CO_2 volume change from gas to aqueous phase.

Schnaar and Digiulio (2009) concluded from their work that changing the CO_2-brine-solid surface area by a given factor is equivalent to the proportionally increased time of reaction by an equal factor. On the other hand, it was indicated that the kinetic rates have a large influence on the permeability changes of the porous formation (Gorke et al., 2010).

2.4.5. Injected gas composition

The composition of the injected CO_2 stream into geological formations including saline aquifers has a noticeable impact on the mineral alteration of the rock matrix and geochemical reactions at all stages of the geological sequestration of CO_2. Co-injection of acid gases (SO_2 and H_2S) with CO_2 is a mature and safe technology because by the end of 2002, approximately 40 facilities in Canada applied this technology to dispose 1.5 Mt CO_2 and 1 Mt H_2S and 16 more have been active in the United States (Bachu et al., 2005). These acid gases are highly soluble in water and produces precipitated carbonate and sulfate minerals when dissolve in the hosted brine. SO_2 dissolves in water forming H_2SO_3 acid which oxidises to form H_2SO_4, while H_2S remains in gaseous form. Many recent researches have assessed the influence of the common contaminants of CO_2 streams with hydrogen sulphide (H_2S) and sulfur dioxide (SO_2) on mineral trapping as well as geochemical reactions.

Mineral reaction kinetics have been modelled by Gunter et al. (2000) using the reaction path computer code PATHARC.94 (Perkins et al., 1997). They investigated the following mineral reactions;

$$\text{Anorthite } (CaAl_2Si_2O_8) + 2H_2O + CO_2 <==> \\ \textit{Calcite } (CaCO_3) + \text{Kaolinite } (Al_2Si_2O_5(OH)_4) \quad (2.28)$$

$$\text{Olivine } ((\text{Mg}, \text{Fe}^{--})_2\text{SiO}_4) + \text{H}_2\text{SO}_4 <==> 6\text{SO}_4^{--} + \text{Mg}^{++} + \text{Quartz } (\text{SiO}_2) + \text{H}_2\text{O} \quad (2.29)$$

$$3\text{Annite } \left(\text{KFe}_3{}^{++}\text{AlSi}_3\text{O}_{10}(\text{OH})_2\right) + 10\text{H}_2\text{S} <==> 9\textit{Pyrrhotite } (Fe\text{S}_2) + \text{S}^{--} + 2\text{K}^{+} +$$
$$\text{Muscovite } (\text{KF}_2(\text{Al}_2\text{O}_3)_3(\text{SiO}_2)_6(\text{H}_2\text{O})) + 6\text{Quartz } (\text{SiO}_2) + 12\text{H}_2\text{O} \quad (2.30)$$

In the case of injecting SO_2 with CO_2 into carbonate formations, the study revealed that calcite breaks neutralizing the acidity of the solution and releasing Ca^{++} cations, which combine with the SiO4 anion to form anhydrite or gypsum (Gunter et al., 2000);

$$\text{Calcite } (\text{CaCO}_3) + \text{H}_2\text{SO}_4 <==> \textit{Anhydrite } (\text{CaSiO}_4) + \text{H}_2\text{O} + \text{CO}_2 \quad (2.31)$$

This reactions rapidly take place and result in CO_2 pressure build-up which may fracture the sealing layers and escape out of the aquifer.

In contrast, in silicate aquifers, reactions are much slower and equilibrium takes hundreds of years to reach after injection, however CO_2 pressure decreases as a result of forming siderite ($FeCO_3$) and the regression of anhydrite back to form calcite ($CaCO_3$).

On the other hand, co-injecting H_2S with CO_2 increases the pH rapidly and breaks down siderite and releases Fe cations, which combine with sulphide to form pyrrhotite;

$$\text{Siderite } (\text{FeCO}_3) + \text{H}_2\text{S} <==> \textit{Pyrrhotite } (Fe\text{S}_2) + \text{H}_2\text{O} + \text{CO}_2 \quad (2.32)$$

Similar to the case of co-injection of SO_2 into silicate aquifers, as a result of the reaction in Equation 2.31, H_2S pressure decreases and CO_2 pressure increases. The increase in CO_2 pressure diminishes later as a result of the breakdown of annite, which releases Fe cations to reproduce siderite. In both case of co-injection, silicate minerals do not capture SO_4 and H_2S, however they mediate the release of CO_2 from the existed carbonates and trap it as siderite or pyrrhotite as a result of annite decomposition (Gunter et al., 2000). The initial abundance of chlorite and oligoclase affects CO_2 mineral-trapping capability because the first provides Fe^{++} for siderite and ankerite precipitation while the second provides Na^{+} for the precipitation of dawsonite.

Furthermore, injecting H_2S with CO_2 has no adverse impact on the injectivity during the injection period however, co-injection of SO_2 results in reduced porosity and permeability of the formation due to the production of sufficient amounts of anhydrite (Xu et al. 2004). In the long-term, the acid is neutralized through silicate dissolution, which leads to more carbon in the

existing fluid that is trapped as mineral carbonate in the case of injecting SO_2 coupled with CO_2. Additionally, co-injection of these contaminants helps minimizing the costs of separation and disposal of them during natural gas production (Knauss et al.,2005).

2.5. Chapter Summary

To address the issue of global warming which is related to an increasing level of emitted carbon dioxide from the main sources, it is crucial to highlight the viability of carbon capture and sequestration (CCS) as an immediate technology to mitigate CO_2 concentration in the atmosphere and assess the feasibility of potential storage areas including saline aquifers to dispose the captured gas.

In this chapter, the concept of geological carbon sequestration (CS) was discussed as one of the steps of CCS technology to safely store CO_2 in geological porous formations focusing on DSAs that are considered to be one of the most feasible means of geological storage of CO_2. The trapping mechanisms of the injected gas in DSAs were briefly introduced and explained. Additionally, a number of related previous works were illustrated in a table to display the studied factors and achieved results by the authors for comparison purposes.

For better understanding of water-CO_2 flow characteristics and behaviour in sedimentary formations, a mathematical description of porous media was described in this chapter beside the influence of the geothermal system on the physical properties of the injected gas.

Furthermore, the effects of the system attributes including, injection rate, formation permeability and heterogeneity, relative permeability, mineral precipitation and injection gas composition on the trapping and migration of carbon dioxide (CO_2) were analysed and discussed in this chapter. Co-injection of acid gases like SO_2 and H_2S with CO_2 has a noticeable impact on the carbon mineralization geochemical reactions at all stages of the geological sequestration of CO_2 in addition to minimizing the costs of their separation during natural gas production.

Chapter 3

Modelling Approach

Overview

In this chapter, a brief review of the employed simulator (STOMP-CO_2) is provided including the algorithm design and the implemented mathematics that are involved in geological carbon sequestration (GCS) technology and how it can be applied using appropriate boundary conditions to investigate the behaviour of CO_2-brine-rock flow system and the involved trapping mechanisms during the time frames of the simulations. The reasons behind the selection of this specific computer code have been clarified along with the capabilities and flexibility of the simulator.

The governing equations and correlations used by the employed simulator are explained in addition to the equations of state (EOSs) that are built in STOMP-CO_2 code to carry out the phase equilibria calculations including the thermodynamic properties of the existing phases in the system.

The numerical simulation runs in this research work were conducted at different scales and organized in chapters four through six as described in the following sections in this chapter.

To establish a robust credibility of the employed simulator, two numerical simulation runs have been accommodated under dynamic and quasi-static flow conditions by utilizing the STOMP-CO_2 mode aiming at further validating the achieved results against the experimentally obtained ones from the in-house experimental set-up that was purposely developed for this comparison study. This study aims at assessing the reliability of the obtained numerical results in terms of investigating P_c-S_w relations and the dynamic effect in CO_2-water flow system.

The simulation code results for a 2D model are validated against a 3D one of the domain, which comprises 4 of 90 degrees injection arcs in the azimuthal direction. The domain was refined to 24 nodes vertically (a thickness of 96 m) and 75 nodes in the lateral direction, which extends to 2750 m. The model was simulated as a 3D once and as a 2D afterward (i. e. considering only one of the four injection arcs) aiming at reducing the extremely long execution times required for carrying out the simulation tests on the 3D model that might extend to several weeks for fine grids.

3.1. Introduction

Modelling geological carbon sequestration (GCS) requires planning injection strategies and methodologies for best results that can be used with increased confidence before moving to pilot plots and further to field-scale projects. Following the planning procedure, a suitable computer code needs to be selected depending on several factors such as the potential site geology, including geomechanical and geochemical characteristics; hydrostatic conditions; hydrodynamics of the fluids; layers heterogeneity; which trapping mechanisms of CO_2 are planned to investigate; modelling time frames and how customizable the software is for further future research works. Selecting a sophisticated simulation code helps employing the best techniques for site-specific characteristics to overcome any possible challenges because an accurate injection model is essential to better understand the flow behaviour of the injected supercritical CO_2, and further enhance the storage efficiency of the site and the ultimate fate of the injected gas.

For this research study, STOMP-CO_2 computer software was employed to run a series of simulation tests for different model-scales; core, large and field-scale domains to investigate the influence of various parameters and methodologies on the CO_2 sequestration porous formations. This mode of STOMP (Subsurface Transport Over Multiple Phases) was developed by the hydrology group at the Pacific Northwest National Laboratory (PNNL) to specifically investigate the geological sequestration of CO_2 in deep saline aquifers. It was selected to employ in this work for several reasons;

1- STOMP-CO_2 simulator has been purposely developed to predict the behaviour of the injected CO_2 at different phases (i. e. gas, liquid and supercritical phases) in saline aquifers at depths greater than 800 m, which are specifically targeted in this study (White et al., 2013).

2- The code has the capability to model all three trapping mechanisms that have been investigated in this research work (i.e., structural, solubility and residual).

3- The simulator is able to incorporate buoyancy and viscous forces driven flow, CO_2 dissolution in aqueous fluid, phase transition, dispersion and diffusivity of the gas.

4- It has several modes to cover different types of hydrological problems including the reactive transport module ECKEChem (Equilibrium-Conservation-Kinetic Equation Chemistry) for

investigating the mineralization trapping of the CO_2 in long time frames and the scalable version (eSTOMP-CO_2), which has the ability to execute on multi-processor computers for simulating large domains that are discretized into more than 100 thousand elements (White et al., 2013; White and Oostrom, 2006).

5- The modularity and readability of the source code makes it easy to read, maintain, modify and configure according to the operational mode and problem requirements.

6- The simulation code is computationally efficient because the memory requirements and code algorithms can be customised to the computational problem for faster executio.

7- The code has been effectively optimized for workstations (HP, IBM and Sun) in addition to mainframes.

8- It offers the user substantial flexibility in controlling the execution of simulations because numerous execution periods can be created within a single simulation depending on time step advancement and convergence control.

3.2. STOMP-CO_2 Simulation Code

STOMP-CO_2 is a dedicated version of STOMP, which is an analytical tool used for laboratory and field investigations for thermal and hydrogeologic flow and transport, and geochemistry phenomena in variably saturated subsurface. The numerical code comprises a collection of source files written in Fortran90 programming language with a variable configuration to customize the execution memory and speed to the problem requirements. These source files need to be assembled and compiled into an executable file using a compiling software (i. e. Gfortran compiler, which comes built-in with most of Unix operating systems as an example), and issuing a series of commands depending on the operating system (commands for UNIX platform can be found in the publication by White and Oostroom, (2006)). The executable file generated on Unix platform has an extension ".e" and can be run in the terminal utility using the following line command;

./stomp-co2.e

where stomp-co2 is the name assigned to the created executable file according to the user's preference.

There are several compilers that support windows platforms (examples; GNU Fortran Compiler, Intel® Fortran Compiler, Absoft Pro Fortran and Silverfrost FTN95) that generate windows platform executable files with the extension of ".exe" to be executed through windows command prompt.

The generated executable file is run to read the input file developed by the user and write outputs of the simulation into output files for post processing to produce different types of figures and tables. The simulator predictions are established on the solution of the partial differential equations that describe the investigated problem and based on the governing conservation equations and related correlations. The coupled conservation equations are solved by converting them to algebraic equations using finite volume method (FVM) and Euler-backward time differencing for spatial and temporal discretizations, respectively. The produced algebraic equations in the discretized equations are closed using a number of constitutive correlations and solved using Newton-Raphson iteration to resolve their nonlinearities (White and Oostrom 2003).

The key role for the user is creating the input files, which are ASCII text files representing a communication channel to pass information about the physical system to the simulator. The input file consists of a number of required cards and optional others depending on the operational mode of the simulator, with associated groups of data that follow a series of logic type statements to make them readable for the simulator (details of these cards can be found in the STOMP technical guide by White and Oostrom, (2006)). Each card starts with a tilde symbol (~) followed by the card name. It's noteworthy to know that these cards can be arranged in any order within the input file. Input files for STOMP can be generated using any text editors and saved in the same folder where the executable file located. However the simulator reading routine is case sensitive, which needs to be taken into consideration when creating input files. Additionally, every input file has to be named "input" with no extension in order to be recognised by the simulation executable file (samples of input files can be found in Appendix C). STOMP simulator outputs are generated in different formats (i. e., text files and printing to device instructions) that can be controlled by the user within the control card in the input file. STOMP simulator is applicable in solving dynamic flow in the subsurface in one, two or three dimensions, however it is limited to maximum of four immiscible fluid phases namely, aqueous, non-aqueous

liquid, hydrate and gas phases. Various boundary conditions can be applied at different surface knowing that unspecified boundaries are considered to be zero flux surfaces.

Similar to all other STOMP operational modes, the flow path of STOMP-CO_2 comprises of three stages. The first one is initialization, when all routines are executed in sequence once during a simulation life time as illustrated in Figure A.1 in Appendix-A. During this stage, all common variables are initialized either to zero or to default values, input and output files are opened and banners are printed to the screen and output file. Following this, the input file is read and data are checked for physical state of the components before setting the Jacopian matrix pointers. Finally in this stage, the values of the secondary variables (saturation properties, physical properties and solute concentration) are read from the initial conditions specified in the input file or restart files.

The second stage consists of two loops namely; time stepping and Newton-Raphson linearizations . In the time stepping loop, the governing equations are solved, previous time step results are written to the output device and final simulation results are written to the output file, plot files, restart files and the screen. During the Newton-Raphson linearization loop the governing equations for mass and energy are solved by calculating the boundary properties and computing all field and surfaces fluxes with the source contributions. The loop terminates either when the specified convergence value is reached or after a violation of the iteration limit. The last stage of the flow path, is running the closure routines to generate final plot and restart files, and close all opened files at the termination of the time stepping loop either when simulation ends or stops for any reason.

Simulation results are reported through output data that comprise records of variables that can be used to create graphs and plots for variables change over the simulation time or screenshots over the computational domain. The generated output, plot and surface files can be post-processed by a set of developed Perl script files, provided by the code developer, to transform the files into a formatted data files for different stylish plotting packages such as Igor, Tecplot, Matlab, Grapher and Gnuplot. The script files (outputTo.pl, plotTo.pl and surfaceTo.pl), can be run through Windows OS command prompt or Unix terminal utility using the following instructions;

```
perl outputTo.pl -av -an Tecplot ref_nodes.dat output

perl plotTo.pl Tecplot plots.dat plot.*
```

perl surfaceTo.pl -av -as Tecplot surface.dat surface

where –av –an refer to all variables at all nodes (grid-cells) to be printed, Tecplot refers to the plotting package used, ref_nodes.dat is the name of the newly created data file (can be named according to the user's preferences). Output, plot.* and surface are the source files (STOMP outputs) that are attempted to be transformed to data files for the plotting packages. Plot.* means all plot files are processed into one file, which can be optionally separated into single files, one for each plot file by replacing the above command with;

perl plotTo.pl Tecplot plot123.dat plot.123

where plot.123 is the generated plot file at time step 123 as an example.

3.2.1. Governing Equations and Correlations

In STOMP simulator, the governing coupled equations for hydrogeological and thermal flow are partial differential equations of mass and thermal energy for the components in the flow system and those for transport are the partial differential equations for the conservation of solute mass (White and Oostrom, 2006). Three coupled mass conservation equations for water, CO_2 and salt are solved by the STOMP-CO_2 simulator.

The mass conservation equations for water and CO_2, which presumably exist in liquid (l) and gas (g) phases under equilibrium conditions, involve components flux by advection and diffusion through mobile phases. The equations of conservation for water and CO_2 are represented by equations 3.1 and 3.2 respectively;

$$\frac{\partial}{\partial x}\left[\sum_{\gamma=l,g}\left(\emptyset\rho_\gamma S_\gamma \omega_\gamma^{H_2O}\right)\right] = -\sum_{\gamma=l,g}\nabla\left(\rho_\gamma \omega_\gamma^{H_2O}\mathbf{V}_\gamma\right) - \sum_{\gamma=l,g}\nabla\left(J_\gamma^{H_2O}\right) + \sum_{\gamma=l,g}\left(\omega_\gamma^{H_2O} m_\gamma\right) \quad (3.1)$$

$$\frac{\partial}{\partial x}\left[\sum_{\gamma=l,g}\left(\emptyset\rho_\gamma S_\gamma \omega_\gamma^{CO_2}\right)\right] = -\sum_{\gamma=l,g}\nabla\left(\rho_\gamma \omega_\gamma^{CO_2}\mathbf{V}_\gamma\right) - \sum_{\gamma=l,g}\nabla\left(J_\gamma^{CO_2}\right) + \sum_{\gamma=l,g}\left(\omega_\gamma^{CO_2} m_\gamma\right) \quad (3.2)$$

$$J_\gamma^i = -\rho_\gamma S_\gamma \frac{M^i}{M_\gamma}\left(\tau_\gamma D_\gamma^i\right)\nabla x_\gamma^i \quad (3.3)$$

where γ refers to aqueous or gas phase, i defines the component (water or CO_2) and all other symbols for this and all following questions are explained in the nomenclature section.

The equation of mass conservation for salt assumes it only exists dissolved in aqueous phase (l) or precipitated (p) as shown in equation 3.4.

$$\frac{\partial}{\partial x}\left[\sum_{\gamma=l,g}\left(\emptyset\rho_l S_l \omega_l^s + \emptyset\rho_p S_p\right)\right] = -\nabla(\rho_l \omega_l^s V_l) - \nabla(J_l^s) + \omega_l^s m_l \quad (3.4)$$

Each one of equations 3.1, 3.2 and 3.4 is solved for one unknown primary variable that is selected to specify the state condition. These primary variables are related to the secondary variables by a set of correlation described in the following sections.

3.2.2. Equations of State

An equation of state (EOS) refers to a collection of formulations that describe the phase conditions, compositions and densities at phase equilibria. Under the hydrostatic conditions in DSAs, five phases exist; liquid-water (aqueous), liquid CO_2, gas CO_2, clathrated CO_2 and precipitated salt (solid). The EOSs in STOMP-CO_2 demonstrate the phases existence dependency on the hydrostatic conditions (temperature and pressure) and the concentrations of the components (water, CO_2 and salt). The equations further describe the densities of the different present phases in the domain.

3.2.2.1 Phase Equilibria

Phase equilibria is a balance condition between two phases of a pure substance or a component in a mixture, when the mass and heat transfer rate in both directions are equal. In carbon geological sequestration, STOMP-CO_2 simulator describes three phase conditions in the domain grid cells where aqueous and gas phases exist;

1- Only aqueous saturated phase with the amount of dissolved CO_2 as a primary unknown. The amount of the dissolved CO_2 is determined via phase equilibria calculations and compared to the maximum CO_2 solubility limit in water. Exceeding this limit changes the phase condition to aqueous with mobile gas.

2- Aqueous phase with mobile gas, which can be in supercritical, subcritical liquid or subcritical gas and a possibility of mobile gas.

3- Aqueous saturated phase with entrapped gas, which again can be in supercritical, subcritical liquid or subcritical gas.

In STOMP simulator, the formulations used in equilibria calculations depend on the thermal conditions of the system. For temperatures less than 100 ℃, the formulation by Spycher et al. (2003) is used, whilst for temperatures above 100 ℃, Spycher and Pruess (2010) formulation is used with corrections for dissolved salt. These formulations are based on Redlich-Kwong EOS with fitted experimental data for CO_2-water system. At equilibrium conditions, the mole fraction of water in gas phase and the mole fraction of CO_2 in aqueous phase are calculated from equations 3.5 and 3.6 respectively:

$$x_g^{H2O} = \frac{(1-B)}{\left(\frac{1}{A}-B\right)} \tag{3.5}$$

$$x_l^{CO_2} = B\left(1 - x_g^{H2O}\right) \tag{3.6}$$

where A and B can be calculated from equations 3.7 and 3.8:

$$A = \frac{K_{H2O}^0}{\emptyset_{H2O}P} exp\left[\frac{(P-P^0)\bar{V}_{H2O}}{RT(K)}\right] \tag{3.7}$$

$$B = \frac{\emptyset_{CO_2}P}{(10^3/M^{H2O})K_{CO_2}^0} exp\left[-\frac{(P-P^0)\bar{V}_{CO_2}}{RT(K)}\right] \tag{3.8}$$

The equilibrium constants K_{H2O}^0 and $K_{CO_2}^0$ are temperature dependent and can be calculated from:

$$\log(K_{H2O}^0) = -2.209 + 3.097x10^{-2}T(C) - 1.098x10^{-4}\left(T(C)\right)^2 - 2.048x10^{-7}\left(T(C)\right)^3 \tag{3.9}$$

$$\log\left(K_{CO2(g)}^0\right) = 1.189 + 1.304x10^{-2}T(C) - 5.446x10^{-5}\left(T(C)\right)^2 \tag{3.10}$$

$$\log\left(K^0_{CO2(l)}\right) = 1.169 + 1.368x10^{-2}T(C) - 5.380x10^{-4}\left(T(C)\right)^2 \quad (3.11)$$

The fugacity coefficient $\emptyset_\gamma$ is calculated by:

$$\ln(\emptyset_{H2O}) = \ln\left(\frac{V}{V-b_{mix}}\right) + \left(\frac{b_{H2O}}{V-b_{mix}}\right) - \left(\frac{2a_{H2O-CO2}}{RT^{1.5}b_{mix}}\right)\ln\left(\frac{V+b_{mix}}{V}\right) + \left(\frac{a_{mix}b_{H2O}}{RT^{1.5}b_{mix}}\right)\left[\ln\left(\frac{V+b_{mix}}{V}\right) - \left(\frac{b_{mix}}{V+b_{mix}}\right)\right] - \ln\left(\frac{PV}{RT(K)}\right) \quad (3.12)$$

$$\ln(\emptyset_{CO2}) = \ln\left(\frac{V}{V-b_{mix}}\right) + \left(\frac{b_{CO2}}{V-b_{mix}}\right) - \left(\frac{2a_{CO2}}{RT^{1.5}b_{mix}}\right)\ln\left(\frac{V+b_{mix}}{V}\right) + \left(\frac{a_{mix}b_{CO2}}{RT^{1.5}b_{mix}}\right)\left[\ln\left(\frac{V+b_{mix}}{V}\right) - \left(\frac{b_{mix}}{V+b_{mix}}\right)\right] - \ln\left(\frac{PV}{RT(K)}\right) \quad (3.13)$$

$$P = \left(\frac{RT(K)}{V-b_{mix}}\right) - \left(\frac{a_{mix}}{T(K)^{0.5}V(V+b_{mix})}\right) \quad (3.14)$$

where: $a_{mix} = a_{CO2}$ and $b_{mix} = b_{CO2}$

$a_{CO2} = 7.54x10^7 - 4.13x10^4T(K), bar\ cm^6K^{0.5}mol^{-2}$

$b_{CO2} = 27.80, cm^3/mol\,;\ b_{H2O} = 18.18, cm^3/mol$

$a_{H2O-CO2} = 7.89x10^7, bar\ cm^6K^{0.5}mol^{-2}$

$P^0 = 1\ bar;\ \bar{V}_{H2O} = 18.1\ cm^3/mol\,;\ \bar{V}_{CO_2} = 32.6\ cm^3/mol$

3.2.2.2 Fluids Densities

The CO_2 thermodynamic properties are read by the simulator from the pre-arranged data table that is stored in a file named “CO2_prop.dat” which is located in the same folder where the input

file located. This data table was developed from the EOS for CO_2 by Span and Wagner (1996). The simulator computes the density of CO_2 in any phase region at temperatures and pressures up to 1100 K and 800 MPa respectively, via interpolation from the read CO_2 data table.

The aqueous density (ρ_l) is calculated from the pure-water density, which is computed as a function of temperature and pressure using the ASME steam tables (Meyer et al., 1993):

$$\rho_l^{H2O} = M^{H2O}\left[V_c^{H2O}\left\{A_{11}a_5Z^{-5/17}A_{12} + A_{13}T_r^{H2O} + A_{14}(T_r^{H2O})^2 + A_{15}(a_6 - T_r^{H2O})^{10} + A_{16}(a_7 + (T_r^{H2O})^{19})^{-1} - (A_{17} + 2A_{18}P_r^{H2O} + 3A_{19}(P_r^{H2O})^2)(a_{8+}(T_r^{H2O})^{11})^{-1} + A_{20}(P_r^{H2O})^{18}(a_9 + (T_r^{H2O})^2)(-3(a_{10+}P_r^{H2O})^{-4} + a_{11}) + 3A_{21}(a_{12} - T_r^{H2O})(P_r^{H2O})^2 + 4A_{22}(P_r^{H2O})^3(T_r^{H2O})^{-20}\right\}\right]^{-1} \quad (3.15)$$

where;

$$Z = Y + (a_3Y^2 - 2a_4T_r^{H2O} + 2a_5P_r^{H2O})^{1/2}$$

$$Y = 1 - a_1(T_r^{H2O})^2 - a_2(T_r^{H2O})^{-6}$$

$$T_r^{H2O} = \frac{T(K)}{T_c^{H2O}(K)} \quad \text{and} \quad P_r^{H2O} = \frac{P}{P_c^{H2O}}$$

$A_{11}\ldots A_{22}$ and $a_5\ldots.a_{12}$ are liquid water primary constants, *P* and *T* are the water pressures and temperatures respectively, P_c^{H2O} and T_c^{H2O} are the critical water pressures and temperatures. $V_c^{H2O}$is the critical specific water volume. Values for the constants are given under liquid water constants in Table 3.1.

Table 3.1. Water saturation line constants (White et al., 2013).

$\boldsymbol{A_{11}}$	7.982692717e+0	$\boldsymbol{A_{18}}$	2.174020350e-8	$\boldsymbol{a_5}$	4.975858870e-2
$\boldsymbol{A_{12}}$	-2.616571843e-2	A_{19}	1.105710498e-9	a_6	6.537154300e-1
$\boldsymbol{A_{13}}$	1.522411790e-3	A_{20}	1.293441934e+1	a_7	1.150000000e-6
$\boldsymbol{A_{14}}$	2.284279054e-2	A_{21}	1.308119072e-5	a_8	1.150800000e-5
$\boldsymbol{A_{15}}$	2.421647003e+2	A_{22}	6.047626338e-14	a_9	1.418800000e-1
$\boldsymbol{A_{16}}$	1.269716088e-10			a_{10}	7.002753165e+0
$\boldsymbol{A_{17}}$	2.074838328e-7			a_{11}	2.995284926e-4
				a_{12}	2.040000000e-1

Brine density (ρ_b) is computed using Haas (1976) formulation from the corrected pure water density:

$$\rho_b = \left(10^3 + b_l^{salt} M^{salt}\right)\left(10^3 V_l^{H2O} + \emptyset b_l^{salt}\right) \tag{3.16}$$

where b_l^{salt} and V_l^{H2O} are salt mass fraction in aqueous phase and molar volume of liquid water;

$b_l^{salt} = \frac{10^3 \omega_l^{salt}}{M^{salt}\left(1-\omega_l^{salt}\right)}$; $V_l^{H2O} = (10^{-3}\rho_l^{H2O})^{-1}$ and

$$\emptyset = c_1 + c_2 V_l^{H2O} + c_3 (V_l^{H2O})^2 + (c_4 + c_5 V_l^{H2O}) \left(\frac{V_l^{H2O}}{V_c^{H2O} - V_l^{H2O}}\right)^2 \left(b_l^{salt}\right)^{0.5}$$

where $c_1 \ldots . c_5$ are the brine thermal conductivity constants with values shown in Table 3.2.

Knowing the brine density (ρ_b), mass fraction of the dissolved CO_2 ($\omega_l^{CO_2}$) and temperature, the aqueous density (ρ_l) can be calculated from the Anderson (1992) formulation and Poython correction factor (Prausnitz et al., 1986):

$$\rho_l = \frac{\rho_b}{\left(1 + c_l^{CO_2} - \omega_l^{CO_2}\right)} \tag{3.17}$$

where;

$$C_l^{CO_2} = \frac{V_l^{CO_2} \rho_{b\omega_l^{CO_2}}}{M^{CO_2}} \quad \text{and} \quad V_l^{CO_2} = d_1 + d_2 T(C) + d_3 \left(T(C)\right)^2 + d_4 \left(T(C)\right)^3$$

where $T(C)$ is the temperature in Celsius and $d_1 \ldots . d_4$ are the pure-water thermal conductivity constants with values shown in Table 3.2.

Table 3.2. Pure-water thermal conductivity constants (White et al., 2013).

c_1	2.3434e-3	c_2	-7.294e-6	c_3	3.924e-8	c_4	1.06e-8	c_5	-2.0e-8
d_1	0.0701309	d_2	0.0118520	d_3	0.00169937	d_4	-1.0200		

CO_2 gas density can be computed from pure CO_2 and water vapour densities using the determined mass fractions from the phase equilibria:

$$\rho_g = \omega_g^{CO_2} \rho_g^{CO_2} + \omega_g^{H2O} \rho_g^{H2O} \tag{3.18}$$

Precipitated salt density is calculated from the formulation by Battistelli et al. (1997):

$$\rho_s = 2165.0 exp(-1.2e^{-4T} + 4.0e^{-11P}) \tag{3.19}$$

where T is the temperature in Kelvin and P is the pressure in Pa.

3.2.2.3 Water-Vapour Pressure

In geological formations, water-vapour pressure, which is temperature and capillary pressure dependent, can be calculated for saturation conditions by the k-function (Meyer et al., 1993):

$$P_{sat}^{H2O} = P_c^{H2O} exp \left[(T_r^{H2O})^{-1} \left(\frac{\sum_{i-1}^{5} k_1 \left(1 - T_r^{H2O}\right)^i}{1 + k_6 \left(1 - T_r^{H2O}\right) + k_7 \left(1 - T_r^{H2O}\right)^2} \right) - \left(\frac{\left(1 - T_r^{H2O}\right)}{k_8 \left(1 - T_r^{H2O}\right)^2 + k_9} \right) \right] \tag{3.20}$$

Where, the k parameters refer to water saturation line constants given in Table 3.3.

Table 3.3. Water saturation line constants (White et al., 2013).

$\boldsymbol{k_1}$	-7.691234564e+0	$\boldsymbol{k_6}$	4.167117320e+0
$\boldsymbol{k_2}$	-2.608023696e+1	$\boldsymbol{k_7}$	2.097506760e+1
$\boldsymbol{k_3}$	-1.681706546e+2	$\boldsymbol{k_8}$	1.e+9
$\boldsymbol{k_4}$	6.423285504e+1	$\boldsymbol{k_9}$	6.e+0
$\boldsymbol{k_5}$	-1.189646225e+2		

Water-vapour pressure depends on the water saturation in the domain, which decreases with time as CO_2 replaces the existing water (brine). Water-vapour partial pressure is related to the saturated water-vapour pressure by the Kelvin equation (Nitao, 1988):

$$P_g^{H2O} = P_{sat}^{H2O} exp\left[\frac{-P_{gl}}{P_l\left(\frac{RT(K)}{M_l}\right)}\right] \tag{3.21}$$

3.3. Simulation Methodology

The numerical simulation runs in this research work were conducted at different scales and organized in chapters four through six as described in the following sections.

3.3.1 Core Scale Simulations

In chapter four, unconsolidated lab-scale samples of coarse and fine-grained sand silica (3D cylindrical samples measuring 10 cm in diameter and 12 cm in height) were used for investigating the capillary pressure (P_c) – saturation (S) relationships for a scCO_2-water flow system at temperatures between 35^{0}C and 65^{0}C and domain pressure of 15 MPa, which is close to the expected values during geological sequestration of CO_2 at injection depths around 1000 m.

Several numerical simulation runs were conducted at static and dynamic flow conditions to investigate the significance of dynamic capillary pressure effect for supercritical carbon dioxide-water flow in terms of a dynamic coefficient (τ) that was determined by measuring the slope of the line corresponding to values of $\left(P_c^{dyn} - P_c^{equ} \right)$ against $\partial S/\partial t$ according to equation 3.22.

$$\left(P_c^{dyn} - P_c^{equ} \right) = -\tau \, \partial S/\partial t \tag{3.22}$$

The influence of the domain permeability, temperature and the injection pressure on the time required for equilibrium to be attained and consequently the value of the dynamic coefficient was investigated for fine, coarse and mixed sand samples. The impact of the system flow condition (static and dynamic) on the $P_c - S$ relationship was highlighted in this chapter. Moreover, the effects of the domain grid-refinement on the values of dynamic coefficient and the accuracy of the simulation results were examined.

3.3.2 Large- Scale Simulations

Chapter five focuses on determining CO_2 gas saturation (i.e., volume fraction) at various time scales, temperatures and pressure conditions taking into consideration the effects of porosity/permeability, heterogeneity and capillarity for CO_2-water system in saline aquifers. This was carried out by conducting a series of numerical simulations (details shown in Table 5.3) at a large-scale 3D-domain, which extends radially to 2500 m and vertically to 100 m at depth of 2900 m, to analyse the saturation, capillary pressure and the amount of dissolved CO_2 change with the change of injection methodology and hydrostatic conditions (i. e. pressure and temperature). The simulation parameters based on Detfurth cycle of Bunter Sandstone Aquifer in North-Eastern Germany as a typical real geological formation that consists of a high permeable sandstone layer and a low permeable layer of sand, silt and clay stones representing reasonable level of heterogeneity in terms of porosity and permeability.

Supercritical CO_2 was injected at pressure and temperature above the CO_2 critical conditions into the lower 40 m at the centre of the computational domain at a constant rate of 40 kg/s (approximately 1.262 MMT/yr) for 20 years followed by 980 years lockup period. Different types of heterogeneities were considered for the simulated model and various boundary

condition (presented in Table 5.4) were applied to investigate the effects of permeability, temperature, porosity, and injection pressure on P_c- S_w relationships at static and dynamic flow conditions, on the ultimate fate of the injected CO_2.

3.3.3 Field - Scale Simulations

In chapter six, an actual field-scale computational domain was adopted based on the geological settings for Sleipner Vest Field, which is located in the Norwegian part of the North Sea at an approximate depth of 1100 m. A 3D cylindrical computational domain characterised by a diameter of 6000 m and a thickness of 96 m, was simulated with two types of grid resolution. A coarse-grid for which the domain was horizontally discretized into 88 grid-blocks and vertically to 24 blocks making 2112 elements and a finer grid with increased refinement by 100% in both directions producing 8448 cells. Supercritical CO_2 (scrCO_2) was injected into the centre of the domain at a constant rate of 32.0 kg/s (about 1 MMT/year), which represents a typical benchmark value via a number of cells either at the bottom section or through the whole thickness of the reservoir.

The simulation tests aimed at evaluating the CO_2 storage capacity and efficiency in an actual field-scale aquifer considering the impact of heterogeneity, permeability, grid resolution and injection methodology on CO_2-water system mobility and behaviour of the injected scrCO_2 at different time frames. An archetype of an actual field heterogeneity in a domain was developed consisting of three stratums of sands intermingled with two layers of low permeability shales, as illustrated in Figure 6.1.

A series of simulation cases (presented in Table 6.3) were conducted to demonstrate different models of computational domains including homogeneous, uniform and non-uniform heterogeneous, with coarse and fine grid refinement. The simulation runs involved two different employed schemes of injection (continuous and cyclic). The continuous injection scheme involved 30 years of continuous injection at a constant rate of 32 kg/s (about 1 million metric tons (MMT) per year) while in the second scenario, the injection period was implicated in three cycles of 10 years separated by two stopping periods of 5 years in between. Furthermore, three models with different values of vertical to horizontal permeability ratio (k_v/k_h) along with other models were developed to assess the influence of injection scope and orientation of the injection

well on the flow behaviour and CO_2 sequestration efficiency. In all 14 cases, the total simulation time was 5000 years including injection and stopping times.

The investigation involved the first three trapping mechanisms (structural, solubility and residual) that dominate through the simulation time that was set for this research work excluding the mineral trapping due to its insignificant influence before few thousands of years of storage.

3.4. Validation of Numerical Results

To establish a robust credibility of our simulation results prior to upscaling them for deployment on practical field-scale projects, a reasonable mapping with a lab-scale setup results is significantly important. This study aims at assessing the reliability of the obtained numerical results in terms of investigating P_c-S_w relations and the dynamic effects in CO_2-water flow system by comparing them against experimentally recorded results.

To validate the numerically predicted results with empirical ones, a water-CO_2-sand flow system was developed to imitate the experimental cell adopted purposely for this comparison study. Two numerical simulation runs had been accommodated under dynamic and quasi-static flow conditions by utilizing a dedicated mode of the simulation code STOMP-CO_2 aiming at further validating the achieved results against the experimentally obtained ones from the in-house experimental set-up mentioned before. The experimental set-up, which was developed by Abidoye (2014) is schematically illustrated in Figure. 3.1. It consists of a cylindrical sample holder measuring 4 cm in height and 10 cm inner diameter. The unit is fitted with a set of sensors (i. e. time-domain reducers TDRs and pressure transducers PTs) to collect phase saturation and pressure data for onward processing using a dedicated computer software. The experimental rig embraces a fluid pump to inject scCO_2 through the top of the sample holder beside an outflow bottle to collect the displaced water from the bottom of the domain. The pump is connected to a pressure regulator to control the injection pressure and fluid flow through the system. More details about the apparatus and running procedure can be viewed in the work by Abidoye (2014).

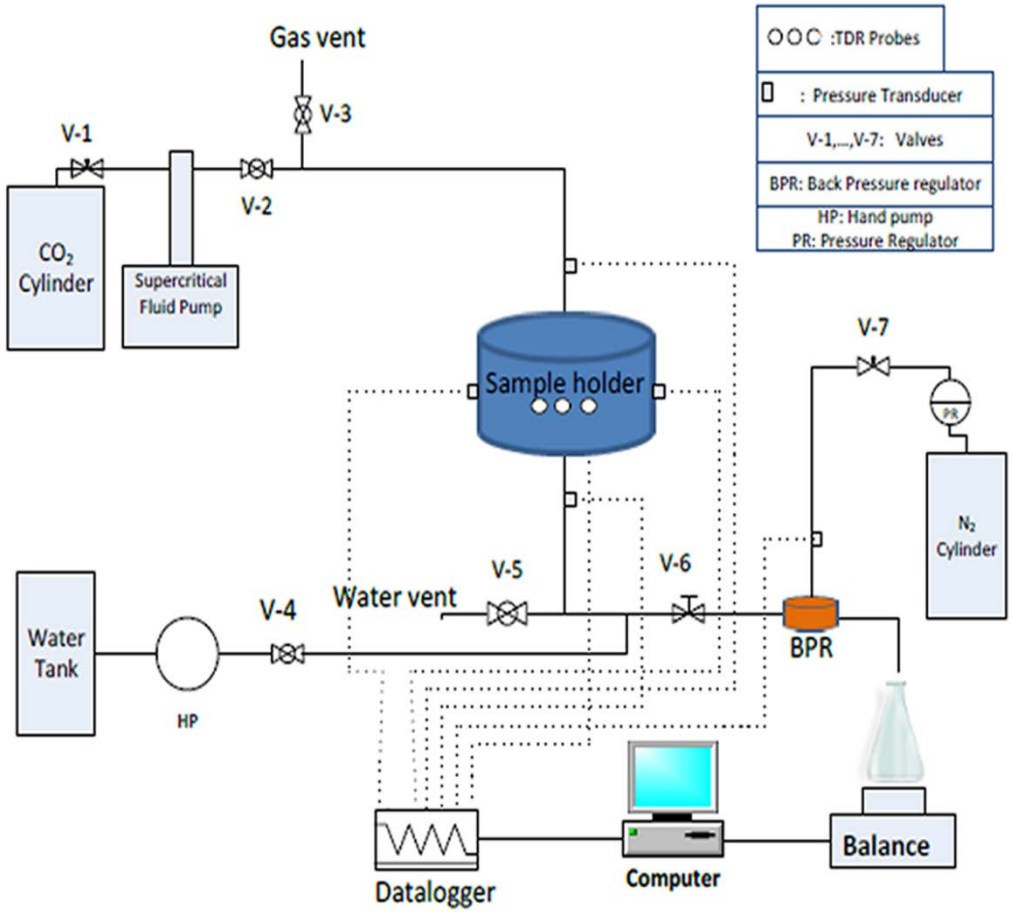

Figure 3.1: Experimental set-up for the scCO$_2$-water system (after Abidoye 2014, reused with written permission from the author).

STOMP-CO$_2$ simulator is a dedicated model, which has been added by the Pacific Northwest National Laboratory (PNNL) to their programming code (STOMP) to simulate CO$_2$ injection into geological formations. The employed simulator has been described in section 3.2 and further details about the software can be found in the guide documentation by White et al. (2013) or in a previously published work (Khudaida and Das, 2014).

The validation procedure was carried out through conducting a series of laboratory experiments to produce a set of water saturation data in the aim of validating the obtained numerical results against. The data comprised of dynamic and quasi-static capillary pressure change with water saturation and the influence of desaturation rate ($\partial S/\partial t$) on the P_c-S_w relation in addition to the impact of the hydrodynamic capillary pressure effect represented by the dynamic capillary

pressure coefficient (τ) on $scCO_2$-water-sand flow system. Investigating the dynamic effects in multiphase flow has been a subject of several previous research publications (Plug and Bruining 2007; Das and Mirzaei, 2013; Hanspal and Das, 2012; Camps-Roach et al., 2010; Hassanizadeh et al., 2002; Bottero et al., 2011(a,b) that affirm the necessity of accounting the dynamic effects when modelling multi-phase flow in porous media.

The porous domain used in this study for both experimental and numerical investigations was a coarse-grained silica sand referenced DA14/25 by the supplier "Minerals Marketing Limited (Buxton, UK)". The sand and fluids properties are shown in Table 3.4. Further details about preparing and calibrating the laboratory set-up and core samples can be found in the work by Abidoye (2014).

Table 3.4. Materials properties and simulation parameters.

Material / Property	Silica sand (D14/25) *	Fluids at: 40 ℃ and 80.5 bar *	
		CO_2	Water
Permeability, K (m^2)	$3.65x10^{-10}$	-	-
Porosity, Ø (-)	0.38	-	-
Density, (Kg/m^3)	2740	288	996
Average particle diameter, D_p (μm)	946.1	-	-
Viscosity, μ (Pa s)	-	23e-8	654e-8
Entry pressure, P^d ($N\ m^{-1}$)	431	-	-
Pore size distribution index, λ (-)	3.50	-	-
Residual water saturation, S_{rw} (-)	0.09	-	-

* All properties were taken from Abidoye (2014).

3.4.1 Domain Grid-Refinement

The simulated 3D cylindrical model measured 10 cm in diameter and 4 cm in height was refined as schematically illustrated in Figure 3.2 and numerically explained in Table 3.5, to accommodate 416 grid cells (nodes). N represents the number of nodes in each direction while Δr, Δθ, Δ*Z* are the node spacing in the radial, azimuthal (θ) and vertical directions respectively.

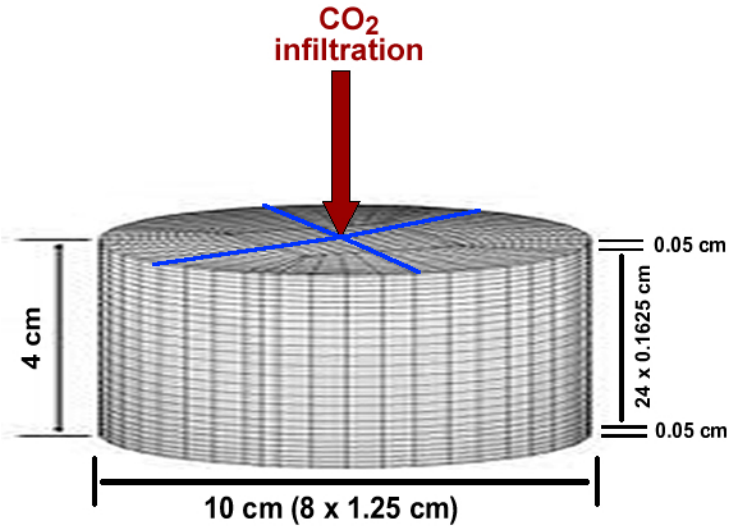

Figure 3.2. A schematic diagram of simulated domain geometry, showing the Number of Nodes and Nodal Spacing.

Table 3.5. Geometry of 3D Cylindrical Domain (d=10 cm m and z=4 cm), showing the Number of Nodes and Nodal Spacing.

Number of Nodes x Nodal Spacing		
***N x* Δ*r* (m)**	***N x* Δ*Θ* (degrees)**	***N x* Δ*Z* (m)**
4 x 0.01275	4 x 90	1 x 0.0005 24 x 0.001625 1 x 0.0005

3.4.2 Initial and Boundary Conditions

Similar initial and boundary conditions used in the experiments were adopted in the numerical simulation runs. Initially, the domain was fully saturated with water as a wetting phase. $ScCO_2$ was injected at the top of the domain at a constant pressure of 80.5 bar for the lifetime of the simulation for the dynamic condition. On the other hand, for the quasi-static case, the injection pressure started from 80 bar and consecutively increased at various time steps throughout the simulation period to reach a final value of 80.5 bar in 38 steps to erect a gradual dislocation of water from the domain. Table 3.6 displays the boundary conditions for both dynamic and quasi-static flow conditions for the drainage process (i.e. water displacement by the injected CO_2 gas), which has been considered in this comparison study.

Table 3.6. Initial and boundary conditions for CO_2-water drainage process for a 3D Cylindrical Domain (d=10 cm m and z=4 cm).

Boundary / Flow Condition	Top		Bottom	
	CO_2	**Water**	**CO_2**	**Water**
Dynamic	Dirichlet 80.5 bar	Zero Flux 80 bar	Zero Flux	Dirichlet 80 bar
Quasi-static	Dirichlet 80 - 80.5 bar	Zero Flux 80 bar	Zero Flux	Dirichlet 80 bar

3.4.3 2D Versus 3D Modelling

To validate the simulation code results for a 2D model against the 3D one of the domain, a cylindrical model with 4 of 90 degrees injection arcs was developed. The domain measured 96 m in height was refined to 24 nodes vertically and 75 nodes in the lateral direction, which extends to 2750 m in radius. The model was simulated as a 3D once and a 2D afterward (i. e. considering only one of the four injection arcs) aiming at reducing the extremely long execution times required for carrying out the simulation tests on the 3D model that might extend to many weeks for fine grids.

3.5. Results and Discussions

3.5.1. Validation of Numerical Results

In accordance to the experimental work described in section 3.4, the same coarse domain of silica sand (DA 14/25) was modelled under similar dynamic and quasi-static flow conditions. Figure 3.3 shows a sharp increase in the dynamic capillary pressure P_c^{dyn} required to overcome the entry pressure to break through the porous domain and snap off water from pore spaces at the beginning of drainage process (i. e. high water saturation values) for both experimental and numerical cases. Then after, P_c change tends to retard at water saturation values between 0.25

and 0.9 due to the fact that relatively smaller capillary pressure is required to snap off water before approaching the irreducible saturation (S_{wc}) of 0.09.

Both dynamic and static capillary pressure profiles (Figures 3.3 and 3.4) show apparent tendency to dramatically increase starting at a saturation value of 0.25 to reach the peak value close to the irreducible saturation when no more water displacement is possible and the system tends to reach the study state (i.e. $\partial S/\partial t=0$).

The deviancy between the experimental and numerical profiles can be noticed from the saturation value of 0.6 and becomes more evident as S_w decreases until a peak value of about 10% is achieved at S_w value of 0.25.

Such deviation was expected due to some errors in calculating the average values of saturation and capillary pressure from only three elevations along the core cell of the empirical set-up in comparison to the numerical domain, which was vertically refined into 26 nodes making 416 grid-cells, all of which were accounted for averaging the values of saturation and pressure.

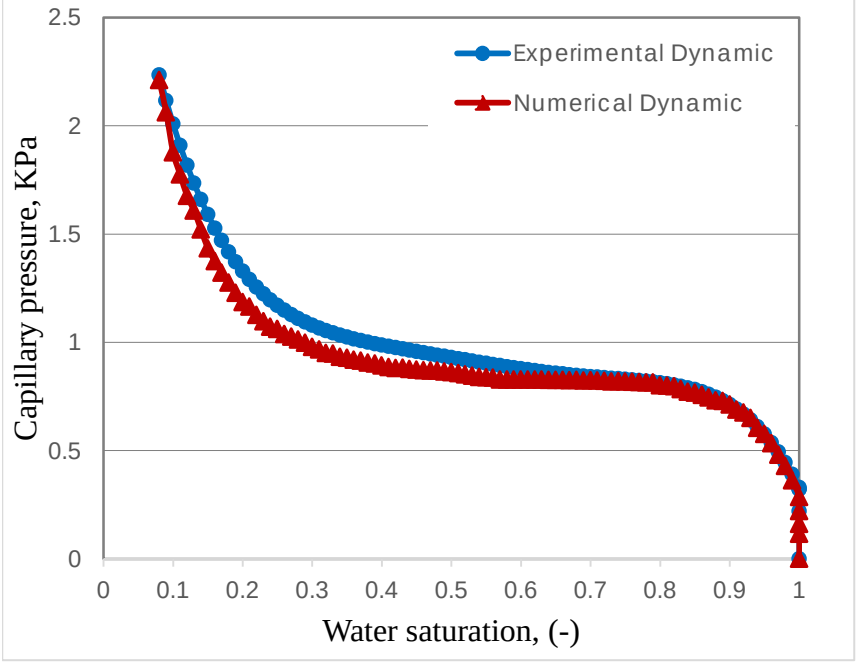

Figure 3.3. A comparision between the numerical and experimental saturation curves for dynamic capillary pressure.

Similarly, the comparison between the experimental and numerical P_c-S_w relation for quasi-static in Figure 3.4 demonstrates good agreement between the curves apart from some fluctuation in the experimental profile in the range of water saturation values between 0.45-0.85. This is again attributed to the experiential errors in logging the variable values as mentioned above because no such fluctuation is expected in this range of water saturation based on many previous published works (Das and Merzaie, 2012; Hsu and Hilpert, 2011; Plug and Brunning, 2007; Fučík et al. 2010; Peszynska and Yi, 2008; Khudaida and Das, 2014; Helmig et al., 2007).

Furthermore, comparing Figures 3.3 and 3.4, it is evident that at any saturation, the capillary pressure required to displace water from the domain remains higher in the case of dynamic flow condition. As soon as the quasi-static capillary pressure overcomes the entry pressure, the P_c trend remains almost constant with the reduction of saturation value until it reaches values around 0.85 as depicted in Figure 3.4.

In contrast, when the entry pressure is reached, the dynamic *Pc* curve continue rising gradually before settling constant close to the irreducible saturation (see Figure 3.3). This can be ascribed to the high-pressure gradient as a result of the large injection pressure employed in a single step, unlike the case of quasi-static in which the increase occurs in very small gradual steps.

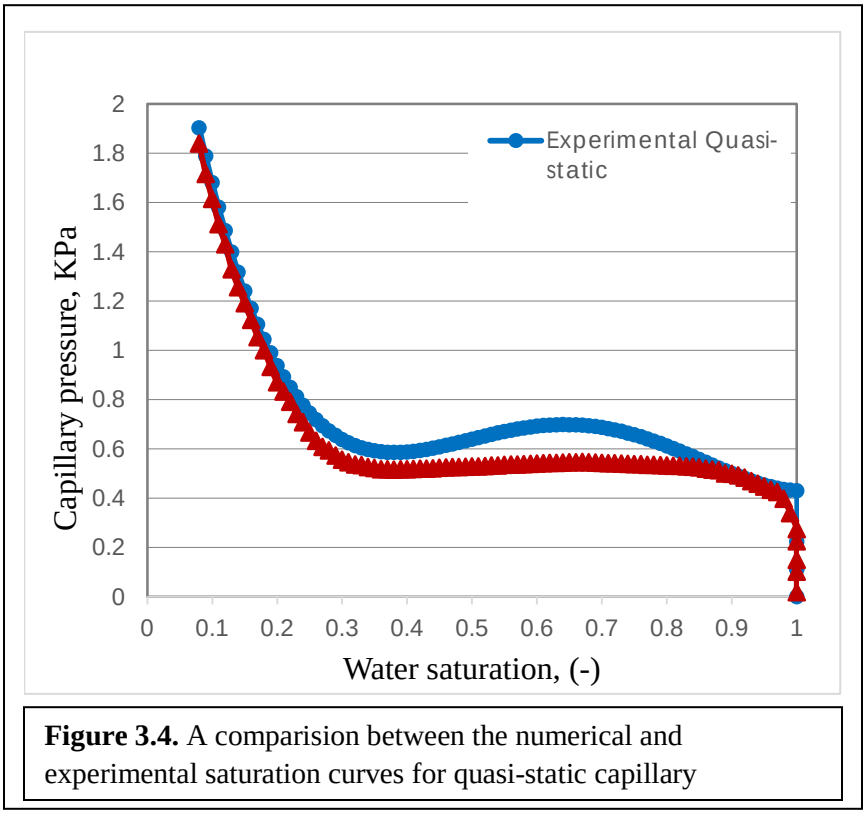

Figure 3.4. A comparision between the numerical and experimental saturation curves for quasi-static capillary

These findings further approve the existence of dynamic capillary pressure effect, which has been a subject of a number of investigations by many researchers mentioned earlier in this section to quantify such influence.

Dynamic coefficient (τ) profiles were found to be adequate up to saturation values of about 0.4 as depicted in Figure 3.5. According to equation 3.22 the dynamic coefficient changes inversely with water saturation and reaches the highest value close to the irreducible saturation at which the desaturation rate approaches zero (i.e. moves towards equilibrium). For both experimental and numerical cases, Figure 3.5 illustrates slight increase in the dynamic coefficient with some fluctuation between saturation values of 0.4-0.9.

This increase tends to be sharp after a saturation value of 0.2 until a steady state is achieved. Overall, the attained patterns of τ-S_w relation for the numerical simulation compared to the experimental one, can be described as good agreement.

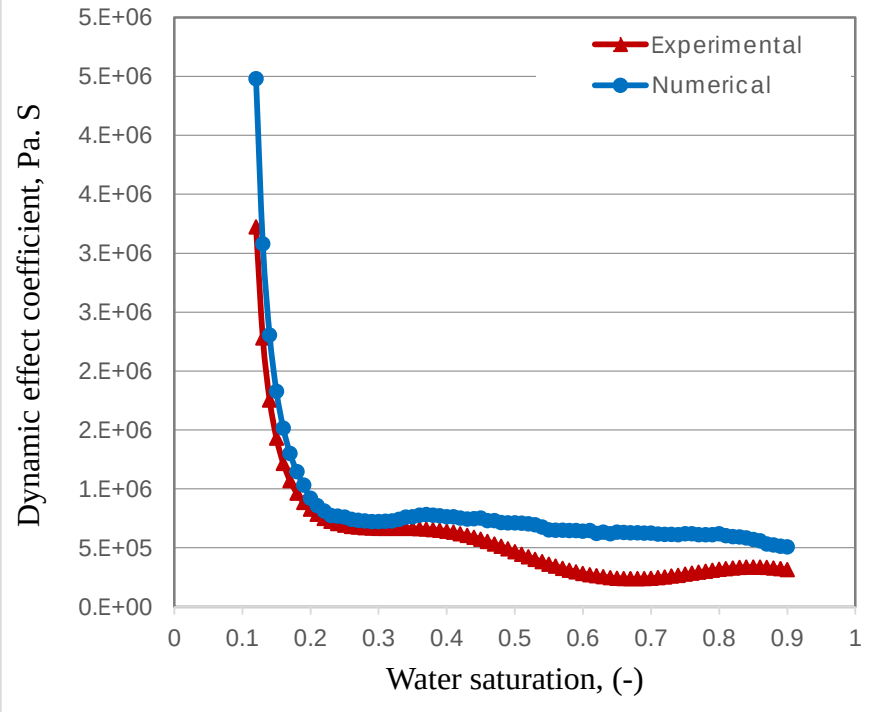

Figure 3.5. A comparision between the numerical and experimental dynamic coefficient (τ) - saturation curves.

In conclusion, it can be noticed that the numerical curves lie slightly above the experimental ones at all saturation values throughout the water displacement process, however it can be affirmed that the agreement between the experimental and numerical profiles was in general good. In consistent with many previous appraisal studies (Abidoye, 2014; Das and Mirzaei, 2013; Bottero et al., 2011a), this level of agreement approves the integrity and reliability of the simulation results, which establishes further credibility of the computer code employed in the course of this research work.

3.5.2. 2D Versus 3D Modelling

Soon after injection starts, the gas bounces upward due to the density difference between the two fluids (water and CO_2) and simultaneously migrates crossway due the pressure gradient between the injected scrCO_2 and the in situ hydrostatic pressure. During this drift, some of the injected gas disperse into the existed brine producing a CO_2-saturated aqueous phase that is heavier than the pure brine and consequently tends to sink down towards the bottom of the domain forming a fingered structure with the formation brine.

Additionally, small part of the injected gas might be forced into some small-sized pores due to the in situ capillarity, which is presented in Figure 3.6(a) leading to residual trapping which is one of the permanent trapping mechanisms that is aimed at increasing in this research work. This figure shows that capillary pressure (P_c) inversely changes with water saturation (S_w) and this change is significantly sharp at the beginning of the imbibition process after the injection ceases and retards later on. Looking at Figure 3.6(a), it can be clearly observed that both models have produced identical profiles throughout the simulation lifetime. The amount of trapped CO_2 in the 3D model was found to be exactly 4 orders of magnitude more than the amount in the 2D model as depicted in Figure 3.6(b). This is due to the fact that only one arc out of four 90-degree injection arcs has been taken into account in the 2D simulated model which represents forth of the whole domain volume (see base-3D and base-2D cases in Table 6.3). In other words, the cylindrical model simulated as a 3D domain was refined in to (75, 4, 24) nodes (i. e. it was discretized into 75 blocks in the radial direction, 4 of 90 degrees azimuthally and vertically into 24 blocks). Approximately 30 million metric tonnes (MMT) of CO_2 was injected into the domain in 30 years via all four injection angles (arcs) in the azimuthal direction at 90, 180, 270 and 360

degrees (i. e. ~7.5 MMT into each segment). In the case of 3D, the whole amount of the injected CO_2 was considered in the calculations because all four segments were modelled. However, in the case of 2D, only one segment of 90 degrees was modelled into which only forth of the total amount of scCO_2 was injected (i. e. only 7.5 MMT). This was reflected on the recorded amounts of dissolved, trapped and free-gas CO_2 within the domain the simulation of the 2D and 3D models as shown for example the amount of the trapped CO_2 in Figure 3.6b and Figure 3.7a for the dissolved CO_2.

Similarly, the amount of dissolved CO_2 in the 3D model was shown to be more than the one in the 2D model by four orders of magnitude at all-time scales as demonstrated in Figure 3.7a.

Accordingly, it is evidenced that modelling the domain as a 3D or 2D produces adequate results and consequently it should have no influence whatsoever on the calculated storage efficiency values throughout our simulation runs. This is deceptively evidenced from Figure 3.7b that spectacles a complete agreement between the storage efficiency curves for both 2D and 3D modelled domains.

Based on these findings, all other simulation runs in this study were conducted considering 2D models instead of those excessively time consuming models of 3D, some of which might extend up to many weeks of time.

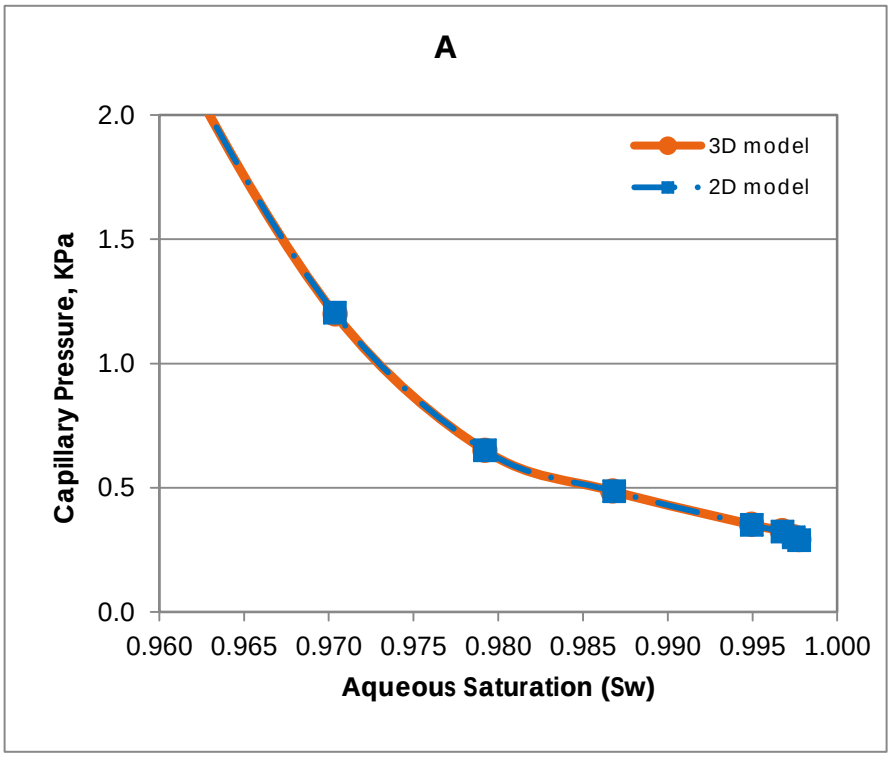

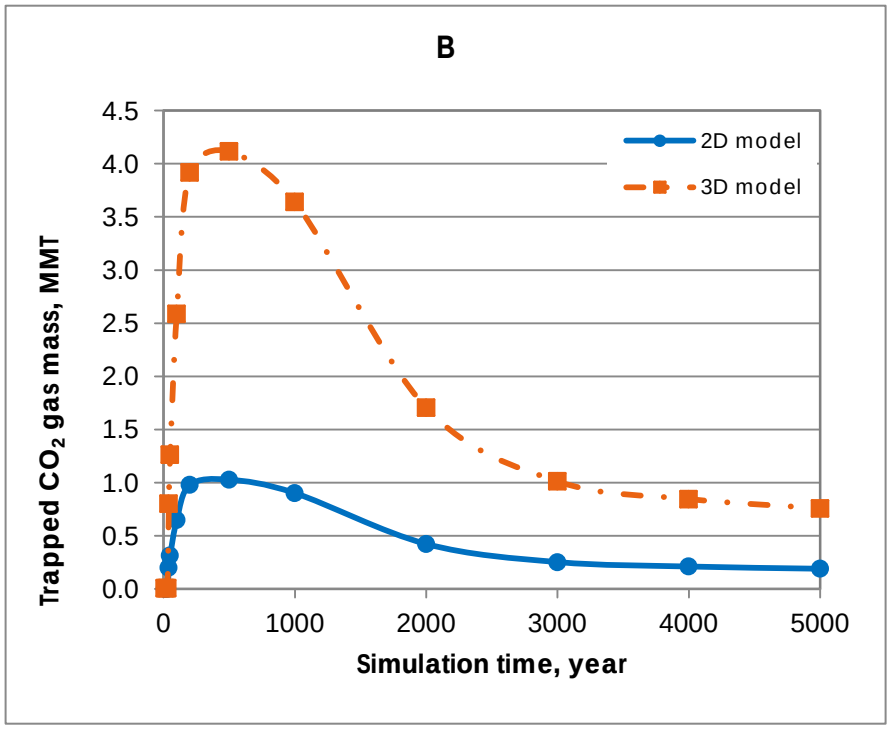

Figure 3.6. 2D versus 3D modelling impact on; (A) S_w – P_c relationships, (B) Trapped gas mass.
For 2D, only one of 4 injection arcs has been considered (i. e. only 4th amount of CO_2 has been injected).

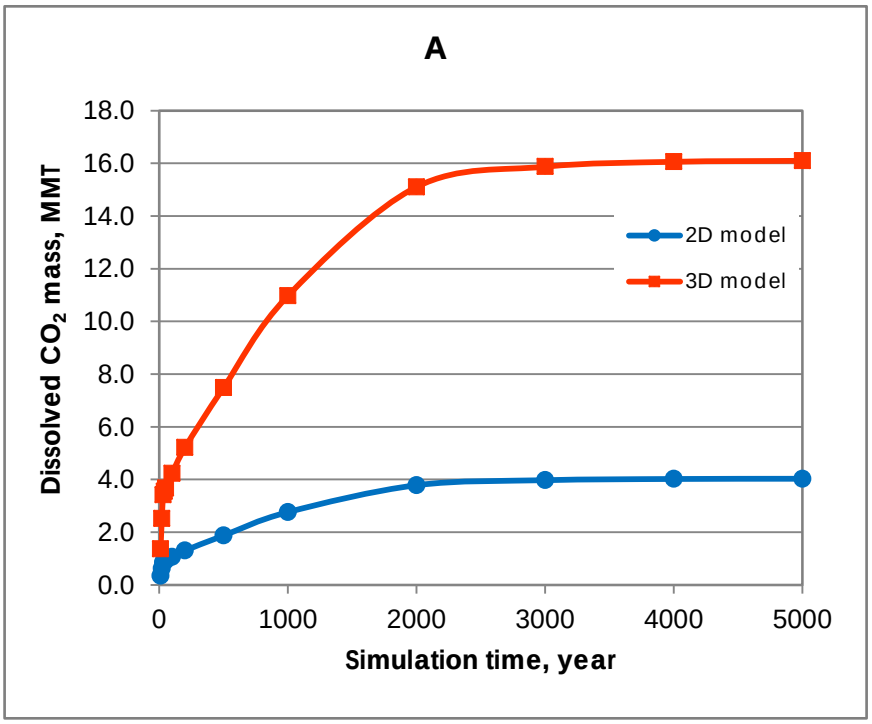

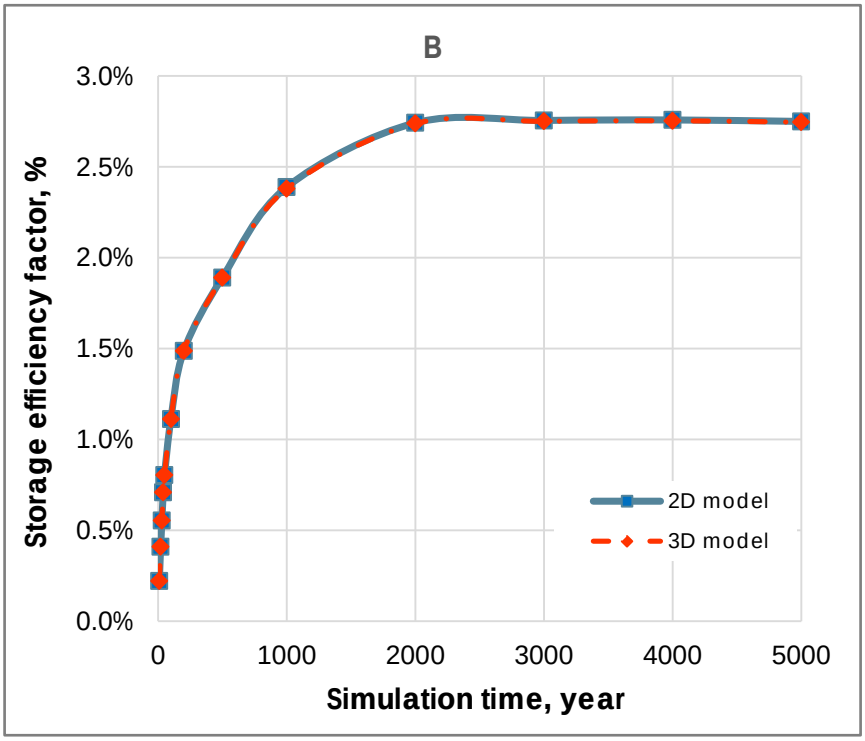

Figure 3.7. 2D versus 3D modelling impact on; (A) CO_2 dissolution rate, (B) storage efficiency.
For 2D, only one of 4 injection arcs has been considered (i. e. only 4th amount of CO_2 has been injected).

3.6. Chapter Summary

Selecting a simulation code for numerical investigation of CO_2 sequestration in geological formations is controlled by several important factors, which have to be taken into consideration for more accurate modelling results. These factors been explored in this chapter in details clarifying the role of each factor in choosing the most appropriate code for any research work.

For this research work, STOMP-CO_2 simulator was employed because it has been purposely developed to investigate the geological sequestration of CO_2 in geological formations including DSAs at depths greater than 800 m in addition to the modularity and readability of the source code that makes it easy to read, maintain, modify and configure according to the operational mode and problem requirements.

The algorithms and capabilities of the employed STOM-CO_2 simulator along with the governing equations and correlations, and the employed EOSs have been explained. The compilation of the simulation code source files and the post-processing of the outputs have also been described.

The simulation methodology used in this research work has been clarified in details explaining the adopted computational models and the investigated parameters in each chapter.

Moreover, the credibility of the simulation code (STOMP-CO_2) employed in this study has been evaluated by comparing the obtained results against an in-house experimental set-up. The comparison has shown good agreement that has established a robust credibility of the employed computer code in modelling CO_2 sequestration in geological formations and assess their storage capacity and efficiency, and the ultimate fate of the injected gas.

Modelling the domain as 2D or 3D has shown no influence on the calculated values of the storage capacity and efficiency. This stimulates that cylindrical domains are simulated as 2D-models instead of using the time expensive 3D-models to save time and computing requirements.

Chapter 4

A Numerical Study of Dynamic Capillary Pressure Effect for Supercritical Carbon Dioxide-Water Flow in Porous Domain at Core Scale

Overview

Numerical simulations for core-scale capillary pressure (P_c)–saturation (S) relationships have been conducted for a supercritical carbon dioxide-water system at temperatures between 35^0C and 65^0C at a domain pressure of 15 MPa as typically expected during geological sequestration of CO_2. As the P_c-S relationships depend on both S and time derivative of saturation ($\partial S/\partial t$) yielding what is known as the 'dynamic capillary pressure effect' or simply 'dynamic effect', this work specifically attempts to determine the significance of these effects for supercritical carbon dioxide-water flow in terms of a coefficient, namely dynamic coefficient (τ). The coefficient establishes the speed at which capillary equilibrium for supercritical CO_2-water flow is reached. The simulations in this work involved the solution of the extended version of Darcy's law, which represents the momentum balance for individual fluid phases in the system, the continuity equation for fluid mass balance, as well as additional correlations for determining the capillary pressure as a function of saturation, and the physical properties of the fluids as a function of temperature. The simulations were carried out for 3D cylindrical porous domains measuring 10 cm in diameter and 12 cm in height. τ was determined by measuring the slope of a best-fit straight line plotted between (i) the differences in dynamic and equilibrium capillary pressures $\left(P_c^{dyn} - P_c^{equ}\right)$ against (ii) the time derivative of saturation($\partial S/\partial t$), both at the same saturation value. The results show rising trends for τ as the saturation values reduce, with noticeable impacts of temperature at 50% saturation of aqueous phase. This means that the time to attain capillary equilibrium for the CO_2-water system increases as the saturation decreases. From a practical point view, it implies that the time to capillary equilibrium during geological sequestration of CO_2 is an important factor and should be accounted for while simulating the flow processes, e.g., to determine the CO_2 storage capacity of a geological aquifer. In this task, one would require both the fundamental understanding of the dynamic capillary pressure effects for scCO_2-water flow as well as τ values. These issues are addressed in this chapter.

This thesis is mainly a paper based research work and this chapter is based on a group published work (Das et al., 2014) in which my contribution was compiling the source files for the simulation code to create the simulation executable file, develop the input files with boundary conditions for simulator reading, conducting part of the simulation tests and additionally involved in discussing the numerical achieved results.

4.1. Introduction

Technologies for carbon dioxide storage into subsurface formations are widely regarded as one of the most viable options to help reduce the amount of carbon dioxide (CO_2) in the atmosphere and its adverse effects. Typically, CO_2 is injected into deep geological formations in a supercritical (sc) state. In this process, the temperatures and pressures within these formations would still be sufficient for the injected CO_2 to exist in its supercritical state (Doughty and Pruess 2004; Khudaida and Das 2014). Under such conditions, the density of the supercritical fluid is significantly higher than that of gaseous CO_2 but, in most circumstances, lower than that of the resident formation water or brine. Likewise, the viscosity of the supercritical CO_2 ($scCO_2$) is lower than that of water/brine.

A vast amount of research has been conducted on carbon capture and subsurface injection processes as indicated by many reviews on the subject (Stanmore and Gilot, 2005; Abu-Khader, 2006; Zakkour and Haines, 2007; Tsang et al., 2008; Huh and Kang et al., 2009; Michael et al., 2010; Daneshfar et al., 2009; Shukla et al., 2010; Müller, 2011; Zahid et al., 2011; Abidoye et al., 2015) which also reference a large number of other research publications. It is obvious from these literatures that computational methods have been widely used for resolving questions associated with the injection of CO_2 into deep geological formations. These computational techniques are applied to address issues related to the site characterisation and monitoring, and making assessments of potential leakage. Specifically for models on supercritical CO_2 flow and transport in these media, it is clear that two approaches are most commonly used in these studies. In the first approach, the authors apply models of convection-diffusion-dissolution processes (Ennis-King and Paterson, 2003; Riaz et al., 2006; Pruess and Zhang, 2008). The CO_2-rich fluid resulting from the dissolution of CO_2 into brine at the interface of the CO_2-brine system after CO_2 injection is defined to be slightly denser than the surrounding brine causing negative buoyancy. This increase in density causes downward movement of the CO_2-rich fluid towards the bottom of the aquifer. Convective mixing may be considered in these models as it promotes the dissolution of CO_2 into the brine (Ozgur and Gumrah 2009). However, this approach does not consider the concept of fine scale capillary pressure in the porous media (Pruess and Zhang 2008).

In the second approach, the supercritical CO_2 and water/brine are defined to behave as two immiscible fluid phases, particularly at very early period of injection and displacement in the aquifer. They are therefore described by capillary pressure-saturation (P_c-S) relationships along with relative permeability-saturation (k_r-S) functions (Plug and Bruining 2007; Perrin et al. 2009; Lopez et al. 2011; Khudaida and Das 2014).

This research does not use the first approach of convection-diffusion-dissolution and is concerned with the second modelling approach. The second approach applies the extended version of Darcy's law for multiphase flow together with the constitutive relationship for capillary pressure as a function of saturation.

$$P_{nw} - P_w = P_c^{equ}(\mathrm{S}) = \mathrm{f}(\mathrm{S}) \tag{4.1}$$

where,

$P_{nw} = \text{average pressure for non} - \text{wetting phase } [\mathrm{ML^{-1}T^{-2}}]$
$P_w = \text{average pressure for wetting phase } [\mathrm{ML^{-1}T^{-2}}]$
$S = \text{wetting phase saturation } [-]$
$P_c^{equ} = \text{equilibrium (steady state) capillary pressure } [\mathrm{ML^{-1}T^{-2}}]$

Traditionally, equation (4.1) is defined to include the effects of all factors that determine equilibrium saturation distribution of fluids in porous domains. However, the P_c-S relationship has been shown to depend on both S and $\partial \mathrm{S}/\partial \mathrm{t}$ (i.e. desaturation rate) in a number of studies (Topp et al. 1967; Kalaydjian 1992; Bottero et al. 2011(b); Camps-Roach et al. 2010; Das and Mirzaei 2012; Das and Mirzaei 2013). This dependence is known as the 'dynamic capillary pressure effect' or simply 'dynamic effect'. In the publications on multiphase flow in porous media, there have been significant amounts of discussions on the role of dynamic capillary pressure where it has been shown that the definition of P_c may suffer setback owing to its inability to address the dynamic characteristics of the capillary pressure prior to attainment of capillary equilibrium (Hassanizadeh and Gray 1990; Hassanizadeh and Gray 1993a,b; Das and Mirzaei 2012; Das and Mirzaei 2013). The need for modification of the traditional capillary pressure - saturation relation was the conclusion of many authors. This was suggested to accommodate a more complete description of the capillary pressure (Hassanizadeh and Gray 1990; Hassanizadeh and Gray 1993a,b) with the inclusion of a phenomenal factor, namely, a

dynamic coefficient (τ) (Hanspal et al. 2013; Das and Mirzaei 2012; Das and Mirzaei 2013; Hanspal and Das 2012; Bottero et al. 2011(a,b); Camps-Roach et al. 2010; Mirzaei and Das 2007; Dahle et al. 2005; Hassanizadeh et al. 2002). The modification to equation (4.1) has been proposed by Hassanizadeh and Gray (1993a,b) as expressed in equation (4.2):

$$(P_c^{dyn} - P_c^{equ})\big|_s = -\tau\, \partial S/\partial t|_s \tag{4.2}$$

where,

$P_c^{dyn} \equiv$ dynamic capillary pressure $[ML^{-1}T^{-2}]$

$P_c^{equ} \equiv$ equilibrium (steady state)capillary pressure $[ML^{-1}T^{-2}]$

$\partial S/\partial t \equiv$ desaturation rate $[T^{-1}]$

$\tau \equiv$ dynamic coefficient $[ML^{-1}T^{-1}]$

The physical interpretation of P_c^{dyn} and P_c^{equ} together with the difference between them have been discussed previously extensively (Hassanizadeh et al. 2002; Bottero et al. 2011(a,b); Das and Mirzaei 2012, 2013). The slope of the linear relationship between ($P_c^{dyn} - P_c^{equ}$) and $\partial S/\partial t$ in equation (4.2) is the dynamic coefficient (τ) and it provides a quantitative basis for determining the significance of the dynamic capillary pressure effect. For example, if τ is small, the equivalence between P_c^{dyn} and P_c^{equ} is established quickly, and/or vice versa. In the context of dynamic capillary pressure effect, the determination of τ values may be viewed as an 'inverse approach' where all other quantities are assumed known except the values of the dynamic coefficient. Once the significance of its values is understood, a 'forward problem' for simulating the dynamic two-phase flow processes which couples equation (4.2) may be set up, e.g., please see the papers by Fučík et al. (2010) and Peszynska and Yi (2008).

It seems that although there are no significant inconsistencies in the definitions of equilibrium capillary pressure, P_c^{equ}, the interpretation of P_c^{dyn} may vary. For example, Bottero et al. (2011(a)) argue that P_c^{dyn} should be viewed as an 'apparent' capillary pressure. Maintain continuity from some previous work (Mirzaei and Das 2007; Das et al. 2007; Hanspal and Das 2012; Das and Mirzaei 2012, 2013) the dynamic capillary pressure coefficient τ (when $\partial S/\partial t$ is non-zero) has been used in order to describe P_c^{dyn}. There is now a good amount of literatures on simulation and experimental work performed to explore the significance of τ in a number of

circumstances involving two-phase flow process, as well as to explore its range of values. A number of factors have subsequently been reported to have effects on values of τ, some of which include, e.g., permeability anisotropy and media heterogeneities (Manthey et al., 2005; Mirzaei and Das, 2007), temperature (Hanspal and Das, 2012; Civan 2012), fluid properties (Das et al., 2007; Goel and O'Carroll 2011) and porous media mean grain size (Camps-Roach et al., 2010; Das and Mirzaei, 2012, 2013).

In a number of recent papers on dynamic capillary pressure effect, geological sequestration of CO_2 has been used as an example of multiphase flow in porous media (Juanes, 2008; Camps-Roach et al. 2010; Goel and O'Carroll 2011; Khudaida and Das 2014). These papers suggest that dynamic capillary pressure effect is an important consideration of the in-situ conditions of the geological formation for CO_2 sequestration despite the fact that fluid flow or saturation change may occur slowly. This is similar to other processes in the subsurface (e.g., oil extraction) where fluid flow velocity may be slow but the dynamic capillary pressure effect has been shown to be important. Dynamic effect is defined to be the dependence of $P_c^{dyn} - P_c^{equ}$ on $\partial S/\partial t$ as shown in equation (4.2), and is not directly related to the flow velocity of the fluid phases. As such, it is not clear how significant the dynamic capillary pressure effect is in the context of this study. Furthermore, it seems that there is no work currently in the literature specifically for the dynamic capillary pressure effects in the $scCO_2$-water system.

From the above discussion, it is clear that a number of questions have remained unaddressed, e.g., is the dynamic capillary pressure effect really significant in $scCO_2$-water flow in porous media and if so how can the dynamic coefficient be calculated in this case, what is its range of values and how does it compare with the values reported in the literature for other two-phase systems? Indeed, there is no work at the moment that shows the quantitative significance of the dynamic capillary pressure effect for $scCO_2$-water flow in any kind of porous media in general and, geological sequestration of CO_2, in specific. Since geological sequestration of CO_2 takes place at much higher temperature and pressure as compared to other typical laboratory studies on dynamic capillary pressure effect (Camps-Roach et al., 2010; Bottero et al., 2011(a,b); Das and Mirzaei, 2012, 2013), it is also uncertain if any of the reported values of the dynamic coefficient would represent the significance of dynamic effect in the case of CO_2 sequestration. This research work aims to address these knowledge gaps by determining the dynamic capillary

pressure effect (dynamic coefficient) for scCO_2-water flow in porous media. In particular, it's aimed to carry out simulations for core scale porous domain where the porous materials are unconsolidated (discussed further in the next section). The numerical simulations are needed as they help determine the significance of the dynamic effects on direct future experiments and simulations for different porous media properties (e.g., heterogeneous domains, ultra-low or ultra-high permeability domains, larger or smaller domain).

In order to achieve these aims, numerical simulations are conducted for homogeneous domains of laboratory scale. The simulations are carried for a 3D cylindrical domain measuring 10 cm in diameter and 12 cm in height with a view to determine the dynamic capillary pressure effects indicated by a dynamic coefficient (τ). The geological formations can have varying temperatures depending on their respective geothermal gradients (G) and average land surface temperatures. Therefore, the temperature effects on the dynamic coefficient are accounted for with inclusion of other physical effects such as temperature dependent properties of the two-phase system. In order to obtain correlated material properties for the simulations, well-defined core samples (column) of sand particles of known particle size range are prepared and the corresponding properties (e.g., porosity and intrinsic permeability) are determined experimentally. The capillary pressure-saturation curves at equilibrium and dynamic conditions as well as dynamic coefficients were then determined numerically as described in the following sections. Furthermore, the detailed procedures for the numerical simulations including the details of the method are described in the next section.

4.2. Modelling Strategy

In the context of this work, modelling the two-phase flow processes involves the solution of the conservation laws for fluid mass and momentum while taking into account the relevant P_c-S-k_r relationships at different temperatures. In specific, this involves the solution of the extended version of Darcy's law, which represents the momentum balance for individual fluid phases in the system. It also involves the solution of the continuity equation as a statement of the fluid mass balance as well as additional models for determining the capillary pressure as a function of saturation, and the physical properties of the fluids as a function of temperature. In order to characterise the dynamics of the system, the dynamic coefficient is determined by measuring the slope of the line corresponding to values of $\left(P_c^{dyn} - P_c^{equ} \right)$ against $\partial \mathrm{S}/\partial \mathrm{t}$ from equation (4.2).

4.2.1. Governing Model Equations for Two-Phase Flow in Porous Media

The numerical simulations in this work are designed to mimic the pressure cell type of experiments, which are typically used to determine the P_c-S curves in laboratory conditions. In this type of experiments, the top and bottom boundaries are permeable to only one of the fluid phases. Such flow cells have been used by several previous authors (Plug and Bruining, 2007; Das and Mirzaei, 2012, 2013). The two-phase flow behaviour in this pressure cell can be described by the extended version of Darcy's law.

The conventional Darcy's law is an experimentally derived equation of motion based on many assumptions to simplify the solution, and hence it has several limitation:

- Only one dimensional flow is considered.
- It considers homogeneous and isotropic porous medium.
- Incompressible fluid at constant density.
- Incompressible rigid solid matrix.
- It is applicable to flow at low Reynolds number R ≤ 10.

In the case of this research work, none of these assumption is applicable and hence an extended generalized version of Darcy's low is used as a governing conservation equation of motion for both wetting (*w*) and non-wetting phases (*nw*) ss shown in equation (4.3):

$$\mathrm{q}_\gamma + \frac{K_{r\gamma}k}{\mu_\gamma} \cdot \nabla P_\gamma = 0 \qquad \text{for } \gamma \equiv \mathrm{w}, \mathrm{nw} \tag{4.3}$$

where,

$\mathrm{q} \equiv$ fluid flow velocity $[\mathrm{LT}^{-1}]$

$k_\mathrm{r} \equiv$ relative permeability $[-]$

$k \equiv$ intrinsic permeability tensor $[\mathrm{L}^2]$

$\mu \equiv$ viscosity $[\mathrm{ML}^{-1}\mathrm{T}^{-1}]$

$P \equiv$ average pore pressure $[\mathrm{ML}^{-1}\mathrm{T}^{-2}]$

The conservation of mass for the wetting ($_\mathrm{w}$) and non-wetting ($_\mathrm{nw}$) phases is described with equation (3.4).

$$\frac{\partial}{\partial \mathrm{t}}\left(\emptyset \rho_\gamma S_\gamma\right) + \nabla \cdot \left(\rho_\gamma q_\gamma\right) = 0 \qquad \text{for } \gamma \equiv \mathrm{w}, \mathrm{nw} \tag{4.4}$$

where,

$\emptyset \equiv$ porosity of the medium $[-]$

$\rho \equiv$ fluid density $[\mathrm{ML}^{-3}]$

$S \equiv$ average fluid saturation $[-]$

The Brooks-Corey formulations shown in equations (4.5)-(4.7), are used as the governing equations for capillary pressure-saturation relationships (Brooks and Corey 1964).

$$S_{ew} = \left(\frac{P_c}{\mathrm{P^d}}\right)^{-\lambda} \quad \text{for } P_c \geq P^d \tag{4.5}$$

$$S_{ew} = 1 \quad \text{for } P_c \leq P^d \tag{4.6}$$

$$S_{ew} = \left(\frac{S_w - S_{rw}}{1 - S_{rw}}\right) \quad \text{for } 0 \leq S_{ew} \leq 1 \tag{4.7}$$

where,

$\mathrm{S_{ew}} \equiv$ effective saturation of the wetting phase $[-]$

$P^d \equiv$ entry pressure for non $-$ wetting phase $[\mathrm{ML^{-1}T^{-2}}]$

$\lambda \equiv$ pore size distribution index $[-]$

$S_{rw} \equiv$ irreducible wetting phase saturation $[-]$

The Brooks-Corey-Burdine formulae (Brooks and Corey 1964) were employed for relative permeabilities (k_{r}) of the porous media to the wetting and non-wetting phases:

$$k_{rw} = S_{ew}^{(2+\lambda)/\lambda} \tag{4.8}$$

$$k_{rnw} = (1 - S_{ew})^2 \left(1 - S_{ew}^{\frac{2+\lambda}{\lambda}}\right) \tag{4.9}$$

The numerical simulator, STOMP (Subsurface Transport Over Multiple Phases), was used for conducting the modelling exercises. STOMP is a computer model developed by the hydrology group at the Pacific Northwest National Laboratory (White and Oostrom 2006). It has abilities that allow the user to specify and manipulate capillary pressure-saturation-relative permeability (P_c-S-k_r) relationships via a variety of functions, making it ideal for describing fundamental two-phase flow mechanisms. While using STOMP, the user can choose the governing equations for the modelling purpose. In the case of this work, STOMP has been used to solve equations (4.3) – (4.9). The code discretises the partial differential equations (equations 4.3 and 4.4) into the non-

linear algebraic equations useing the finite volume method (FVM) method and Euler-backward time differencing for spatial and temporal discretizations, respectively. The produced algebraic equations are closed using a number of constitutive relationships (equations 4.5 through 4.9) and solved using the Newton-Raphson iteration to resolve their nonlinearities (White and Oostrom 2006).

4.2.2. Selection of Simulation Conditions

It is important to define the temperatures and pressures at which sequestration occurs in order to accurately determine the densities and viscosities of carbon dioxide and water under such conditions. This is mainly because buoyancy forces and mobility ratio between the two fluid phases tend to differ depending on the physical conditions, thus affecting the dynamic flow mechanisms. Nordbotten et al. (2005) classify sedimentary basins according to geothermal regimes as "warm" or "cold" depending on their respective geothermal gradients (G) and average land surface temperatures. Warm basins have G values of around 45^0C/km with a surface temperature of around 20^0C. On the other hand, cold basins have G values of around 25^0C/km with a surface temperature of around 10^0C. CO_2 storage ideally takes place at depths below 800 m. The depths at which injection occurs can be classified as "shallow" for depths up to 1000 m, or "deep" at depths of around 3000 m. An injection depth of 1000 m was assumed for the purpose of this study, which equates to temperatures ranging between 35^0C for "cold" basins and 65^0C for "warm" basins. This depth was set because it lays within the ideal range of depths (800 – 3000 m) for CO_2 sequestration at which the injected gas can stay at supercritical state that leads to larger amounts of the gas injected into a specific volume of the formation.

Birkholzer et al. (2009) measured a pressure gradient of around 18.1 kPa/m (in saline aquifers, which equates to a pressure of 18.1 MPa at a depth of 1000 m knowing that the surface pressure is 101.325 kPa (i. e. 1 atm). This pressure gradient can vary depending on the compositions and structures of the sedimentary rocks. Additionally, in a recent paper by Benson et al. (2011), sequestration experiments and simulations were conducted at pressures of around 12.4 MPa. Based on these figures a domain pressure of 15 MPa was selected for this study.

The critical temperature and pressure of carbon dioxide are 31.1°C and 7.382 MPa, respectively, above which it exists as a supercritical fluid. In all our simulations, temperatures were varied

between 35^0C and 65^0C while maintaining the domain pressure (15 MPa). Under such conditions, the carbon dioxide would remain in a supercritical state. Furthermore, the simulations were carried out for the case when the geological formation contains water and not brine.

4.2.2.1 TEMPERATURE DEPENDENT DENSITY AND VISCOSITY OF WATER AND SUPERCRITICAL CARBON DIOXIDE

The densities of supercritical carbon dioxide and pure water at the conditions selected for the simulations are summarised in Table 4.1.

The carbon dioxide densities were obtained by interpolating experimental results reported by (Chiquet et al. 2007). Water densities were calculated as shown in equations (4.10) – (4.14):

$$\rho_l = \mathrm{v_c^{w^{-1}}}\{\mathrm{A_{11}a_5Z^{-5/17}} + \mathrm{A_{12}} + \mathrm{A_{13}T_r^w} + \mathrm{A_{14}(T_r^w)^2} + \mathrm{A_{15}(a_6 - T_r^w)^{10}} + \mathrm{A_{16}(a_7 + (T_r^w)^{19})^{-1}} - \mathrm{(a_8 + (T_r^w)^{11})^{-1}(A_{17} + 2A_{18}P_r^w + 3A_{19}(P_r^w)^2 - A_{20}(T_r^w)^{18}(a_9 + (T_r^w)^2(-3(a_{10} + P_r^w)^{-4} + a_{11})\, 3A_{21}(a_{12} - T_r^w)(P_r^w)^2 + 4A_{22}(T_r^w)^{-20}(P_r^w)^3\}^{-1} \quad (4.10)$$

$$P_r^w = {}^{P}\!/_{P_c^w} \quad (4.11)$$

$$T_r^w = {}^{T}\!/_{T_c^w} \quad (4.12)$$

$$\mathrm{Y} = 1 - \mathrm{a_1}(T_r^w)^2 - \mathrm{a_2}(T_r^w)^{-6} \quad (4.13)$$

$$\mathrm{Z} = \mathrm{Y} + (\mathrm{a_3Y^2} - 2\mathrm{a_4}(T_r^w) + 2\mathrm{a_5}P_r^w)^{1/2}. \quad (4.14)$$

Where A_{11}…A_{22} and a_5….a_{12} are liquid water primary constants, *P* and *T* are the water pressures and temperatures respectively, P_c^w and T_c^w are the critical water pressures and temperatures. $V_c^w$is the critical specific water volume. Values for the constants are given under liquid water constants in Table 4.2.

Table 4.1. Carbon dioxide and water densities for various temperatures at 15 MPa Pressure.

Temperature (K)	**Carbon dioxide Density, (kg m^{-3})** (Obtained from experimental results by Chiquest et al. (2007**)**)	**Water Density, (kg m^{-3})** **(**calculated from equation 4.10)
308.15	815	994
318.15	735	990
328.15	645	986
338.15	535	980

Table 4.2. Liquid Water Constants for equation (4.10) (Hanspal and Das, 2012).

A_{11}	7.98E+00	a_1	8.44E-01
A_{12}	-2.62E02	a_2	5.36E-04
A_{13}	1.52E-03	a_3	1.72E+00
A_{14}	2.28E-02	a_4	7.34E-02
A_{15}	2.42E+02	a_5	4.98E-02
A_{16}	1.27E-10	a_6	6.54E-01
A_{17}	2.07E-07	a_7	1.15E-06
A_{18}	2.17E-08	a_8	1.51E-05
A_{19}	1.11E-09	a_9	1.42E-01
A_{20}	1.29E+01	a_{10}	7.00E+00
A_{21}	1.31E-05	a_{11}	3.00E-04
A_{22}	6.05E-14	a_{12}	2.04E-01

As expected, Table 4.1 shows that the densities of both carbon dioxide and brine decrease when the temperature is increased,. Furthermore, the rate at which the carbon dioxide density decreases is much greater than that for water. Table 4.3 summarises the viscosities of carbon dioxide and pure water. Carbon dioxide viscosities were obtained by interpolating experimental results reported by Fenghour et al. (1998). Water viscosities were calculated using equation (4.15) by Hanspal and Das (2012) as a function of temperature.

$$\mu_l = \exp(-24.71 + {}^{4209}/_{T} + 0.04527T - 3.376 \times 10^{-5}T^2) \quad (4.15)$$

where,

$\mu_l \equiv$ liquid water viscosity [Pa. s]

$T \equiv$ temperature [K]

Table 4.3. Supercritical Carbon Dioxide and Water Viscosities for various Temperatures at 15 MPa Pressure.

Temperature (K)	**308.15**	**318.15**	**328.15**	**338.15**
Carbon dioxide Viscosity (10^{-5} Pa s) (Experimentally by Fenghour et al. (1998)	7.2	6.2	5.0	4.2
Water Viscosity (10^{-4} Pa s) (Calculated by equation 4.15)	7.4	6.1	5.2	4.4

The table shows that as temperature is increased, the viscosities of both carbon dioxide and brine decrease. The density and viscosity values as determined above were supplied for the simulations.

It is appreciated that there are other approaches, which may be used to determine the temperature dependency of liquid properties. For example, Civan (2007) has reported a modification to the Vogel-Tammann-Fulcher (VTF) equation for calculating temperature effects on water density. These approaches may require lesser number of coefficients and exponents in the correlations in comparison to equations (4.10) – (4.15). Therefore, the alternative approaches may be attractive in some cases. Equations (4.10) - (4.14), which have been used in this work, represent the data in steam tables by Meyer et al. (1967) that are well recognised. These equations also maintain continuity from previous work by Hanspal and Das (2012). For these reasons, the equations mentioned in this section have been used rather than an approach such as the one reported by Civan (2007).

4.2.2.2 INTERFACIAL TENSIONS

Interfacial tensions have a noticeable impact on P_c-S relationships in two-phase flow behaviour. Thus, the simulator also required specifying carbon dioxide-water and water-air interfacial tensions under the various simulation conditions. Carbon dioxide-water interfacial tensions at 15 MPa between 35^0C and 65^0C were obtained using experimental results reported by Bachu and Bennion (2009). Water-air interfacial tensions were calculated using equation (4.16).

$$\gamma^{lg} = a_0^{lg} + a_1^{lg} T \ln(T) + c^{lg} T \tag{4.16}$$

where,

$\gamma^{lg} \equiv$ water $-$ air interfacial tension [Nm^{-1}]

constants a_0^{lg}, a_1^{lg} and $c^{lg} = 67.82, -0.16889,$ and 0.9766 respectively [dyn $cm^{-1}K^{-1}$]

$T \equiv$ temperature [K], (Hanspal and Das 2012).

Values for the interfacial tensions are presented in Table 4.4.

Table 4.4. Supercritical Carbon Supercritical Carbon Dioxide-Water and Air-Water Interfacial Tensions at different Temperatures.

Temperature, K	**308.15**	**318.15**	**328.15**	**338.15**
Carbon dioxide-Water Interfacial Tension, (dyn cm^{-1}) **	18.1	21.3	27.2	31.3
Water-Air Interfacial Tension, (dyn cm^{-1}) ***	70.4	68.8	67.1	65.4
** Obtained using experimental results reported by Bachu and Bennion (2009). *** Calculated using equation (4.16).				

4.2.2.3 IRREDUCIBLE SATURATION

Irreducible water saturation in the porous media increases by increasing the temperature. Equation (4.17) was used to account for the effects of temperature on irreducible saturation, S_{rw} with the calculated values presented in Table 4.5:

$$S_{rw} = a_r + b_r T \tag{4.17}$$

where, constants a_r and $b_r \equiv$ -1.274 and 0.00438, respectively [-], (Hanspal and Das, 2012).

$T \equiv$ temperature [K]

Table 4.5. Irreducible water Saturation at Different Temperature (calculated using equation 4.17).

Temperature (K)	**308.15**	**318.15**	**328.15**	**338.15**
Irreducible Saturation (-)	0.0757	0.1195	0.1633	0.2071

The table shows that at 35^0C, if the porous sample is initially fully saturated with water, it is theoretically possible to displace approximately 93% of the water with carbon dioxide using capillary forces. As the temperature is increased to 65^0C, only 79% of the water can be displaced.

Therefore, selecting injection sites in high temperature sedimentary basins could cause significant reduction in storage capacities.

4.3. Description of Porous Media Properties for Simulations

For the purpose of this study, various properties of fine and coarse-grained sand were determined experimentally for core samples. This was done with a view to utilize realistic sample properties for the simulations as well as to relate the particle size to the dynamic effect in capillary pressure relationship for CO_2 injection as done previously for other fluid systems (Camps-Roach et al. 2010; Das and Mirzaei, 2012, 2013). The porous media samples were silica sand (quartz) with coarse-grained sample (DA 14/25) and fine-grained sample (CH30) which were purchased from Minerals Marketing Ltd, Nantwich Cheshire, UK.

The particle densities for the sand samples used for simulations in this work were measured using a helium pycnometer (Micromeritics Model 1305, Norcross, USA). Unlike the traditional method of fluid displacement, gas pycnometry systems are fully automated and rather use inert gases, such as helium and nitrogen as the displacement media. This method is based on the ideal gas equation of state (EOS), which helium gas precisely fulfils. It was employed in this work because helium is a non-reactive gas and can easily penetrate into pores of as small as one angstrom in diameter. Firstly, the sand samples were washed in deionised water and dried in a vacuum oven before getting sealed in the filling compartment of the pycnometer, which is of 0.1 litre in size as schematically shown in Figure 4.1. Helium gas was introduced at 0.15 MPa through the filling valve and rapidly filled the whole void volume of the sample compartment (filling chamber) and continues till the equilibrium was reached. Then after, the gas was allowed to the second compartment (expansion chamber) via the expansion valve for volume measurement, till equilibrium was reached again before allowing the gas out of the system via the venting valve. This process was repeated 10 times to fully purge the system and clean the sample before starting the actual measurements. The pressures in both chambers P_1 and P_2 were recorded by the system and the volume of the sample V_{samp} was calculated from the filling chamber volume V_{cel} and the expansion chamber volume V_{exp} by the equipment according to the following equation;

$$V_{samp} = V_{cel} - \frac{V_{exp}}{\frac{P_1}{P_2} - 1} \tag{4.18}$$

Knowing the mass of the sample material (m_{samp}), the density of the sample was calculated;

$$\rho_{samp} = \frac{m_{samp}}{V_{samp}} \tag{4.19}$$

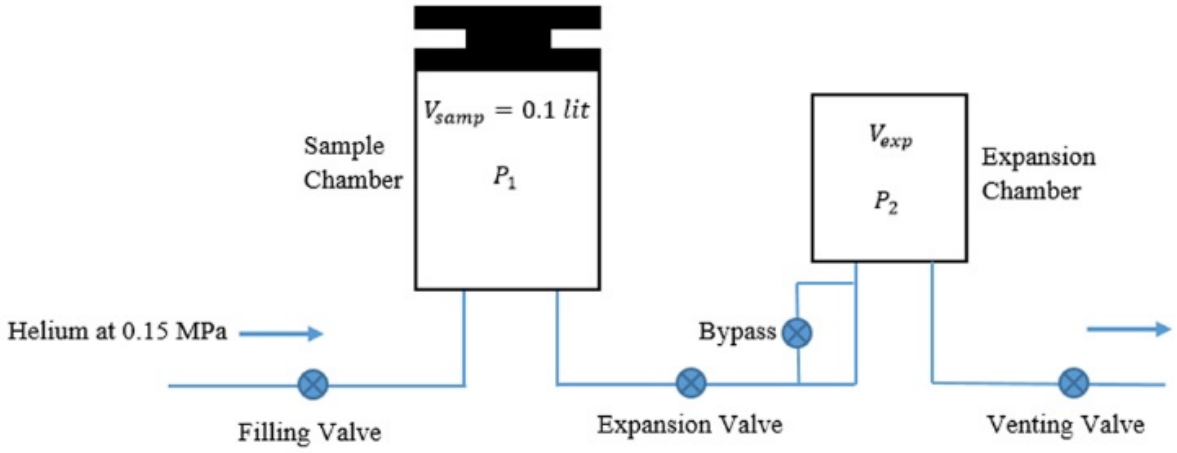

Figure 4.1. Schematic diagram for the helium pycnometer used in determining the particle density for the simulation samples.

On the other hand, the intrinsic permeabilities for the simulation samples were determined using a constant head permeameter, which is schematically displayed in Figure 4.2. The setup consists of a cylindrical specimen (sample cell) with an inlet and outlet, two supportive plates, a funnel and a graduated flask as well as a set of flow pipes. The sand sample was filled into the sample cell and water was allowed to flow into the permeameter through the funnel until the cell was full. The outlet was opened and water was continuously added through the funnel until no bubbles of air were noticed out of the discharge pipe and the water level kept constant (steady state was attained). The water head was measured as the distance between the water surface in the funnel and the bottom of the specimen and kept constant till the end of the measuring run. The discharge water was collected for one minute in the pre-weighed graduated flask, which was further weighed with the collected water then after, the volume of the collected water was measured in the flask. From the achieved measurements, the intrinsic permeability k was calculated from Darcy's equation;

$$k = \left(\frac{QL}{Aht}\right)\left(\frac{\mu}{\rho g}\right) \tag{4.20}$$

where Q is the volume of the discharged water, L and A are the length and cross-sectional area of the cell respectively, h is the head of water and t is the time elapsed to collect the amount of discharged water. ρ and μ are the density and viscosity of water respectively.

The procedure was repeated four times with different water head values and the average value of the permeability was determined for the simulations as displayed in Table 4.6.

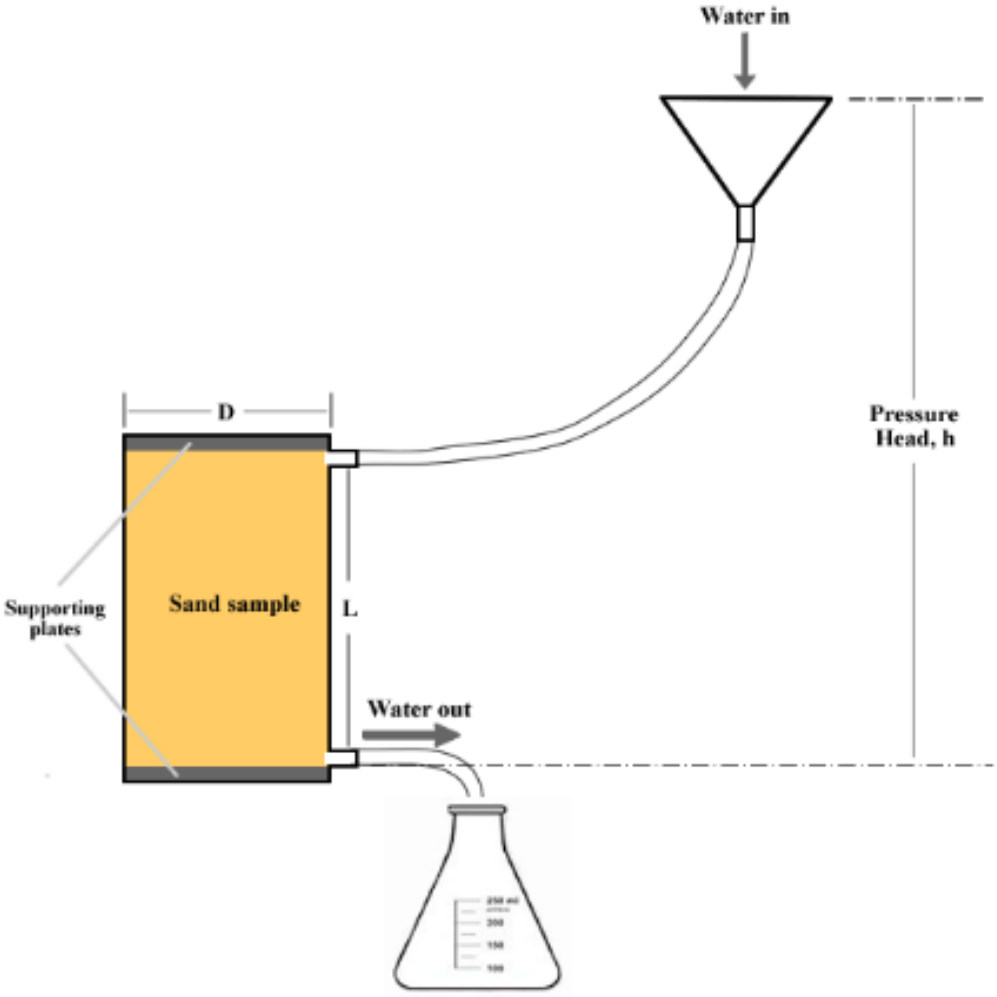

Figure 4.2 Schematic diagram for the constant head permeameter.

Similarly, the physical properties of a mixture consisting 50% fine grained sand and 50% coarse-grained sand were determined and used in the simulations. All simulations were based on a porous domain on a core-scale, which is homogeneous in terms of porosity and intrinsic permeability.

Table 4.6. Experimentally Measured Physical Properties of the Porous Media that were used in the numerical simulations in this work.

Material Properties	**Fine Sand**	**Coarse Sand**	**50% Coarse and 50% Fine Sand Mixture**
Permeability, k (m^2)	5.66×10^{-11}	3.65×10^{-10}	5.95×10^{-11}
Particle Density, ρ (kg m^{-3})	2660	2740	2700
Porosity, Φ (-)	0.37	0.38	0.34
Pore Size Distribution Index, λ (-)	3.86	3.50	3.18
Entry Pressure, P^d (N m^{-2})	660	431	848

The porous samples chosen for this research are for unconsolidated laboratory scale where the correlation between particle size, porosity, permeability and level of compaction can be maintained. In a similar approach, Plug and Bruining (2007) have used porous domains for studying supercritical CO_2 injection which have porosities (0.37-0.38) like the domains simulated in this work, and permeability of $k \sim 2 \times 10^{-10}$ m^2, which is larger than the fine grained sand permeability and almost the same as coarse grained sand permeability used in this study. The main reason for choosing these porous samples is to avoid using uncorrelated parameter values (e.g., particle size, porosity, permeability, Brooks-Corey parameters) because a number of papers (Khudaida and Das, 2014; Das and Mirzaei 2013; Shubao et al. 2012; Civan 2012; Hanspal and Das 2012; Nordbotten et al. 2010; Sakaki et al. 2010; Fučík et al. 2010; Camps-Roach et al. 2010; Oung et al. 2005; Dahle et al. 2005; Hassanizadeh et al. 2002) relating to the dynamic effect show that there is an interplay of variables which affect the dynamic coefficient. The correlated medium parameters are chosen to ensure that correct lumped effects of the material parameters on the dynamic coefficient are accounted for. Furthermore, this approach allows to place the significance of the dynamic effect for CO_2-water system in the context of other studies on dynamic capillary pressure effect (e.g., silicone oil-water flow in porous media) which have used porous domains of similar properties. As shown in this work, the study does suggest that the dynamic effect could be important for supercritical CO_2-water flow in porous media and so it should direct further work, e.g., design of future laboratory experiments. It is

understood that in the field scale the porous medium properties may vary (Daneshfar et al. 2009). However, for the purpose of this research study, which deals with core scale domains, this variability was ignored and isotropic porous domains were used, where the average permeability is constant in all directions. This is done in an attempt to determine the presence of dynamic capillary pressure effect for CO_2-water flow in porous medium in absence of any other factors.

4.4. Domain Geometry

A 3-dimensional cylindrical domain was chosen with the following geometry. It had a diameter of 10 cm and a vertical length of 12 cm and discretised into 26 grid blocks horizontally and 4 blocks radially and azimuthally as illustrated in Figure 4.3. In Table 4.7, N represents the number of nodes, Δr is the node spacing in r-direction, $\Delta\theta$ is the node spacing in θ direction, and ΔZ is the node spacing in the Z-direction. The chosen cylindrical grid is composed of 416 nodes.

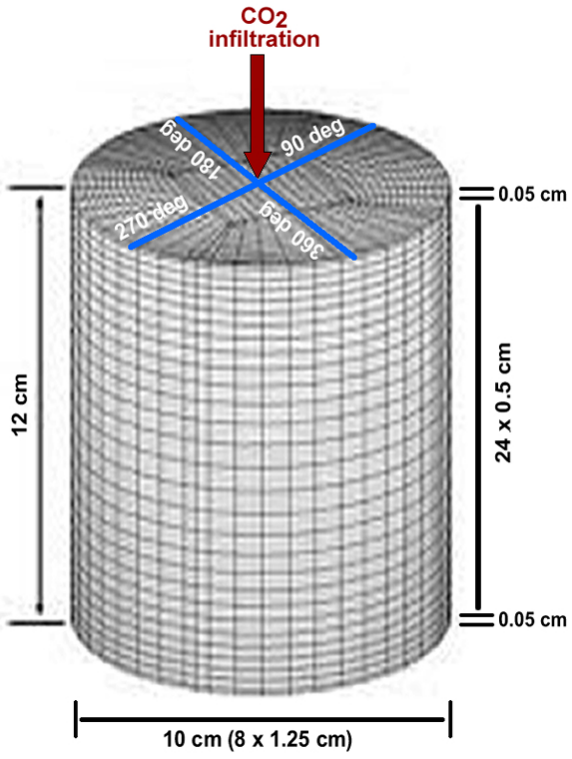

Figure 4.3. A schematic diagram of simulated domain geometry, showing the Number of Nodes and Nodal Spacing.

Table 4.7. Geometry of 3D Cylindrical Domain, showing the number of nodes and nodal spacing.

Number of Nodes x Nodal Spacing		
***N x* Δr (m)**	***N x* $\Delta\Theta$ (degrees)**	***N x* ΔZ (m)**
4 x 0.01275	4 x 90	1 x 0.0005 24 x 0.005 1 x 0.0005

4.5. Initial and Boundary Conditions for Simulations

All simulations were conducted for 3D models as explained in section 4.4 and the boundary conditions were set such that the porous domain was initially fully saturated with water (wetting phase). In order to simulate the dynamic two-phase flow behaviour, the $scCO_2$ (non-wetting phase) was introduced through the top of the domain at a constant pressure until the domain attained irreducible wetting phase (water) saturation.

The conditions were set such that there was no out-flow of water through the top of the domain. Neither carbon dioxide nor water could flow out of the domain through the sides. Additionally, only water could flow out via the bottom boundary of the domain. In all simulations, the porous media were assumed to possess homogeneity in bulk properties (e.g., porosity and permeability).

A total of four sets of dynamic simulations were conducted for each of the three porous samples at 35^0C, 45^0C, 55^0C and 65^0C. The series of simulations at each temperature were conducted by successively increasing the carbon dioxide pressure head, i.e., simulation 1 at 50 cm head, simulation 2 at 70 cm head, simulation 3 at 100 cm head and simulation 4 at 135 cm head. At each dynamic condition, the pressure, as CO_2 head, was imposed at once and the water drainage was allowed to continue until irreducible water saturation was attained.

Table 4.8 summarises the boundary conditions for the dynamic simulations conducted in this work. The initial and bottom water pressures in the domain were calculated by taking into account the domain pressure of 15 MPa, water densities and gravity effects. CO_2 pressures, as heads of CO_2 above the domain, were calculated in a similar way but carbon dioxide densities were taken into account instead.

Table 4.8. Initial and Boundary Conditions for the Dynamic Simulations.

Temperature (K)		**308.15**	**318.15**	**328.15**	**338.15**
Initial Water Pressure (Pa)		15001144	15001139	15001134	15001128
Top Carbon dioxide Pressure (Pa)	Dynamic 1	15003991	15003599	15003185	15002620
	Dynamic 2	15005587	15005039	15004422	15003668
	Dynamic 3	15007982	15007198	15006317	15005240
	Dynamic 4	15010775	15009718	15008528	15007073
Bottom Water Pressure (Pa)		15001178	15001173	15001168	15001162

In order to calculate the dynamic coefficient, one quasi-static simulation was conducted for each of the porous samples at the corresponding temperatures. In the quasi-static simulations, the initial and bottom water pressures were kept constant at each of the temperatures shown in Table 4.8. For the quasi-static process, rather than introducing the carbon dioxide at a single constant pressure, the conditions were set such that pressure was successively increased at various steps within each simulation period. Starting from an arbitrary but very small initial pressure, gradual step increase in pressure followed. At the entry pressure, P^d of the domain, the supercritical CO_2 entered and the water displacement began. This continued until the irreducible saturation was attained. This depends on the imposed tolerance limit. In this work, the limit is reached when saturation at all grid points remains unchanged or desaturation rate ($\partial S/\partial t$) is less than tolerance limit of 10^{-10}.

Each calculated average P_c-S_w point at a particular time for the domain provides a point in the P_c-S_w curve. It corresponds to the wetting phase saturation value, S_w, at which a particular capillary pressure, P_c, is generated in the domain. For the system under quasi-static condition, this is the point where fluid phases move to equilibrium positions such that the imposed forces are the same as forces within the domain (Das et al., 2007). Upon further imposition of pressure on the supercritical CO_2, the displacement continues and drives the system to a new state of equilibrium when the governing forces are once more balanced. This provides a second point on the curve and the procedure follows the same pattern until the 135 cm head is reached which is believed to correspond to condition for irreducible saturation.

During the course of this work, two approaches for averaging the capillary pressure were used. The first one is the approach of using an arithmetic mean of the data and the second one involved using saturation weighted average of capillary pressure as discussed by some of the previous

papers (Das et al., 2007; Hanspal and Das, 2012; Das and Mirzaei, 2012). Both averaging approaches produced similar results in this work. However, at high water saturation, it was observed that the results from the saturation weighted averaging method were more fluctuating than the results from the arithmetic mean as illustrated in Figure 4.4, and hence the arithmetic averaging method was used. It is noted that (Nordbotten et al. 2007; Nordbotten et al. 2008; Nordbotten et al. 2010) have discussed alternative ways of averaging capillary pressure and relative permeability data; however, they were not attempted in this work.

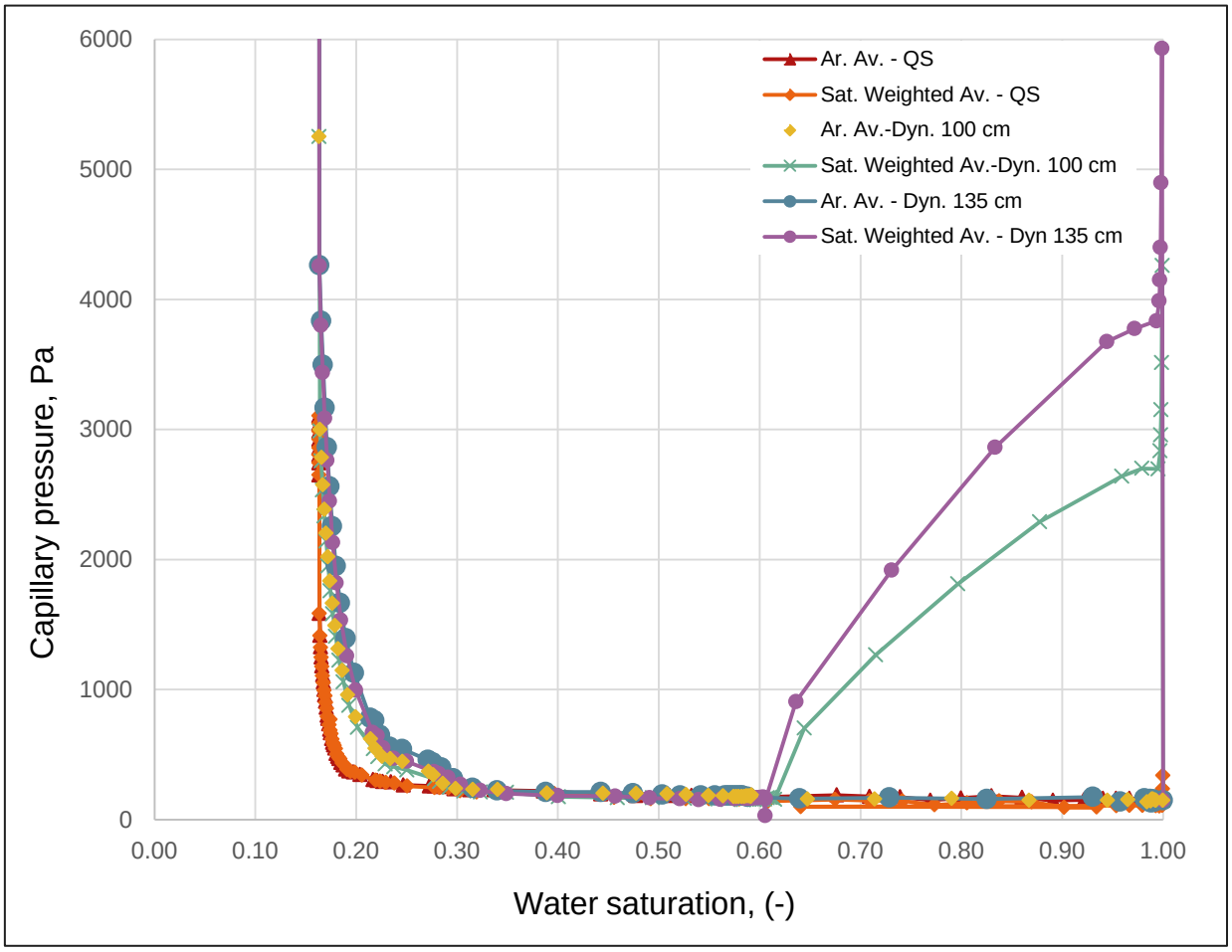

Figure 4.4. Capillary pressure-water saturation curves for Coarse sand at 55^0C and different pressure heads for quasi-static and dynamic flow conditions. These curves are based on porous medium properties obtained from experimental measurements (Table 4.6).

4.6. Determination of Dynamic Coefficient (τ)

The P^c-S curves obtained for the dynamic and quasi static simulations from the above procedures were used in determining the dynamic coefficient (τ) for the domain. For the boundary conditions, respective $P_c^{dyn} - P_c^{equ}$ was plotted against $-\partial S/\partial t$ at the same wetting phase saturation. The plots were fitted to a straight line, the slope of which gives the dynamic coefficient. This is in accordance with Eq. (4.2) which shows that if $P_c^{dyn} - P_c^{equ}$ and time derivative of saturation ($\partial S/\partial t$) are known at a given saturation value, τ can be determined. The determined values of the dynamic coefficient are reported in Figures 4.11 through 4.13 in section 4.8.3.

4.7. Governing Equations and Calculations

CO_2-water as a two-phase flow system is governed by the extended version of Darcy's law representing the conservation equation of momentum (equation 4.3) in association with the conservation equation of mass for water as a wetting phase and CO_2 as the non-wetting phase (equation 4.4). To determine the capillary pressure, Brooks-Corey model (Brooks and Corey 1964), which is represented in equations 4.5 through 4.7 are employed, whereas for relative permeabilities, Brooks-Corey correlation combined with Burden theorem (Burdine, 1953) are used (see equations 4.8 and 4.9).

The calculations in this study involve quantifying the average water saturation and capillary pressure at each time step. For water saturation, the volume-weighted approach is used. It accounts the influence of each grid-cell according to its volume to calculate the average water saturation according to equation 4.21,

$$S_w|_{t_n} = \frac{\sum_{j=1}^{m} S_{wj} * V_j}{\sum_{j=1}^{m} V_j} \tag{4.21}$$

While the average capillary pressure is calculated using the saturation-weighted method taking into account the volume fraction of the phases within each grid-cell.

$$P_c|_{t_n} = \left[\frac{\sum_{j=1}^{m} S_{nwj} * P_{nwj}}{\sum_{j=1}^{m} S_{nwj}} - \frac{\sum_{j=1}^{m} S_{wj} * P_{wj}}{\sum_{j=1}^{m} S_{wj}}\right]\Bigg|_{t_n} \tag{4.22}$$

where $S_w|_{t_n}$ and $P_c|_{t_n}$ are the average water saturation and average capillary pressure in the whole domain respectively, $S_{wj}$and S_{nwj} represent the water and CO_2 saturation within cell (j) and likewise $P_{wj}$and P_{nwj}, identify their pressures, whereas V_j refers to the volume of grid-cell (j).

All variables were taken at each time step to calculate the average water saturation and capillary pressure for the whole domain at that specific time step to produce the first point for plotting P_c-S_w curves. This procedure was repeated for all 48 time steps achieving 48 points of (S_w, P_c) for both dynamic and quasi-static cases for the purpose of comparison.

Aiming at avoiding the existed fluctuations in the produced curves of average capillary pressure versus water saturation, the arithmetic averaging method was adopted because it produced more stable curves with close values to the ones from the saturation-weighted approach.

Then after, the desaturation rate $\partial S/\partial t$ at each time step (t_n) was calculated using equation 4.23,

$$\partial S/\partial t|_{t_n} = \frac{S_w|_{t_{n+1}} - S_w|_{t_{n-1}}}{t_{n+1} - t_{n-1}} \tag{4.23}$$

where S_w is the average water saturation in the whole domain at that specific time step.

Looking at equation 4.2, the terms $\left(P_c^{dyn} - P_c^{static}\right)$ and $(\partial S/\partial t)$ can be calculated at each value of average water saturation and consequently the value of the dynamic pressure effect coefficient (τ) in the domain at each saturation value can be calculated by equation 4.24,

$$\tau|_{S_w} = -\left[\frac{\left(P_c^{dyn} - P_c^{static}\right)}{(\partial S/\partial t)}\right]\Bigg|_{S_w} \tag{4.24}$$

Where $\left(P_c^{dyn} - P_c^{static}\right)$ is the difference between the dynamic and quasi-static capillary pressure.

The dynamic coefficient (τ) in the whole domain can be quantified by plotting $\left(P_c^{dyn} - P_c^{static}\right)$ versus $(\partial S/\partial t)$ at all-time steps and the slope of the best fit line would signify the value of (τ).

4.8. Results and Discussions

4.8.1. Dynamic Water Saturation Profiles

Figure 4.5 represents the saturation (*S*)-time (t) curves for the three samples at 35^0C and 50 cm carbon dioxide pressure heads. Although the saturation-time curves are discussed earlier in the context of other flow problems, they are important in this study, as they are needed to calculate $\partial S/\partial t$ and subsequently the dynamic coefficient. All the simulated curves in this work show that approximately 50% of the water was displaced within seconds of starting the flow (drainage). In the coarse sand sample, approximately 50% of the water was displaced within 5 seconds while the fine sand attained this saturation in less than 180 seconds. The 50% coarse and 50% fine sand mixture attained 50% water saturation within 90 seconds. The time reduced further as the carbon dioxide pressures were increased. Such rapid initial water displacements were most likely due to the high pressures (approximately 15 MPa) imposed on a relatively small domain, measuring only 10 cm in diameter and 12 cm in height.

The importance of the $\partial S/\partial t$ curves and their implications were discussed earlier (e.g., Hassanizadeh et al., 2002; Das and Mirzaei, 2012) and is not discussed in detail in this work. However it must be stated that in consistent with previous studies (e.g., Das and Mirzaei, 2012), the $\partial S/\partial t$ is calculated from equation 4.23.

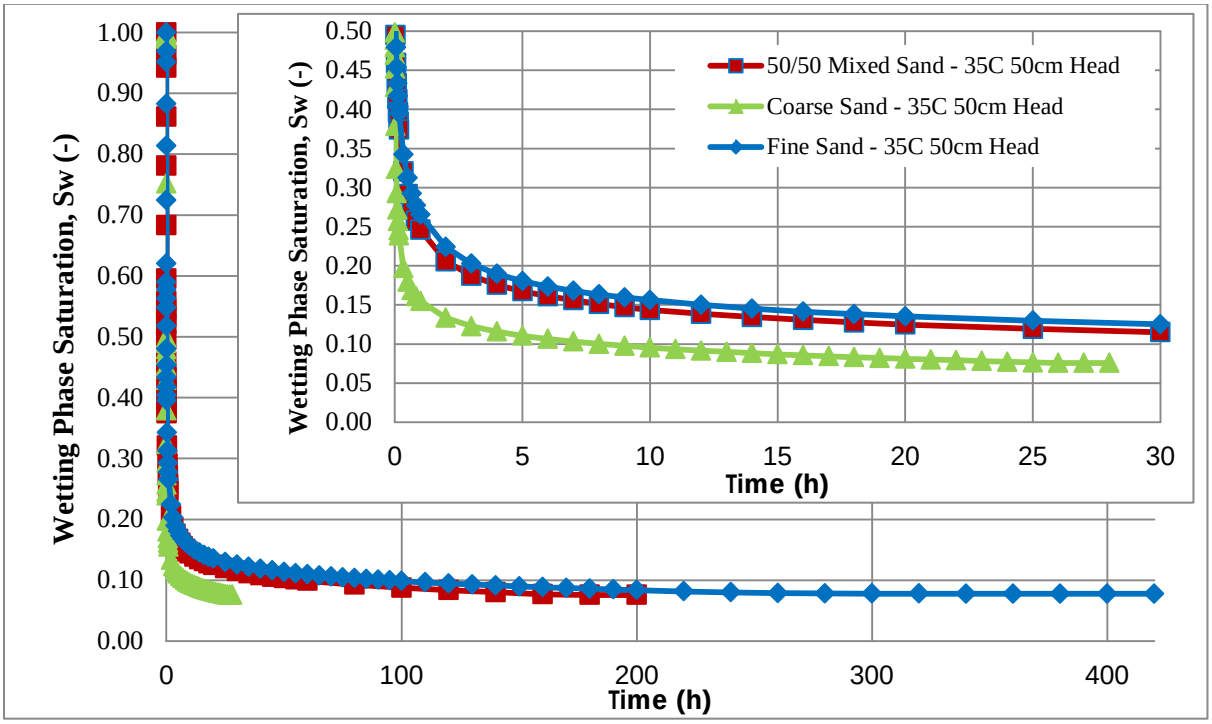

Figure 4.5. Saturation-Time curves for Coarse, Fine and Mixed Sands at 35^0C and 50 cm pressure. These curves are based on porous medium properties obtained from experimental measurements (Table 4.6).

In general, the desaturation rate ($\partial S/\partial t$) changes with saturation and time and, this determines when two-phase flow system reaches capillary equilibrium. As expected, the $\partial S/\partial t$ values were the highest at wetting phase saturation values close to 1. The rate falls with the decrease in saturation and was the least at irreducible saturation. For example, $\partial S/\partial t$ values for coarse sand at 35^0C and pressure head of 50 cm ranged between -2.389×10^{-1} s^{-1} at 0.9 wetting phase saturation and -7.222×10^{-7} s^{-1} at 0.1 wetting phase saturation. Similar trends are observed for fine and mixed sands. It is noteworthy from the results that at low wetting phase saturations, it becomes increasingly difficult to displace water as the domain approaches irreducible saturation. This explains why the time derivatives of saturation for all samples were the highest at wetting phase saturation values close to unity. It also explains the dramatic rise in capillary pressures as water saturation values fall from 0.3 close to irreducible saturation. Similar trends were reported for silicone oil-water system in fine sand (Das and Mirzaei, 2012, 2013) where the desaturation rate was smaller than in the coarse sand sample. It should also be noted that the $\partial S/\partial t$ values are related to the mobility ratios, which depend on the relative permeabilities of the fluid phases and the fluid viscosity ratios (Das et al. 2007). In other words, if the mobility ratios change, then $\partial S/\partial t$ and, hence, the dynamic coefficient may also change.

In this work, no significant effect of temperature on $\partial S/\partial t$ values at high water saturations was found for all the modelled porous samples. However, the $\partial S/\partial t$ values at low saturations displayed small increases as temperature was increased. In addition, the coarse sand simulation at a temperature of 35^0C and CO_2 pressure head of 50 cm readily achieved the irreducible saturation value of 0.0757 within a simulated time of 26 hours. Due to the fine sand sample having the lowest permeability value, irreducible saturation was never achieved at the same time. So, a simulation time of 300 hours on a personal computer (Intel i3 Core, DELL INSPIRON N5040) was required in order to achieve a final saturation value of 0.0778. The mixed sand sample with an intermediate permeability value took 180 hours to attain a final saturation of 0.0758. The simulation times reduced as the carbon dioxide injection pressures were increased, while temperature appeared to have no significant effect on the time taken to achieve irreducible saturation.

4.8.2. Dynamic and Quasi-Static Capillary Pressure-Saturation Curves

Figures 4.6 and 4.7 represent the dynamic and quasi-static capillary pressure (P_c)-saturation (S) curves for coarse-grained sand at 35^0C, 45^0C, 55^0C and 65^0C, respectively. In consistent with the trends in the literature, the quasi-static curves lie below the dynamic curves in the figures. This means that at the quasi-static condition, the same saturation is attained at a lower capillary pressure compared with the dynamic condition and as such, it is important to differentiate between a quasi-static condition and dynamic condition. Also, as the carbon dioxide pressure heads increase, so does the capillary pressures. This can be observed more clearly at the wetting phase saturations below 0.4. It was observed that the distinction between the curves decreased as temperatures were increased. One point of note in this regard is that all P_c-S curves in Figures 4.6 and 4.7 are calculated using P_c data from all directions (e.g., axial and radial directions). Whether the P_c-S relationships would vary depending on the directions, and if so, how significant these variations would be, are not investigated in this study.

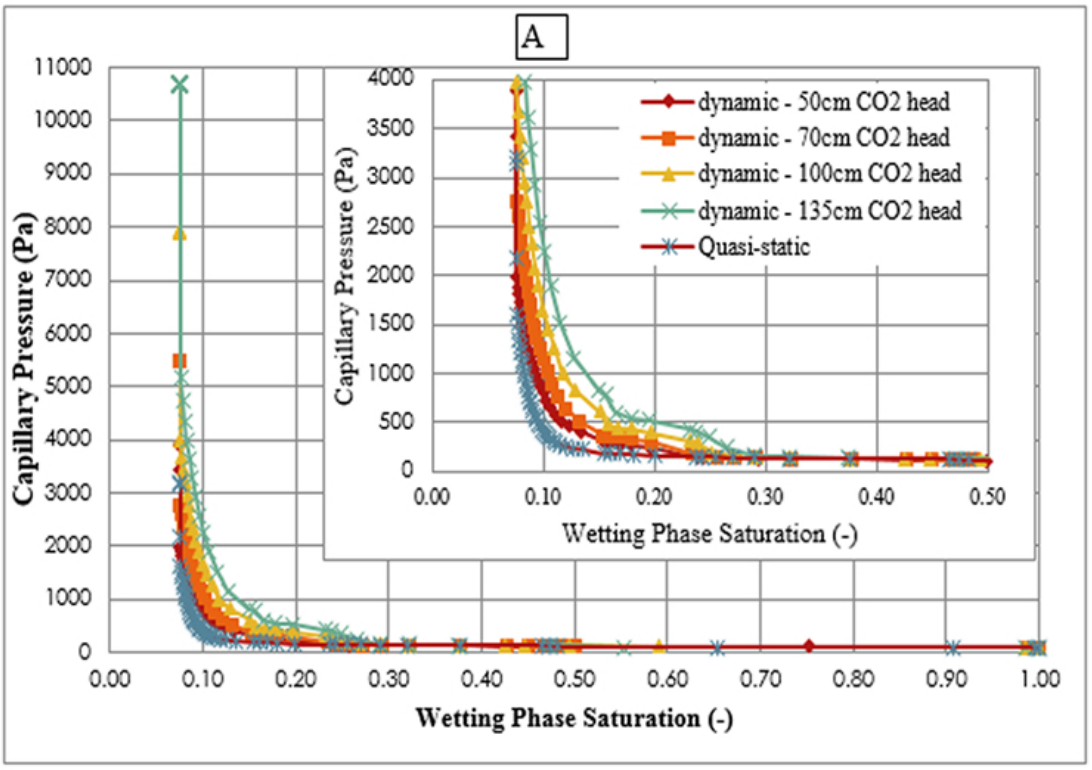

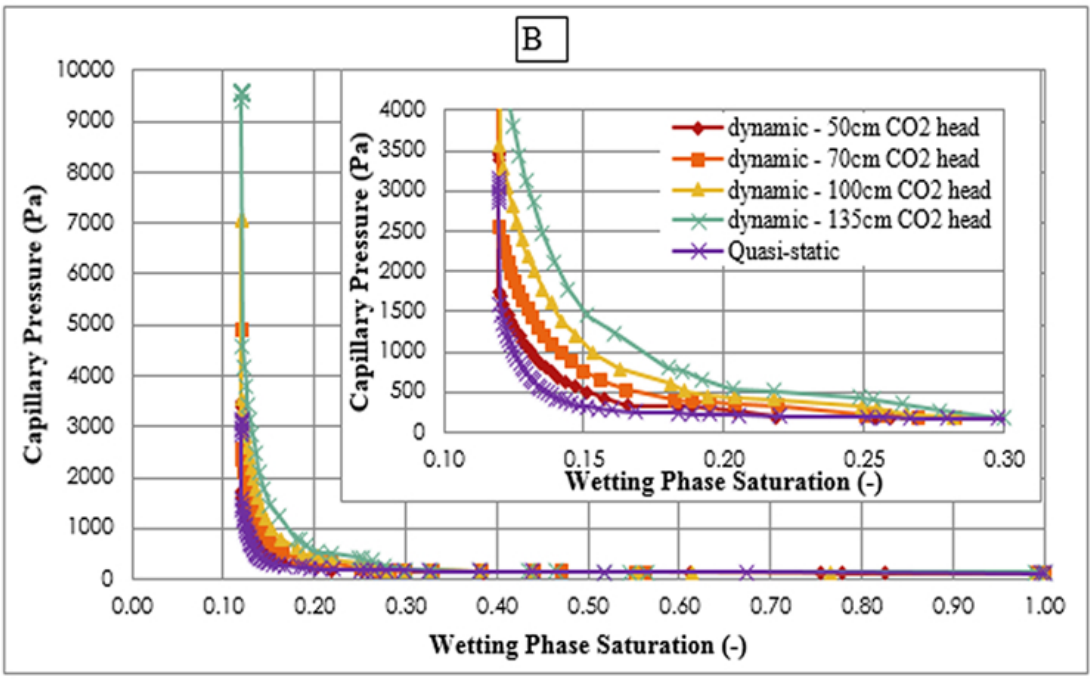

Figure 4.6. Dynamic and Quasi-Static Capillary Pressure – Saturation Curves for Coarse Sand at (a) 35°C, (b) 45°C. These curves are based on porous medium properties obtained from experimental measurements (Table 4.6).

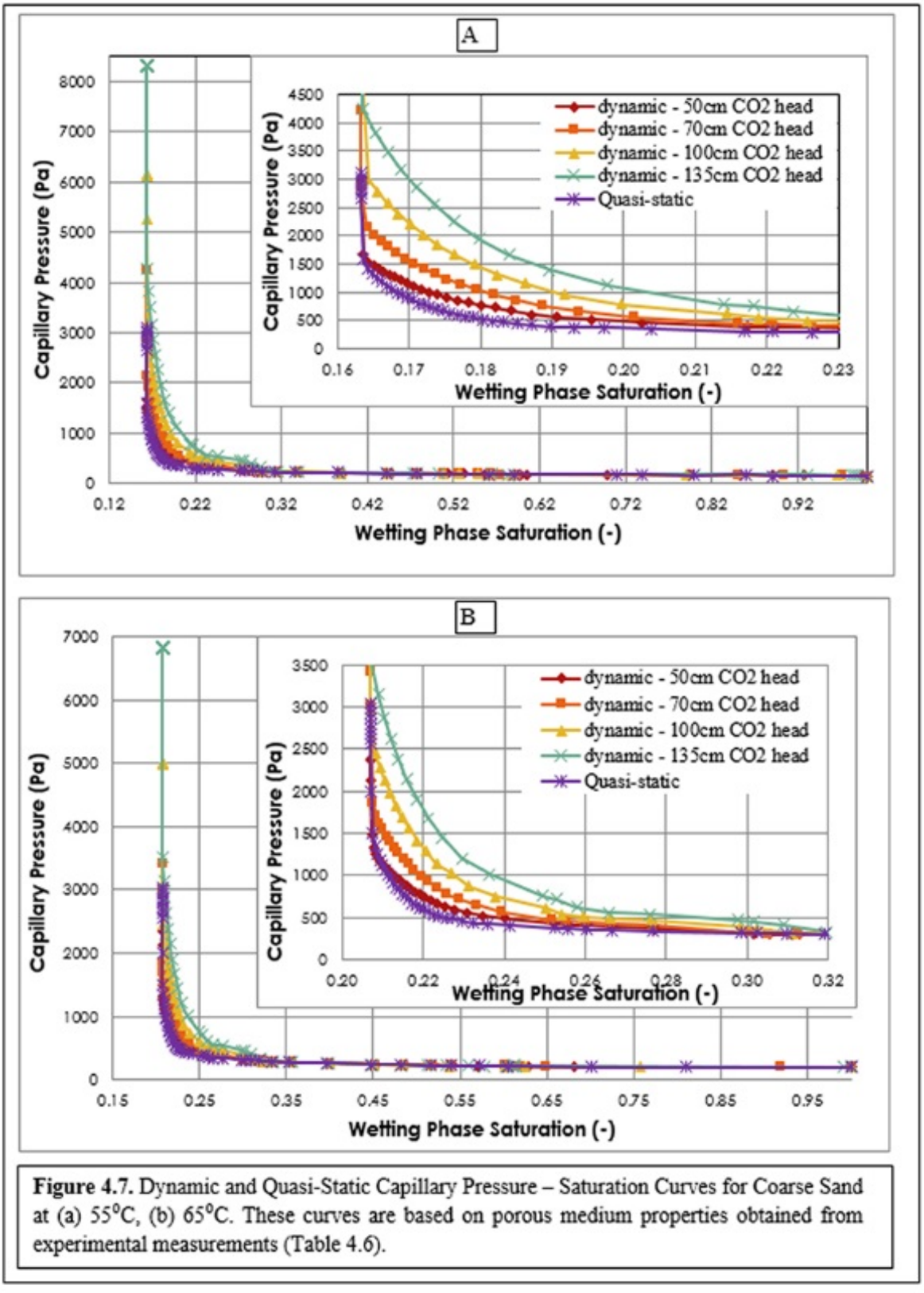

Figure 4.7. Dynamic and Quasi-Static Capillary Pressure – Saturation Curves for Coarse Sand at (a) 55°C, (b) 65°C. These curves are based on porous medium properties obtained from experimental measurements (Table 4.6).

It should be noted that the dynamic capillary pressure effect is given by the extent of the dependence of $P_c^{dyn} - P_c^{equ}$ on $\partial S/\partial t$, and not simply $P_c^{dyn} - P_c^{equ}$. Therefore, although some curves in Figures 4.6 – 4.9 may almost overlap, it does not mean that dynamic capillary pressure effect is not significant in these cases. These points are discussed further in section 4.8.3.

Findings in this work show that moderate increase in P_c is needed to drain the domain close to irreducible saturation while dramatic capillary pressure rise is often encountered as the system approaches irreducible water saturation. In line with this, Figures 4.6 and 4.7 show that relatively low capillary pressure increases were required to reduce water saturations from its initial value of 1.0 to a lower saturation of around 0.3. Further reduction in water saturations closer to the irreducible saturation requires large capillary pressure increases. For example, at a temperature of 35^0C and carbon dioxide pressure head of 50 cm, wetting phase saturation of 0.3 was achieved at a capillary pressure of 131 Pa, while residual saturation was achieved at a capillary pressure of 3888 Pa (approximately).

It is also evident that the capillary pressures at irreducible saturation, at higher temperature, were lower than those at 35^0C because irreducible saturation increased from 0.0757 to 0.2071 as the domain temperatures were increased from 35^0C to 65^0C. The closeness of the capillary pressure-saturation curves at higher temperatures can be due to change in viscosity and density at high pressure of supercritical CO_2. Gases at high pressure were reported to undergo rapid change in density resulting in large increase in viscosity (Viswanath et al., 2007). Figures 4.8 and 4.9 represent the dynamic and quasi-static capillary pressure-saturation curves for fine sand at 35^0C, 45^0C, 55^0C and 65^0C, respectively. The trends in these figures are similar to those observed for coarse sand (Figures 4.6 and 4.7) and are not discussed in length. Figures 4.10 compares the quasi-static curves for the three porous samples at 35^0C. It clearly shows how the capillary pressures tend to vary at various saturations for the three samples with different permeability values. In this case, capillary pressure values at high wetting phase saturations for the mixed sand sample were between those calculated for coarse sand and fine sand. This is because the mixed sand had a permeability value of 5.95×10^{-11} m^2, which is an intermediary between those determined for fine and coarse samples.

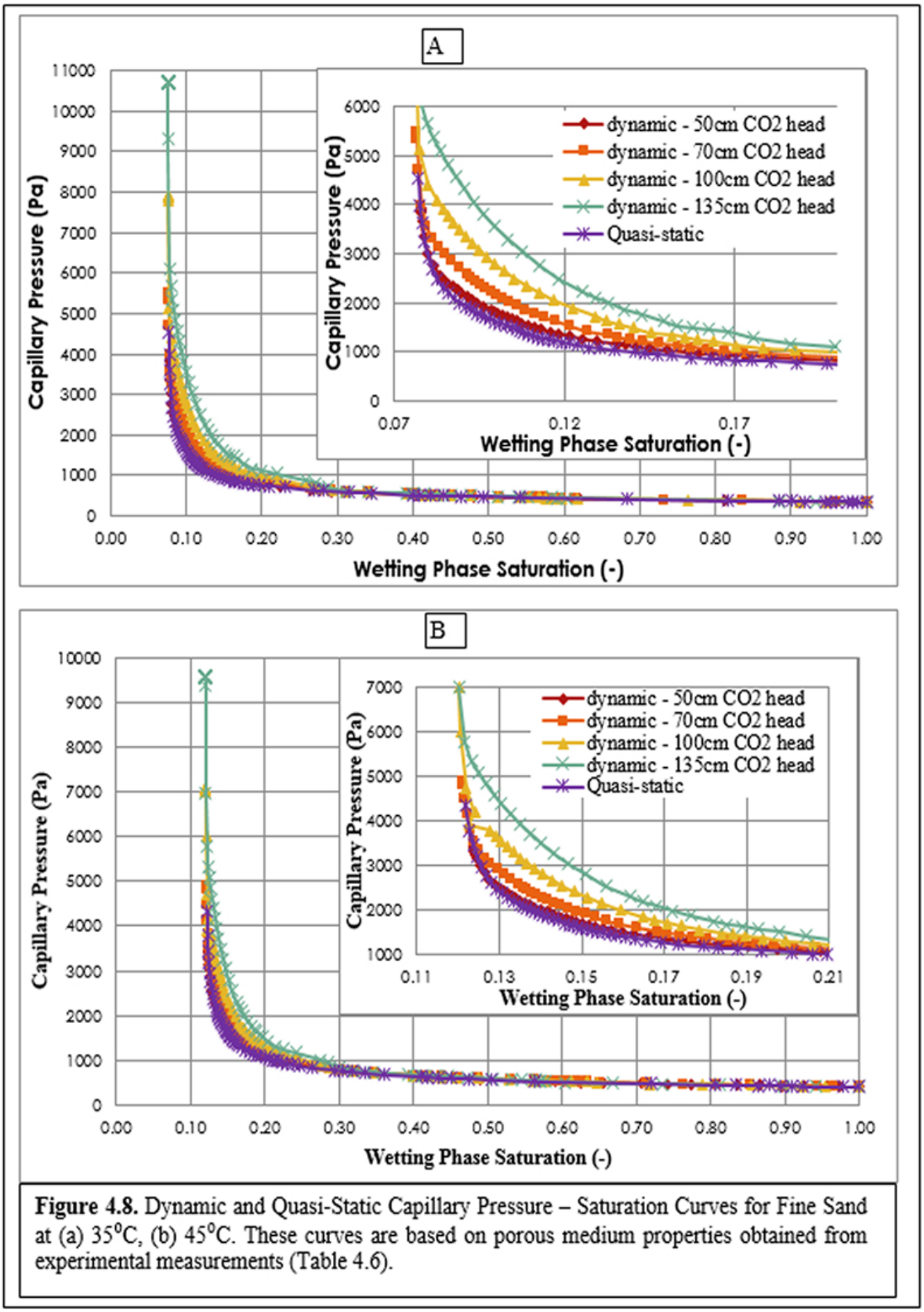

Figure 4.8. Dynamic and Quasi-Static Capillary Pressure – Saturation Curves for Fine Sand at (a) 35°C, (b) 45°C. These curves are based on porous medium properties obtained from experimental measurements (Table 4.6).

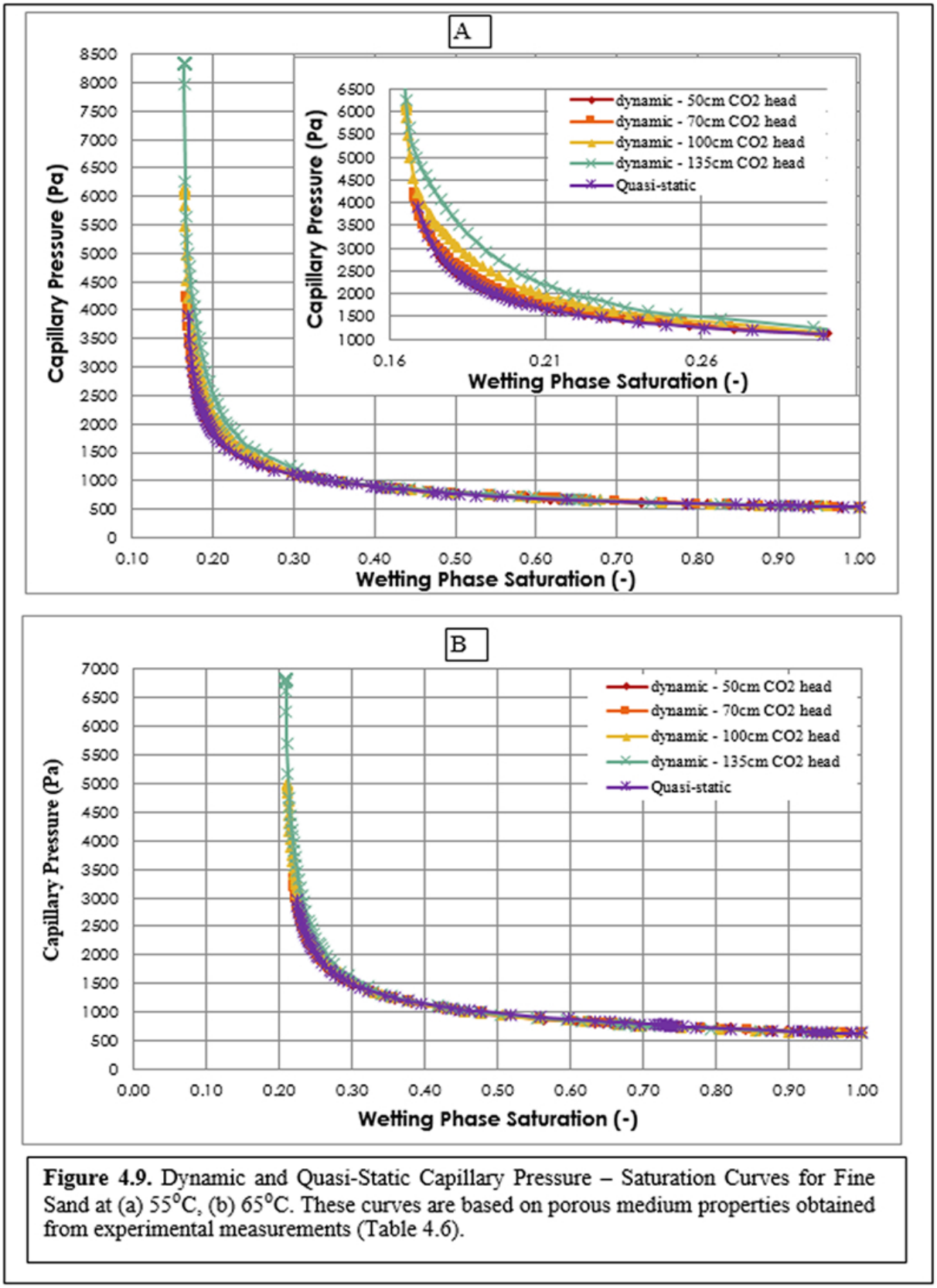

Figure 4.9. Dynamic and Quasi-Static Capillary Pressure – Saturation Curves for Fine Sand at (a) 55°C, (b) 65°C. These curves are based on porous medium properties obtained from experimental measurements (Table 4.6).

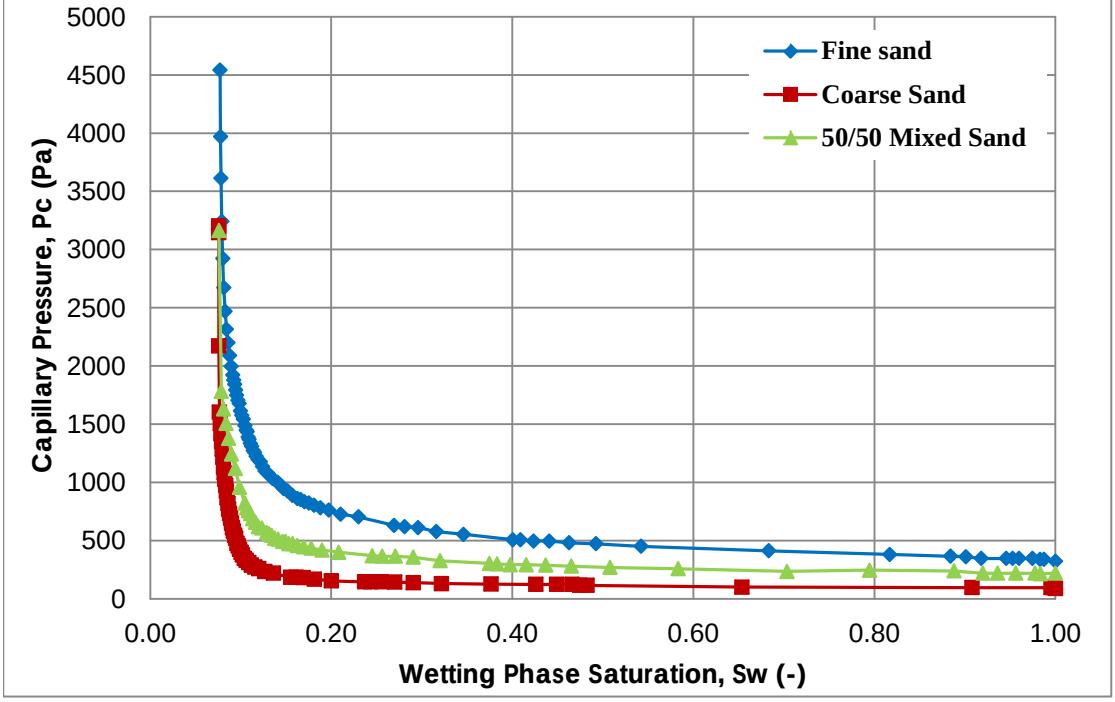

Figure 4.10. Comparison of Quasi-Static Capillary Pressure–Saturation Curves for Fine Sand, Coarse Sand and 50% Fine Sand and 50% Coarse Sand Mixture at 35^0C. These curves are based on porous medium properties obtained from experimental measurements (Table 4.6).

4.8.3. Dynamic Capillary Pressure Effect

The origin of the dynamic capillary pressure effect has been discussed in the introduction of the study and is avoided here. As mentioned earlier, the dynamic capillary pressure effect, indicated by the dynamic coefficient (τ), was determined from the simulation results of all the porous samples over a range of saturations. Figure 4.11(a) shows a plot of the dynamic coefficient in coarse sand under various simulation conditions. It shows that at all the temperatures, dynamic coefficient values decreased as the wetting phase saturation increased and the values increased dramatically as the wetting phase saturation declined towards the irreducible value. This has been the general experience in most publications (Hasanizadeh et al., 2002; Manthey et al., 2005; Das and Mirzaei, 2012; Sakaki et al., 2010; Hanspal and Das, 2012) and it is said to be indicative of how far the process is away from equilibrium (Das et al., 2007). As discussed by Das et al.

(2007), at high wetting phase saturations, the two fluid phases are well connected, thus shorter times are required for equilibrium to be attained. As the wetting phase saturations decrease, and more supercritical carbon dioxide continuously enters the pore spaces, the remaining water tend to disconnect. In such cases, the dynamic coefficient may be non-monotonic in behaviour (Das et al., 2007; Mirzaei and Das, 2007). Similar behaviour is found in this work.

As visible from Figures 4.11(a-c), the dynamic coefficient at higher temperatures overlie the lower temperature ones at the same saturation point with the exception for simulations at high saturation (>0.75) and 65^{o}C where the starting point lies slightly below the values of τ at 55^{o}C. In addition, the dynamic coefficient at 45^{o}C shows fluctuations throughout the entire saturation profile but the average effect overlies the τ values at lower temperature, i.e., 35^{o}C. This is similar to the experience of Hanspal and Das, (2012) who noted the increase in τ values as the temperature rises. The fluctuations experienced were most likely due to the high pressures (approximately 15 MPa) imposed on a domain measuring only 10 cm in diameter and 12 cm in height. Variation in saturation distribution of supercritical CO_2 may arise from temperature dependency of its density and viscosity. This may result in the change of the mobility ratios of the two fluid phases present in the domain. However, these are not studied in this research. At water saturation of 0.1, τ value of 8.73 x10^8 Pa.s was calculated for coarse domain at 35^{o}C. From Figure 4.11(a-c), the general trend is the rising τ values as the temperature increases. However, because the simulations at high temperature could not be conducted for low saturation values as irreducible saturation increases with temperature, it is difficult to estimate the τ values at these points. However, it can be inferred that the τ values at saturation close to or less than 0.1, for higher temperatures will be higher than the value at 35^{o}C.

In comparison, Hanspal and Das, (2012) reported the highest τ values of 5.33 x 10^8 Pa.s at 80^{o}C and 9.1 x 10^6 Pa.s at 20^{o}C in coarse sand of closely comparable properties at saturation points of 0.33 and 0.191, respectively. This is a slightly lower τ value in our case (8.73 x 10^8 Pa.s) at 35^{o}C, though it is noteworthy that the final saturation values of estimations in their publication were well above 0.1. Bottero et al. (2011b), in their experiment on tetrachloroethylene-water system, reported average values for dynamic coefficient, at the scale length of 11cm, in the range of 0.5 x 10^6 Pa.s and 1.2 x 10^6 Pa.s. These are upscaled values of the dynamic coefficients and were

found to have increased by one order of magnitude than the local-scale coefficients (1.3 x 10^5 to 2 x 10^5 Pa.s).

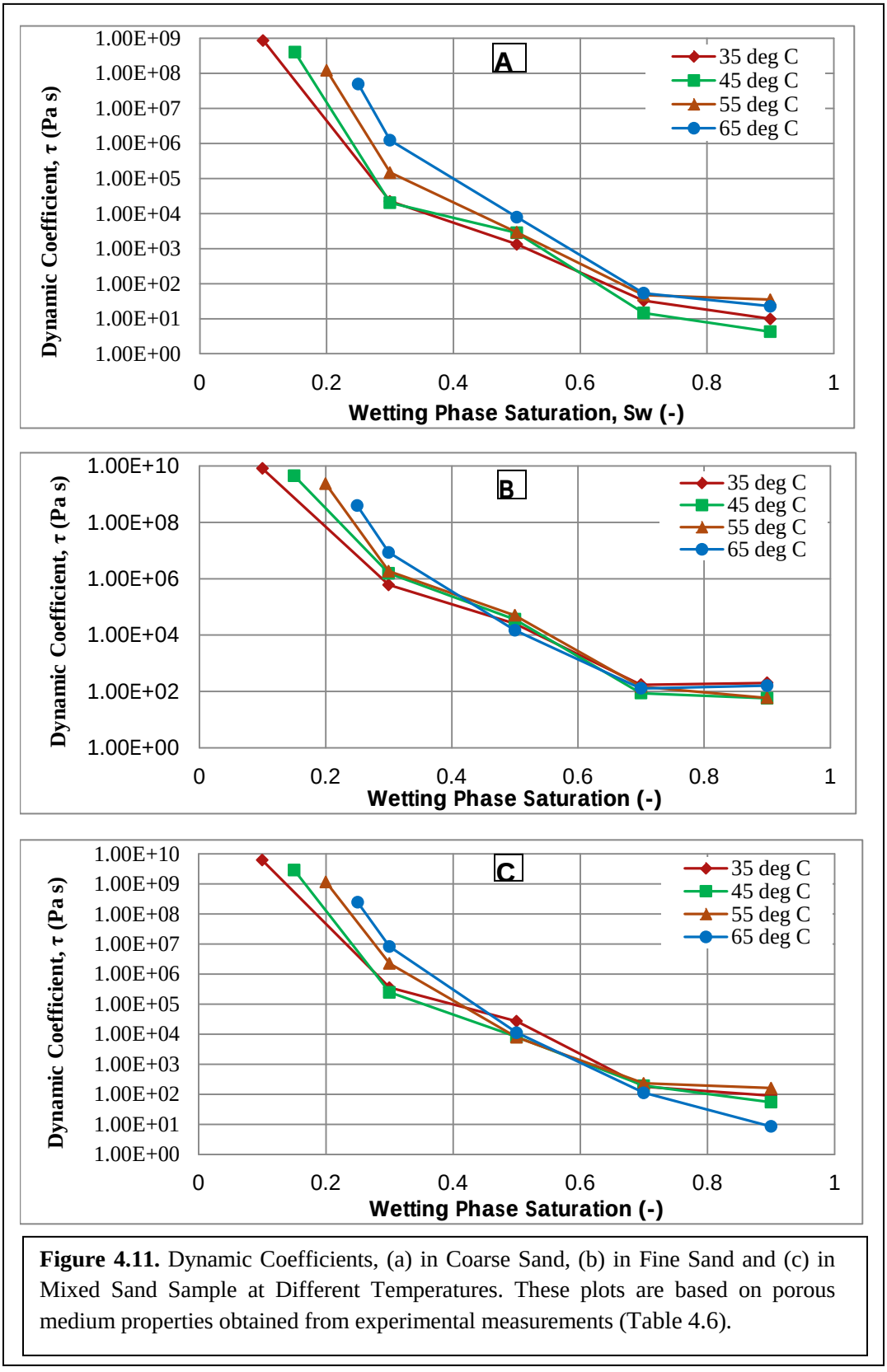

Figure 4.11. Dynamic Coefficients, (a) in Coarse Sand, (b) in Fine Sand and (c) in Mixed Sand Sample at Different Temperatures. These plots are based on porous medium properties obtained from experimental measurements (Table 4.6).

Furthermore, their up scaled values at scale length of 18 cm were 1.5 x 10^6 and 2.5 x 10^6 Pa.s. Juxtaposing these values with our results, especially at 12 cm scale which correspond to the domain size in our simulation, it is clear that the dynamic effects in CO_2-water system is more significant.

Similarly, the values of τ for the CO_2-H_2O system in this work maintain a large gap from the values reported by Das and Mirzaei (2012) in their work on silicone oil-water system. The same domain size was used while the fine and coarse sand samples used in their work were of comparable properties to the ones used in this work. They reported the highest average values less than 1 x 10^6 and 8 x 10^5 Pa.s for fine and coarse sand samples, respectively. Therefore, it can again be inferred that supercritical CO_2 undergoes pore scale processes, which raise the dynamism of the CO_2-H_2O-sand system to a higher degree than the silicone oil-water and tetrachloroethylene-water systems.

Figure 4.11(b) shows that the fluctuating patterns experienced under coarse sand for one or two conditions are more pronounced in fine sand. This could be attributed to low permeability of the fine sand sample. Again, changes in temperature dependent density and viscosity ratios coupled with the domain properties are responsible for this observation. Calculated dynamic coefficient values in the fine sand are significantly higher than those determined for coarse sand, with a value as high as 8.10 x 10^9 Pa.s calculated at a temperature of 35^0C and wetting phase saturation of 0.1. This implies that it would take much longer to attain capillary equilibrium in porous media with lower permeability values.

As expected, the mixed porous sample had dynamic coefficient values between those reported for coarse and fine-grained sand samples. This is due to the fact that the mixed sand has a permeability value lower than coarse sand but higher than fine sand. In this case, τ values as high as 6.02 x 10^9 Pa.s were found as shown in Figure 4.11(c). A comparison of the dynamic effects in the three different sand samples is shown in Figure 4.12. It is visible that the effect has the highest magnitude in the fine sand. This trend is consistent with observations in previous studies (e.g., Das and Mirzaei 2012, 2013).

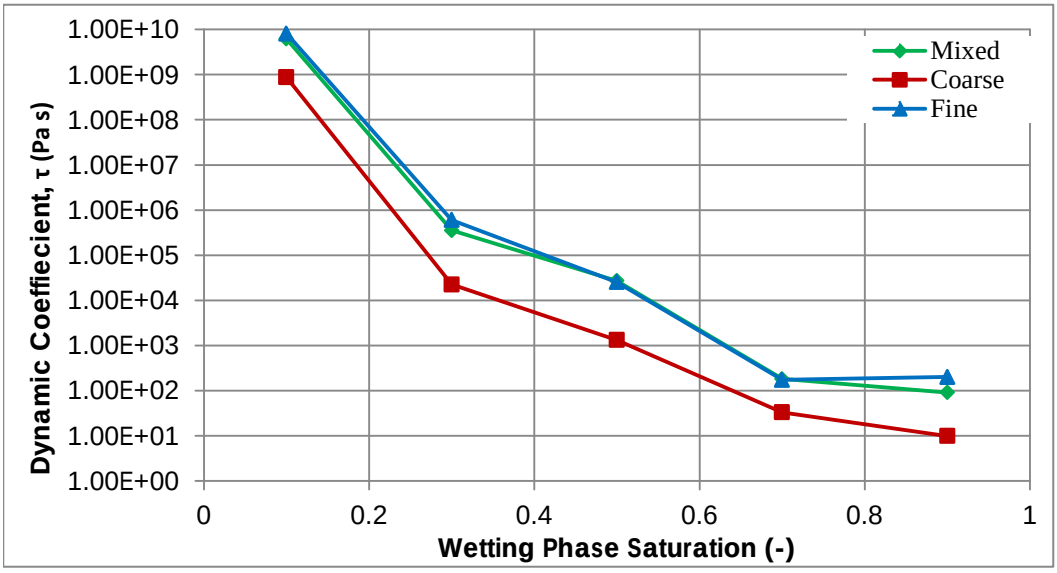

Figure 4.12. Dynamic Coefficients in Coarse, Fine and Mixed Sand Samples at 35°C. These plots are based on porous medium properties obtained from experimental measurements (Table 4.6).

The effects of the boundary conditions were also investigated on τ values and the results are shown in Figure 4.13. In general, the dynamic coefficient is known to vary slightly as the boundary conditions; however some authors have shown no or negligible effects of boundary conditions (Camps-Roach et al., 2010). The extent of this change is not known for the system under investigation.

As explained before, four different dynamic boundary pressures were used to determine τ so far. To investigate the effects of the imposed pressure, 50, 70 , 100 and 135 cm CO_2 heads were used in one set of simulation (Table 4.8) and 150, 200, 250 and 300 cm are used as a new set of boundary conditions. In both of these cases, the boundary condition at the bottom of the domain and initial pressure for water are as stated in Table 4.8 for 35°C (308.15K). For the new set of boundary condition, a set of simulation runs were carried out to calculate the dynamic coefficient and the results are presented in Figure 4.13. From the figure, it can be seen that the τ values at different imposed pressure sets are mostly similar at the same wetting phase saturation, see for example, the τ values at water saturations of 0.1 and 0.9. All τ values for the two sets of boundary pressures could not be obtained at exactly the same water saturations, and, therefore, they should be compared carefully; however, it can be reasonably inferred that different sets of boundary conditions exhibit similar trend at similar water saturations. However, as the imposed

pressure is increased, the dynamic coefficient may be increased slightly at the same temperature. In this work, results from the first set of boundary pressures were reported. One further point that should be noted is that although the exact saturation for a typical CO_2 plume may vary from case to case depending on a number of issues, the results in this work (Figures 4.11 – 4.13) show that the dynamic effect is significantly increased from a fully saturated domain as the saturation decreases, particularly at lower water saturation (<40%).

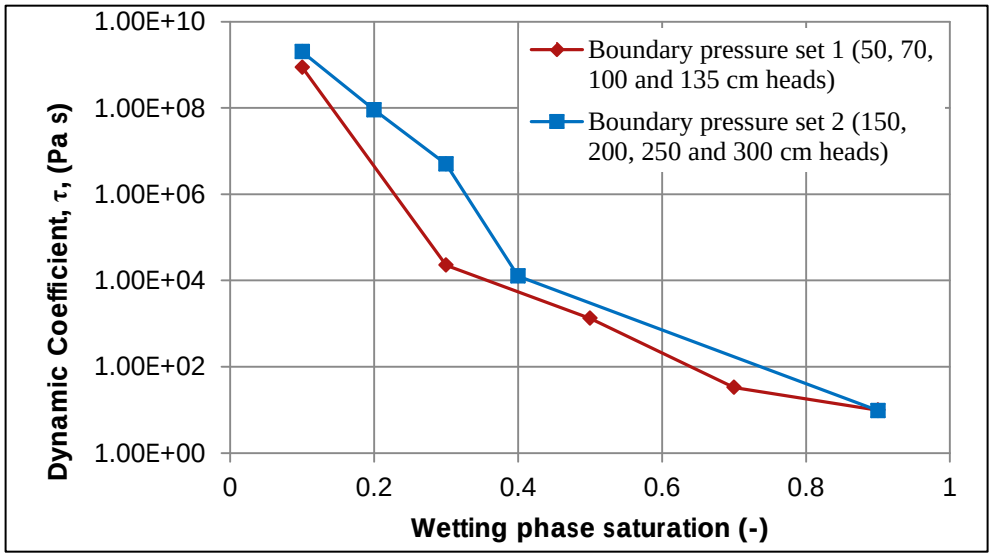

Figure 4.13. Dynamic coefficients from different set of boundary conditions. Please note that boundary pressure set 1 was applied in all other results in this work including grid convergence test (Figures 4.3 – 4.10). These plots are based on porous medium properties obtained from experimental measurements (Table 4.6).

The effects of domain grid-refinement on the values of the dynamic coefficient have also been investigated, so as to confirm the reliability of the results. Two different grid sizes were chosen and their effects on the dynamic coefficient (τ) were then determined. The same domain (i.e., 3D cylindrical domain measuring 10 cm in diameter and 12 cm in height) was discretised into 40 nodes for the coarse grid and 416 for the fine one as displayed in Table 4.9.

The finer grid was used to generate the results presented in this research work. The other grid involved a case where the number of nodes was decreased approximately 10 folds. The simulation runs were then carried out for a typical case, namely, coarse domain at 55^{o}C for the same boundary conditions (see Table 4.8). Quasi-static and dynamic capillary pressure curves were generated for these two meshes, which were then used to determine the dynamic

coefficients for the respective cases. Closeness was observed in the τ values obtained under the two different grid resolutions, which provides the confidence that the grid size does not have significant effect on the numerical results in this work as depicted in Table 4.9. Due to the large extend of the values, it was not practically possible to plot them versus water saturation, however the effect of grid resolution on capillary pressure has been illustrated in Figure 4.14 that clearly shows no significant impact of grid refinement on the values of capillary pressure in both static and dynamic conditions for core-scale domains. Similar conclusion for grid size effect was obtained earlier by other publications (Das et al., 2006; Das et. al., 2007; Hanspal and Das, 2012).

Table 4.9. 3D Cylindrical domain grid refinement (d=10 cm m and z=12 cm), showing the number of nodes and nodal spacing in all directions.

Number of Nodes x Nodal Spacing				
	Total grid cells	***N x Δr* (m)**	***N x Δθ* (degrees)**	***N x ΔZ* (m)**
Coarse Grid	40	2 x 0.025	4 x 90	1 x 0.01 3 x 0.0333 1 x 0.01
Fine Grid	416	4 x 0.0125	4 x 90	1 x 0.0015 24 x 0.004875 1 x 0.0015

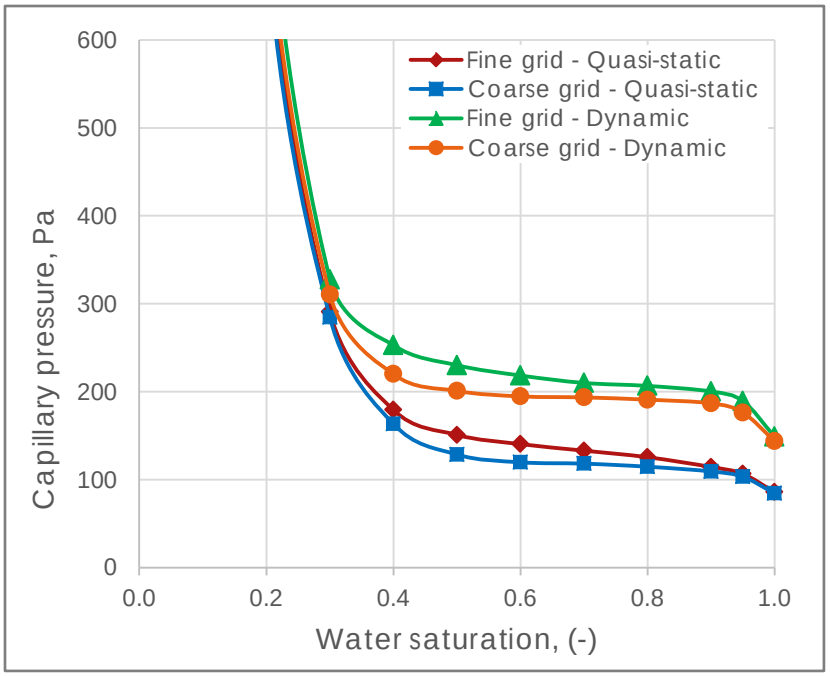

Figure 4.14. Effect of grid refinement on Static and dynamic capillary pressures in a coarse sand domain at 35 ℃ and 15 MPa injection presure. The figure based on the simulation results with employed values of grid refinement from Table 4.9.

4.9. Chapter Summary

Well-defined numerical simulations to determine dynamic and quasi-static P_c-S relationships have been conducted for a supercritical carbon dioxide-water flow in homogeneous core scale porous samples. Much like other reported studies on two-phase flow in porous media, the P_c-S relationships in CO_2-H_2O-sand system follow a regular pattern with increasing capillary pressure as the water saturation decreases. The results also show that the dynamic and quasi-static P^c-S relationships do not vary significantly for the fluid properties at a particular temperature. However, they depend on S and time derivative of saturation ($\partial S/\partial t$), and as such, it can be concluded that the dynamic capillary pressure effect is an important factor to consider. Three dynamic P^c-S curves (corresponding to three different dynamic pressure heads) and one quasi-static P^c-S curve have been used to determine an average value of (τ) at a particular saturation.

The results in this work suggest that the time to capillary equilibrium during geological sequestration of CO_2 should be accounted for, while simulating the flow processes, e.g., to determine the CO_2 storage capacity of a geological aquifer. To simulate the field scale processes, one would require both the fundamental understanding of the dynamic capillary pressure effects for supercritical CO_2-water flow in terms of P_c-S relationship as well as the knowledge on how significant the τ values are for these cases. These are addressed in this research. The approach used in this work to determine the τ values should be viewed as an 'inverse approach' where all the necessary process variables are assumed known except the values of the dynamic coefficient. As its values are determined in this study, a 'forward problem' for simulating the dynamic CO_2-H_2O flow which couples the dynamic capillary pressure equation with traditional two-phase flow modelling approaches can be set up. To apply the results of this work in the field setting, one would need to upscale these core scale results to field scale.

The most significant contribution of this work is that it provides a fundamental understanding of the significance of dynamic capillary pressure effect for supercritical CO_2-water flow in porous media. For example, the dynamic coefficients determined in this work reflect a higher value than some contemporary reports for oil-water system in the literatures under comparable conditions. It is shown that the flow of CO_2-H_2O is affected by the factors of fluid and media properties. Under similar conditions, increasing (τ) values of 8.73×10^8 Pa.s, 6.02×10^9 Pa.s and 8.1×10^9 Pa.s were respectively calculated in coarse, mixed and fine-grained sand samples whose permeabilities were 3.65×10^{-10} m^2, 5.95×10^{-11} m^2 and 5.66×10^{-11} m^2, respectively. This

indicates that the system experiences more gap away from equilibrium as the media permeability decreases. This similar effect reflects in the simulation times required to attain irreducible saturation in the various porous media as the time increases with decreasing permeability. The results further show that τ increases with temperature and may increase slightly at higher flow rate/pressure at the same pressure.

As it has been explained in the research work, some studies have simulated CO_2-water flow in porous media without the consideration of dynamic effects, however they may introduce some errors in the modelling calculations. Not considering the dynamic effects (i.e., $(\tau = 0)$) obviously implies that dynamic and quasi-static P_c-S relationships are the same. However, the results from this research show that $\tau \neq 0$ and it varies as a function of saturation. The results suggest that at large water saturation, the (τ) values are small. In other words, there would be smaller errors in the modelling calculations if one chose to use a traditional modelling scheme based on quasi-static P_c relation (i.e., equation 4.1). As the water saturation decreases, the (τ) values increase. In other words, the errors in the calculation are likely to increase should one choose to use equation (4.1) to account for the capillary pressures in the modelling calculations.

The key point here is that any error calculations should really be done for a range of saturations, as the error estimate is likely to be saturation dependent as illustrated in Figure 4.11(a,b). The error estimation is represented by the values of (τ) that range from $2.04x10^{+04}$ to $2.26x10^{+01}$ Pa.s for the coarse sand domain and $1.83x10^{+06}$ to $5.916x10^{+01}$ Pa.s for the fine domain at saturation values from 0.3 to 0.9.

It also needs a ‘forward problem’ as discussed in the study so that a typical modelling solution may be compared for a range of dynamic coefficients. Such an approach has been tried by Fučík et al. (2010) and Peszyinska and Yi (2008) for a two-phase flow problem (i.e., not CO_2-water flow); but, these authors have assumed that (τ) is independent of saturation. A detailed study on error estimates for flow of CO_2-water flow in porous media for the cases when the dynamic coefficient is saturation dependent should be tried in the future.

Chapter 5

Capillary pressure-saturation relationship for supercritical carbon dioxide (CO_2) injection in deep saline aquifers (Large Scale)

Overview

Carbon capture and sequestration (CCS) is expected to play a major role in reducing greenhouse gas emissions into the atmosphere. It is applied using different methods including geological, oceanic and mineral sequestration. Geological sequestration refers to storing of CO_2 in underground geological formations including deep saline aquifers (DSAs). This process induces multiphase fluid flow and solute transport behaviour besides some geochemical reactions between the fluids and minerals in the geological formation. In this work, a series of numerical simulations are carried out to investigate the injection and transport behaviour of supercritical CO_2 in DSAs as a two-phase flow in porous media in addition to studying the influence of different parameters such as time scale, temperature, pressure, permeability and geochemical conditions on the supercritical CO_2 injection into the subsurface. In contrast to most works which are focussed on determining the mass fraction of CO_2, this research work focuses on determining CO_2 gas saturation (i.e., volume fraction) at various time scales, temperatures and pressure conditions taking into consideration the effects of porosity/permeability, heterogeneity and capillarity for CO_2-water system. A series of numerical simulations was carried out to illustrate how saturation, capillary pressure and the amount of dissolved CO_2 change with the change of injection process, hydrostatic pressure and geothermal gradient. For example, the obtained results are used to correlate how an increase in the mean permeability of the geological formation allows greater injectivity and mobility of CO_2, which should lead to an increase in CO_2 dissolution into the resident brine in the subsurface.

5.1. Introduction

Carbon sequestration is a technique for managing carbon dioxide (CO_2) that has been emitted into the atmosphere by various activities, e.g., combustion of carbon-based fuels. It is a relatively new concept that had been developed to address the problem of global warming, which is attributed to high levels of atmospheric CO_2. In a more specific approach, geological sequestration aims to inject supercritical CO_2 into porous formations underground while attempting to prevent leakage of CO_2 to the surface again. This method can be applied to declining oil fields, un-minable coal seams as well as deep saline aquifers (DSAs). Injecting CO_2 into DSAs is considered to be one of the most feasible sequestration methods of CO_2. From a

fluid mechanics point of view, injecting supercritical CO_2 into geological formations can be treated as a two-phase flow in a porous medium (Tsang et al. 2008). Supercritical CO_2 is considerably denser than the gaseous CO_2 phase but has lower density and viscosity than the occupant brine in the porous space. As a result of the differences of fluid densities, supercritical CO_2 migrates buoyantly towards the upper confining layer. The preferred depths to inject CO_2 are greater than 800 m as they provide the required conditions above the critical points of CO_2 for it to stay in supercritical phase (Prevost et al. 2005). This increases the storage capacity of the site because more CO_2 can be stored within a specific volume of the domain.

It must be emphasised that particular conditions have to be met by a geological formation for a successful CO_2 storage. According to Bachu and Bennion (2008), three basic conditions must be met, namely, (i) capacity, i.e., the geological media must have the capacity to allow the anticipated amount of CO_2 over the duration of the project operation; (ii) injectivity, i.e., the media must be able to allow the CO_2 at its injection rate and, (iii) confinement, i.e., the media must be able to impede leakage of CO_2 from the storage zone or minimize leakage to the tolerable levels. Furthermore, geological storage of CO_2 is determined by four foremost trapping mechanisms as discussed below:

(a) Structural trapping, which takes place when CO_2 gas becomes immobile in the porous sedimentary layers with the existed brine by impermeable barriers (White et al. 2013).

(b) Residual trapping that takes place as a result of the hysteresis effect when the saturation direction is reversed after the injection process stops and, the existing brine moves back and tries to displace CO_2 in the pores (Ide et al. 2007).

(c) Solubility trapping takes place when the injected CO_2 dissolves in the resident fluid and increases the acidity and density of the brine creating convective currents that allow the denser brine with high concentration of CO_2 to settle at the bottom part of the aquifer where the CO_2 is trapped more securely (Silin et al. 2009).

(d) Mineral trapping occurs when the dissolved CO_2 reacts with the hosted brine producing carbonic acid that reacts with the dissolved ions within the aquifer brine and minerals forming the host rock resulting in chemical precipitation of solid carbonate minerals (Beni et al. 2012).

Modelling of underground injection of CO_2 primarily represents modelling a system of two-phase flow in porous media, which requires one to identify the relevant parameters. These parameters describe various physical and chemical properties of the geological formation such as entry pressure (depending on pore/particle size of the domain), hydrodynamic conditions (e.g., pressure difference, groundwater velocity), fluid properties, rock permeability, chemical species from geochemical reactions and fluid/fluid interfacial mass transfer (Ide et al. 2007). Considerable uncertainty may however exist with regards to the formation-related parameters because of the difficulty in collecting sufficient data across huge areas that should be taken into account for any geologic sequestration project. A number of studies have been conducted to determine the capillary pressure-saturation-relative permeability relationships for subsurface injection of CO_2 into porous media (e.g., Bachu et al. 1994; Pruess et al. 2003; Kumar et al. 2005; Knauss et al. 2005; Juanes et al. 2006; Birkholzer et al. 2009; Schnaar and Digiulio 2009). They demonstrate that by employing statistical routines, computational models are able to replicate complex formation heterogeneities, residual CO_2 trapping and hysteretic relative permeability curves, dissolution reactions and mineral precipitation and others. For example, Nordbotten et al. (2004b) analytically described the time evolution of the CO_2 plume dominated by viscous forces with irrelevant effects of the CO_2 buoyancy forces using a simplified form of Buckley-Leverett equation. They utilized their modelling results to inspect the accuracy/implication of assuming constant properties for the fluids in the storage formation. They discussed some cases where buoyancy and non-zero residual saturations have more influence on the mobility of CO_2 plume in addition to the effects of CO_2 dissolution in the existing brine.

One of the critical issues in CO_2 geological sequestration is the phase transition from liquid or supercritical to gas according to the temperature and pressure changes during the injection progression as illustrated in Figure 5.1. Therefore, the numerical simulation code utilized to model CO_2 sequestration in saline aquifers needs to be able to predict the CO_2 phase transition. It must also be able to determine the buoyancy and viscous forces influence on the fluid flow and, CO_2 dissolution in the aqueous fluid (White and Oostrom 2003).

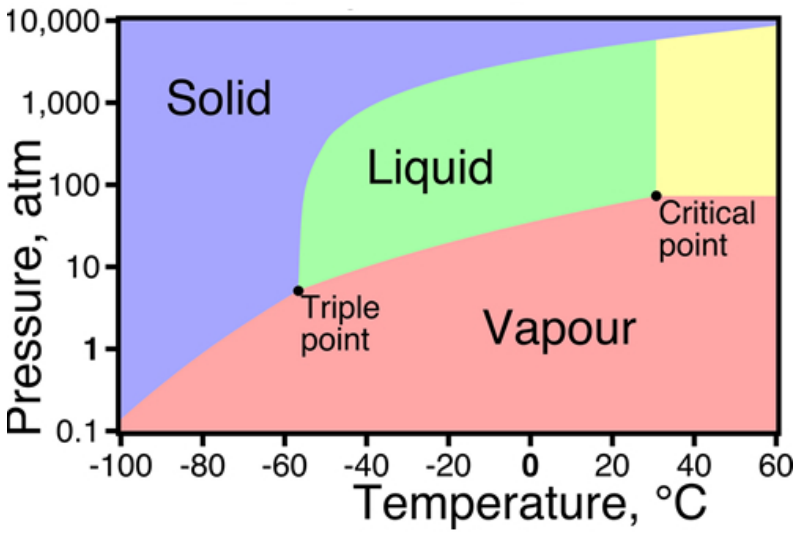

Figure 5.1. Carbon dioxide phase change diagram. (http://www.chemistry-blog.com - accessed on 13/01/2016 - free license to reuse).

Though capillarity plays a crucial role in assessing saline aquifers for CO_2 sequestration, there is not much real (field) data available about the behaviour of CO_2-brine flow system in the porous rocks. Plug and Bruining (2007) developed a laboratory scale method to investigate the static capillary pressure change as a function of saturation at different pressure and temperature conditions. They examined the influence of CO_2 dissolution in water by comparing its behaviour to the behaviour of nitrogen (N_2) under the same conditions. They observed that the residual water saturation (S_{wc}) for CO_2 is much smaller than that for N_2 due to the difference in interfacial tension.

Capillary trapping, which is also called residual trapping, is closely related to the capillary forces between CO_2 and the resident fluid at the scale of the grains of reservoir rock, which is controlled, by interfacial forces, pore size and wettability (Alkan et al. 2010). Experimental studies conducted by Bennion and Bachu (2008) and Plug and Bruning (2007) reported that permeability and capillarity are influenced by interfacial forces and wettability of CO_2-brine-rock systems. Another study on CO_2 sequestration has been conducted by Bickle et al. (2007) who modelled CO_2 flow behaviour in Sleipner field in the North Sea. They used a theoretical model and validated it with experimental results from the work by Lyle et al. (2005) to characterise the gravity flow in porous media. To attain their solutions they employed a number of assumptions, e.g., neglecting the motion of the existing fluid within the hosting formation and ignored both capillary and viscous forces in the fluid flow system which exhibited some

limitations in the applicability of their solutions. Bickle et al. (2007) concluded that the radius of accumulated CO_2 ponds in the subsurface increases linearly with the square root of the elapsed time. They observed an increase in CO_2 input in higher layers of the domain with a decrease in lower ones due to the leakage into the upper structures of the modelled formation. Their solutions provide important predictions on CO_2 behaviour with no need to carry out full simulation for any potential storage sites.

Unlike most conventional approaches for determining capillary pressure relationships which are based on equilibrium flow conditions (i.e., desaturation is zero), dynamic capillary pressure effects have been shown to have a great influence on two-phase flow in porous media (Helmig et al., 2007; Mirzaei and Das, 2007; Hanspal and Das, 2012). A number of fundamental studies (e.g., Oung et al., 2005; Manthey et al., 2005; Bottero et al., 2006) have investigated the dynamic capillary pressure effects in two-phase flow systems, and this gives rise to the possibility of applying these understandings to determine if these effects are significant for supercritical CO_2 flow in the geological formation as well.

In addressing most of the above issues, the main goal of this study is to carry out a simulation study to determine static and dynamic capillary pressures for CO_2-water system as a function of saturation for different permeability and heterogeneity at various time scales, temperature and pressure conditions in order to evaluate the implications of different CO_2 injection strategy and its storage capacity in briny aquifers. For this purpose a series of numerical simulations were carried out under various pressure, temperature, heterogeneity and injection rate conditions. It is envisaged that this numerical analysis would help the prediction of the optimized injection process and CO_2 behaviour within the aquifer formation during sequestration lifetime, which has a vast impact on the energy cost and storage process safety. It is believed that this study will provide better understanding of the injection and sequestration processes.

5.2. Modelling Approach

5.2.1. Main Equations

In this work, the injection of CO_2 into saline aquifers is defined to represent the flow of two immiscible fluids, namely, water (brine) as a wetting phase and CO_2 as a non-wetting phase in a porous medium where supercritical CO_2 replaces the existing fluid in a process called drainage.

5.2.1.1. Mass and Momentum Conservation Equations

Modelling CO_2 injection into geological formation is governed by the equations of mass and momentum conservation.

The conservation of momentum is described by the following form of Darcy's law:

$$\frac{\partial(S_\alpha \phi \rho_\alpha)}{\partial t} + \nabla.(\rho_\alpha v_\alpha) - \rho_\alpha q_\alpha = 0 \quad (5.1)$$

where S_α is the phase α (water or CO_2) saturation, ϕ is the porosity, ρ_α is the density, t refers to the elapsed time, v_α is the average pore velocity of the phase and q_α refers to the phase flux.

From the generalized Darcy's law (equation of momentum), velocity vector v_α is calculated by

$$v_\alpha = -\frac{k_{r\alpha}}{\mu_\alpha} k\,(\nabla p_\alpha - \rho_\alpha g) \quad (5.2)$$

$k_{r\alpha}$ identifies the relative permeability for the phase α (water or CO_2), μ refers to the dynamic velocity, p_α identifies the pressure, k is the tensor of absolute permeability (defined to be isotropic) and g the vector of gravity. The phase permeability (effective permeability) (k_α) is related to the relative permeability ($k_{r\alpha}$) as:

$$k_{r\alpha} = \frac{k_\alpha}{k} \quad (5.3)$$

where k signifies the domain permeability for a single-phase flow (the absolute permeability).

By substituting equation (5.2) in equation (5.1) the following general form of mass conservation equation is obtained for both fluid phases:

$$\frac{\partial(S_\alpha \phi \rho_\alpha)}{\partial t} - \nabla.\left(\rho_\alpha \frac{k_{r\alpha}}{\mu_\alpha} k\,(\nabla p_\alpha - \rho_\alpha g)\right) - \rho_\alpha q_\alpha = 0 \quad (5.4)$$

5.2.1.2. Constitutive Relationships

The two fluid flow process is dominated by capillary pressure (P_C) - saturation (S_w) - relative permeability (k_r) relationships because any decrease in the wetting phase saturation results in non-wetting fluid retreatment into smaller pores which is due to the increase in the capillary pressure. In a two phase flow the capillary pressure is defined as the difference between the average phase pressures of non-wetting (*nw*) and wetting (*w*) phases,

$$P_{c=}P_{nw} - P_w \tag{5.5}$$

One of the most common formulations used to determine P_c-S_w-K_r relationships is Brooks-Corey function (Brooks and Corey 1964), in which the displacement pressure of the wetting fluid from the largest pore (P_d) is involved while this pressure has been ignored by other authors for fully saturated porous media. The relationship defines the effective saturation as:

$$S_{ew} = \left(\frac{P_c}{P_d}\right)^{-\lambda} \quad \text{for } P_c \geq P_d \tag{5.6}$$

$$S_{ew}=1 \quad \text{for } P_c \leq P_d \tag{5.7}$$

$$S_{ew} = \frac{(S_w - S_{wr})}{(1 - S_{wr})} \quad \text{for } 0 \leq S_{ew} \leq 1 \tag{5.8}$$

where, (S_{ew}) denotes the effective water saturation, (S_{wr}) is the residual water saturation, (P_d) represents entry (displacement) pressure, (λ) is the pore size distribution index.

Brooks-Corey correlations in conjunction with the Burdine theorem (Burdine 1953) are used to define the relative permeability-saturation relationships for wetting ($_w$) and non-wetting ($_{nw}$) phases.

$$k_{rw} = S_{ew}^{\frac{2+3\lambda}{\lambda}} \tag{5.9}$$

$$k_{rnw} = (1 - S_{ew})^2\left(1 - S_{ew}^{\frac{2+\lambda}{\lambda}}\right) \tag{5.10}$$

The coupled equations are solved for the primary variables where the porous domain is assumed to be a rigid rock and both fluids are defined as incompressible. Furthermore, the dynamic viscosities of the fluids are assumed to be constant and all source and sink terms are ignored.

5.2.2. Simulation Methodology

The scope of this research is to simulate the process of injecting CO_2 as a supercritical fluid into DSAs. It focuses on the flow of multiphase fluid (H_2O-CO_2-NaCl*)* in a porous media for which STOMP-CO_2 operational mode of STOMP (*subsurface transport over multiple phases*) simulation code is used. In this mode, water (brine) is the wetting phase and CO_2 is a non-wetting fluid, which is injected at different pressure rates into the porous domain, which is fully saturated with water (brine). This leads to a situation where CO_2 drains water out of the domain

in a process called drainage followed by an imbibition process when CO_2 injection ends and water flows back into the domain to replace CO_2 in the domain pores leaving some traces of it trapped.

This operational mode is able to incorporate buoyancy and viscous forces driven flow, CO_2 dissolution in aqueous fluid, phase transition, dispersion and diffusivity of the gas. The code uses the finite volume technique to numerically simulate the process. These are discussed in detail by White and Oostrom (2003) and are not repeated in this study. However, it should be mentioned that STOMP-CO_2 simulator is written in FORTRAN 90 with a capability of dynamic memory allocation for faster execution. The collection of source files is required to be compiled into an executable file that can be used on various computing platforms including Linux and Windows to read the input file that is created by the user including a number of cards that contain calculation instructions and required parameters to solve the simulation problem. The code has been effectively optimized for workstations (HP, IBM and Sun) in addition to mainframes. The speed and memory requirements for running STOMP-CO_2 executable files depend on the complexity of the problem and computational grid refinement. There is no minimum memory or processor speed provided by the developer. However, from the experience it has been found that the code better functions on UNIX operating system with 2.4 GHz CPU and 1 GB memory.

CO_2 properties adopted in the simulation code have been arranged in a data table developed from the equation of state by Span and Wagner (1996). The phase equilibria calculations in STOMP-CO_2 code are conducted via a couple of formulations by Spycher et al. (2003) and Spycher and Pruess (2010) that are based on Redlich-Kwong equation of state with fitted experimental data for water-CO_2 flow systems (White et al., 2013).

STOMP-CO_2 is utilized to numerically solve the coupled conservation equations (water mass, CO_2 mass and NaCl mass) by converting them to algebraic equations using finite volume method (FVM) and Euler-backward time differencing for spatial and temporal discretizations, respectively. Backword Euler method is a first order time stepping method that makes an error of Δt^2 for each time step. This method offers more stability and accuracy than forward Euler method especially for problems with large and nonlinear functions like diffusion equations. The produced algebraic equations in the discretized equations are closed using a number of constitutive relationships as explained in section 5.2.1.1, and solved using Newton-Raphson iteration to resolve their nonlinearities (White and Oostrom 2003).

5.2.3. Initial and Boundary Conditions

The domain is considered to be anisotropic and almost fully saturated with brine before injecting supercritical CO_2 into the centre of it. The initial condition for all simulation runs are shown in Table 5.1. Two-phase condition was generated within the computational domain by setting the aqueous saturation value at 0.9999 as an initial condition for the employed equations of state in the simulation code (e.g., Kelvin equation (Nitao 1988), and the formulation by Battistelli et al. (1997)) that take into account the changes in thermodynamic properties of the fluid phases as the simulation conditions change. The non-wetting fluid (CO_2) saturation was assumed to be 1.0 at the injection source at the outer wall of the reservoir and 0.00001 in the rest of the computation domain as initial condition for the reason above. It is injected into the lower three grid cells (i.e. 30 m from the bottom of the domain). Vertically, zero flux is considered for aqueous phase at the well case as inner boundary while the outer boundary was assumed to be infinite with zero flux for gas phase. Horizontally, zero flux is considered at the upper and lower surfaces, which force the injected gas to spread laterally. For both dynamic and static conditions, fluids saturation, pressure and volume are measured at each node for producing a set of plots representing various relations of CO_2 saturation, capillary pressure, integrated gas mass and dynamic coefficient (τ). This procedure is repeated twice: once for sandstone (coarse) and another for wechselfolgen (fine) homogeneous domains.

Table 5.1. Selected aquifer parameters for simulation

Parameter	Value/Function		Reference
Diameter (m)	5000		-
Thickness (m)	100		-
Depth (m)	2900		-
Grid-cells (nodes)	71 x 4 x 10		-
Porosity	Sandstone 0.25	(Wechselfolgen) 0.16	May et al. (2004)
Horizontal Permeability (m^2)	5.625e-13	(0.5428e-13)	May et al. (2004)
Vertical Permeability (m^2)	(1.688e-13)	(11.15e-16)	May et al. (2004)
rock density (kg/m^3)	2430	2470	May et al. (2004)
specific storativity (1/m)	9.2e-4		May et al. (2004)
Surface temperature (℃)	8		May et al. (2004)
Reservoir temperature (℃)	58		Beni et al. (2012)
Temperature gradient (K/m)	0.035		May et al. (2004)
Reservoir pressure (MPa)	32		Beni et al. (2012)
Pressure gradient (KPa/m)	10.5		May et al. (2004)

5.2.4. Dynamic and Quasi-static Simulations

In this research work, simulations are carried out by injecting CO_2 into the centre of the computational domain, which is initially fully saturated with brine. The gas pressure is defined to be zero all over the domain. The CO_2 injection starts at 32 MPa and increased at a rate of 0.1 MPa every 0.5 year for 20 years for quasi-static simulations. This increment in injection pressure increases the capillary pressure (P_c) in the domain until it reaches the displacement pressure (P_d) when the injected CO_2 starts displacing the existing brine and continues till a steady state is reached when average values of the aqueous saturation and capillary pressure are calculated to give a single point for the $P_c - S_w$ relationship. This procedure is repeated for each time step from which the P_c-S_w curves are produced. For dynamic simulations, the imposed injection pressure is increased to 36 MPa in one-step and maintained until the end of injection period. This injection pressure was set because the hydrostatic pressure was estimated to be about 32 MPa and to avoid any possible pressure build-up in the reservoir, which may cause damage to the overlaying caprock and subsequent gas leakage.

5.2.5. Capillary Pressure and Saturation Averaging

From the locally predicted values of saturation and pressure at each grid node for each time step (t_n) the volume-weighted average water saturation (S_w) and saturation-weighted average capillary pressure (P_c) values for the whole domain are determined using the following equations.

The average saturation at any time step (t_n) is calculated by

$$S_w \mid_{tn} = \frac{\sum_{j=1}^{m} S_{wj} V_j \mid_{tn}}{\sum_{j=1}^{m} V_j} \tag{5.11}$$

And the average capillary pressure is calculated by

$$P_c \mid_{t_n} = \left[\frac{\sum_{j=1}^{m} (1 - S_{wj}) P_{nwj}}{\sum_{j=1}^{m} (1 - S_{wj})} - \frac{\sum_{j=1}^{m} S_{wj} P_{wj}}{\sum_{j=1}^{m} S_{wj}} \right] \mid_{t_n} \tag{5.12}$$

where, V_j, is the volume of node j, and, S_{wj}, P_{wj} and P_{nwj} denote water saturation, water pressure and CO_2 pressure at node j, respectively.

The time derivative of saturation dependency can be calculated from the average saturation values calculated from equation (5.13) as follows:

$$\frac{\partial s}{\partial t} \mid_{S_w t_n} = \frac{S_w \mid_{t_{n+1}} - S_w \mid_{t_{n-1}}}{t_{n+1} - t_{n-1}} \tag{5.13}$$

As shown in equations (5.11) and (5.12), both calculated average values are based on water saturation and, hence, they are called volume-weighted and saturation-weighted averages respectively (Mirzaei and Das, 2007; Hanspal and Das, 2012).

Conventional theories (Collins, 1961; Scheidegger, 1974; Bear and Verruijt, 1987; Helmig 1997) define capillary pressure as a function of fluid saturation only for fluids at equilibrium conditions. However, this is not always the case, as fluids might not flow under steady conditions especially at early stages of flow when the change rate of saturation is thought to be high. Therefore, it has been suggested by many authors that an additional term ought to be added to the capillary pressure equation (5.5) for dynamic fluid flow in porous media (Hassanizadeh and Gray 1993a; Beliaev and Schotting 2002; Dahle et al. 2005; Hanyga and Seredynska 2005; Oung et al. 2005).

In this study, the dynamic effects at a large-scale domain to be investigated. The additional term is called the dynamic coefficient (τ) which represents dynamic capillary pressure effect on the flow behaviour and is determined from the slope of a linear relationship between the capillary pressures at dynamic and static flow conditions, and the time derivative of saturation as shown in equation (5.14):

$$(P_c^{dyn} - P_c^{stat})|_s = -\tau \frac{\partial s}{\partial t} \Big|_s \quad (5.14)$$

where P_c^{dyn} and P_c^{stat} represent dynamic and static capillary pressures calculated at a specific value of saturation (s), respectively. The dynamic coefficient has been used by many previously published works (e.g. Das et al. 2014; Shubao et al. 2012; Fucik 2010; Mirzaei and Das 2007; Hanspal and Das 2012; Das and Mirzaei 2013; Mirzaei and Das 2013; Hanspal et al. 2013) to take into account dynamic capillary pressure effect and, therefore, a detailed discussion on dynamic capillary pressure effect is avoided in this research.

5.2.6. Computational Domain

The simulation parameters of the hypothetical computational domain based on Bunter Sandstone Aquifer in North German Basin in North-Eastern Germany as a well-known potential storage formation that has been a subject of several deep wells investigations and seismic surveys to assess the site efficiency for CO_2 sequestration. The aquifer demonstrates a well permeable sandstone layer as well as favourite hydrostatic conditions of 10.5-10.9 kPa/m and temperature gradient of 35 K/km (May et al., 2004). This aquifer consists of four cycles beginning with basal sandstone, which has three cycles of permeable layers (Detfurth, Hardegsen and Solling-Folge), and ending with an alternating succession of silt, sand and clay stone (May et al., 2004). This research study focuses on Detfurth cycle which is divided into a lower sandstone with high permeability and upper alternating succession of sand, silt and clay stones which is called (Wechselfolgen) with low permeability, because it demonstrates heterogeneity in regards to porosity and permeability.

The simulated three-dimensional cylindrical domain extends laterally (r-direction) from the injection point, which is represented by the well radius of 0.2, to 2500 m and vertically from

2900 to 3000 m below land surface, while at the top and bottom there are two impermeable layers that preserve the injected CO_2 safely in the storage formation. This depth ensures that the injected CO_2 remains in supercritical state, which increases the storage capacity of the site. The system can be simulated as a two-dimensional model because there is no heterogeneity in the azimuthal direction. The field was segregated into 71x4x10 mesh making 2840 grid cells. This grid refinement was optimized for a balanced accuracy of the results with reasonable computational time through a series of experiments that showed no significant effect of the grid refinement up to several magnitudes, on the average gas-CO_2 saturation in the domain at different time scales as illustrated in Figure B.1 in Appendix B. Finer block grids may produce smoother contours, however noticeable reduction of execution time was observed by using coarser grids with no momentous influence on the CO_2 saturation profiles as depicted in Figure B.2 in Appendix B. This is consistent with studies by Gonzalez-Nicolas et al. (2011) and Hanspal and Das (2012), which indicate that grid refinement has no significant influence on $P_c - S_w$ profiles.

Supercritical CO_2 was injected at pressure and temperature above the CO_2 critical conditions into the lower 40 m at the centre of the computational domain at a constant rate of 40 kg/s (approximately 1.262 MMT/yr) for 20 years followed by 980 years lockup period as illustrated in Figure 5.2. This injection rate represents about 25% of an annual CO_2 emission from an 800 MW coal-fired power generation plant. Different types of heterogeneities were considered for the simulated model and various scenarios of injection process were applied to investigate the effects of permeability, temperature, porosity, and injection pressure on P_c- S_w relationships at static and dynamic flow conditions, on the ultimate fate of the injected CO_2.

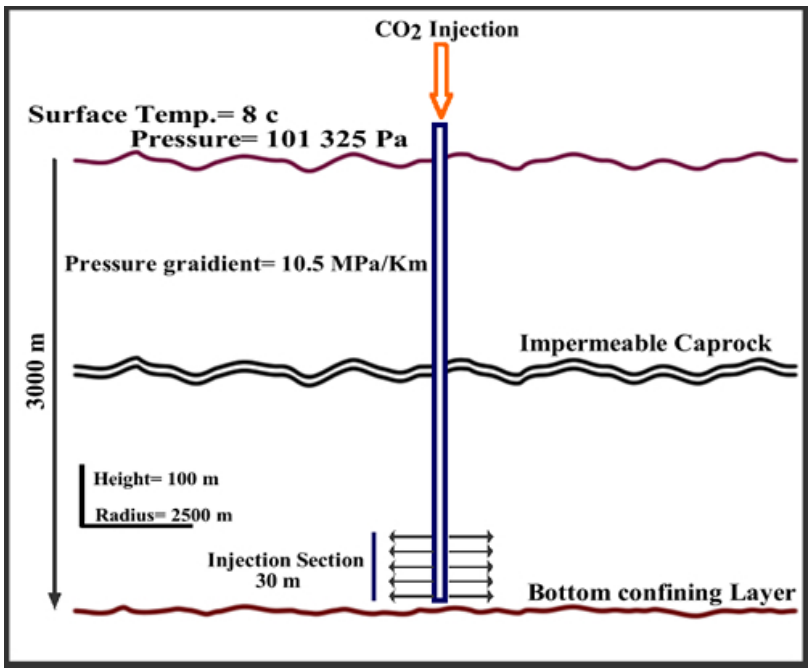

Figure 5.2. A schematic diagram of geological CO_2 sequestration process in a deep saline aquifer (DSA).

Firstly, simulations were run on fine and course homogenous domains with porosity of 0.16 and 0.25, respectively, to determine the effect of porosity and permeability on $P_c - S_w$ relationships. Unlike other works (Mirzaei and Das 2007; Peszynska and Yi 2008; Hsu and Hilpert 2011), dynamic and quasi-static simulations were conducted for comparison purposes. The simulated aquifer and simulation parameters are illustrated in details in Tables 5.2 and 5.3, respectively.

Table 5.2. Important parameters and initial conditions

Parameter	Value	Reference
Irreducible saturations; water, S_{lr} CO_2, S_{gr}	0.1 0.05	Beni et al. (2012)
Brooks/Corey Exponent, λ	0.457	Beni et al. (2012))
Strength coefficient, P_0	19,610 Pa	Beni et al. (2012)
Pore compressibility, k	$1xe^{-9}$ Pa^{-1}	Beni et al. (2012)
Pore expansivity, β	$1xe^{-6}$ K^{-1}	Beni et al. (2012)
Injection Pressure	36 MPa	-
Temperature	58 ℃	Beni et al. (2012)
Salinity	0.2	Beni et al. (2012)
Pressure gradient	10.5 MPa/Km	May et al. (2004)
Salinity gradient	80 g/L.Km	May et al. (2004)
CO_2 injection rate	40 Kg/s	-
Injection time	20 Yrs.	-
Simulation time	1000 Yrs.	-

In spite of considering three-dimensional flow in a permeable media, it is noted by Domenico and Schwartz (1998) that under the same hydraulic gradient, horizontal flow is of six orders of magnitude faster than the vertical flow. In this work, the conducted simulation runs are dominated by the lateral flow. Accordingly, the reference nodes within the computational domain have been declared in the output control card in the input file vertically at distances from the bottom of the formation at 30, 50 and 80 m while horizontally at radial distances of 100, 200, 500, 800, and 1000 m, from the injection well while azimuthally a single reference plane is considered at 45° to measure our simulation variables for two-dimensional scenarios.

5.3. Results and Discussions

To evaluate the behaviour of CO_2 in a three-dimensional cylindrical large-scale formation, a medium-term of 1000 years numerical modelling of CO_2 injection into homogeneous and heterogeneous formations were carried out in this work. The injection process continued for 20 years followed by 980 years of lockup. supercritical CO_2 was injected azimuthally at 4 nodes, which were uniformly distributed towards the lower 30 m of the domain.

As stated earlier, this study aims to examine the effects of injection pressure, temperature, layering heterogeneity, porosity, permeability and injection condition states on the P_c-S_w relationships and the behaviour of the injected CO_2 in terms of its dissolution or mobility. To show how CO_2 behaves over the simulation lifetime, a series of numerical simulation models displayed in Table 5.3 were created for different initial and boundary conditions shown in Table 5.4. The layering heterogeneity has been set as bottom layer of 40 m thickness and 30 m thickness for the middle and upper layer (see cases 7 and 8 in Table 5.3).

Table 5.3. Simulation cases and parameters.

Conditions	Case No.	Domain	Inject. Press. (MPa)	Temp. ℃	Porosity	Horiz. Perm. (m^2)	Vert. Perm. (m^2)
Dynamic	1	Homogeneous (Fine)	36	58	0.16	0.5428e-13	0.01115e-13
	2	Homogeneous (Coarse)	36	58	0.25	5.625e-13	1.6876e-13
	3		36	70			
	4		36	80			
	5		34	58			
	6		32	58			
	7	Heterogeneous fine-coarse-fine (40–30–30 m thickness)	36	58	0.16 - 0.25 - 0.16	Variable	Variable
	8	Heterogeneous coarse-fine-coarse (40–30–30 m thickness)	36	58	0.25 - 0.16 - 0.25	Variable	Variable
Quasi Static	9	Homogeneous (Fine)	36	58	0.16	0.5428e-13	0.01115e-13
	10	Homogeneous (Coarse)	36	58	0.25	5.625e-13	1.6876e-13

Table 5.4. Initial and boundary conditions.

Case No.	Domain Type/Cond.	Horizontal Permeability (m^2)	Domain Temp. (°C)	CO_2 Injection Pressure (MPa)
	Dynamic			
1	*Homogenous Fine Sand*	0.5428e-13	58	36
2	*Homogenous Coarse Sand*	5.625e-13	58	36
3	*Homogenous Coarse Sand*	5.625e-13	70	36
4	*Homogenous Coarse Sand*	5.625e-13	80	36
5	*Homogenous Coarse Sand*	5.625e-13	58	34
6	*Homogenous Coarse Sand*	5.625e-13	58	32
7	*Heterogeneous Coarse in Fine Sand*	0.5428e-13 - 5.625e-13 - 0.5428e-13	58	36
8	*Heterogeneous Coarse in Fine Sand*	5.625e-13 - 0.5428e-13 - 5.625e-13	58	36
	Quasi-Static			
9	*Homogenous Fine Sand*	0.5428e-13	58	36
10	*Homogenous Fine Sand*	0.5428e-13	58	36

Porosity **Fine** Sand = 0.16, **Coarse** Sand = 0.25

Vertical Permeability **Fine** Sand = 0.01115e-13 , **Coarse** Sand = 1.6876e-13

Hydrostatic Pressure = 32 MPa, Pressure Gradient = 10.5 MPa/Km, Salinity = 0.2

Source: illustrated in Tables 5.1 and 5.2

5.3.1. CO_2 Migration

As soon as the injection process starts, the supercritical CO_2 displaces the existing brine and migrates away from the injection well as illustrated in Figure 5.3. For different time levels, the simulated CO_2 spatial distribution profiles are shown for drainage process (Figure 5.3 (a-d)) during the injection period and imbibition process (Figure 5.3 (e-h)) presenting the post injection period for case 1 simulation conditions (see Table 5.3). CO_2 continues to migrate laterally due to the governing forces, e.g., (i) hydrostatic pressure difference between the injection point and aquifer, and (ii) capillary forces. Furthermore, as a result of densities difference between the ambient brine and injected supercritical CO_2 buoyancy forces push the latter upwards until it reaches the impervious confining layer (caprock) under which it is trapped or extends further laterally. Figure 5.3 (e-h) demonstrates that when injection process ends the domain is invaded by brine which displaces most of the CO_2 leaving part of it trapped in small pores. This leads to residual trapping of the injected CO_2. Meanwhile a volume fraction of the injected CO_2 is dissolved in the brine during and after the injection process to produce a rich CO_2 layer that sinks down and settles permanently at the bottom of the domain.

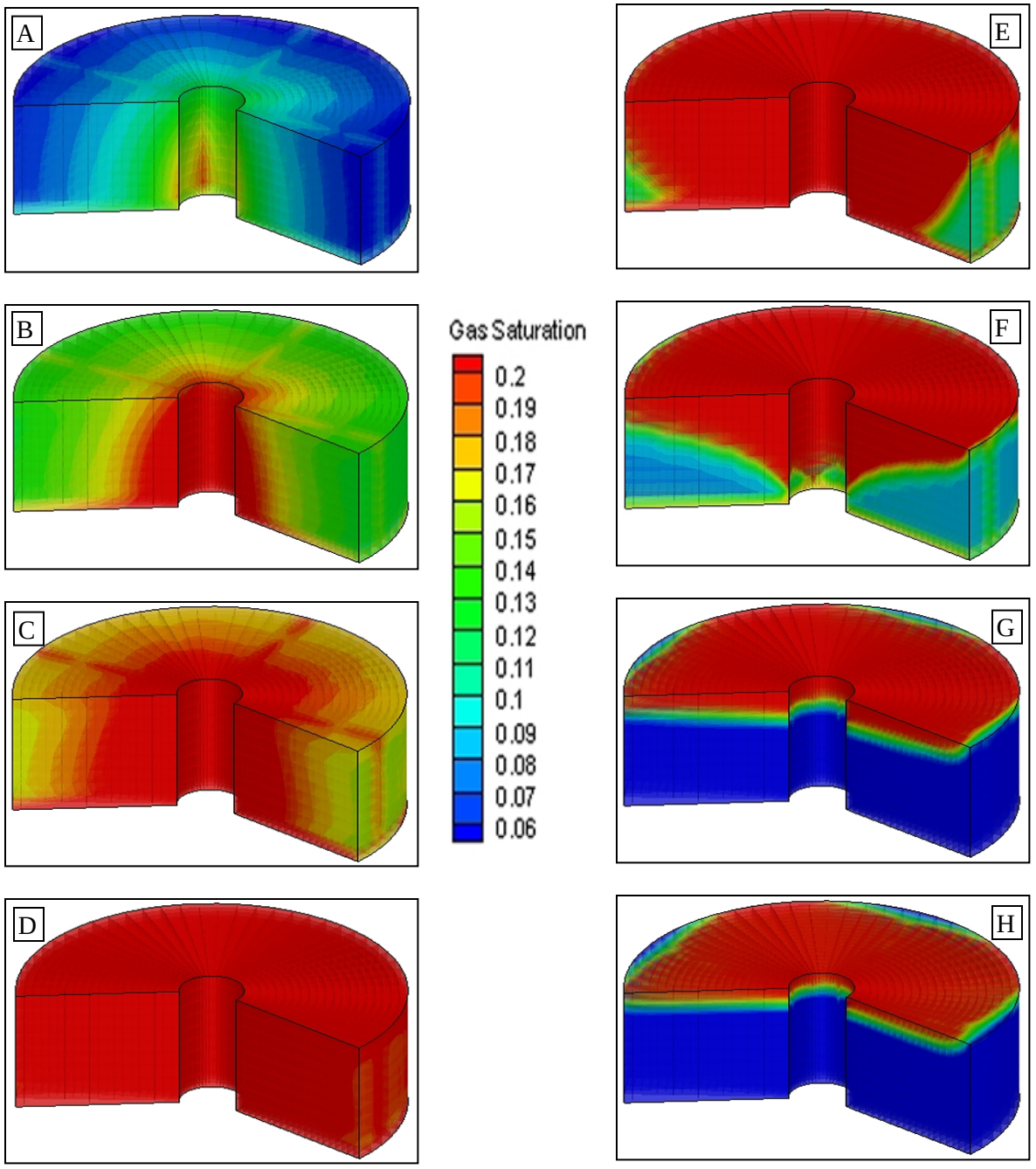

Figure 5.3. Evolution of CO_2 plume in low permeability homogenous aquifer (case1 in Table 5.3):
(A-D) CO_2 distribution after 1, 5, 10 and 20 years of simulation during injection process (drainage).
(E-H) CO_2 distribution after 50, 200, 500 and 1000 years post injection process (imbibition).

5.3.2. Effects of Porosity and Permeability

It has been suggested by some researches (e.g., Kumar et al. 2005; Xu et al. 2006; Kopp et al. 2009; Chasset et al. 2011) that an increase in the mean permeability results in greater injectivity and mobility of CO_2 which increases dissolution into the formation brine. To explore this further and, in particular, determine the effects of porosity and permeability on the injectivity of CO_2, two sets of simulations were carried out in this study. The first set in cases 1 and 2 explores these effects in fine and coarse homogeneous domains, respectively as illustrated in Table 5.3. The second set (cases 7 and 8) looks at the effects of two heterogeneous porous layers involving fine-coarse-fine and coarse-fine-coarse layering patterns. In all injection cases illustrated in Figure 5.4, it is observed that the coarse domain produces larger CO_2 plumes during the injection time at middle altitudes of the domain. This means that the higher the permeability the higher the CO_2 saturation is during the drainage process when the hydrostatic forces dominate. Different plumes are produced during the imbibition process when the aquifer brine reverses back to displace the CO_2. Though CO_2 plume size (red area) looks larger for the fine sand domain (Figure 5.4 (a-d)) the actual sequestration of CO_2 was still higher because by then a considerable amount of injected CO_2 would have dissolved in the existing brine and most of it would have settled at the top of the domain. This is clearly displayed in the coarse domain contours illustrated in Figure 5.4(e, h), knowing that the red area represents pure CO_2 gas, blue area refers to pure water (brine) and the green area illustrates the aqueous phase of water-CO_2.

CO_2 distribution profiles in Figure 5.5 demonstrates a different behaviour of the injected CO_2 in the fine domain where CO_2 residual saturation was never reached though some tendency was noticed at a radial distance of 1000 m after 800 years of simulation. In contrast, all CO_2 profiles in the coarse domain reached the CO_2 residual saturation levels after 200 years. This is because lower permeability porous media limit both lateral and vertical CO_2 mobility and maintain more contact with the surrounding brine, which enhances the solubility trapping to keep the injected gas more securely within the aquifer. In addition, the small size pores in the fine domain play like meniscus tubes, which allow CO_2 to break through due to capillary forces to enhance residual trapping. These results are consistent with those obtained by Nordbotten et al. (2005) and Kumar et al. (2005). In the case of heterogeneity, these profiles show completely different trends, which will be discussed in more details in section 5.3.6.

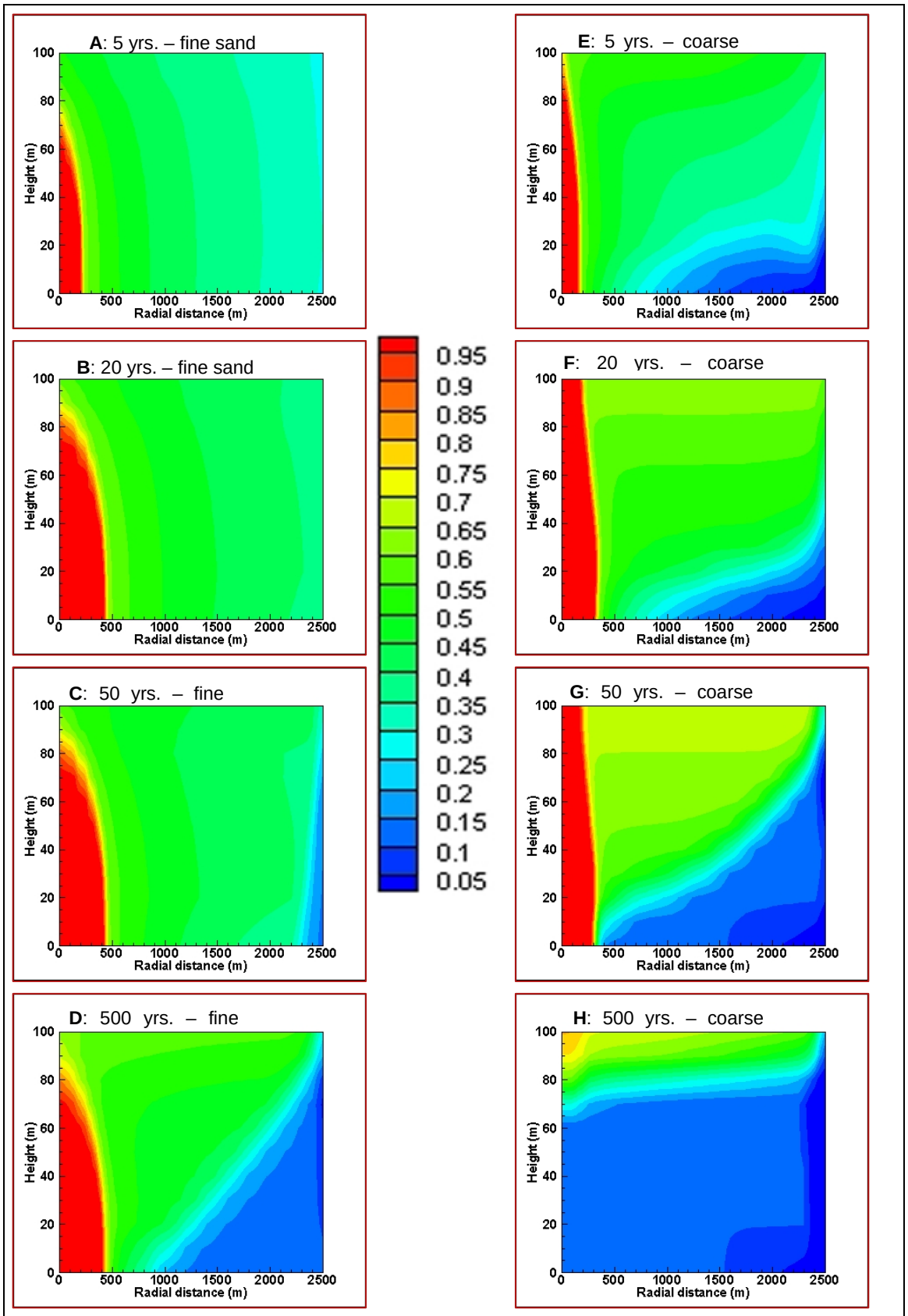

Figure 5.4. CO_2 plume evolution in low and high permeability homogenous aquifers at different time scales; (a-d) fine sand domain (case 1), (e-h) coarse sand domain (case 2). CO_2 injected at aproximately 1.262 MMT/yr for 20 years for all simulation cases.

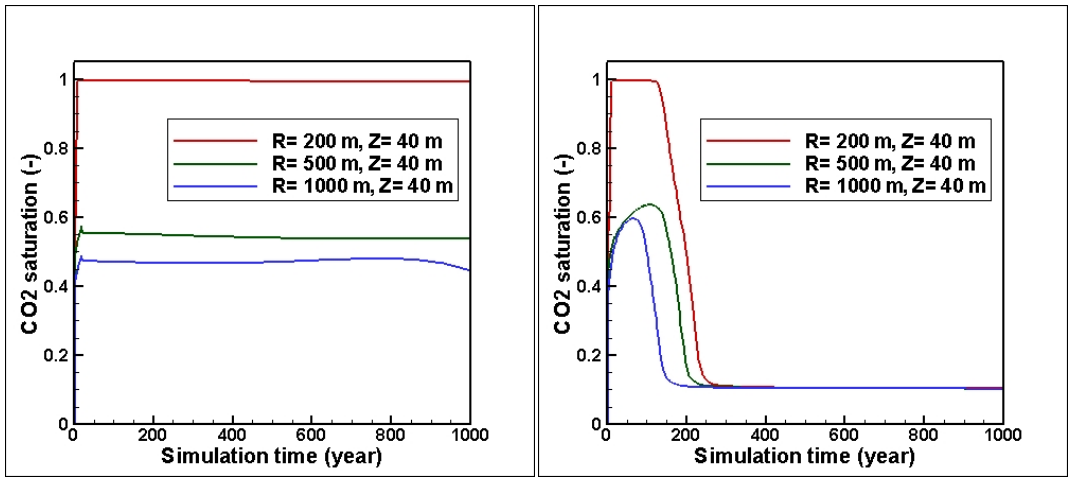

Figure 5.5. CO_2 saturation plots for homogenous domains: case 1 - fine sand (left) and case 2 - coarse sand (right).

5.3.3. Effects of Injectivity

Capillarity plays an important role in sequestering CO_2 in geological formations because it enhances the residual trapping (one of the sequestration mechanisms). To investigate the effect of injection pressure on capillarity in the domain, supercritical CO_2 was injected into a coarse sand domain at 36, 34 and 32 MPa (cases 2, 5 and 6 in Table 5.3), respectively, under dynamic flow conditions. The results presented in Figure 5.6(a) show no significant influence of the injection pressure on capillary pressure at all saturation values which is most likely due to the employed values of the injection pressure being very close to the hydrostatic pressure in the aquifer, in fact in case 6 the same value of 32 MPa was used, in addition to the high permeability of the domain which offers easier migration of CO_2 laterally and vertically. These results are qualitatively consistent with the experimental results achieved by Plug and Brunning (2007) who conducted a series of simulation runs using a wide range of injection pressures (1 – 85 bar) and geothermal conditions on coarse and fine unconsolidated sand-CO_2-water system under quasi-static and dynamic conditions to show the effect on capillary pressure curves. They validated their experimental results by the numerically predicted ones and achieved good agreement apart from small discrepancies near the end point saturations that are attributed to the fact that the input capillary pressure curves based on the Leverett-J function, which ignores the dynamic effects. The influence of injection pressure on CO_2 saturation profiles is displayed in Figure 5.6(b), which shows a steep increase in CO_2 saturation at 70 m altitude for all injection pressures as a result of the gravity forces, which cause most of the injected CO_2 to migrate up towards the

top of the aquifer. This increase reaches the highest value after 200 years when the trends sharply steep down until they reach CO_2 residual saturation. The results indicate that the higher the injection pressure, the larger the amount of CO_2 accumulated at the top of the aquifer at times between 200 – 500 years of simulation. This amount of CO_2 is unlikely subject to any permanent trapping in short-term periods of simulation because it is not affected by the imbibition process.

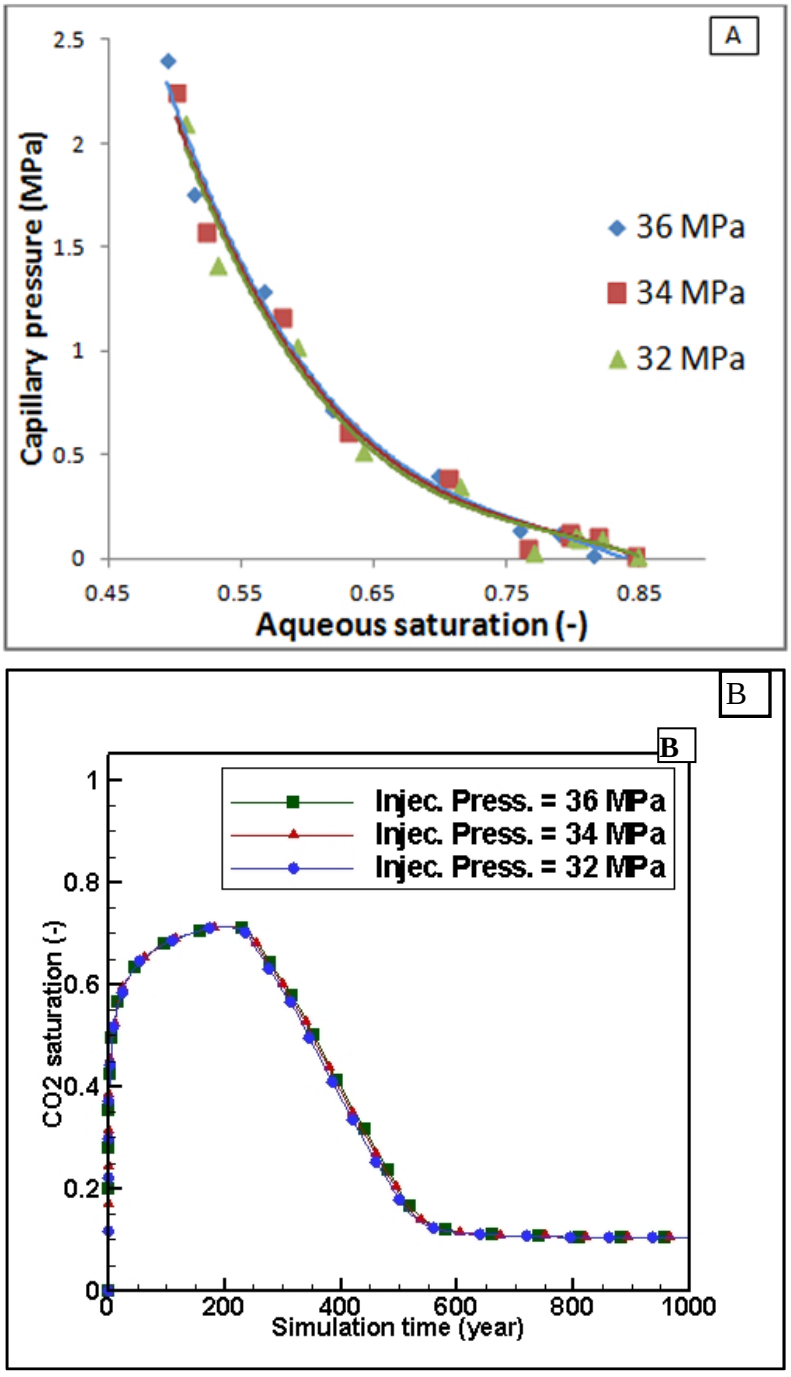

Figure 5.6. A- Capillary pressure vs. aqueous saturation at different injection pressures. B- CO_2 saturation curves at R=500 m and Z=70 m in a coarse homogeneous domain.

5.3.4. Temperature Effects on CO_2 Distribution

In this research work, the effect of temperature on CO_2 distribution during drainage and imbibition processes was inspected. CO_2 saturation contours in Figure 5.7 demonstrate smaller plumes of CO_2 after 20 years of injection (i.e. end of drainage process) and 200 years (during imbibition process) at a domain temperature of 80℃ (case 5 in Table 5.3) compared to those for 58℃ (case 3) under the same injection pressure conditions. This is because increasing the temperature decreases the density and viscosity of the injected CO_2 and consequently increases buoyancy and gravity forces that contribute in spreading CO_2 further laterally and vertically.

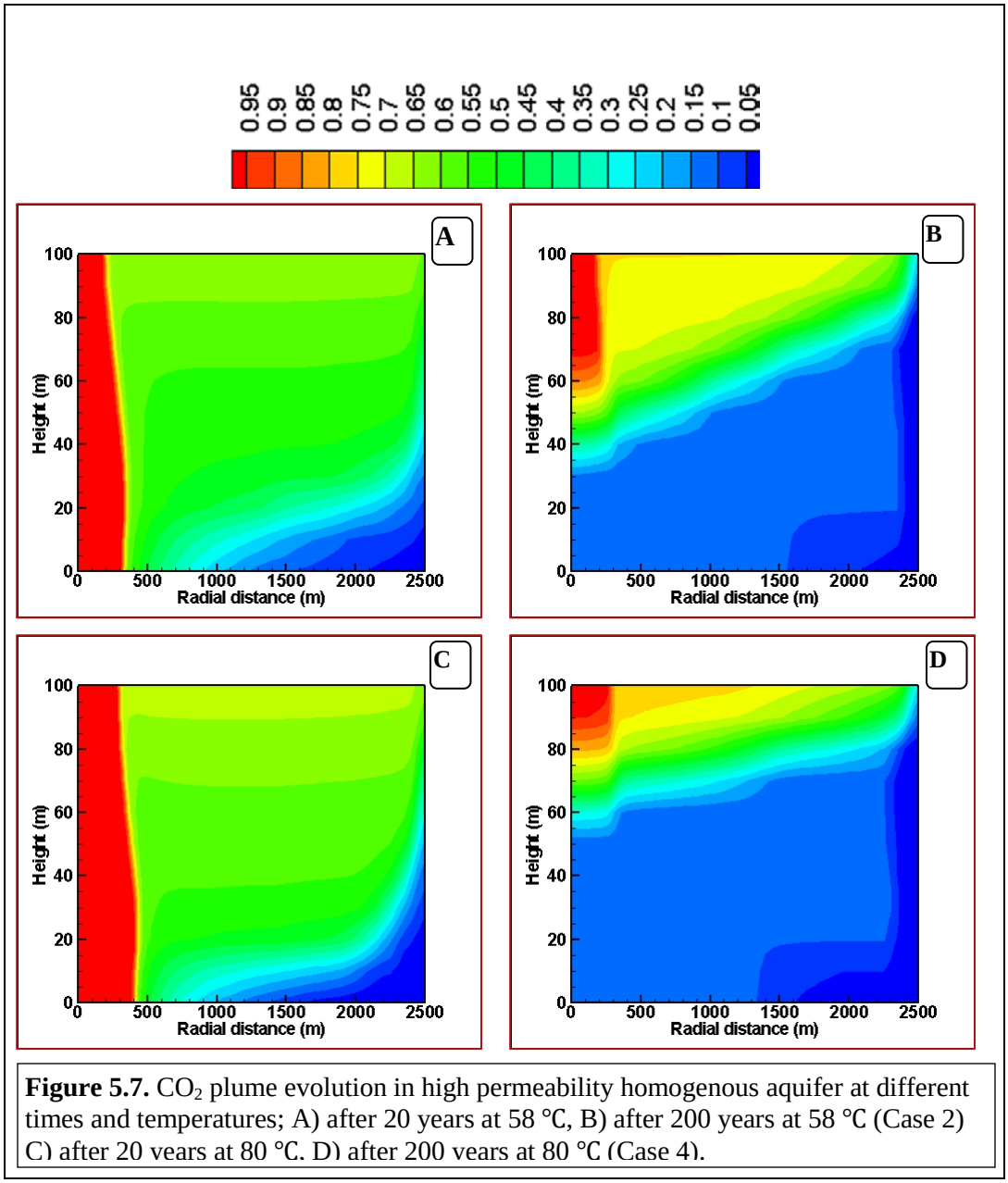

Figure 5.7. CO_2 plume evolution in high permeability homogenous aquifer at different times and temperatures; A) after 20 years at 58 ℃, B) after 200 years at 58 ℃ (Case 2) C) after 20 years at 80 ℃, D) after 200 years at 80 ℃ (Case 4).

The effect of temperature on CO_2 dissolution in the hosted brine is illustrated in Figure 5.8, which shows that after about 200 years of simulation, higher temperature results in more CO_2 dissolved due to the decrease in the density of CO_2, which migrates upwards to get in contact with more fresh brine that enhances the solubility trapping mechanism.

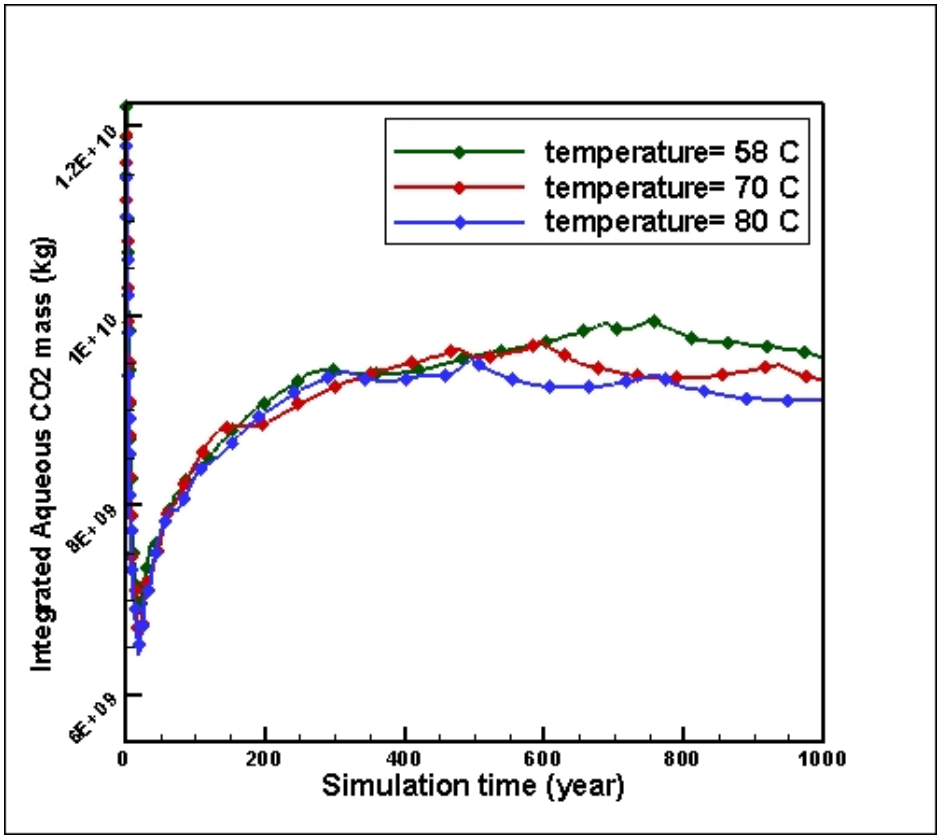

Figure 5.8. Temperature effects on dissolved CO_2 mass (cases 2, 3 and 4).

Moreover it can be observed in Figure 5.9 that capillary pressure increases proportionally with temperature and this change is more prominent between saturation values of 0.55 - 0.7. The results in Figure 5.9 demonstrate that at saturation value of 0.65, about 50% increase in capillary pressure is obtained when the temperature is increased from 58℃ to 80℃. This increase in capillary pressure permits more CO_2 flow into the small pores where it is trapped as a residual solute, which is referred to as residual trapping.

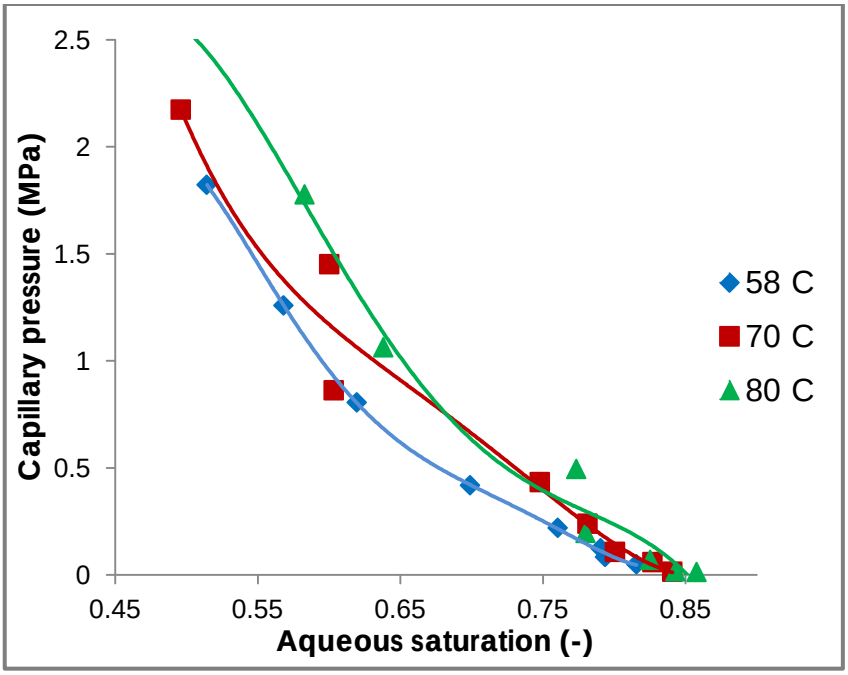

Figure 5.9. Capillary pressure vs. aqueous saturation at different temperatures (cases 2, 3 and 4).

5.3.5. Dynamic Capillary Pressure Effects

Our investigations explain that in addition to the saturation, capillary pressure is strongly influenced by the flow conditions in the system. Several simulation tests were carried out to compare the CO_2 saturation change in homogeneous and heterogeneous computational domains under quasi-static and dynamic conditions. The results are illustrated in Figure 5.10, which demonstrates lower CO_2 saturations under quasi-static flow conditions at any radial distance from the injection well at all time levels. The longer elapsed time to attain static conditions allows more CO_2 into small pores by capillary forces and this may increase convective mixing between the two fluids, which enhances the solubility trapping of the injected CO_2. Additionally, it is noticed from Figure 5.11 that at saturation values above 0.55 higher capillary pressures are generated in fine-grained domain, which is consistent to the theories, which relate capillary pressure directly to the pore size.

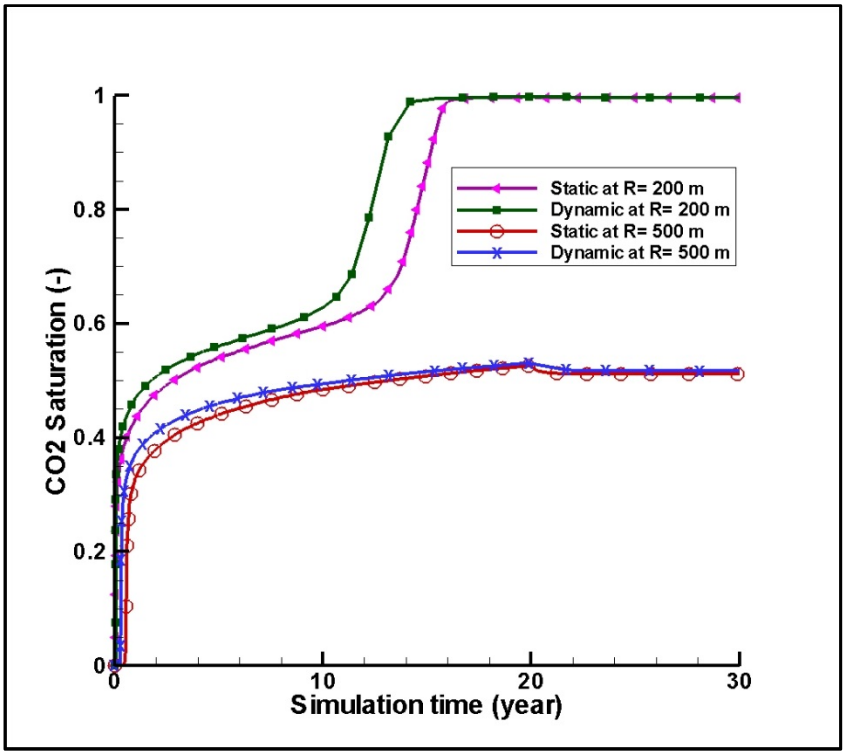

Figure 5.10. CO_2 saturation (volume fraction) curves for homogenous fine domain under static and dynamic conditions at altitude of 40 m (cases 1 and 9).

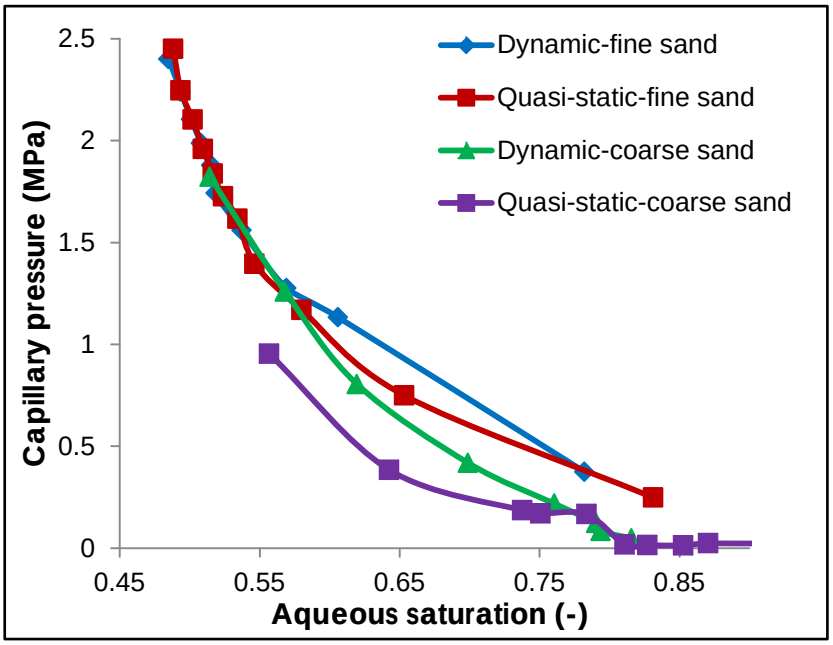

Figure 5.11. Dynamic and quasi-static capillary pressure-saturation curves for homogenous domains.

To determine the dynamic or damping coefficient (τ), which indicates the extent of dynamic capillary pressure effect, two numerical simulations (cases 2 and 10 in Table 5.3) were run under dynamic and quasi-static condition, respectively. All calculation results are displayed in Figure 5.12. The dynamic coefficient for each average value of the aqueous saturation was calculated by equation (5.14), the corresponding average values of dynamic and static capillary pressures (P_c^{dyn}, P_c^{stat}), and the calculated values of the time derivative of saturation (∂S/∂t). Figure 5.12 shows that the value of dynamic coefficient decreases when the aqueous desaturation rate increases and this decline is very sharp at low saturation values when the desaturation rate is slow (i.e. lower values of ∂S/∂t). The attained relationship between the dynamic coefficient and aqueous saturation can be clarified by the longer time required to attain the residual saturation at higher values of dynamic coefficient.

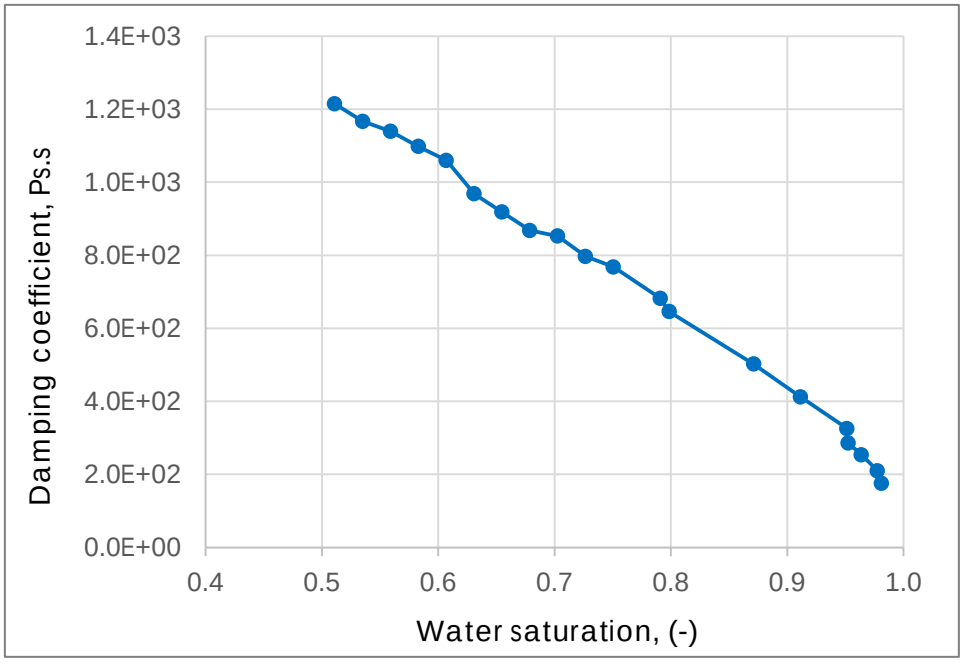

Figure 5.12. Dynamic Coefficient change with aqueous saturation in a homogeneous coarse sand domain (cases 2 and 10 in Table 5.3).

5.3.6. Effects of Heterogeneity

Heterogeneity is closely related to the disparity in permeability, which strongly rules the CO_2 transport through different parts of the domain. To investigate this influence, four study cases (1, 2, 7 and 8) were compared in terms of CO_2 saturation distribution in homogenous and heterogeneous domains. As expected, and in agreement with some previous studies (e.g., Ataie-Ashtiani et al. 2001; Das et al. 2006), heterogeneity has shown an important influence on the characteristics of two-phase flow in porous media. It is shown in Figure 5.13 that all trends behave similarly at 200 m and 40 m horizontal and vertical distances respectively, as they display an increase in the integrated aqueous CO_2 upon injection stops and tend to plateau after about 200 years except in case 8 (fine sand embedded in coarse), which starts to drop after 50 years of simulation. This behaviour is related to the injection section into which the supercritical CO_2 was injected (lower 40 m), which for this case is a coarse layer bounded by a fine one above. This scenario restricts the vertical migration of CO_2 due to the lower permeability of the upper strata, which consequently eliminates contact with more fresh brine, which reduces the solubility trapping. However, larger amount of CO_2 was dissolved in the homogenous coarse domain due to the high permeability, which increases CO_2 movement in both directions maintaining more contact with fresh brine in which it dissolves.

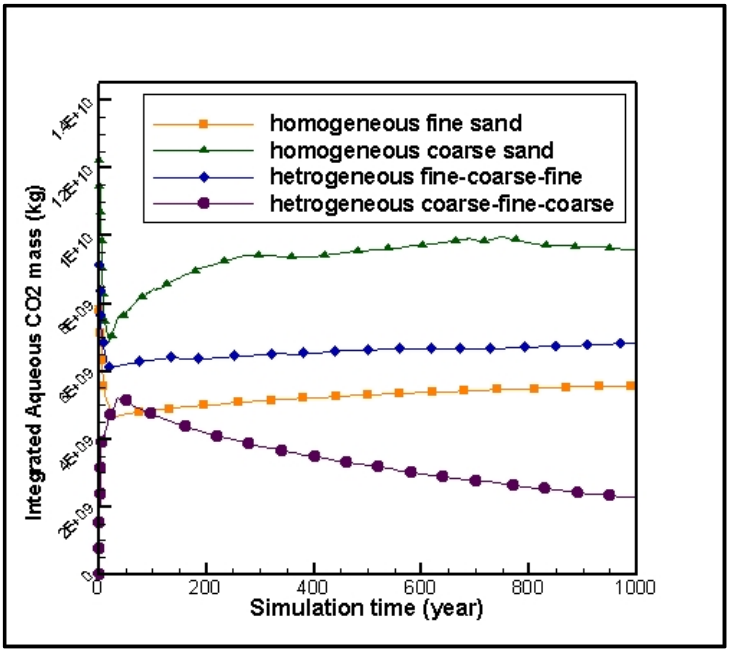

Figure 5.13. Integrated aqueous change for homogeneous and heterogeneous domains (cases 1, 2, 7 and 8) at radial distance of 200 m and altitude of 40 m.

Figure 5.14 presents the total integrated amount of CO_2 in aqueous and gas phases at the same grid block described above. It is apparent that all curves decline and tend to plateau soon after the injection stops except case 8, which shows sharp increase in total integrated CO_2 until about 50 years of simulation and continuously increases until the end of 1000 years of simulation. This can be explained by the fact that the injected CO_2 favourably move through large size pores which increases the hydrodynamic trapping as a result of pressure difference forces and CO_2 concentration. This is combined with the solubility trapping due to the convective mixing of CO_2 and the surrounding brine. Residual trapping is larger in the surrounded fine layer, which slows down the migration of the injected CO_2 providing more chance to enter the small pores.

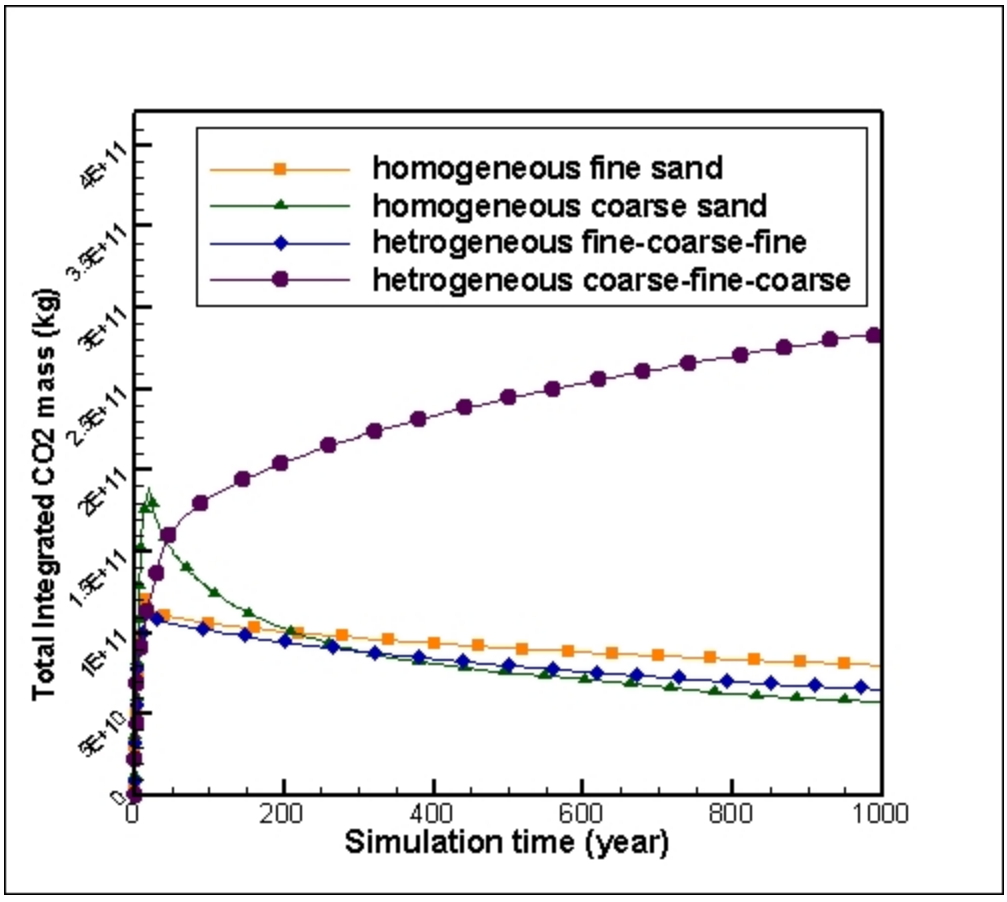

Figure 5.14. Total Integrated CO_2 profiles for homogeneous and heterogeneous domains (cases 1, 2, 7 and 8) at radial distance of 200 m and altitude of 40 m.

CO_2 spatial spread is demonstrated in three-dimensional cylindrical contours in Figure 5.15, which demonstrates how the injected supercritical CO_2 spreads through different heterogeneous domains (cases 7 and 8 in Table 5.3) at different time steps. During a drainage process period of

20 years for case 7 (coarse sand embedded in fine), higher CO_2 saturation values were obtained. This increase is a result of the pressure difference forces that control the lateral migration of CO_2 and vertically due to the buoyancy forces that transfer the supercritical fluid from the low permeability layer up to the higher permeability one as evidently shown in Figures 5.15(a-d).

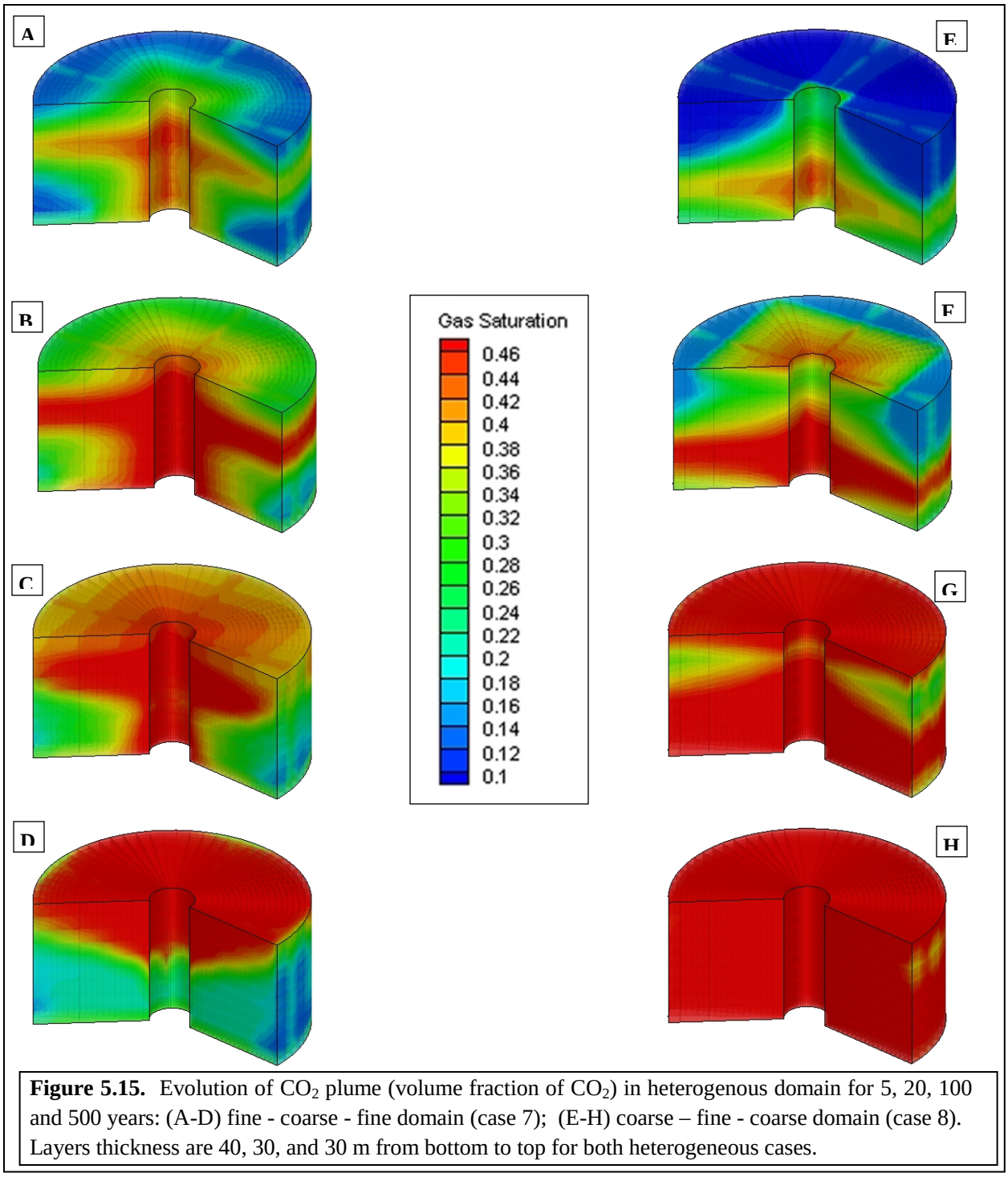

Figure 5.15. Evolution of CO_2 plume (volume fraction of CO_2) in heterogenous domain for 5, 20, 100 and 500 years: (A-D) fine - coarse - fine domain (case 7); (E-H) coarse – fine - coarse domain (case 8). Layers thickness are 40, 30, and 30 m from bottom to top for both heterogeneous cases.

In contrast, for case 8 (fine sand embedded in coarse) during imbibition process (post injection), higher concentrations of CO_2 were achieved as shown in Figures 5.15(e-h) because in this case, advective, diffusive and gravity forces all contribute in trapping the injected CO_2 in addition to the reversed-back movement of the brine behind the CO_2 plume to displace the CO_2 again leaving traces of it as residual contaminants in small-sized pores, which is referred to as residual trapping. Moreover, the low permeability layer retains more contact time between the two fluids, which enhances the solubility trapping mechanism. The results of this work are consistent with those obtained by Nordbotten et al. (2005) as they found out that the buoyancy forces places the highest mobility layer of injected CO_2 at the top of the domain considering that in their case the CO_2 was injected along the whole altitude of the domain.

5.4. Chapter Summary

A series of numerical simulations have been conducted in this work to identify the possible implications of a number of important parameters on the capillary pressure – saturation relationship for supercritical CO_2 in deep saline aquifer. From the results of this work, it is obvious that the higher the injection pressure, the higher the capillary forces are, however the maximum sustainable pressure has to be taken into consideration to avoid any geomechanical fracture to the formation rock. The value of the dynamic coefficient (τ) increases as the desaturation rate ($\partial S/\partial t$) declines because more time is required for the residual saturation to be attained.

It has been found that capillary forces are higher in fine-grained domains and they enhance storage capacity of the site by amplifying the residual trapping mechanism of CO_2 during the imbibition process. Solubility trapping is more efficient in fine domains because they maintain more contact between the fluid phases, which leads to more CO_2 dissolved in the occupant brine. Warm aquifers are found to be more efficient in sequestering CO_2 because higher temperatures increase the capillary pressure and consequently enhance the residual trapping of CO_2. Fine sand embedded in coarse pattern of heterogeneity is found to be a method that is more effective over long periods of storage procedure, however more research is required to clarify how the field distribution of permeability heterogeneity and injection scenarios of $scCO_2$ affect the efficiency of the sequestration.

Chapter 6

A scenario analysis of supercritical CO_2 injection into geological formations (Field Scale)

Overview

One of the most promising means of reducing carbon contents in the ambience, which is aimed at tackling the threats of global warming, is injecting carbon dioxide (CO_2) into deep saline aquifers (DSAs). Selecting a site to store CO_2 depends on its sequestration efficiency and other related parameters including porosity, permeability, heterogeneity, hydrostatic conditions, capacity and others. Unlike many previous works, in this research study, a new term of permanent capacity and efficiency factor of CO_2 immobilization in sedimentary formations has been introduced utilizing STOMP-CO_2 numerical simulation code. The research aims at investigating the influence of different injection scenarios and flow conditions on the storage capacity and efficiency.

Additionally, the effects of various injection schemes/scenarios and aquifer characteristics on enhancing the two permanent sequestration mechanisms namely; residual and solubility trapping of CO_2 is to be examined in this work. This is carried out through a series of numerical simulations employed on 3D hypothetical homogeneous and heterogeneous aquifers based on the geological settings for Sleipner Vest Field, which is located in the Norwegian part of the North Sea. The results of this work are expected to play a key role in providing insight knowledge for assessing the feasibility of various geological formations for CO_2 storage. It also highlights the effects of heterogeneity, permeability isotropy, injection orientation and methodology, and domain-grid refinement on the simulation results in terms of capillary-saturation relationships and the amounts of integrated CO_2 throughout the timeline of the simulation via different trapping mechanisms.

In this study, heterogeneity is defined as the variability of porosity/permeability within the simulated domain and can be quantified using various geostatistical techniques including; Lorenz coefficient (*Lc*) and the coefficient of variation (*Cv*) methods that are commonly used in establishing porosity and permeability models in exploration. Lorenz coefficient measure is based on plotting sorted values of change in the property against depth increment (Lorenz Curve) and comparing it to the “line of perfect equality” that represents a purely homogeneous formation where the cumulative property increases by a constant value with depth. The Lorenz coefficient (*Lc*) that ranges between zero for pure homogeneous and one for maximum heterogeneity, is calculated as twice the area between the two curves.

The coefficient of variation (*Cv*) is a simple methodology that measures the variability of the property relative to the mean values. It is calculated by dividing the standard deviation by the mean value of the property (porosity/permeability in the case of this research) across the domain. *Cv* value ranges from zero for pure homogeneity to ∞ for heterogeneity.

6.1. Introduction

Injecting CO_2 into deep saline aquifers (DSAs) has been proposed as one of the most viable means of tackling the global warming. This is because the technology has developed sufficiently due to the experience gained from oil and gas exploration and waste disposal methodologies. Moreover, these aquifers offer more extensive storage potential than other geological formations like oil and gas fields or coal seams (IPCC 2005). Consequently, many research studies have been conducted to assess their storage capacity and efficiency to safely sequester the injected gas.

As discussed earlier in our previous works (Abidoye et al., 2015; Khudaida and Das, 2014), CO_2 storage methodology in saline aquifers can be categorised into hydrodynamic and chemical mechanisms. The first one includes structural and residual trapping of CO_2 within the aquifer pore space while the second one comprises of the solubility and mineral trapping of CO_2.

Two important factors that should be considered to assess the suitability of an aquifer for sequestering CO_2 are its capacity and injectivity. They should allow for safer and economical storage of large amounts of the disposed gas (Kopp et al. 2009a). Additionally, hydrostatic conditions play a crucial role in increasing the storativity of saline aquifers because the higher pressure in deeper formations induces gas compression resulting in more storage of CO_2 in a specific volume of a porous media (Gough et al. 2006). In this regard, the integrity of the caprock with low permeability is an essential consideration because any existing faults or cracks in the aquifer rock will result in the injected gas escape to the surface. Porosity and permeability of the formation have significant influences on selecting the appropriate site for carbon storage because higher permeability of a medium allows fluids to migrate easily through the better-connected pores away from the injection well case, which subsequently magnifies the capacity and efficiency of the aquifer to store CO_2.

Theoretically, the storage capacity of an aquifer is the substantial limit of CO_2 that can be admitted into it. However, this limit is not practically achievable due to various geological factors and engineering barriers (e.g., pore connectivity, lack of geological data, economic feasibility, legal regulations and infrastructure benchmarks). Therefore, a new term called effective storage capacity has been coined, which has subsequently been a subject of many researches using different calculation methods. These methods include volumetric and compressibility methods (Zhou et al. 2008; Frailey 2009; Ehlig-Economides and Economides 2010), mathematical models (MacMinn and Juanes 2009), dimensional analysis (Kopp et al. 2009(b)), analytical investigations (Okwen et al. 2010) and numerical modelling (Kopp et al. 2009(a); Yang et al. 2010) to assess the efficiency of geological formations to sequester CO_2. Most of these studies are theoretical or analytical based on 2D models that lack accuracy in terms of practical employment. A detailed comparison study by Goodman et al. (2013) has been conducted to evaluate the impact of a variety of approaches and methodologies on estimating CO_2 sequestration in geological formations.

One basic estimation method, which is widely adopted worldwide, is the U. S. Department of Energy (US-DOE) method. As explained in details by Goodman et al. (2011) the method assumes infinitive boundary and defines the efficiency of an aquifer to store CO_2 by the pore volume that is available to be occupied by the injected gas. It determines the CO_2 mass storage capacity and efficiency for an aquifer as:

$$G_{CO_2} = A_t h_g \emptyset_t \rho_{CO_2} E_{aq} \tag{6.1}$$

where A_t is the total cross-sectional area of the domain, h_g defines the gross thickness of the formation, $\emptyset_t$ is the total porosity of the rock, ρ_{CO_2} and E_{aq} represent the density of the injected CO_2 and the storage efficiency of the aquifer respectively.

An approach proposed by Zhou et al. (2008) predicts the pressure build-up history and the impact on the actual storage efficiency in response to the CO_2 injection process. They define the storage efficiency factor as the volumetric fraction of the sequestered CO_2 per unit volume of pores in the potential domain. In spite of achieving good agreement between the analytical results and the numerically predicted values, the authors state that this method is not suitable for geological formations of low permeability that leads to lower injectivity and creates more

non-uniformity in the pressure-build-up within the simulated domain. This is due to many simplifications and assumptions in the analytical solutions in their research work.

A relatively recent method developed by Szulczewski (2013) considers both residual and solubility trapping mechanisms in addition to the CO_2 migration capacity. The method is applicable to both open-boundary and pressure-limited systems. Additionally, this method counts the net thickness of the aquifer to calculate the pores volume instead of the gross thickness in heterogeneous domains. This is because most of the injected CO_2 targets the high-porosity layers like sandstone or carbonate rocks rather than any intermingled layers of shale or clay that store negligible amounts of the injected gas.

For open-boundary systems, the total mass of CO_2 (C_t) stored in an aquifer can be determined by:

$$C_t = \rho_g L_t W H \emptyset (1 - S_{wc}) \frac{2}{\varepsilon_T} \quad (6.2)$$

where ρ_g is the density of CO_2, L_t is the total length of the aquifer, W is the width of the well, H is the net thickness of the aquifer $\emptyset$ is the porosity of the rock, S_{wc} defines the connate water saturation and $\frac{2}{\varepsilon_T}$ represent the storage efficiency factor.

For the pressure-limited systems, the CO_2 mass is calculated by;

$$C_p = \rho_g H W \sqrt{\frac{k_{aq} c T}{\mu_w}} \frac{P_{fraq} - (p_o + \overline{\rho_w} g D)}{4 \tilde{p}_{max}} \quad (6.3)$$

where k_{aq} is the permeability of the aquifer, c is the compressibility, T is the temperature, μ_w is the brine viscosity, P_{fraq} is the fracture pressure of the rock, $p_o$is the hydrostatic pressure, $\overline{\rho_w}$ is the average density of brine, g is the gravitational acceleration, D is the depth to the top of the aquifer and $\tilde{p}_{max}$ represents the maximum dimensionless pressure which can be determined by numerically solving the partial differential equation (PDE) for the pressure-limited flow system (Szulczewski 2013).

Several techniques can be used to increase the capacity and efficiency of CO_2 sequestration in saline aquifers that will consequently support the efforts by the Intergovernmental Panel on Climate Change (IPCC) to incite policy makers with the importance of deploying carbon

capture and sequestration (CCS) as one of the cost effective technologies for confronting the climate change and global warming concern.

Geological formations capacity can be increased by improving the injectivity through increasing the injection mass flow rate or pressure to compensate the loss of permeability due to salt precipitation in the well vicinity. Furthermore injecting into adjacent layers with high permeability helps attenuating pressure build-up and consequently higher injection rates can be employed (Chasset et al. 2011; Birkholzer et al. 2009).

Using horizontal injection wells instead of vertical ones is one of the methods implemented to increase the injectivity and capacity of aquifers because it helps to diminish the pressure-build-up peaks around the injection well and spread pressure uniformly within the domain. Deploying this technique requires determination of the minimum length of the horizontal well that is dependent on the effective radius of pressure disturbance around the vertical injection well (Ghaderi et al. 2009; Vilarrasa 2013; Jikich et al. 2003; De Silva et al. 2012).

It has been evidenced that the solubility of CO_2 into brine can be accelerated by injecting slugs of fresh brine on top of the storage formation during and after CO_2 injection. This can increase CO_2 dissolution by more than 40% within a period of 200 years, which reduces the risk of CO_2 leakage in the long-terms of sequestration according to the study by Hassanzadeh et al. (2009). The study also investigated further factors that have significant impact on increasing the storage efficiency in saline aquifers including optimizing the rate of the injected brine and transporting the injected and existing fluids within the reservoir in addition to the effect of aquifer properties like thickness, vertical anisotropy and layers of heterogeneity included within the media.

In their work, De Silva and Ranjith (2012) concluded that while using horizontal injection wells in the absence of chase brine injection improves the storage of aquifers, vertical injection wells with chase brine injection performs better storage efficiency. However, the authors suggest that the injection process should be carried out over the whole thickness of the aquifer to maximize the storage capacity. In contrast, Khudaida and Das (2014) observed that injecting CO_2 into the lower section of a reservoir enhances the solubility trapping mechanism and subsequently increases the storage efficiency.

Introducing hydraulic fractures in formation rock can improve the injectivity by increasing the effective permeability of the aquifer, which facilitates migration and consequently preserves

more contact between the injected CO_2 and the existed brine in addition to preventing any pressure build-up within the aquifer. However, this technique needs a detailed characterization of the formation and has to be implemented with extra care to avoid causing any gas leakage (Ghaderi et al. 2009).

Keeping the above discussion in mind, this work aims to provide further understanding on how to assess the feasibility of any potential storage site by investigating the behaviour and migration of CO_2-brine as a two-phase flow system in porous geological formations under various injection conditions and scenarios. It also demonstrates the effect of various site characteristics like heterogeneity and anisotropy on the injectivity and safe storage of the injected CO_2. The results will also address the applicability of different injection techniques in terms of orientation and continuity to enhance the capacity and efficiency of sequestering CO_2 in geological formations.

6.2. Model Setup

To assess storage capacity and efficiency of an unconfined aquifer (i.e., migration-limited domain), a cylindrical computational domain extending from 0.3 m (the radius of the injection-well case) to 6000 m laterally and 96 m vertically, was simulated with two types of grid resolution, namely, coarse and fine grids. For the coarse-grid, the domain was horizontally discretized into 88 grid-blocks with a finer mesh in the vicinity of the injection well and gradually coarser further away. Vertically, the domain was discretized to 24 of 4 m blocks. This mesh refinement has made 2112 elements as shown in Figure 6.1. For the fine resolution, the grid spacing was increased by 100% in both directions producing 8448 cells. Supercritical CO_2 (scrCO_2) is injected into the centre of the domain at a constant rate of 32.0 kg/s (about 1 MMT/year), which represents a typical benchmark value (Ghaderi et al. 2009) via a number of cells either at the bottom section or through the whole thickness of the reservoir.

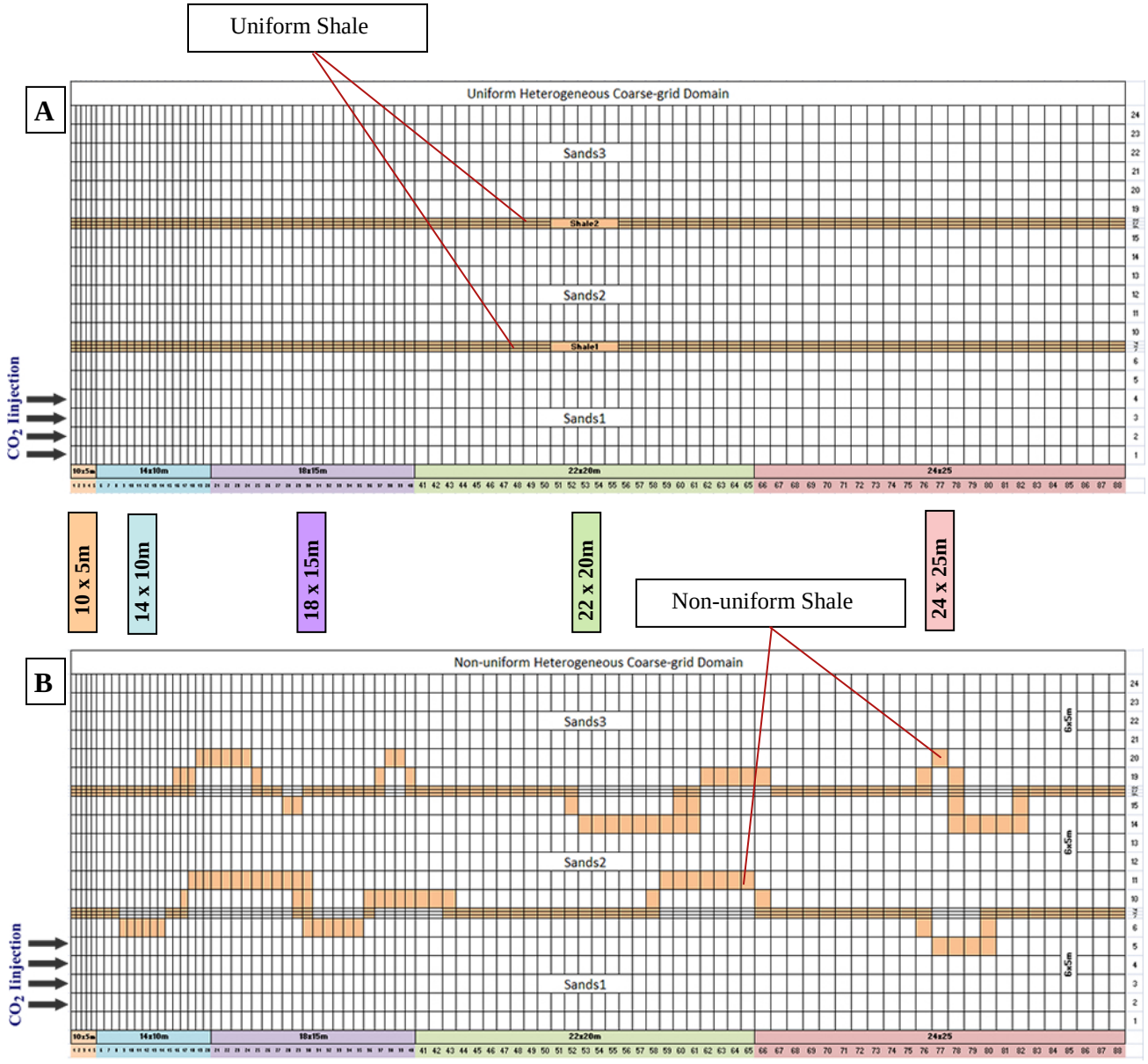

Figure 6.1. A schematic diagram of the two modelled heterogeneous domains: (A) uniform heterogeneity and (B) non-uniform heterogeneity.

6.2.1. Parameters and Calculations

The simulation parameters used for this work are based on the geological settings for Sleipner Vest Field, which is located in the Norwegian part of the North Sea at an approximate depth of 1100 m. It is identified to be one of the typical CO_2 disposal sites offering anticipated hydrostatic conditions to keep the injected CO_2 in supercritical conditions. All petrophysical parameters and formulations factors are listed in Tables 6.1 and 6.2. CO_2 properties adopted in the simulation code have been arranged in a data table developed from the equation of state by Span and Wagner (1996), which is considered to be the most accurate reference EOS for CO_2 because it gives very accurate results in the most technically important ranges of pressure up to 30 MPa and temperature up to 523 K, the condition that are common in geological sequestration of CO_2. Span and Wagner equation is based on an extensive range of fitted experimental thermal properties of the single–phase region, the liquid-vapour saturation curve , the speed of sound, the specific heat capacities, the specific internal energy and the Joule-Thomson coefficient (Giljarhus et al., 2011). This equation is expressed in a form of the Helmholtz energy ($\emptyset$);

$$\emptyset(\delta,\mathcal{T}) = \phi^o(\delta,\mathcal{T}) + \phi^r(\delta,\mathcal{T}) \tag{6.4}$$

where $\delta = \rho/\rho_c$, $\mathcal{T} = T_c/T$, ρ_c and T_c are the critical density and critical temperature of CO_2 respectively. ϕ^o is the ideal gas part of the Helmholtz energy and ϕ^r is the residual part of the Helmholtz energy.

The two parts of the Helmholtz energy (the basic and phase diagram elements) of this equation of state are explained in details in a published literature by Span and Wagner (1996) and are not repeated in this study. Span and Wagner EOS has been employed in this research to calculate the density of CO_2 at different simulation conditions for the following reasons (Span and Wagner, 1996);

1- It is based on a wide range of experimental data with uncertainty values of $\pm$ 0.03% - $\pm$ 0.05% in the density.
2- It is valid for a wide range of pressures and temperatures even beyond the triple (critical) point in the phase-diagram of CO_2 (see Figure 5.1).
3- The equation can be extrapolated up to the limits of the chemical stability of CO_2.

The only limitation of this EOS is that it is time-expensive to evaluate in dynamic numerical simulations because it consists of a large number of algorithms and exponentials.

The phase equilibria calculations in STOMP-CO_2 code are conducted via a couple of formulations by Spycher et al. (2003) and Spycher and Pruess (2010) that are based on Redlich-Kwong equation of state with fitted experimental data for water-CO_2 flow systems.

The mole fraction of water in the gas phase ($X_g^{H_{2o}}$) and mole fraction of the CO_2 in the aqueous phase ($X_l^{CO_2}$) are calculated by the following equations:

$$X_g^{H_{2o}} = \frac{(1-B)}{(\frac{1}{A}-B)} \tag{6.5}$$

$$X_l^{CO_2} = B(1 - X_g^{H_{2o}}) \tag{6.6}$$

Where:

$$A = \frac{K^0_{H_{2o}}}{\emptyset_{H_{2o}P}} exp\left[\frac{(P-P^{)})\bar{V}_{H_{2o}}}{RT(K)}\right] \tag{6.7}$$

$$B = \frac{\emptyset_{CO_{2o}P}}{(10^3/M^{H_{2o}})K^0_{CO_2}} exp\left[-\frac{(P-P^0)\bar{V}_{CO_2}}{RT(K)}\right] \tag{6.8}$$

In equations 6.7 and 6.8, K^0 is the thermodynamic equilibrium constant for water or CO_2 at temperature T in Kelvin (K), reference pressure $P^0 = 1\ bar$, P is the total pressure, $\bar{V}$ represents the average partial molar volume of each pure condensed phase, $\emptyset$ is the fugacity coefficient of each component in the CO_2-rich aqueous phase and R is the gas constant (White et al. 2013).

The aqueous saturation (S_w) is calculated by Van Genuchten (1980) formulation that correlates the capillary pressure (P_c) to the effective saturation (S_e):

$$\mathrm{S_e} = \frac{S_w - S_{wr}}{1-S_{wr}} = [1 + (\alpha.P_c)^{\mathrm{n}}]^{\mathrm{m}} \qquad \text{for } P_c>0 \tag{6.9}$$

where S_{wr} is the water residual saturation and α, n and m are the Van Gunechten parameters that describe the characteristics of the porous media.

During the injection period (drainage process), there is no gas entrapment because it only occurs during the imbibition process when the displaced water invades the domain back as soon as CO_2 injection stops leaving some traces of it trapped behind in some small-sized pores. As a result, the injected CO_2 can either exist as free or trapped gas.

The effective trapped gas is computed using a model developed by Kaluarachchi and Parker (1992):

$$\hat{S}_{gt}^{potential} = \left[\frac{1-\hat{S}_l^{min}}{1-R(\hat{S}_l^{min})}\right] \tag{6.10}$$

where $\hat{S}_l^{min}$ is the minimum aqueous saturation (irreducible water saturation) and R is the Land's parameter (Land 1968) which relates to the maximum trapped gas saturation;

$$R = \frac{1}{\hat{S}_{gt}^{max}} - 1 \tag{6.11}$$

$\hat{S}_{gt}^{max}$ is the maximum trapped gas saturation that can be achieved during the drainage process.

Maximum trapped gas and minimum aqueous (irreducible water) saturation are calculated by the following correlations by Holtz (2002):

$$S_{gr}^{max} = 0.5473 - 0.969\,\emptyset \tag{6.12}$$

$$S_{wirr} = 5.6709[\log(k)/\emptyset]^{-1.6349} \tag{6.13}$$

where $\emptyset$ and k are the porosity and intrinsic permeability of the medium respectively.

The aqueous and gas relative permeabilities are computed by Mualem (1976) correlation in combination with Van Genuchten (1980) formulation according to the following equations (6.14) and (6.15) respectively;

$$k_{rl} = (\bar{S}_l)^{1/2}\left[1-\left(1-\left(1-(\bar{S}_l)^{1/m}\right)^m\right)\right]^2 \tag{6.14}$$

$$k_{rg} = \left(1-\bar{\bar{S}}_l\right)^{1/2}\left[1-\left(1-\left(\bar{\bar{S}}_l\right)^{1/m}\right)^m\right]^2 \tag{6.15}$$

where m is the pore distribution index, $\bar{S}_l$ is the effective aqueous saturation which is calculated from equation (6.9) and $\bar{\bar{S}}_l$ represents the apparent aqueous saturation which is defined as the sum of the effective aqueous and entrapped CO_2 saturations (White et al. 2004).

Table 6.1, Lithostratigraphic division and petrophysical parameters from Sleipner Vest Field, after (White et al. 2013).

layer	Units	Sand 1	Sand 2	Sand 3	Shale 1	Shale 2
Thickness	(m)	30	30	30	3	3
Porosity	-	0.35			0.1025	
Horizontal permeability	(md) (m^2)	304 3.0e-13			10.13 0.1e-13	
Vertical permeability	(md) (m^2)	304 3.0e-13			10.13 0.1e-13	
Density	(kg/m^3)	2650				
Pore Compressibility	(Pa^{-1})	4.5e-10				
Aquifer pressure	(MPa)	11.2				
Pressure gradient	(KPa/m)	10.012				
Aquifer temperature	(°C)	37				
Salinity (mass fraction)	-	0.032				
Aquifer depth	(m)	800-1100				
Water depth	(m)	110				

Table 6.2. Capillary pressure – saturation - permeability functions parameters of the simulated aquifer, after (White et al. 2013*; Holtz 2002**).

Description	Symbol	Value	Units
Irreducible aqueous saturation*	S_{lr}	0.2	-
Irreducible gas saturation*	S_{gr}	0.05	-
Saturation function parameters for (Sand)*	α	2.735	m^{-1}
Saturation function parameters for (Shale)*	α	0.158	m^{-1}
Saturation function parameters*	m	0.4	-
	n	1.667	-
Pore index parameter $\boldsymbol{\lambda} = \frac{\boldsymbol{m}}{\boldsymbol{1-m}}\left(1-0.5^{\frac{1}{m}}\right) = n-1$	λ	0.667	-
Maximum residual gas saturation for aquifer**	S_{grm}	0.208	-
Maximum residual gas saturation for aquitard**	S_{grm}	0.448	-

6.2.2. Initial and Boundary Conditions

Three types of simulated domains namely homogeneous, uniform heterogeneous and non-uniform heterogeneous are modelled in this study. They are assumed to be isotropic for most simulation runs and isothermal under hydrostatic pressure gradient of 10.012 KPa/m with an open boundary condition leading to scattered pressure build-up. The models are presumed to have no heterogeneity in the azimuthal direction but different vertical to horizontal permeability

ratios to be studied in some specific cases to investigate the effect of anisotropy on the storage capacity and efficiency. The system is to be modelled as a 3D cylindrical domain and the results to be compared to those when the system was considered as a two-dimensional radial flow to save computational time and requirements. The gravity and inertial effects are neglected.

Prior to injecting scrCO_2 into the centre of the domain, it is considered to be fully saturated with brine with initial conditions illustrated in Tables 6.1 and 6.2. ScrCO_2 to be injected through four grid-cells at the bottom layer of the grid for 30 years followed by a lockup period of 4970 years. No flux boundary condition is considered for the aqueous wetting phase (brine) at the injection well case as a West boundary whilst the East boundary is set to be infinite with zero flux for CO_2 as a non-wetting gas phase. Zero flux is also considered at the top and bottom confining layers forcing the injected CO_2 to swell crossways.

As an open storage system, the pressure build-up is not considered to be a limiting factor however, the value of the maximum bottom-hole pressure at the injection well and hydrological effect on shallow groundwater sources have to be taken into consideration (Birkholzer et al. 2007; Zhou et al. 2008). The injection rate for this simulation system was set according to the rock fracture pressure (P_{frac}) using the simplified model adopted by Szulczewski et al. (2011) which calculates the pressure-limited storage capacity by;

$$M_p = 2\rho_{CO_2} HW \sqrt{\frac{kC}{\mu_b T}} \frac{P_{frac}}{\hat{p}_{max}} \tag{6.16}$$

where ρ_{CO_2} is the density of the injected gas, H and W are the height and width of the domain respectively, k represents the intrinsic permeability and C is the compressibility of the formation, μ_b is the bulk viscosity and P_{frac} is the fracture pressure.

For infinite aquifer the value of the maximum dimensionless pressure ($\hat{p}_{max}$) in Equation (6.16) is ~ 0.87 (Szulczewski et al. 2011).

All parameters in Equation (6.16) are known except the fracture pressure of the rock which can be defined as the effective vertical stress for deep aquifers and determined by the following equation (Szulczewski 2009):

$$\sigma'_{\mathrm{v}} = (\rho_b - \rho_w)\mathrm{Z} \tag{6.17}$$

where ρ_b, ρ_w represent bulk and brine densities respectively and Z is the depth at which the aquifer is located.

$$\rho_b = \rho_r \emptyset \tag{6.18}$$

where ρ_r is the rock density and $\emptyset$ is the formation porosity.

From equations (6.16 - 6.18), the value of the injection rate for the model is set at 32 kg/s, which according to equation (6.16), results a pressure build-up value less than 1.5 magnitudes of the hydrostatic pressure. This value is far away from the average default values of the sustainable pressure (181% of the hydrostatic pressure gradient) reported for the Dundee Limestone in the Michigan Basin in USA, which is located at 1200 m depth (Zhou et al. 2008).

6.3. Methodology

Theoretically, CO_2 sequestration efficiency in saline aquifers can be assessed by calculating the efficiency storage factor, which refers to the volume fraction of the pores occupied by the injected CO_2:

$$E_{aq} = \frac{V_{CO_2}}{V_\emptyset} \tag{6.19}$$

V_{CO_2} is the volume of injected CO_2, which can be calculated from the known mass rate of the injected gas under the hydrostatic conditions of the formation. $V_\emptyset$ is the volume of the pores in the domain:

$$V_\emptyset = V_t \emptyset_t \tag{6.20}$$

where V_t and $\emptyset_t$ are the total volume and total porosity of the domain respectively.

To calculate the storage capacity in the research work, the modern equation developed by Szulczewski (2013) is employed:

$$E_{aq} = {G_{CO_2}}\Big/{\rho_g L_t W H \emptyset (1 - S_{wc})} \tag{6.21}$$

where G_{CO_2} is the total mass of the integrated CO_2, ρ_g is the density of CO_2 at hydrostatic conditions, $W,\ L_t, and\ H$ represent the width, total length and net thickness of the aquifer

respectively. ∅ defines the porosity of the rock and S_{wc} defines the connate (irriducable) water saturation.

This methodology has been implemented in because it accounts for the net thickness of the aquifer rather than the whole thickness. This can be justified by the fact that only the higher permeability layers are targeted by the injected gas (Szulczewski 2013).

This study aims to investigate the impact of heterogeneity, permeability, grid resolution and injection methodology on CO_2-water system mobility and the behaviour of the injected scrCO_2 at different time steps on the CO_2 storage capacity and efficiency at a field-scaled domain. An archetype of an actual field heterogeneity in a domain has been developed. The domain consists of three stratums of sands intermingled with two layers of low permeability shales, as illustrated in Figure 6.1. All petrophysical and simulation parameters are shown in Tables 6.1 and 6.2 respectively.

A series of simulation cases (presented in Table 6.3) were setup to demonstrate different models of a computational domain including homogeneous, uniform and non-uniform heterogeneous with coarse and fine grid resolutions. The simulation runs comprised two different employed schemes of injection (continuous and cyclic). The continuous injection scheme involved 30 years of continuous injection at a constant rate of 32 kg/s (about 1 million metric tons (MMT) per year) while in the second scenario, the injection period was implicated in three cycles of 10 years separated by two stopping periods of 5 years in between in order to ensure that structural trapping mechanism ends and other trapping mechanisms take their role before injecting a new cycle. Furthermore, three models with different values of vertical to horizontal permeability ratio (k_v/k_h) were developed along with other models to assess the influence of injection scope and orientation of the injection well on the flow behaviour and CO_2 sequestration efficiency. In all 14 cases, the total simulation time was 5000 years including injection and pausing times.

Table 6.3. Simulation cases and conditions.

Case No.	Domain	Heterogeneity And Layers thickness	Grid resolution	Nodes distribution (r, θ, z)	Permeability Ratio (k_v/k_h)	Injection Scheme (30 years)
Base-3D	homogeneous	N/A 1 x 96 m	coarse	(75, 4, 24)	1	vertical continuous into lower section
Base-2D	homogeneous	N/A 1 x 96 m	coarse	(75, 1, 24)	1	vertical continuous into lower section
1	homogeneous	N/A 1 x 96 m	coarse	(88, 1, 24)	1	vertical continuous into lower section
2	heterogeneous	Uniform 3 x 30 m 2 x 3 m	coarse	(88, 1, 24)	1	vertical Continuous into lower section
3	heterogeneous	Non-uniform 3 x 30 m 2 x variable	coarse	(88, 1, 24)	1	vertical continuous into lower section
4	heterogeneous	Non-uniform 3 x 30 m 2 x variable	coarse	(88, 1, 24)	1	Vertical batch* (10-5-10-5-10) into lower section
5	homogeneous	N/A 3 x 30 m 2 x variable	coarse	(88, 1, 24)	1	Vertical batch* (10-5-10-5-10) into lower section
6	homogeneous	N/A 3 x 30 m 2 x variable	Fine (+100%)	(176, 1, 48)	1	vertical continuous into lower section
7	homogeneous	N/A 3 x 30 m 2 x variable	coarse	(88, 1, 24)	1	vertical continuous into lower section
8	homogeneous	N/A 3 x 30 m 2 x variable	coarse	(88, 1, 24)	1	vertical continuous into whole thickness
9	homogeneous	N/A 3 x 30 m 2 x variable	coarse	(88, 1, 24)	0.1	vertical continuous into the whole thickness
10	homogeneous	N/A 3 x 30 m 2 x variable	coarse	(88, 1, 24)	0.01	vertical continuous into whole thickness 96 m**
11	homogeneous	N/A 3 x 30 m 2 x variable	coarse	(88, 1, 24)	0.01	horizontal continuous 96 m**
12	homogeneous	N/A 3 x 30 m 2 x variable	coarse	(88, 1, 24)	0.01	horizontal Continuous 192 m**

*** Batch injection schemes refer to the years of (injection – stop – injection – stop – injection).**
**** Width of the injection well maintaining constant injection rate.**

As the permanent sequestration of the injected CO_2 is the focus of this work, a new term of permanent sequestration factor of the aquifer (E_{aq}^{perm}) has been introduced. This factor is calculated from the numerical simulation results by STOMP-CO_2 code (White et al. 2013) and compared for different cases under different conditions through various time scales.

Due to the density difference between the injected CO_2 and the existing brine (i. e. gravity driving forces), initially the former fluid percolates upward to be physically trapped under the upper impervious layer (caprock). During this time, part of the gas dissolves in the existing brine to form an aqueous phase rich of CO_2 which is heavier than the ambient liquid and hence sinks down to settle at the bottom of the aquifer. As soon as the injection stops the replaced brine invades the domain to reinstate the CO_2 leaving some traces of it behind in some small-sized pores in a process called residual or capillary trapping. These amounts of CO_2 are determined by the simulation code for different cases and utilized to calculate the capacity and efficiency of the simulated aquifer. The latter values are used to calculate the sequestration efficiency by;

Total integrated CO_2 = Integrated aqueous CO_2 (CO_2^{aq}) + Integrated gas CO_2 (CO_2^{g}) (6.22)

Integrated gas CO_2^{g} = Trapped gas CO_2 (CO_2^{gt})+ Free gas CO_2 (CO_2^{gf}) (6.23)

$$E_{aq}^{perm} = \frac{CO_2^{aq}+(CO_2^{gt})}{\rho_g L_t W H \emptyset (1-S_{wc})} \quad (6.24)$$

where all parameters were explained in equation (6.21).

Because the system was assumed to be boundless with no pressure build-up concern, most of the integrated free gas is subject to migrate away from the injection well along the overlapping layer and small amount of it may sweep out of the domain through any existing fractures or faults in the overlaying caprock. Therefore, in this work the focus is on the storage efficiency of the aquifer in terms of the permanent sequestration of the injected CO_2, which occurs mainly through solubility and residual trapping mechanisms due to the insignificant influence of the mineral trapping mechanism before few thousands of years according to De Silva and Ranjith (2012).

6.4. Results and Discussions

Injecting scCO2 into a brine-saturated porous formation produces spatial distribution maps of both fluids. Figure 6.2 illustrates the integrated gas saturation maps and spatial distribution of the aqueous CO_2 mass fraction within the 3D cylindrical model of the simulated domain at different time scales. It is apparently shown that soon after injection, the gas bounces upward due to the density difference between the two fluids and simultaneously migrates crossway due the pressure gradient between the injected scrCO_2 and the in situ hydrostatic pressure. During this drift, some of the injected gas disperse into the existed brine producing a CO_2-saturated aqueous phase that is heavier than the pure brine and consequently tends to sink down towards the bottom of the domain forming a fingered structure as displayed in Figure 6.2(right).

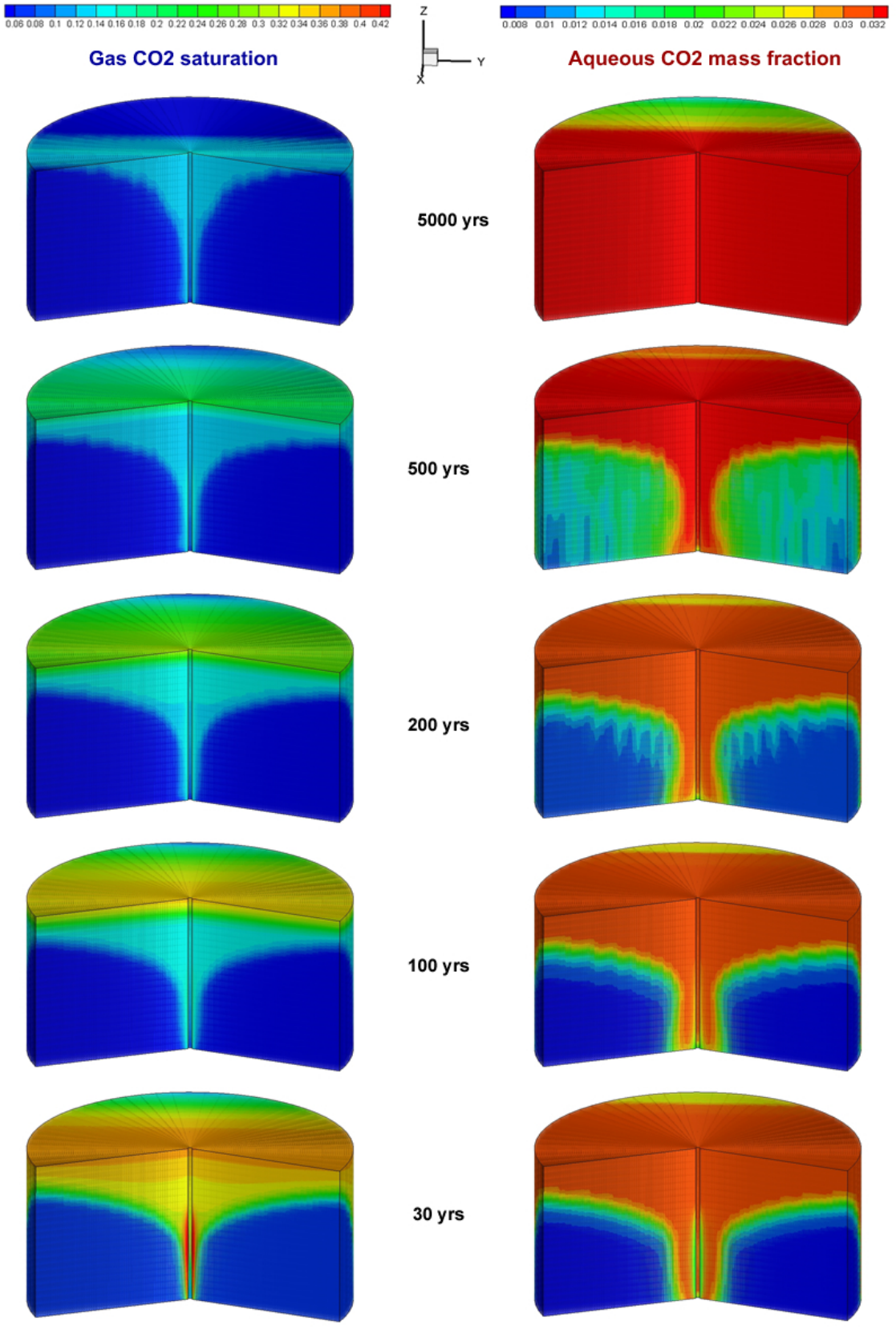

Figure 6.2. Gas saturation and aqueous CO_2 mass fraction contours for a 3D model at different time

6.4.1. CO_2 Mobility and Behaviour

Due to the density difference between the injected gas and the hosted brine, the buoyancy forces initially dominates the water-CO_2 flow system. The injected scrCO_2 displaces the existing brine soon after the injection starts and the gas moves upwards to be physically trapped under the overlaying impermeable layer (caprock). The flow system involves interfacial contact between the two fluids that results in considerable amounts of the free CO_2 gas tend to dissolve in the accommodated brine representing the solubility trapping mechanism. This is in addition to the amount of the gas that is trapped because of the capillarity and interfacial forces between the pore surface and the percolating gas. The impact of these three trapping mechanisms (structural, solubility and residual) in different types of domains can be noticed in Figure 6.3(a, c, d). The profiles demonstrate sharp decline in the integrated free-gas trends accompanied with the significant increase in the trends of the dissolved and trapped CO_2 after the cease of injection.

Simultaneously, the results show limited traces of CO_2 trapped in the locale even during the injection lifetime due to the injection pressure that forces some drops of the gas into some small-sized pores. However, these amounts are insignificant and further subject to be snapped off by the invading brine during imbibition. The actual capillary trapping is noticeable only after the gas injection stops as evidenced in Figure 6.3(b). As soon as the injection ceases after 30 years, the residual trapping mechanism dominates when the replaced brine invades back the domain to sweep the integrated gas out of the pores. During this process, traces of the CO_2 get detached from the trailing part of the gas plume and pierce into the small-sized pores due to the capillary forces as evidenced by the sharp increase in the trapped CO_2 trends in Figure 6.3 for all modelled domains.

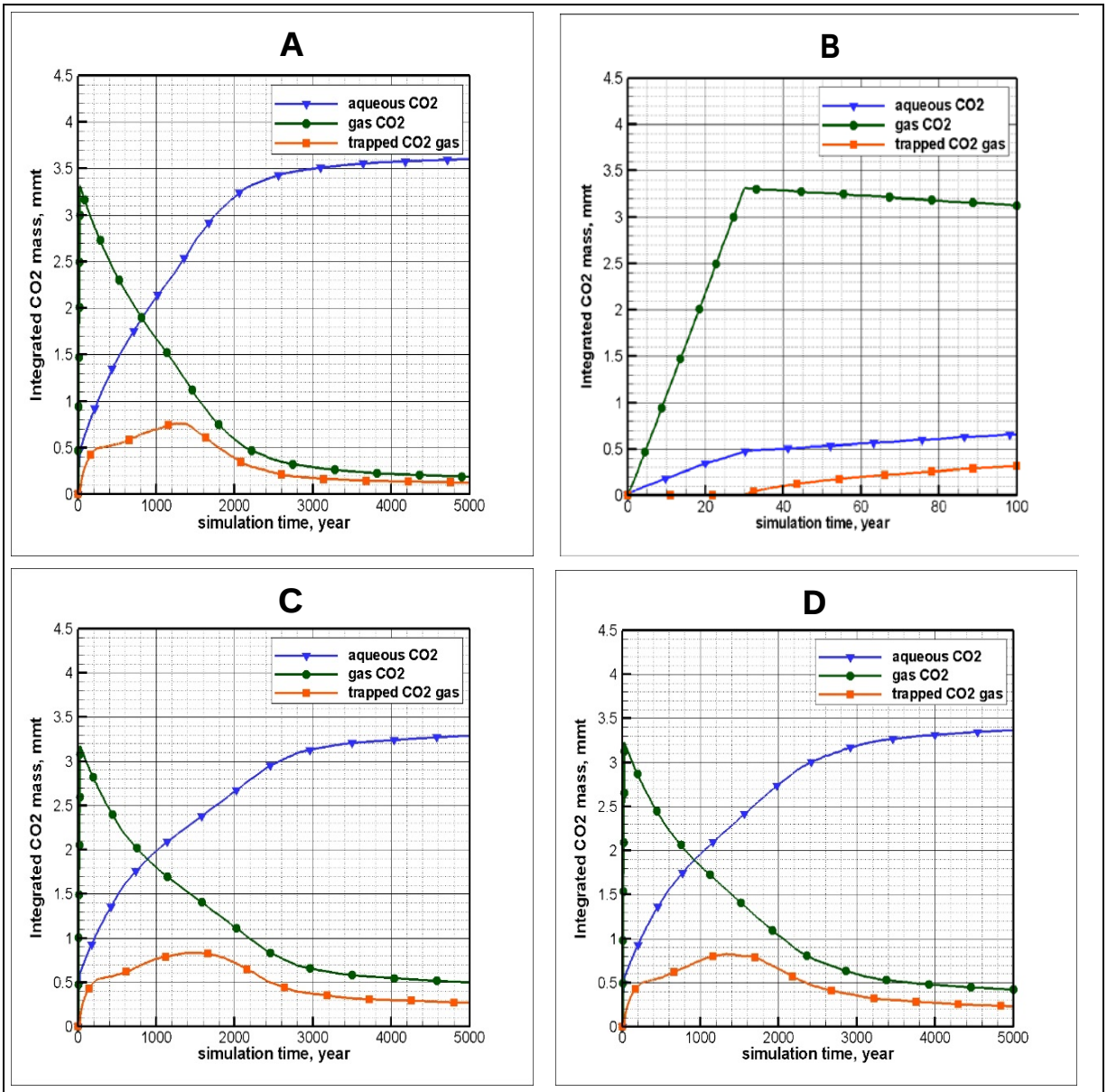

Figure 6.3. Comparision of integrated CO_2 profiles in:

(A-B) homogeneous porous domain (case 1). B is a magnified plot of A.

(C) uniform-heterogeneous domain (case 2)

(D) nonuniform-heterogeneous domain (case 3)

Displayed trends in Figure 6.4(a) exhibit that after 100 years, ~74% of the injected scrCO$_2$ was structurally trapped as a free integrated gas in the homogeneous domain. ~17.5% of the injected CO$_2$ was dissolved in brine and the rest 8% was residually trapped in small-sized pores due to the capillarity. For the heterogeneous model in Figure 6.4(b) on the other hand, it has been observed that ~70% of the injected gas was trapped as a free gas, 20.49% was dissolved in the brine while 9.4% was disconnected from the plume trailing edge and adhered to the rock surface inside some small-sized pores due to the surface tension forces.

The findings from this study has shown that under similar hydrostatic conditions and petrophysical characteristics, homogeneous formations promote more CO$_2$ dissolution owing to the fact that under the same hydraulic gradient, fluid flows faster in homogeneous porous media compared to that in heterogeneous porous medium which limits fluid seepage, which is consistent with some previously published studies (example; Alabi 2011; Zhao et al. 2014). This fast migration induces more contact with fresh brine leading to higher dissolution rates of CO$_2$. This can be evidently seen in Figure 6.4(a-b), which shows that only 1.7% of the injected CO$_2$ was left as a free gas in the homogeneous model at the end of the simulation compared to the heterogeneous case in which more than 6% of free gas was recorded.

The timing maps of CO$_2$ sequestration by each trapping mechanism are depicted in Figure 6.4 for homogeneous and heterogeneous formations. It can be verified from the figure that during early hundreds of years the structural trapping mechanism dominates while after thousands of years the solubility trapping becomes the dominant mechanism. The maximum amount of CO$_2$ is residually trapped at about 1000 years and declines later because some of it dissolves into the surrounding brine to form weak carbonic acid that reacts with the rock material and precipitate as solid carbonates after few thousands of years.

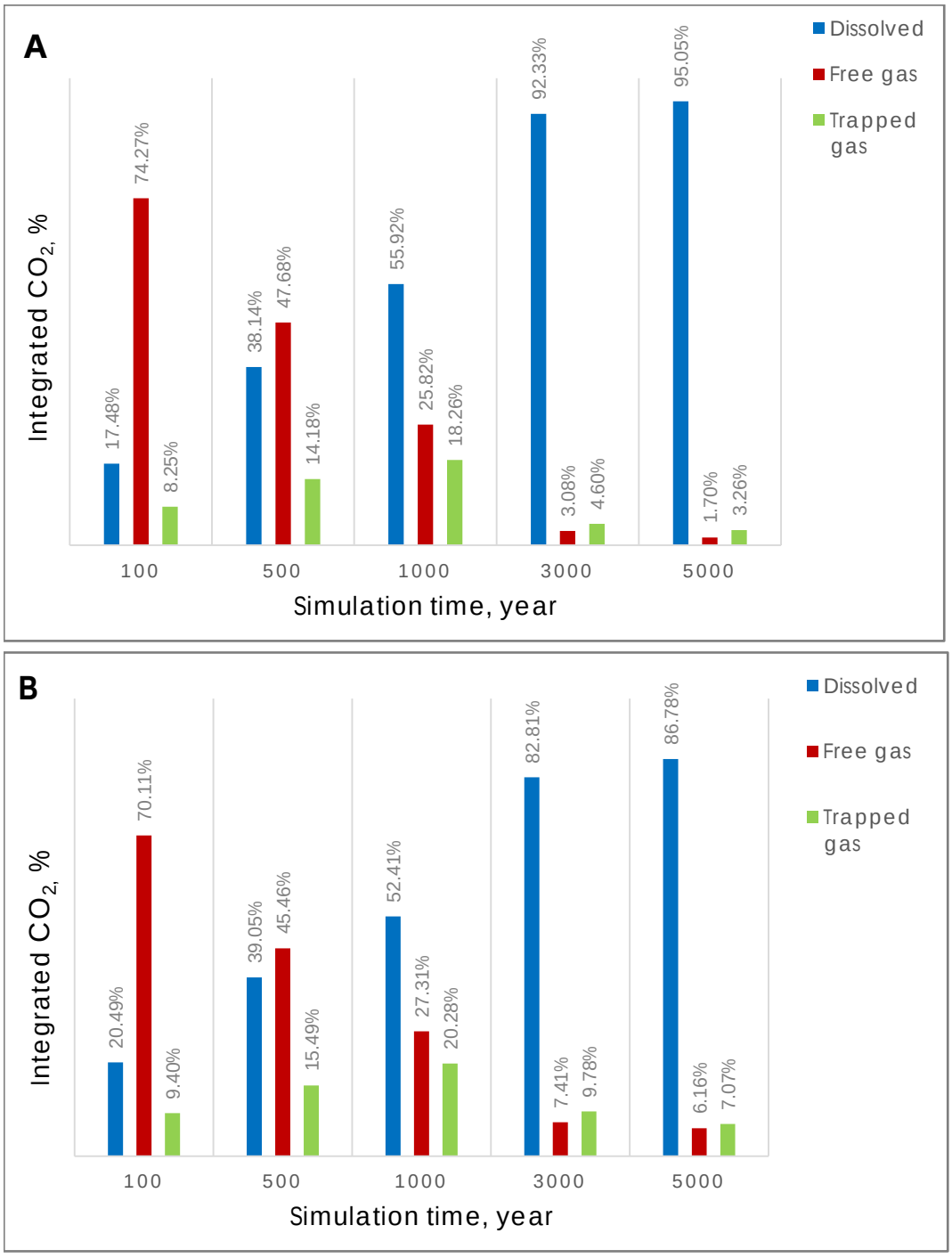

Figure 6.4. Various phases of integrated CO_2 trends in:
(A) a homogeneous porous domain (case 1), (B) a heterogeneous domain (case 2).

6.4.2. Impact of Heterogeneity

To investigate the impact of different types of heterogeneity (Uniform and Non-uniform) on the propagation of CO_2 profiles, P_c - S_w relationships and storage efficiency, three numerical cases namely 1, 2 and 3 with their employed conditions illustrated in Table 6.3, have been developed and implemented in this study. It is a fact that the permeability of geological formations is strongly dependent on their porosity and heterogeneity, and plays a key role in understanding water-CO_2 flow in the subsurface. This influence is clearly exposed in Figure 6.5, which demonstrates different maps of gas distribution in the modelled domains. The achieved maps depict that the homogeneous domain has produced sharp-edged contours while the heterogeneous media resulted in irregular edges exposing more contact surface area between the CO_2 and the local brine, which enhances the storage efficiency (see Figure 6.8). The irregular frontages in the heterogeneous media are due to the intermingled layers of shale that restrict the injected gas from moving across different layers of the domain that results in less contact with the ambient brine and less subjectivity to entrapment in more small-sized pores.

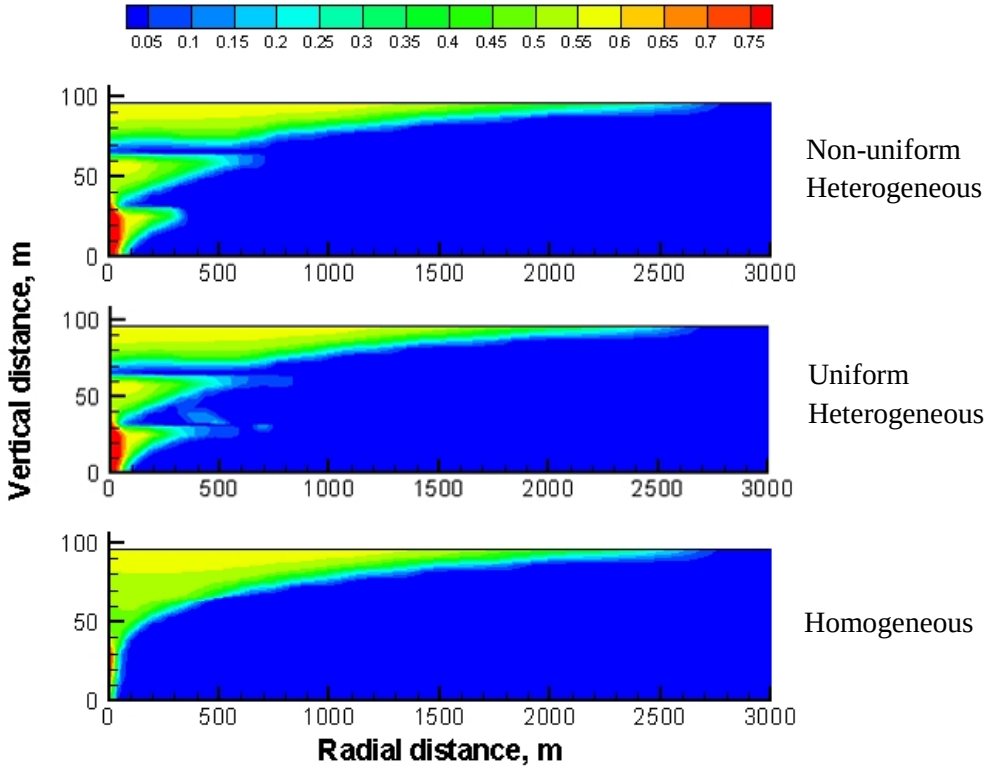

Figure 6.5. Spatial distribution of CO_2 after 30 years of simulation (end of injection) for homogeneous media (case 1) and heterogeneous media (cases 2 and 3)

Heterogeneity is found to have substantial impact on capillary pressure-saturation relationship as illustrated in Figure 6.6(a), which significantly demonstrates higher values of capillary pressure for both heterogeneous models. This is directly imitated on an increase in the amount of the residually trapped CO_2 as presented in Figure 6.6(b). It is also shown in the figure that uniform-heterogeneous media produced slightly larger values of capillary pressure at all values of water saturation, which contributes in larger amounts of trapped CO_2 that leads to higher

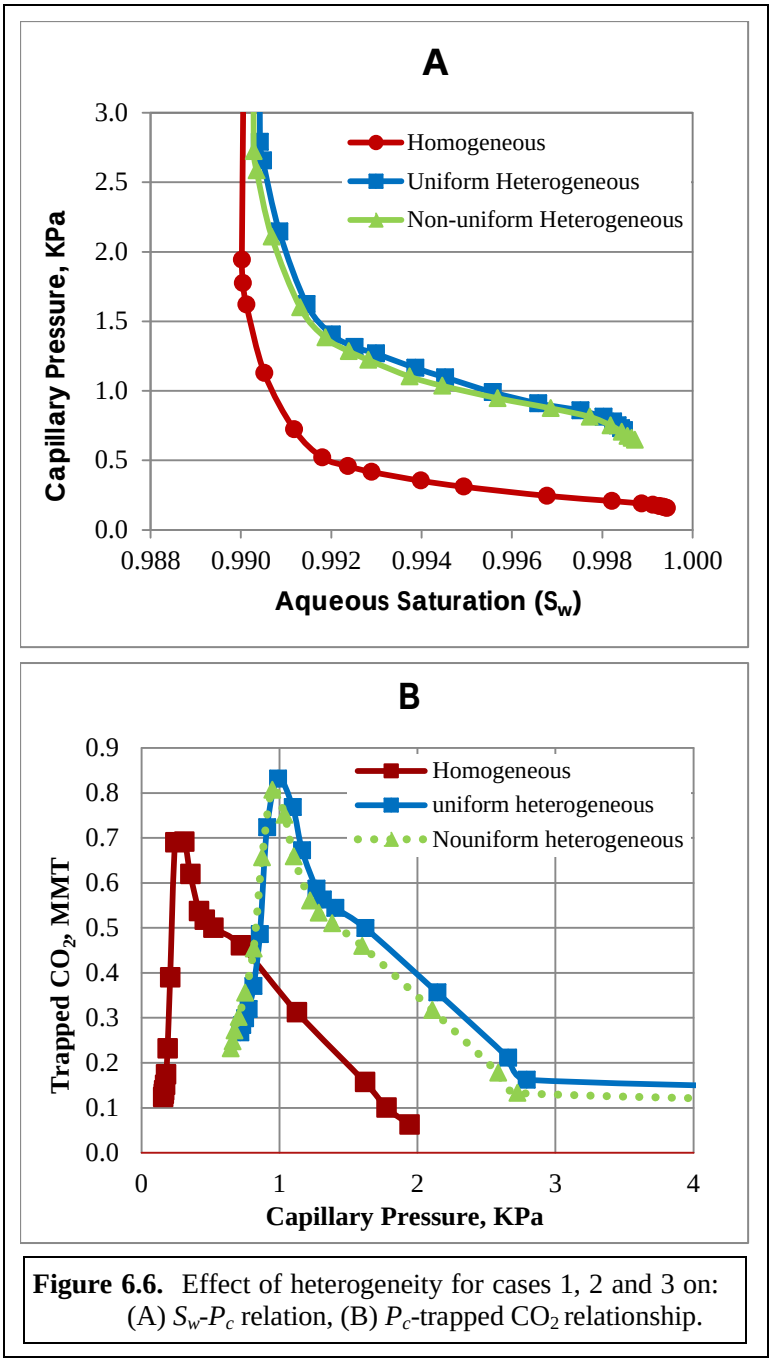

Figure 6.6. Effect of heterogeneity for cases 1, 2 and 3 on: (A) S_w-P_c relation, (B) P_c-trapped CO_2 relationship.

storage capacity and efficiency of the aquifer.

Figure 6.7(a) shows that soon after gas injection stops (i.e. imbibition process starts), the amount of the trapped gas sharply increases when the replaced brine invades back the domain and isolate some blobs of CO_2 from the trailing edge of the mobile CO_2 plume. After 200 years, this progress slightly retards because part of the trapped gas tends to dissolve in the brine. This increase continues until 1400 years of simulation when the trapped gas profiles steeply decline before tending to settle after 3000 years. The figure further demonstrates more residually trapped gas in the heterogeneous models compared to the homogeneous one at the end of the simulation.

In contrast to the results by Chasset et al. (2011), the increase in CO_2 dissolution can be justified by the presence of intermingled layers of shale that play as internal barriers to retard the vertical migration and promote lateral flow of the injected CO_2. However, this horizontal movement retards after injection period due to the limited hydraulic gradient which limits gas contact with more fresh brine leading to reduction in gas assimilation and dissolution. The values of trapped and dissolved CO_2 surely affect the storage capacity of the site however, this impact is applicable to a very limited extent in agreement to the results from a recent study by Zhao et al. (2014) which, reveals that strong heterogeneity in geological formations reduces the storage capacity because it limits gas seepage.

In Figure 6.7(b), no effect of heterogeneity on CO_2 solubility has been detected before 800 years of simulation because the system was totally dominated by buoyancy and hydrostatic forces. Afterward, it was observed that more CO_2 dissolved in the homogeneous domain compared to both types of heterogeneous ones by ~17% after 2000 years. However, this influence declined after 4000 years to ~9%. It is apparent from the results displayed in Figure 6.7(b) that both types of heterogeneity provide almost identical but lower trends of dissolved CO_2 compared to the homogeneous media throughout the simulation time. This evidences that gas migration is more straightforward through homogeneous media owing to the lesser resistance to flow.

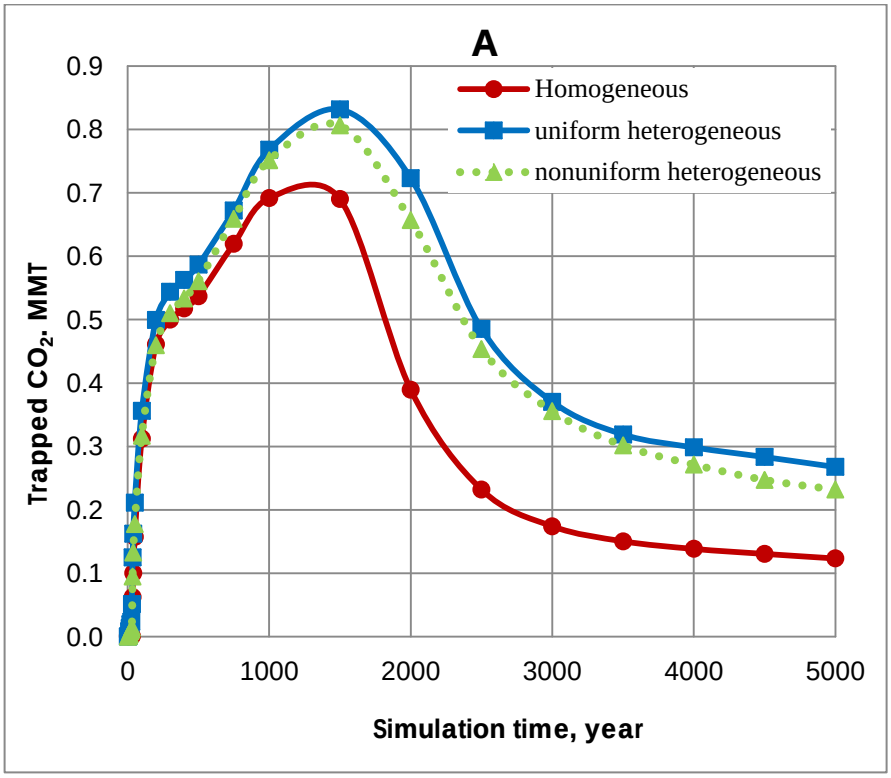

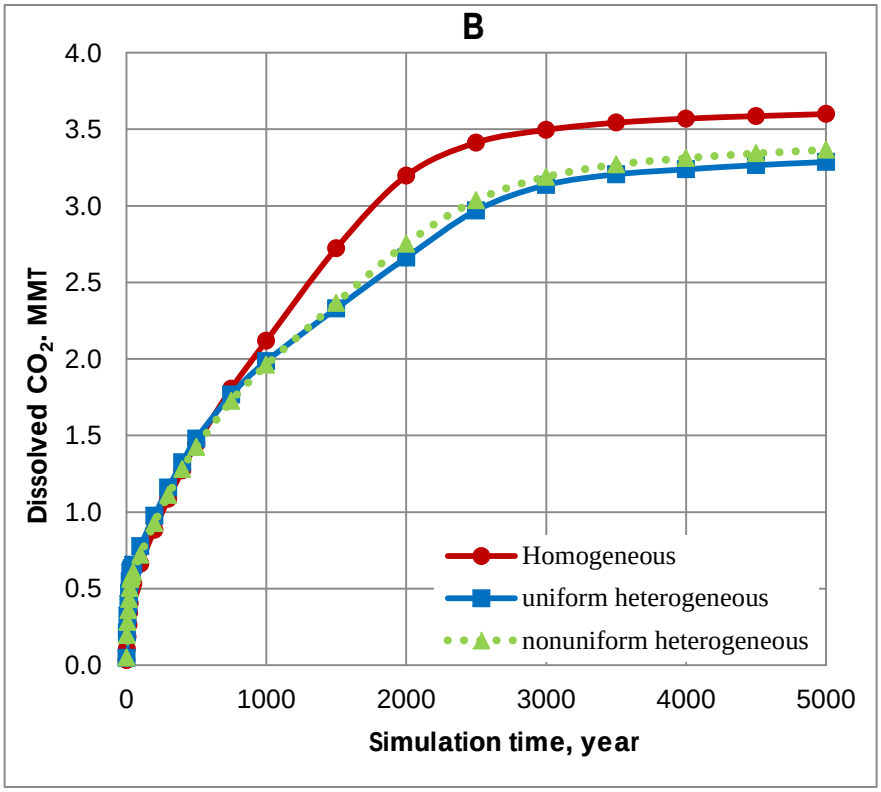

Figure 6.7. Effect of heterogeneity for cases 1, 2 and 3 on: (A) CO_2 residual trapping, (B) dissolved CO_2

In spite of the two contrary trends, Figure 6.8 shows that heterogeneous domains are more efficient in storing the disposed gas by about 15% compared to the homogeneous ones under similar conditions. This does not comply with the numerical results depicted in Figure 6.4 that shows higher values of free-gas CO_2 left off by the end of simulation in the homogenous domain compared to the heterogeneous one. This controversy is due to the net thickness parameter suggested by Szulczewski (2013) for equation 6.21 instead of the total thickness of the modelled domain. To implement this in our calculations, the thickness of the shale layers were excluded and this resulted in less values of the net thickness in cases 2 and 3 (see Table 6.3) leading to smaller pore volume available to store the injected CO_2 and consequently higher values of storage efficiency were achieved for the heterogeneous domains using equation 6.21. This is an important point that needs further investigation to assess the effectiveness of this method to more accurately determine the storage efficiency in open-boundary domains.

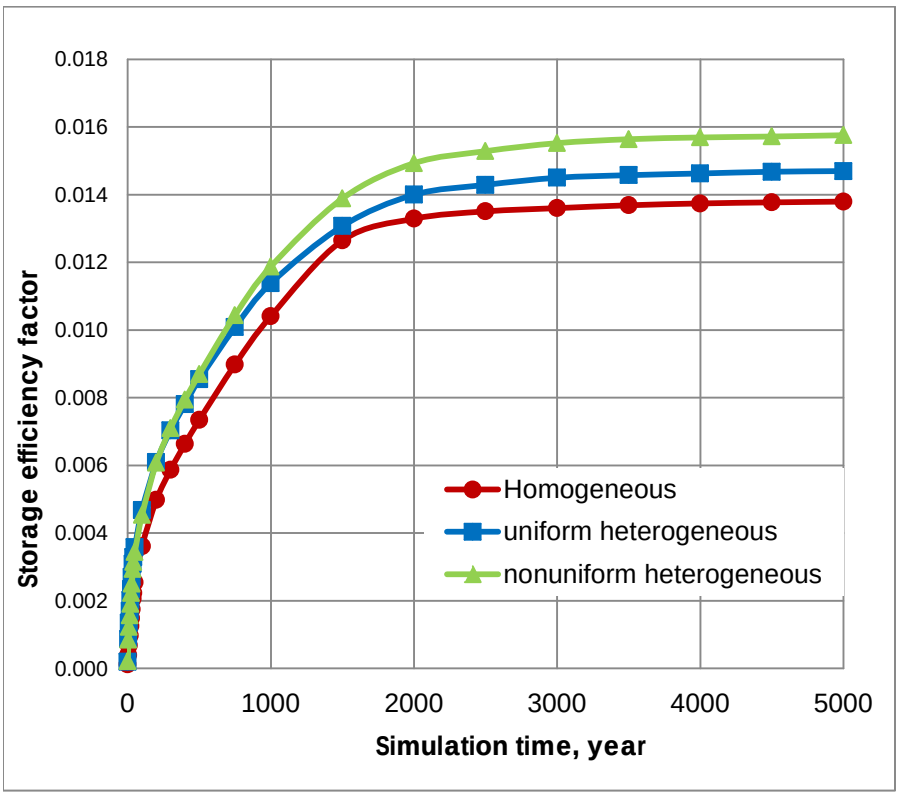

Figure 6.8. Influence of heterogeneity on storage efficiency factor. cases 1, 2 and 3 in Table 6.3.

6.4.3. Effects of Cyclic Injection on CO_2 Mobility and Sequestration

Saturation (S_w) – relative permeability (k_r) relationship is a key feature that describes CO_2-water flow system because it has a huge influence on the behaviour and fate of the injected gas in the subsurface. This study has investigated the impact of the injection methodology on the S_w-k_r relationships and eventually on the effectiveness of the disposed gas storage. Purposely, an observation point was setup at 200 m radially away from the injection well (to avoid the effect of the high pressure difference forces close to the wellbore) and 15 m from the bottom of the aquifer, which represents the midpoint of the lower segment of the domain into which the gas injection takes place.

The achieved results from implementing cyclic injection techniques are demonstrated in Figure 6.9(a) that manifest the development of gas relative permeability profiles for continuous and cyclic injection methods (see cases 3 and 4 in Table 6.3). The influence of the cyclic injection is obvious from the fluctuating profiles from which it can be observed that for the continuous injection method, the relative permeability of CO_2 curve was declined from a peak value of (0.43) after 10 years to zero by the end of the injection period (30 years). The figure further displays the three cycles of injection impact on the permeability curves with highest peak values of (0.43, 0.66 and 0.7). This impact has been directly imitated on the gas saturation trends in Figure 6.9(b), which evidences the favourite of cyclic injection method because higher amounts of injected CO_2 were found to be safely trapped after the cease of injection. This is comparable to the continuous injection case, which depicts higher values of gas saturation after the end of injection, however, these values decline soon after that to reach a value of (0.01) after 2000 years of simulation (this is not shown on Figure 6.9 which is magnified to show more details about the drainage period). This variation can be justified by the two additional cycles of imbibition process that lead to more blobs of CO_2 get disconnected from the trailing edge of the ascending gas plume.

Gas distribution contours after 100 years of simulation in Figure 6.10(a-b) display almost equal maps of carbon dioxide distribution in the homogeneous domain for both continuous and cyclic injection. However, the impact of the injection scenario is more obvious in the maps of the heterogeneous model in Figure 6.10(c-d), which shows more spread out of the injected gas in the lower and middle segments of the domain. This spread out escalates the interfacial area between the integrated gas and the ambient brine for more consequent CO_2 dissolution.

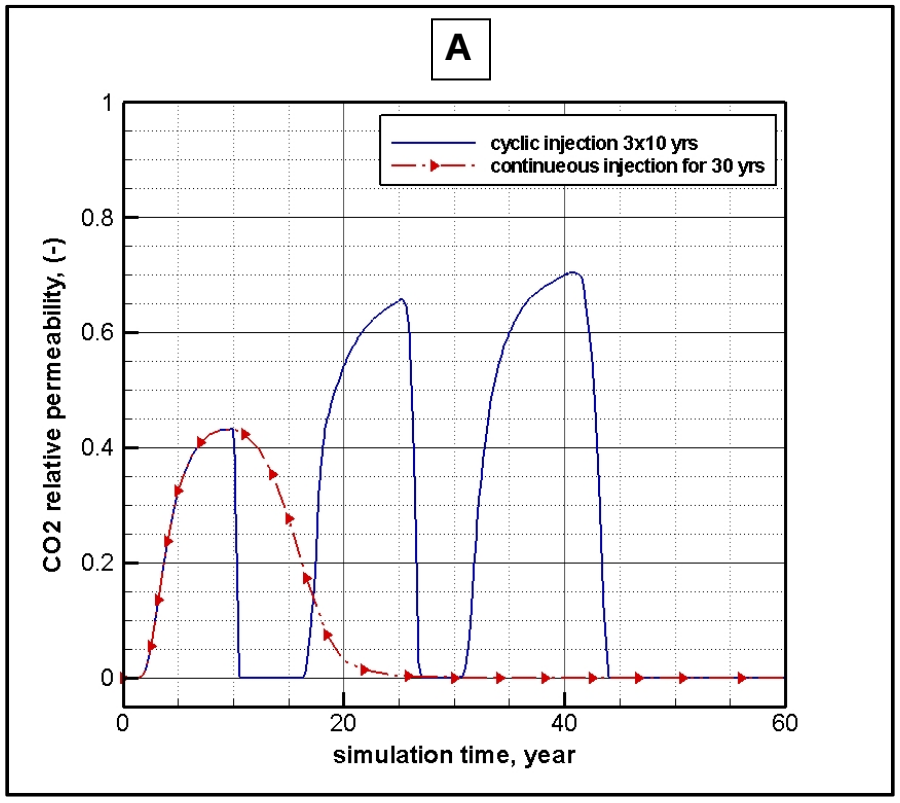

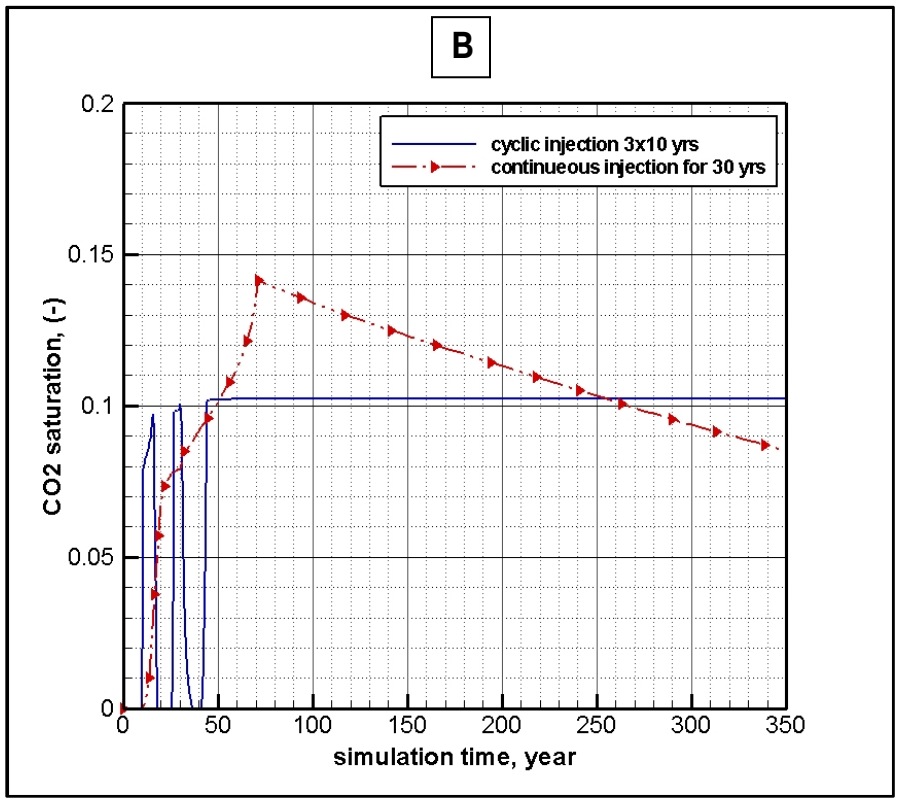

Figure 6.9. Impact of cyclic injection for cases 3 and 4 in Table 6.3 on: (A) CO_2 relative permeabilty, (B) CO_2 saturation.

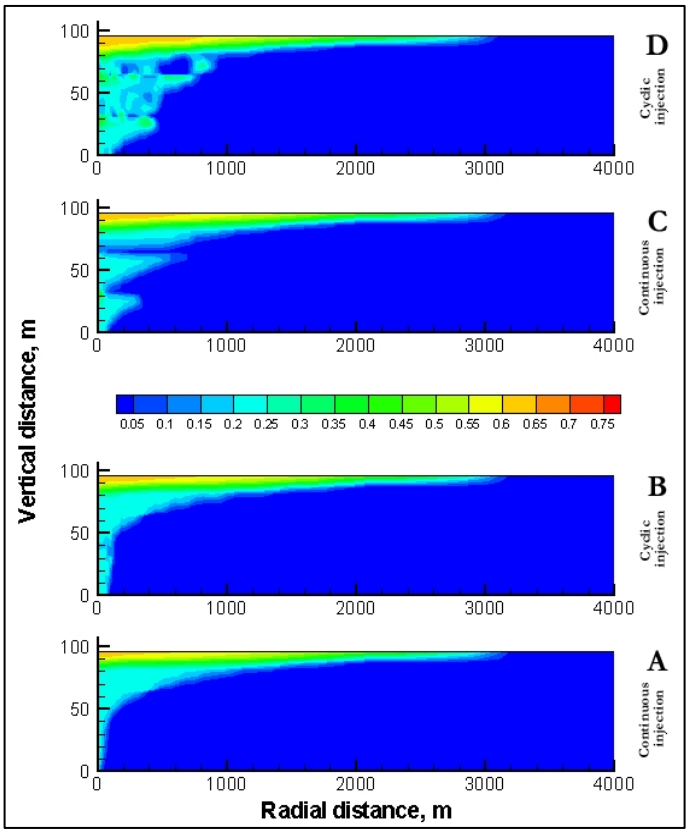

Figure 6.10. Effect of cyclic injection on CO_2 distribution after 100 years of simulation. (A-B) for the homogeneous domain (cases 1 and 5) and (C-D) for the heterogeneous domain (cases 3 and 4).

For the homogeneous models (see cases 1 and 5 in Table 6.3), cyclic injection has confirmed no effect on CO_2 dissolution and almost equal amounts of free gas left off in the domain by the end of the simulation runs as shown Figure 6.11. However, for the heterogeneous domains (cases 3 and 4), continuous injection produced slightly greater profiles of CO_2 dissolution.

In contrast, residual trapping of CO_2 in heterogeneous media was found to be more sensitive to the cyclic injection because the simulation results revealed that more CO_2 was trapped using cyclic injection method in the heterogeneous modelled domain compared to the continuous one specifically after 5000 years as illustrated in Figure 6.12.

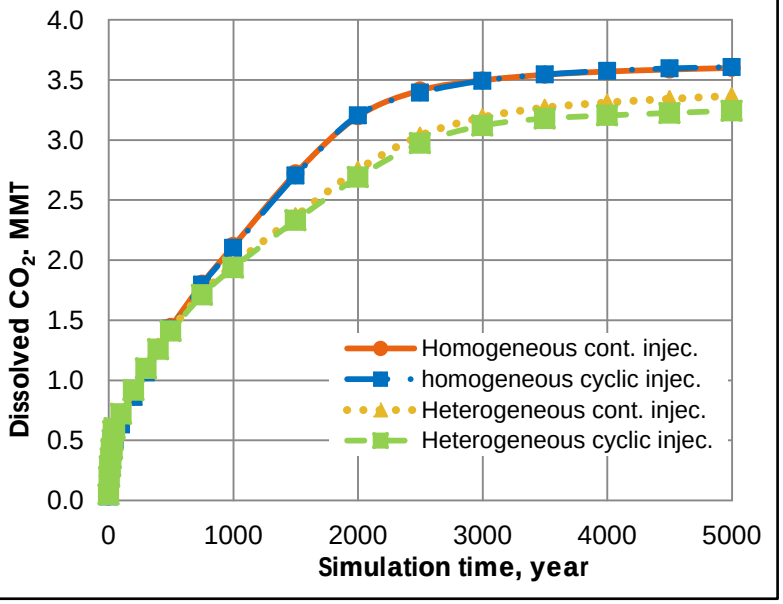

Figure 6.11. Effect of injection scheme on CO_2 dissolution in homogeneous and heterogeneous aquifers. Cases 1, 5, 3 and 4 respectively.

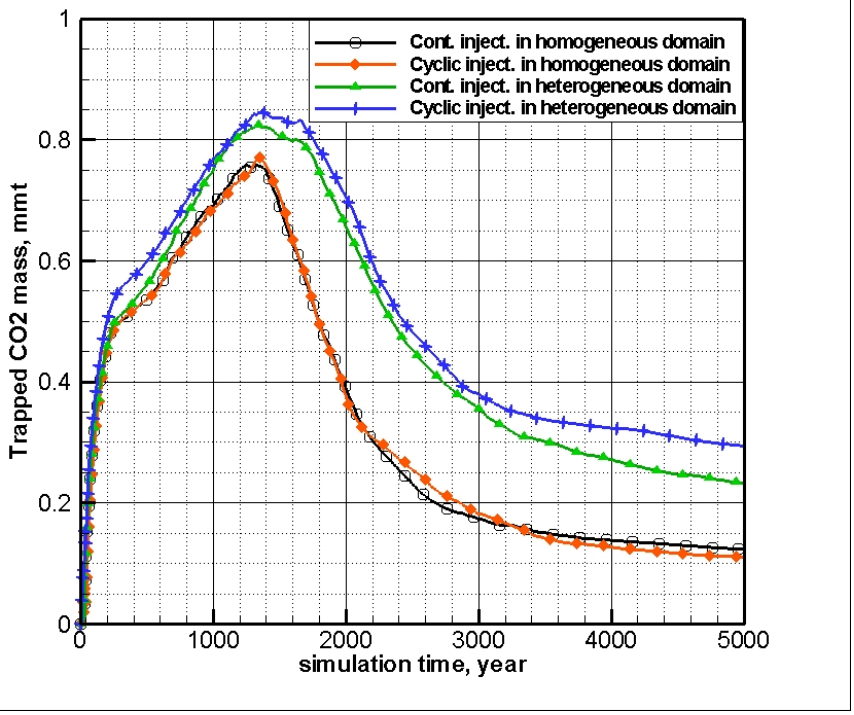

Figure 6.12. Impact of cyclic injection on residual trapping of CO_2 in DSAs for cases 1, 5, 3 and 4 respectively.

Table 6.4 concludes that cyclic injection into homogeneous domains increases the amount of trapped CO_2 gas to some extent (compare cases 1 and 5). However, continuous injection into heterogeneous formations enhances the storage efficiency factor (determined by equation 6.21) by about 0.0003 that represents 1.7% (compare cases 3 and 4), because it can be noticed from the table that by applying continuous injection (case 3), 0.773 MMT (approximately 0.17%) more of the injected gas was permanently sequestered either by residual or solubility sequestration mechanism using continuous injection techniques. This effect can be further noticed in Figure 6.13, which evidently shows the greater influence of the cyclic injection into heterogeneous media. In agreement with the results by Juanes et al. (2006), this can be justified by the increase in capillary pressure which forces more CO_2 into smaller-sized pores to be trapped and exposed to dissolution in the brine at later stages of storage. In contrary for the cyclic injection, releasing pressure after 10 years encourages the gas plume to percolate upwards through larger pores to accumulate at the top of the domain as a free gas.

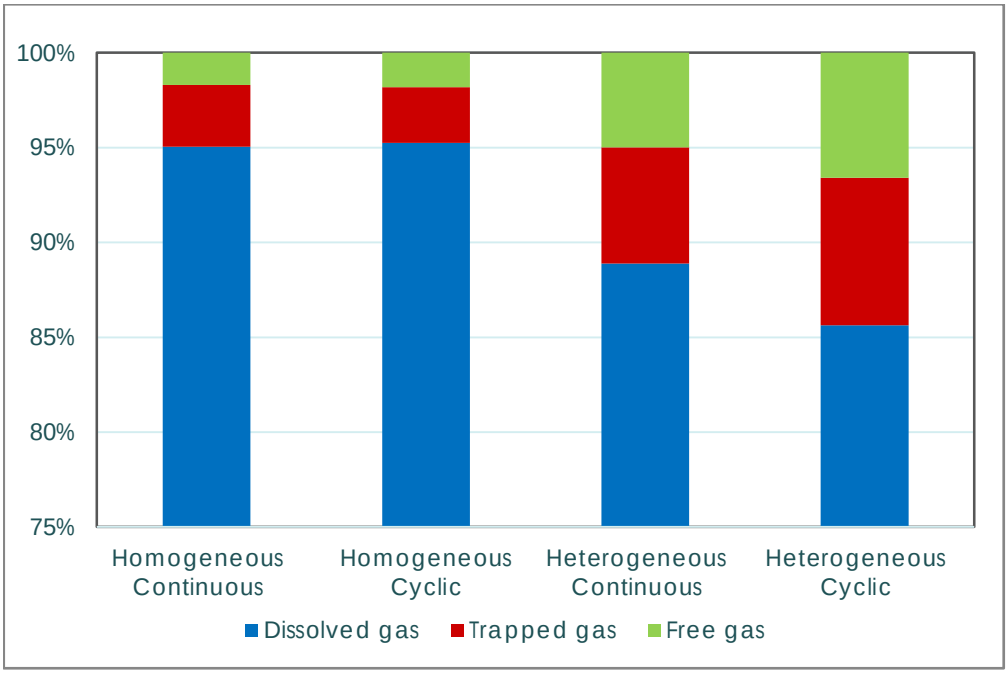

Figure 6.13. Impact of cyclic injection on different integrated CO_2 phases after 5000 years for cases 1, 5, 3 and 4 respectively.

Table 6.4. Simulation results and calculated efficiency factor for all cases.

Case No.	Description	Dissolved Gas MMT**	Trapped Gas MMT**	Free Gas MMT**	Storage Efficiency Factor
1	Homogeneous Isotropic Coarse grid, Cont. Vert. inj. Into lower section	28.795	0.986	0.514	0.013794
2	Regular Heterogeneous Isotropic Coarse grid, Cont. Vert. inj. Into lower section	26.290	2.140	1.865	0.0147
3	Irregular Heterogeneous Isotropic Coarse grid Cont. Vert. inj. Into lower section	26.929	1.854	1.512	0.0158
4	Irregular Heterogeneous Isotropic Coarse grid Cyclic Vert. inj. Into lower section	25.941	2.355	1.999	0.0155
5	Homogeneous Isotropic Coarse grid Cyclic. Vert. inj. Into lower section	28.858	0.886	0.551	0.013776
6	Homogeneous Isotropic Fine grid Cont. Vert. Inj. Into lower section	29.161	0.637	0.497	0.0138
7	Homogeneous Isotropic Coarse grid Cont. Vert. inj. Into lower section	28.147	1.282	0.866	0.0136
8	Homogeneous Isotropic Coarse grid Cont. Vert. inj. Into whole thickness	28.240	1.217	0.838	0.0136
9	Homogeneous Anisotropic Coarse grid Cont. Vert. inj. Into lower section	26.190	2.360	1.745	0.0132
10	Homogeneous Anisotropic Coarse grid Cont. inj. Vertical inj. well 96 m	21.367	4.699	4.230	0.0120
11	Homogeneous Anisotropic Coarse grid Cont. inj. Horiz. well, 96 m*	18.787	6.977	4.532	0.0119
12	Homogeneous Anisotropic Coarse grid Cont. inj. Horiz. inj. well 192 m*	19.885	5.167	5.244	0.0116

*** Horizontal injection well located at the bottom of the domain starting from the centre point.**
**** MMT= million metric ton (10^9 kg)**

6.4.4. Effect of Vertical Injection Scope

This section extends a previous work (Kudaida and Das, 2014) to further optimize the vertical injection method with the aim to investigate the storage efficiency enhancement. To carry out this, two simulation cases were conducted implementing two different scopes of vertical injection (see cases 7 and 8 in Table 6.3). In case 7, scrCO$_2$ was injected into the lower segment of the aquifer through four vertical grid cells of 4 m while for case 8, the injection was executed overall 24 blocks (i. e. over the whole thickness of the aquifer that extends to 96 m).

Looking at the dissolution contours of the injected scrCO$_2$ (i.e. aqueous CO$_2$ mass fraction maps) in Figure 6.14, unexpectedly no significant effect can be observed at all-time scales. On the other hand, Figure 6.15 demonstrates slightly more trapped gas concentrations within the vicinity of the injection well at all time steps for case 7. This is because the whole amount of the gas was injected through the lower segment of the domain, most of which was influenced by the reversing brine tendency to disconnect more blobs of CO$_2$ from the rambling edge of the gas plume. In contrast, when the injection applied into the whole thickness of the domain (case 8), only sixth of the scrCO$_2$ mass rate was injected into the lower section of the model and most of this amount had bounced upwards before the imbibition process started. This means that only a significantly small part of the injected gas was affected by the raiding brine leading to reduced trapped gas.

It is evidenced from the achieved results that injecting CO$_2$ through the whole thickness of the domain slightly reduced the amount of the free gas left within the domain in medium-terms of storage by 0.028 MMT (~ 3.2%) as depicted in Table 6.4 and illustrated in Figure 6.16. However, the injection scope has shown no sensible influence on the storage efficiency because both cases returned almost identical values of storage efficiency factor as presented in Table 6.4 and produced similar trends through the timeline of the simulation as displayed in Figure 6.17.

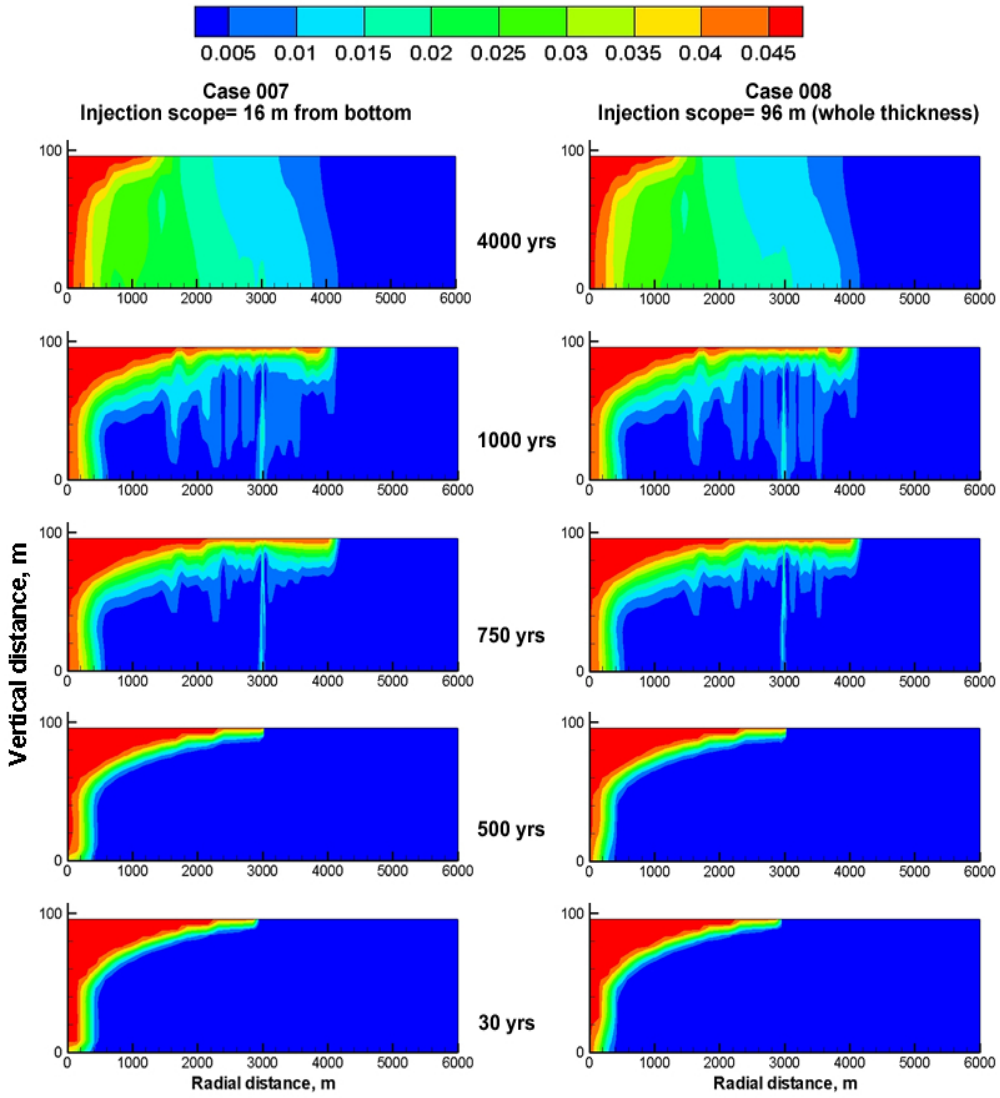

Figure 6.14. Impact of injection scope on aqueous CO_2 mass.

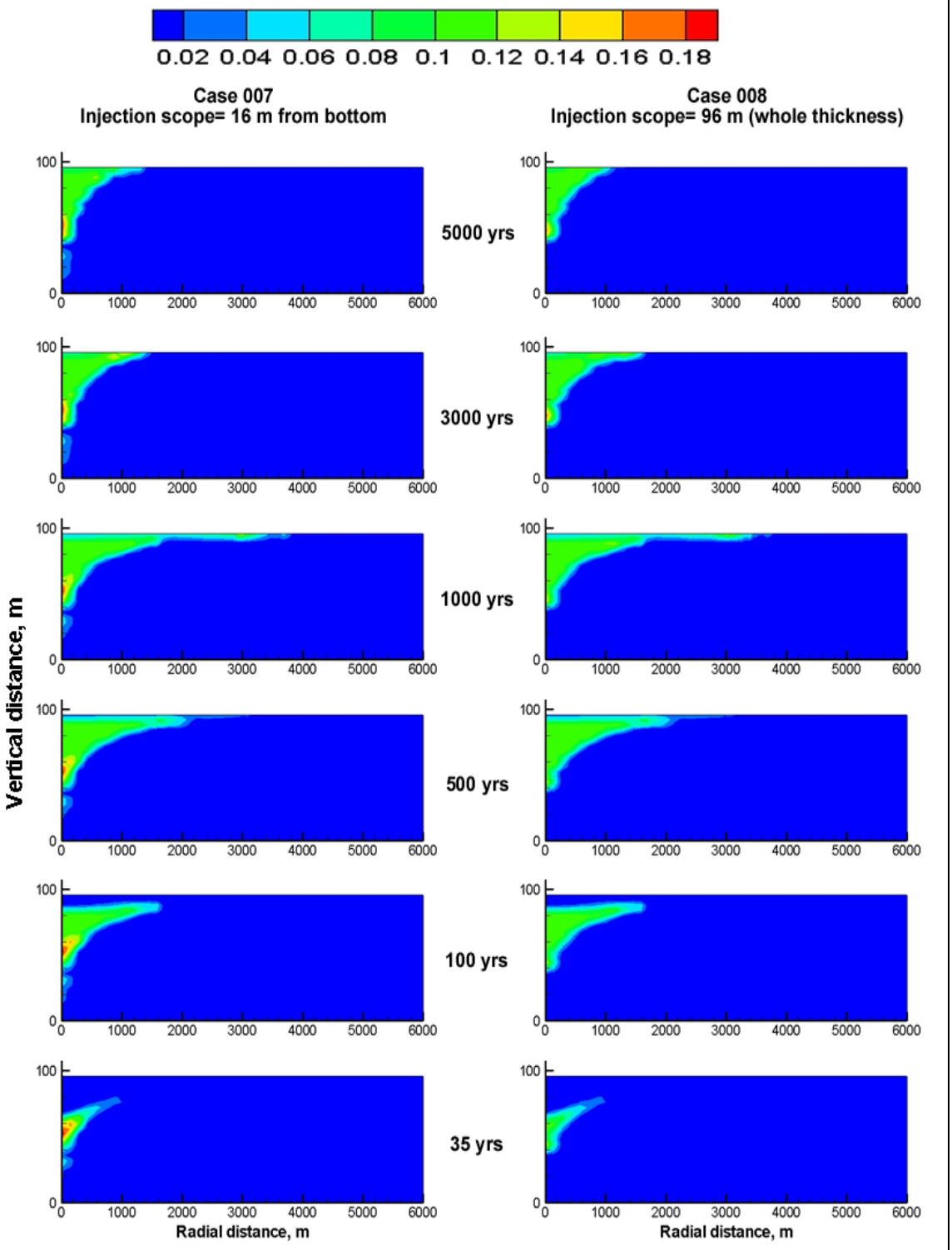

Figure 6.15. Impact of injection scope on trapped CO_2 mass distribution

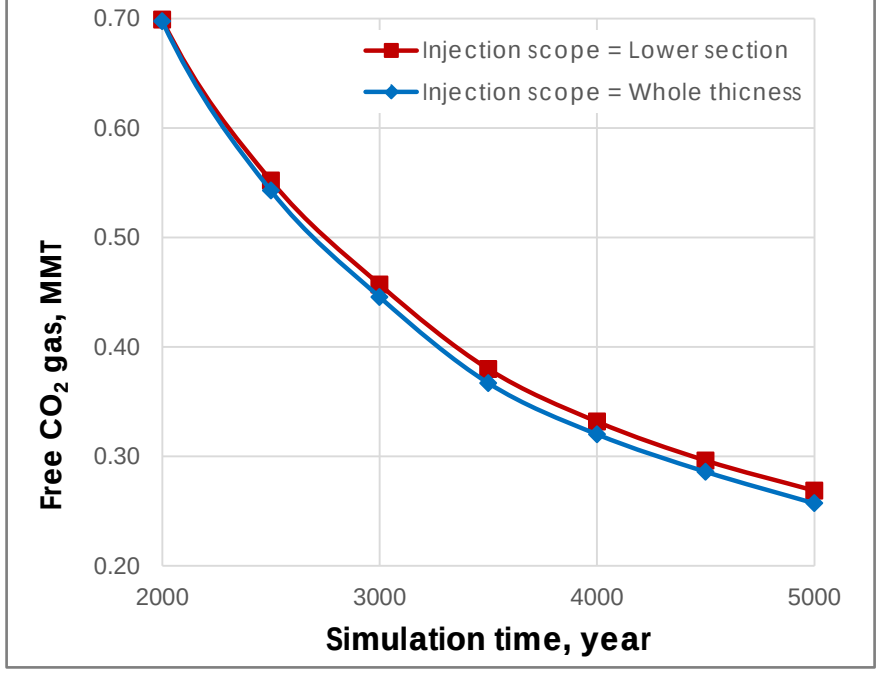

Figure 6.16. Free CO_2 gas mass rate as an impact of injection scope in a homogenous computational domain. Cases 7 and 8.

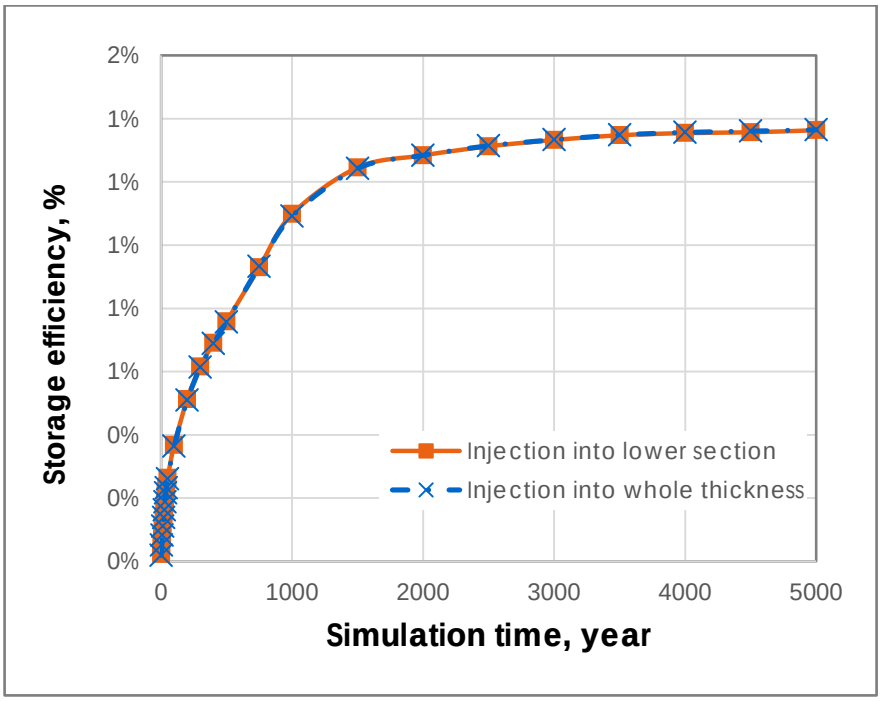

Figure 6.17. Influence of injection scope on the storage efficiency in a homogenous computational domain. Cases 7 and 8.

6.4.5. Impact of Directional Permeability Ratio

In the aim of assessing the effect of heterogeneity anisotropy in geological formations on the efficiency of storage, three models of a hypothetical aquifer with values of vertical to horizontal permeability ratio (k_v/k_h) equivalent to 1.0, 0.1 and 0.01 were developed and modelled (see cases 8, 9 and 10 in Table 6.3). This array has been set up as a realistic figure for most sandstone rocks according to a relatively new study by Widarsono et al. (2007).

The obtained results depicted in Figure 6.18 show deceptive influence of the permeability ratio on the CO_2 plume shape and spatial distribution maps. While the plume tends to horizontally extend further along the overlaying layer at higher permeability ratios, more CO_2 shows the tendency to migrate laterally within the two lower layers of the domain for lower values of permeability ratio. This owes to that lower permeability in the vertical direction restraints the upward movement of CO_2 forcing the injected gas to migrate across the domain proposing more gas into small-sized pores where it is more likely to be permanently entrapped when the brine invades back the domain after the injection stops. The latter impact is evidenced in Figure 6.19, which shows significantly greater amounts of trapped gas in cases of lower permeability ratios at all post injection time steps.

A snapshot of the results at an elevation of 82 m and 200 m away from the well case has been illustrated in Figure 6.20 describing the water saturation (S_w)–gas relative permeability (k_{rg}) relationship. The figure shows no influence of the permeability ratio on the drainage curves when the brine is displaced by the injected scrCO_2. However, anisotropy showed small influence on the relative permeability profiles for the imbibition curves as illuminated in the figure that demonstrates stronger hysteresis at higher permeability ratios. This can be further explained by the lower irreducible water saturations attained at higher permeability ratios (i. e. less trapped gas is snapped out of some pores, which increases the residual trapping of CO_2). In agreement with the findings by Chadwick et al. (2008) that indicate an increase in the trapped blobs of CO_2 left behind the gas plume during imbibition at higher permeability ratios.

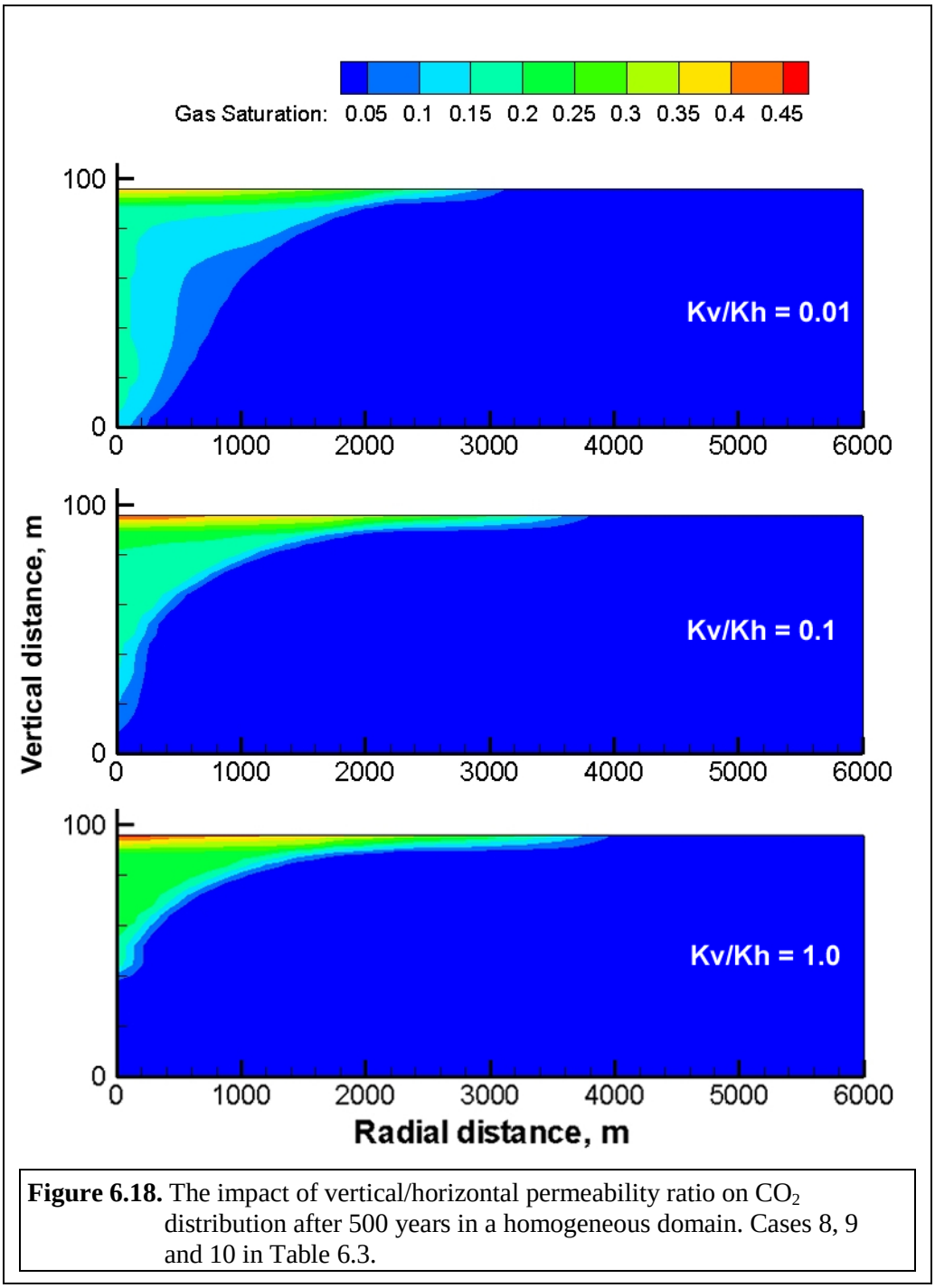

Figure 6.18. The impact of vertical/horizontal permeability ratio on CO_2 distribution after 500 years in a homogeneous domain. Cases 8, 9 and 10 in Table 6.3.

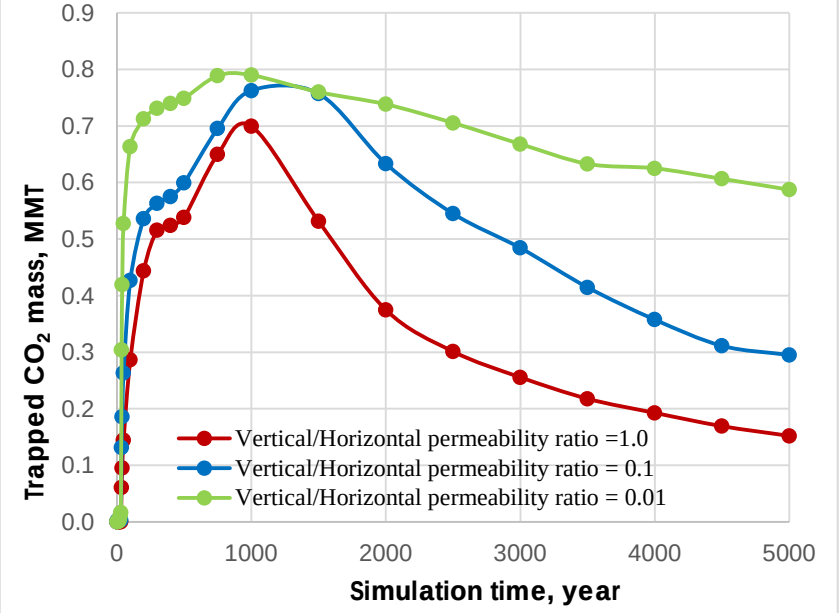

Figure 6.19. Influence of vertical to horizontal permeability ratio on CO_2 residual trapping. Cases 8, 9 and 10.

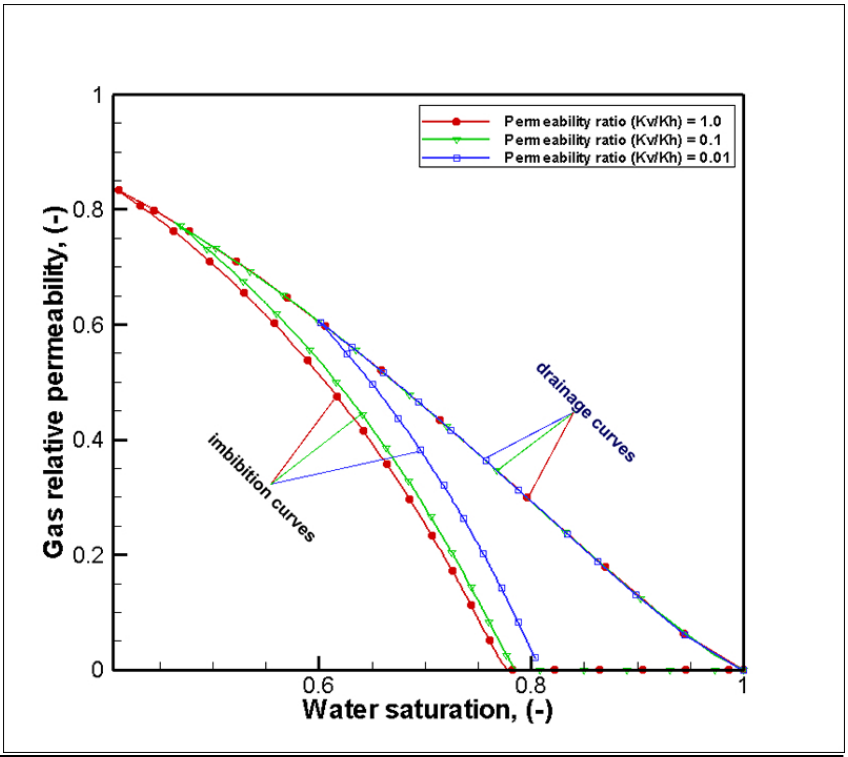

Figure 6.20. Water sequestration-relative permeability relationships at elevation of 82 m and radius of 200 m for different (k_v/k_h) ratios. Cases 8, 9 and 10.

One of the stupendous returns from this study is the inflection point in the gas dissolution trends around 800 years of the simulation lifetime as noticeable in Figure 6.21. This deviation occurred because at early stages, the flow system was entirely dominated by the structural trapping mechanism in which most of the injected gas remained in free-phase as depicted in Figure 6.22(a). This mechanism is mainly dependent on the upwards movement of the free gas that is more effective at higher vertical permeability values (i. e. larger values of (k_v/k_h)) as explained previously in this section. The horizontal movement of the gas due to the pressure gradient and low vertical permeability promotes more contact between the two fluids leading to more dissolution of CO_2 in the formation brine at early stages. However, this migration has no significant impact compared to the large buoyancy forces at later stages.

This clarifies the larger amounts of dissolved CO_2 at lower values of (k_v/k_h) before 800 years in Figure 6.21. By approaching 1000 years of simulation, the solubility trapping mechanism takes the control because the density and pressure gradient driving forces decline when most of the integrated gas had either settled at the top of the domain or within the vicinity of the injection well as illustrated in Figure 6.18 (see case 8 in Table 6.3). Consequently, the domain becomes dominated by the solubility trapping which is based on the contact interfacial area between the two fluids and the hydrostatic conditions that influence the CO_2 dissolution rate in the surrounding brine.

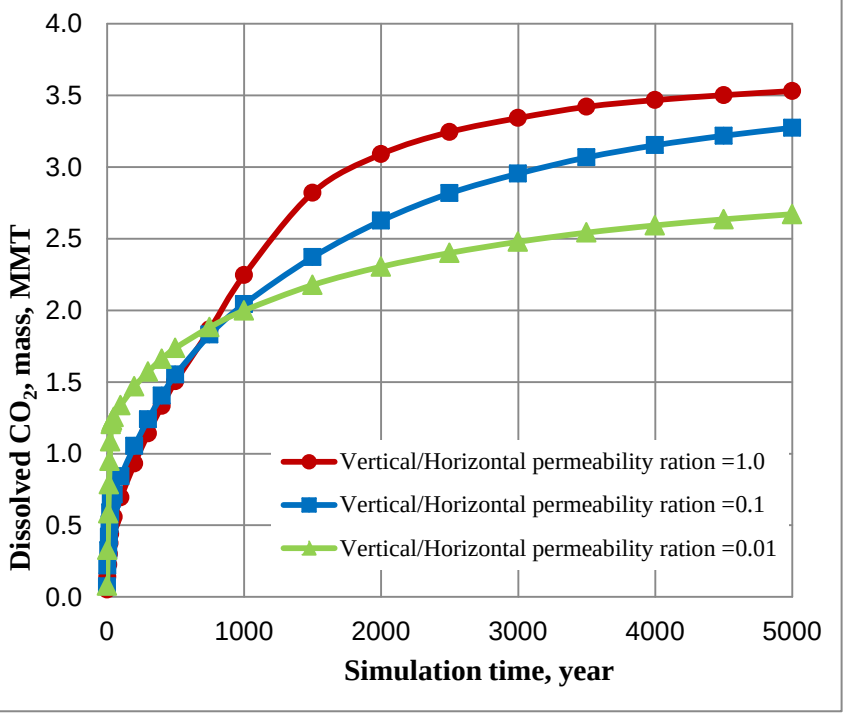

Figure 6.21. Effect of vertical to horizontal permeability ratio on solubility trapping of CO_2. Cases 8, 9 and 10.

CO_2 dissolution into the formation brine creates a denser aqueous phase that tends to sink downwards when the vertical movement becomes important to maintain more gas contact with the fresh brine leading to more dissolution of the gas into the brine. This convectional movement is easier at higher permeability ratios that results in larger amount of gas dissolution as presented in Figure 6.22(b), which evidences that the amount of dissolved CO_2 increases with the increase in the permeability ratio. The Figure shows that by the end of simulation, 28.240 MMT (more than 93% of the integrated gas) was dissolved in the brine for the higher permeability ratio (1.0) while 26.190 MMT (just above 86%) and 21.367 MMT (70%) was dissolved at lower ratios of 0.1 and 0.01 respectively. This is further supported by the lower amounts of 0.838 MMT free-gas CO_2 (2.7% of the injected gas) left off after 5000 years in the case of higher permeability ratio as presented in Figure 6.22(a).

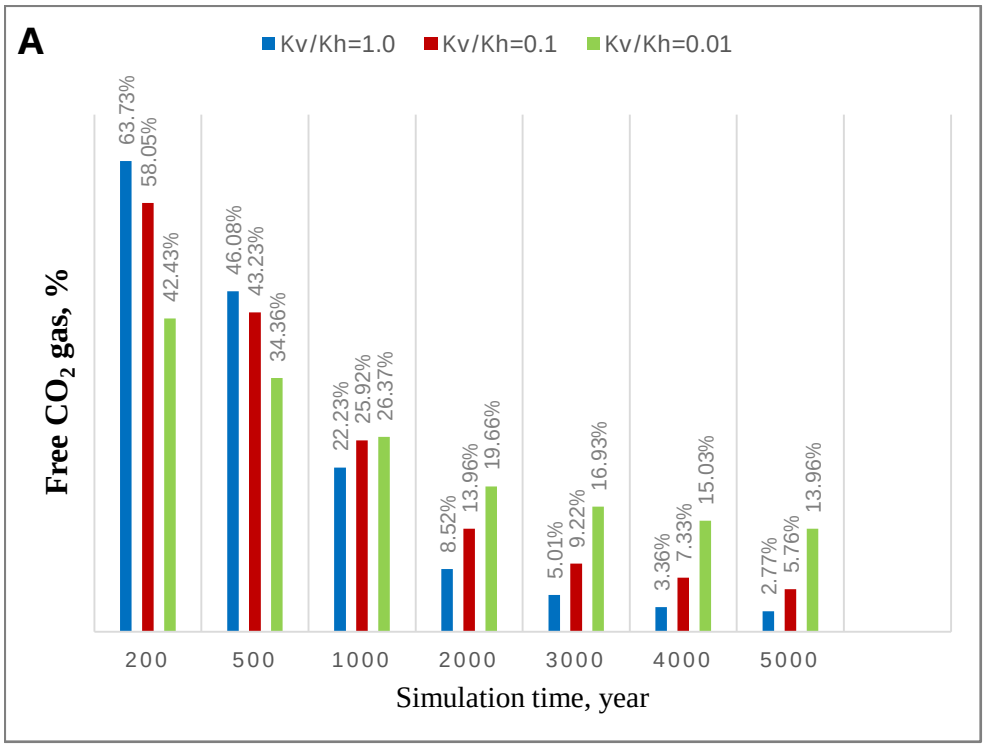

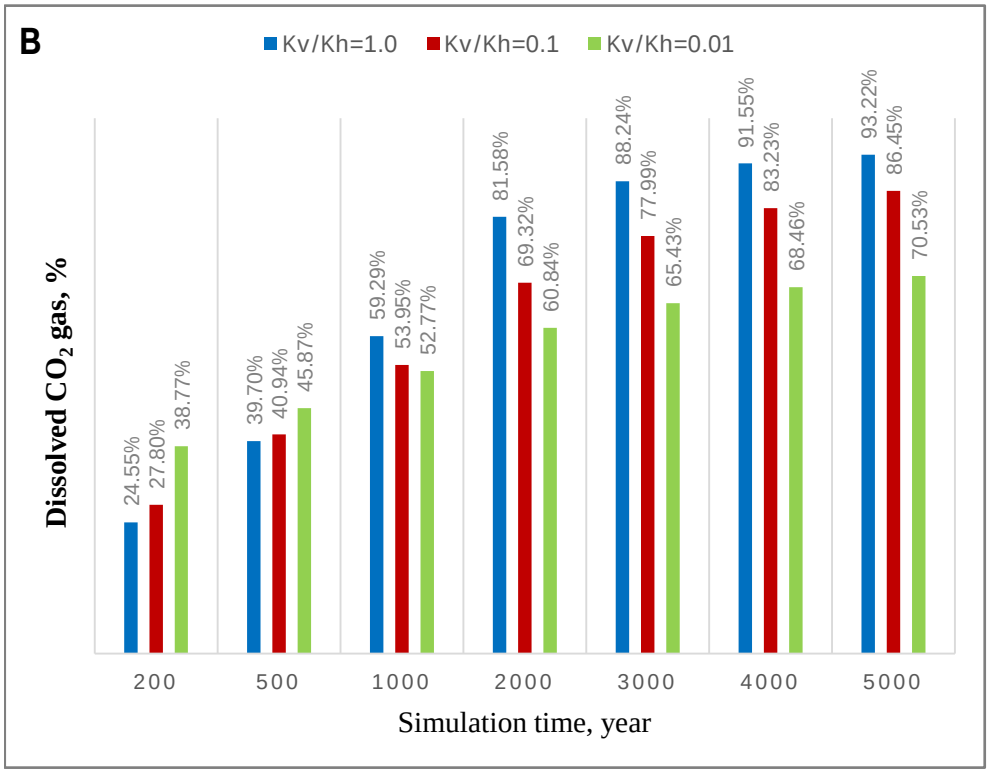

Figure 6.22. Impact of vertical to horizontal permeability ratio on; A) the integrated free CO_2 , B) dissolved CO_2 gas in a homogeneous domain for cases 8, 9 and 10.

Despite all these evidences, the determined storage efficiency for different permeability ratios using equation 6.21 by Szulczewski (2013) for open boundary domains has shown better storage efficiency at lower permeability ratios. This is significantly controversial and requires more investigation and discussion because our repeated numerical experiments have revealed contrast results (see Figures 6.21 through 6.23). This can be referred to the length parameter used in equation 6.21 to calculate the effective volume of the domain and consequently the CO_2 mass that can be sequestered in the aquifer.

The author suggested using the maximum extent of the gas plume to calculate the effective volume however, our simulation results revealed a huge difference in the obtained plume lengths for cases 8, 9 and 10. They were found to be 3965, 3802 and 3135 m for permeability ratios of 1.0, 0.1 and 0.01 respectively. This significant difference has returned unrealistic values of the storage efficiency when implemented in equation 6.21, because looking at Figure 6.23, it can be evidently noticed that higher permeability ratios produced greater amounts of dissolved and trapped CO_2, and less amounts of free-gas (i. e. enhanced solubility and residual trapping of the injected gas). It is evident from the figure that for (k_v/k_h) values of 1.0, 0.1 and 0.01, the achieved permanent trapping rates were 29.457 MMT (97%), 28.55 MMT (87%) and 26.066 MMT (71%) respectively.

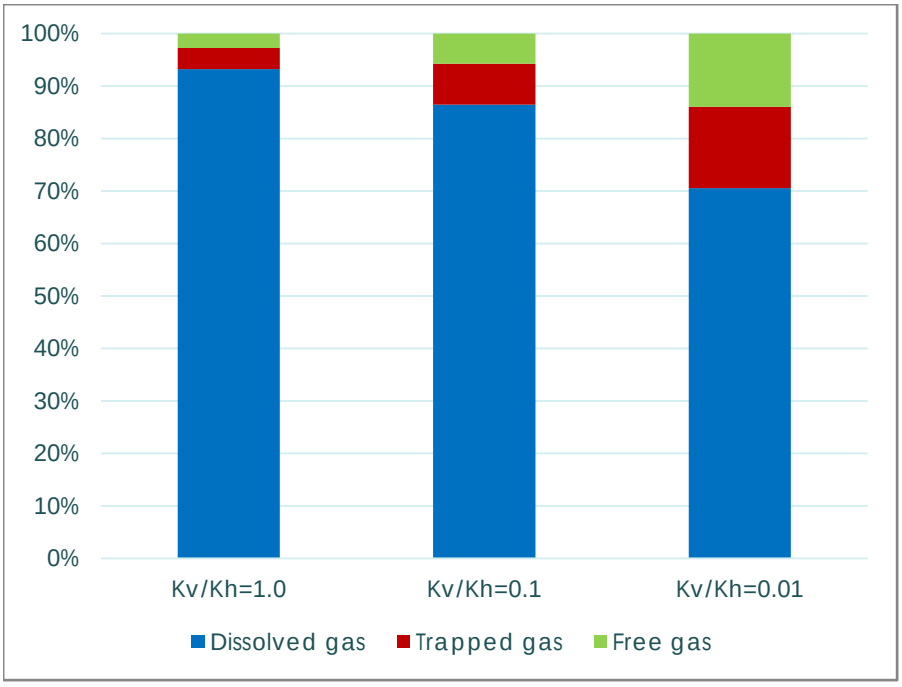

Figure 6.23. CO_2 storage efficiency at different permeability ratios based on the numerical results for cases 8, 9 and 10.

Depending on the findings from this study, it is suggested that the plume length parameter in equation 6.21 is reviewed and presented by a more realistic value to make the equation further applicable to various injection scenarios into geological formations. In this work, the total length of the domain, which extends far enough that the gas plume does not reach, was used in order to avoid any boundary effects on the in situ pressure build-up or gas seepage from the computational domain for all simulation runs (i. e. to employ an open boundary condition away from the injection well). This means that the whole aquifer volume was sued to calculate the storage efficiency factor that explains the small-obtained values of the efficiency factors in Table 6.4. Using this total length in equation 6.21 to determine the sequestration efficiency has returned more realistic values of the storage efficiency in terms of the directional permeability effect as shown in Figure 6.24 which indicates that the storage efficiency factor of any aquifer increases proportionally with the vertical to horizontal permeability ratio (see cases 8, 9 and 10 in Table 6.4).

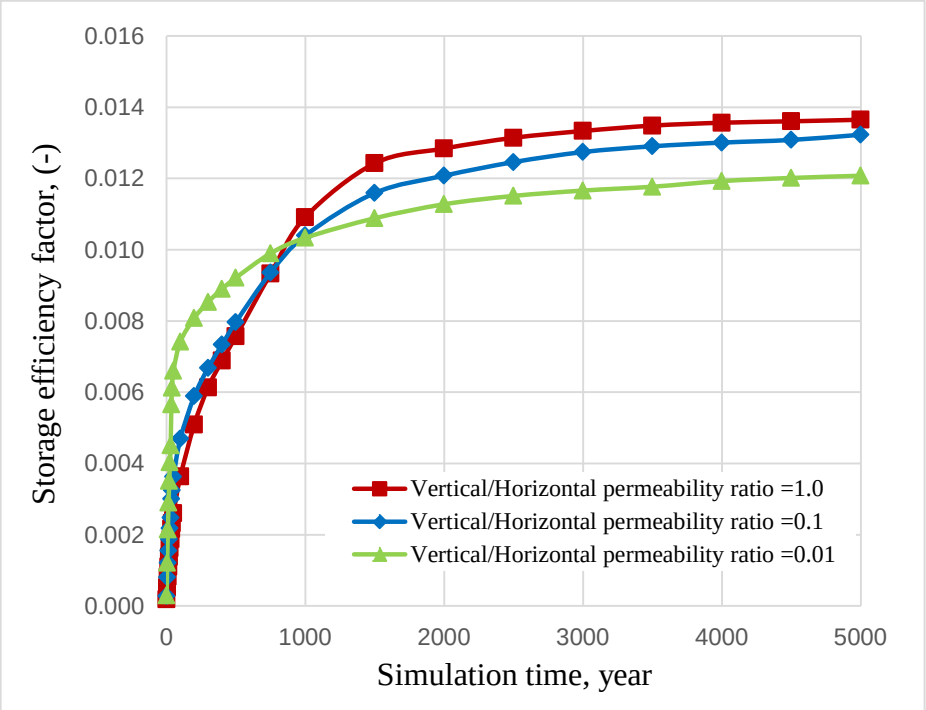

Figure 6.24. Impact of vertical to horizontal permeability ratio on CO_2 storage efficiency based on the total length of the domain used in equation 5.20 for cases 8, 9 and 10.

6.4.6. Influence of Injection Orientation

Injecting CO_2 into sedimentary formations through horizontal wells has been a subject of many research works and review studies most of which based on applying horizontal injection into confined geological formations considering the induced pressure build-up. While some authors conclude that injecting CO_2 via horizontal injection wells improves the trapping efficiency (De Silva and Ranjith 2012), others find that such methodology influences the mechanical stability of the overlaid caprock and does not improve the storage efficiency in long terms (Vilarrasa 2014; Okwen et al. 2011).

In this study, we investigated the influence of the injection orientation on the hydrodynamic behaviour of CO_2 and storage efficiency for an open-boundary model, and compare the results with those for the conventional vertical injection methodology. Purposely three simulation models were developed (see cases 10, 11 and 12 in Table 6.3) to identify the impact of the injection orientation on the storage efficiency and P_c-S_w relationship in geological formations.

The achieved numerical results revealed that injection orientation has significant influence on the gas migration and behaviour in unconfined geological formations as depicted in Figure 6.25 that highlights the disparity between the gas distribution contours achieved through using horizontal injection wells (cases 11 and 12) and those obtained from the vertical injection methodology (case 10). The figure exhibits a noticeable portion of the injected gas was trapped by the displacing brine in the case of the aquifer-thickness equivalent horizontal injection well (96 m) compared to the longer horizontal well (192 m). This can be attributed to the large injection mass flow rate per unit area (i.e. limited number of gridlocks) which delayed the upwards propagation of the buoyant CO_2 leading to only part of it reached the top of the domain to create a thin tongue-like shape that migrated crossway. The other portion of the injected gas was exposed to be encountered by the invading brine that physically isolated blobs of it within the local pores-network to be dissolved at later stages.

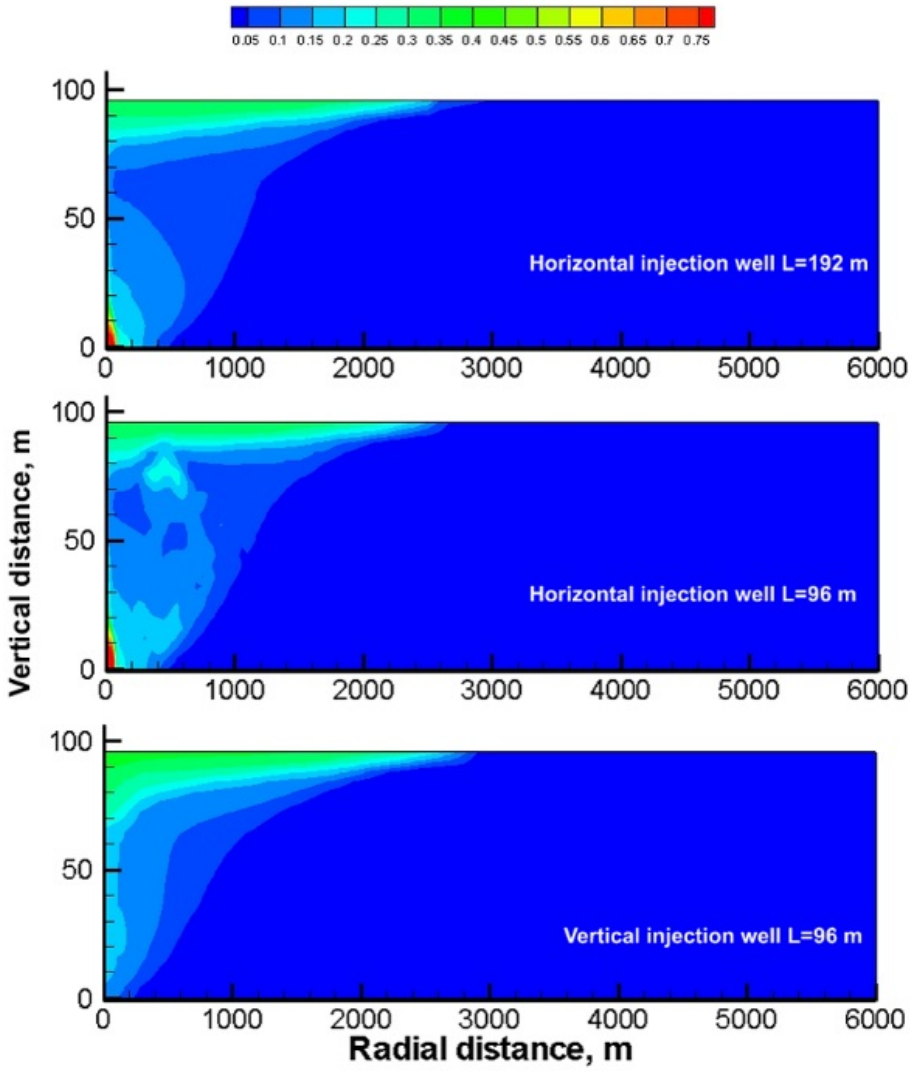

Figure 6.25. Integrated CO_2 distribution maps for different injection methods after 50 years in a homogeneous domain for cases 10, 11

Using horizontal injection techniques was found to magnify the values of average capillary pressure and consequently enhances the trapping mechanism as can be apparently noticed from the disparity in the *Pc-Sw* relationships in Figure 6.26(a) and likewise, increases the quantities of the trapped gas as presented in Figure 6.26(b). Unexpectedly and in spite of the higher values of capillary pressure attained through the longer horizontal injection well, the amount of the trapped gas was found to be significantly less than that was achieved by the shorter horizontal well. This can be explained by the smaller injection rate per unit area in the first case, which promotes more percolation of the free-gas towards the top of the aquifer as illustrated in Figure 6.26(b). Despite

the relative increase in the gas dissolution depicted in Figure 6.27(a) for the longer horizontal well, the amount of the free-gas left off by the end of simulation was higher as shown in Figure 6.27(b) leading to lower storage efficiency as evidenced in Figure 6.28.

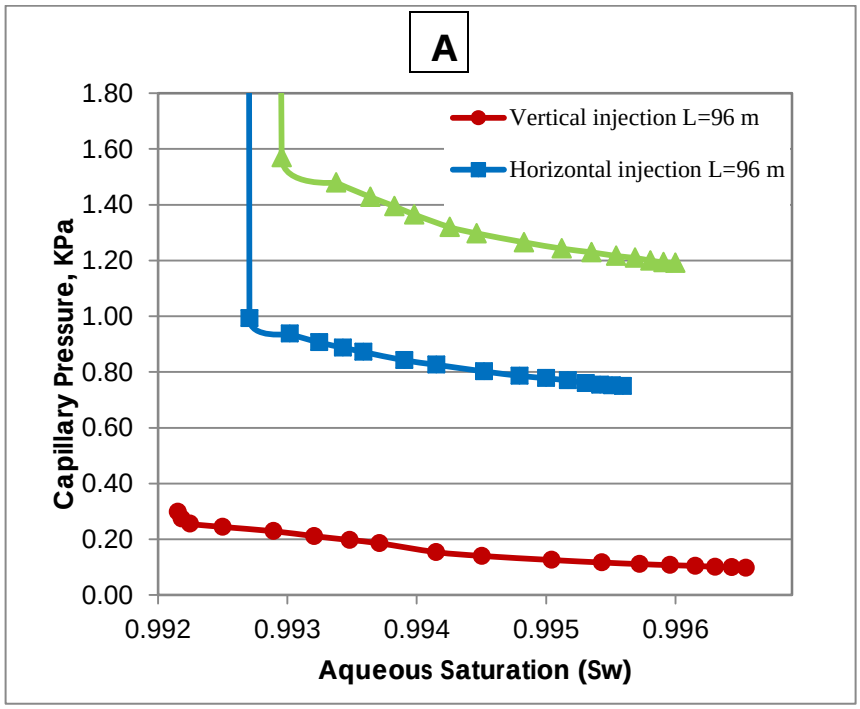

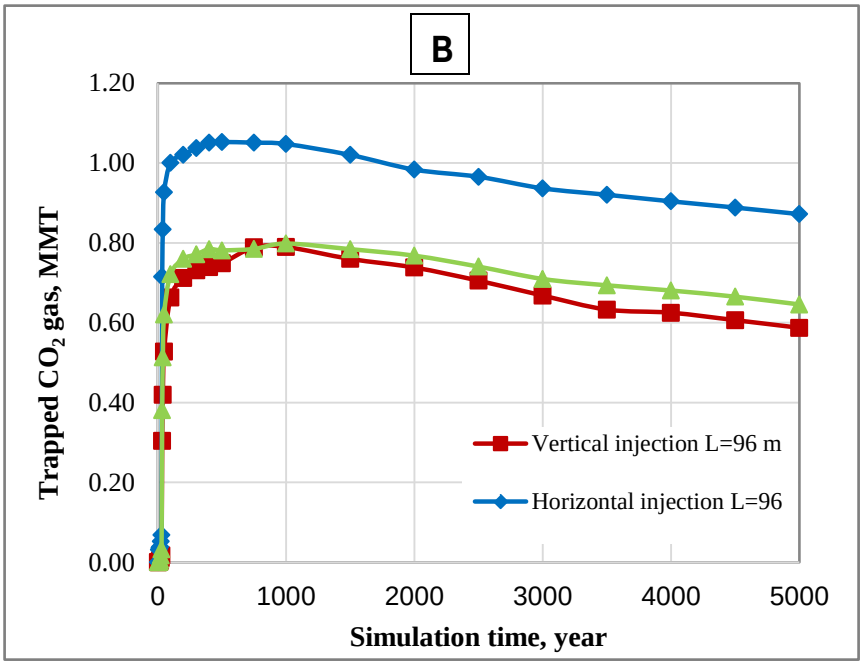

Figure 6.26. Influence of injection orientation on; (A) capillary distribution **(**B) trapped CO_2 in a homogeneous domain for cases 10, 11 and 12 in Table 6.3.

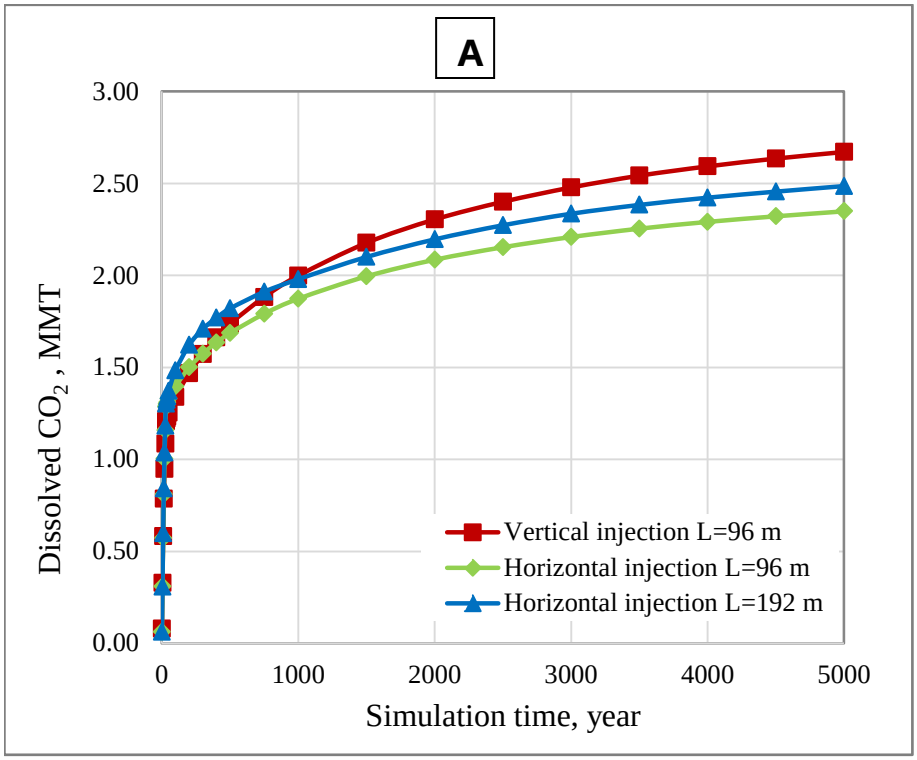

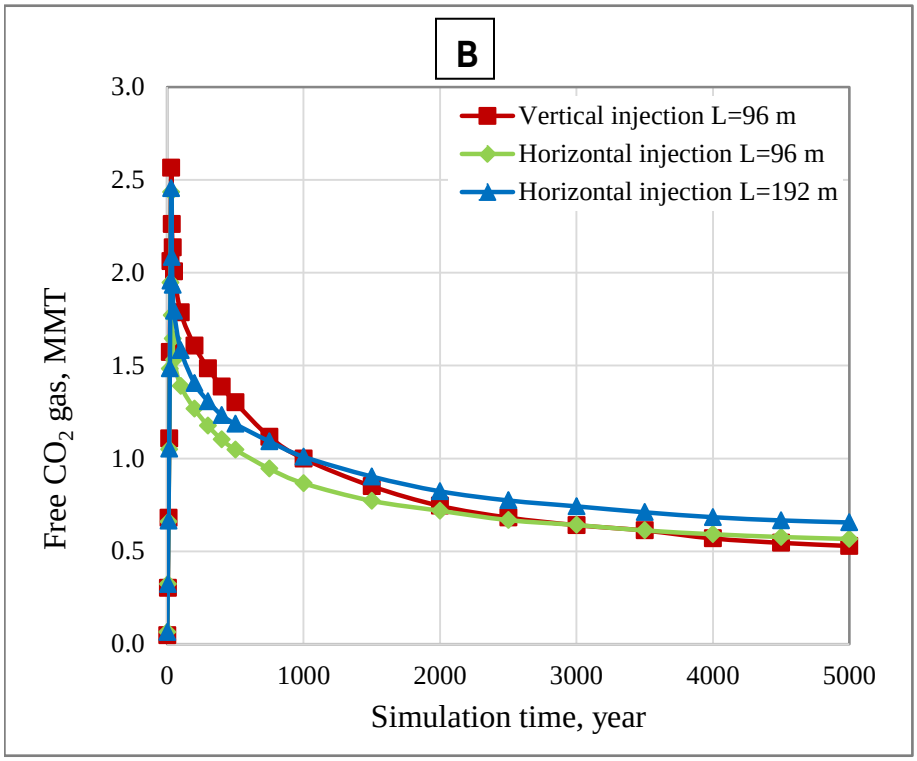

Figure 6.27. Effect of injection orientation on; (A) CO_2 solubility **(**B) free-gas CO_2 in a homogeneous domain for cases 10, 11 and 12.

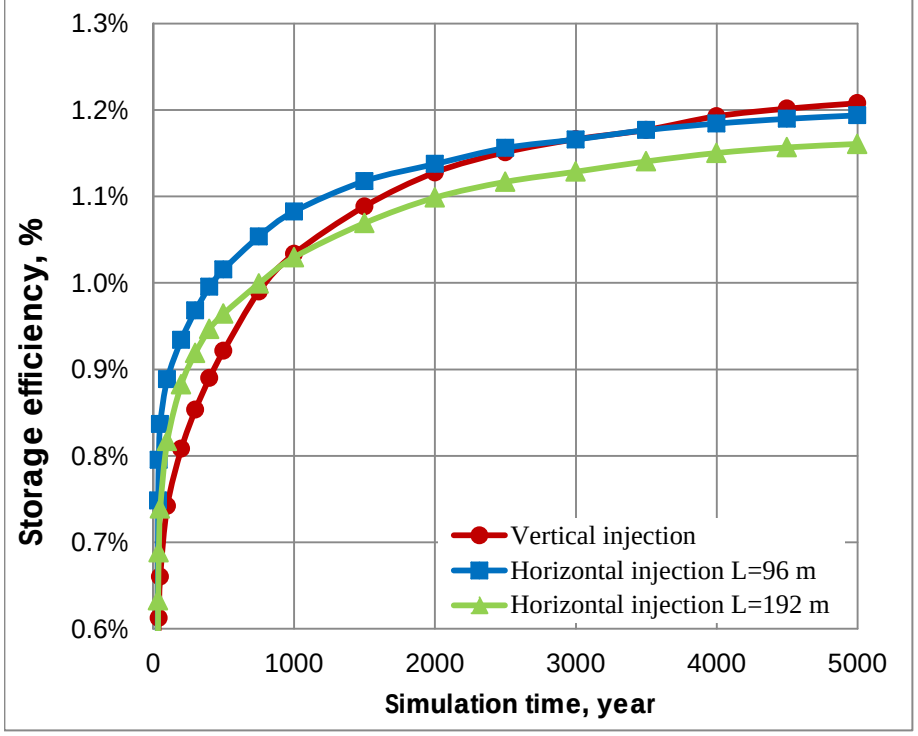

Figure 6.28. CO_2 storage efficiency for different injection orientation scenarios for cases 10, 11 and 12 in Table 6.3.

Additionally, the results reveal that horizontal injection into migration-controlled domains (i. e. open-boundary domains), returns slightly higher storage efficiency in short terms of simulation, however, after 2000 years, vertical injection methodology found to be more efficient as evidenced in Figure 6.28. This is consistent with the findings by Okwen et al. (2011) who suggest that using horizontal wells is preferable for pressure-limited domains and for sequestering large amount of CO_2 in a short time frame. Accordingly, implementing longer horizontal injection wells does not significantly enhance the storage capacity and the economical factor has to be taken into consideration should they need to be used for injecting large amounts of gas within limited periods of time.

6.4.7. Sensitivity to Domain Grid- resolution

The grid discretization of any simulated domain is an important factor used to accurately capture the occurrence of different flow dynamics and assess the sensitivity of modelling results to the spatial gridding schemes. As mentioned earlier, in this study, two levels of grid refinement, a coarse grid (88 x 1 x 24) and a fine grid (176 x 1 x 48) have been used to record the simulation code outputs (see cases 1 and 6 in Table 6.3).

The influence of the grid resolution is illustrated in Figure 6.29, where more detailed fingering maps of CO_2 dissolution can be observed in the fine-grid domain compared to those for the coarse one. Moreover, longer gas plumes were detected in the finer grid, which means that more accurate records of different forms of integrated gas were netted. This is further evidenced in Figure 6.30(a-b) in which it can be observed that after 1500 years, ~ 20% larger amount of dissolved gas and 54% lesser amount of free-gas were logged by the simulation code when a finer grid was implemented. These figures declined to ~1.3% and 3.2% respectively, by the end of simulation. In Figure 6.30(a), less impact of the grid resolution on CO_2 dissolution in the hosted brine was noted for both grids up to around 300 years of simulation. Then after, an obvious increase in the dissolved gas trends for the finer grid specifically between 800-2000 years. This deviancy diminishes after 2000 years, which, approves the findings by (Gonzalez-Nicolas et al. 2011; Bielinski 2007). This can be justified by the findings from this work (see Figure 6.29), which demonstrate the influence of grid resolution on the plume shape and number of formed fingers in the simulated domain due to the convection forces and gravity instability. Consequently, more accurate results were logged using finer grids which justifies the relatively higher efficiency achieved in the case of fine-resolution grid as illustrated in Figure 6.32.

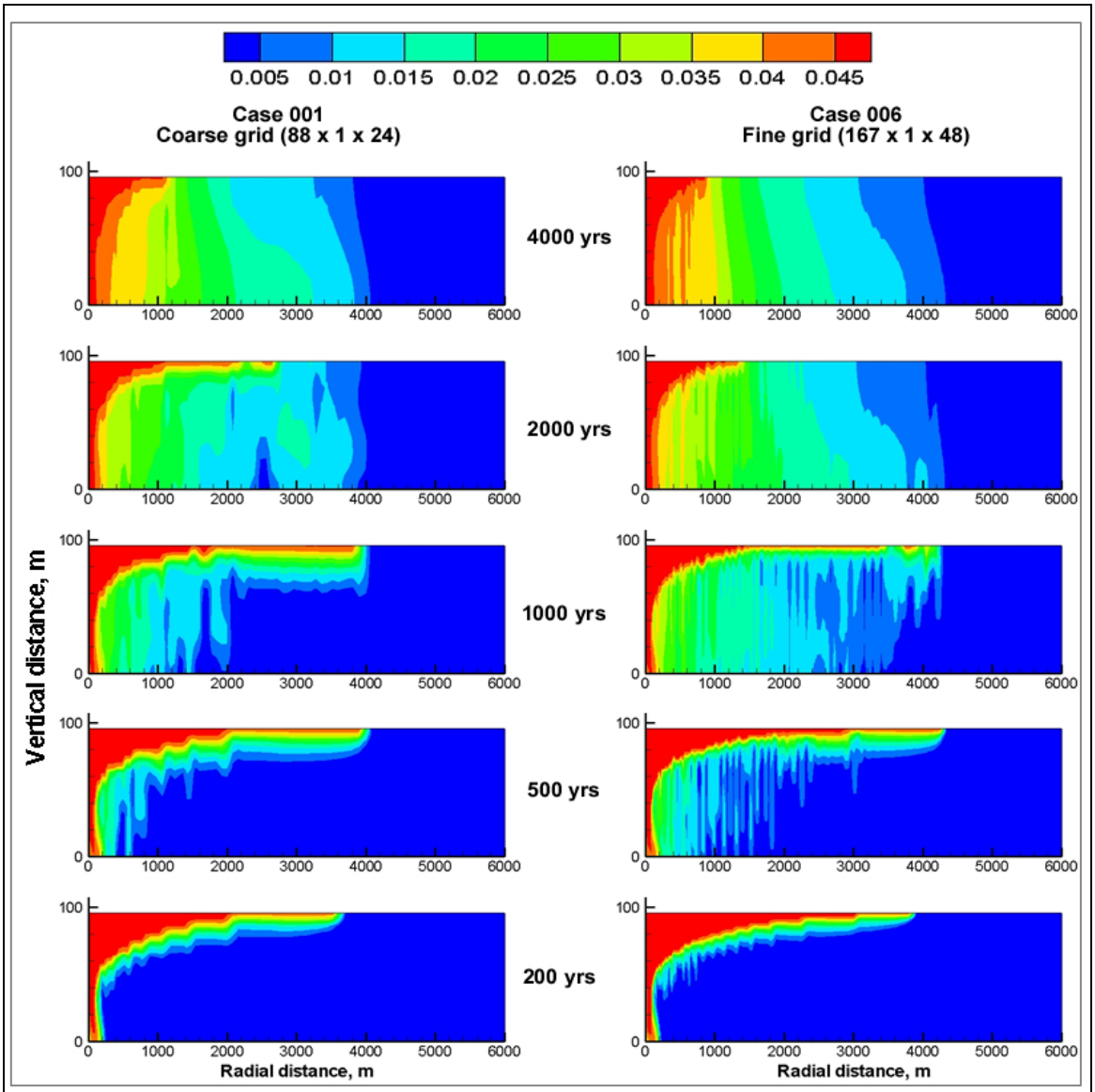

Figure 6.29. Aqueous CO_2 distribution in coarse and fine-grid homogeneous domains at different time scales.

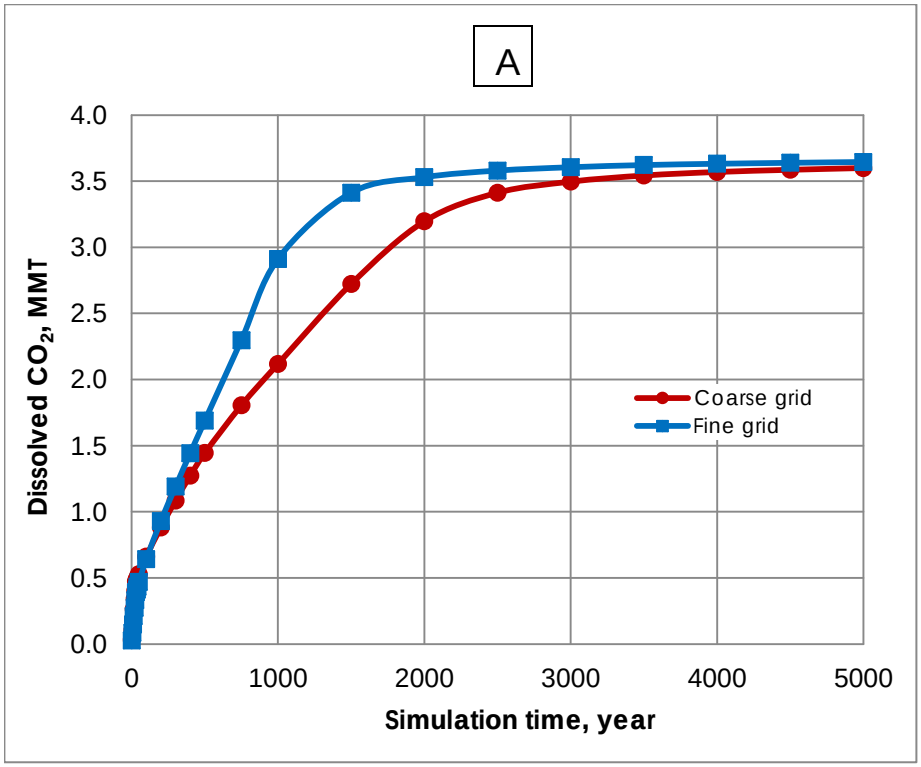

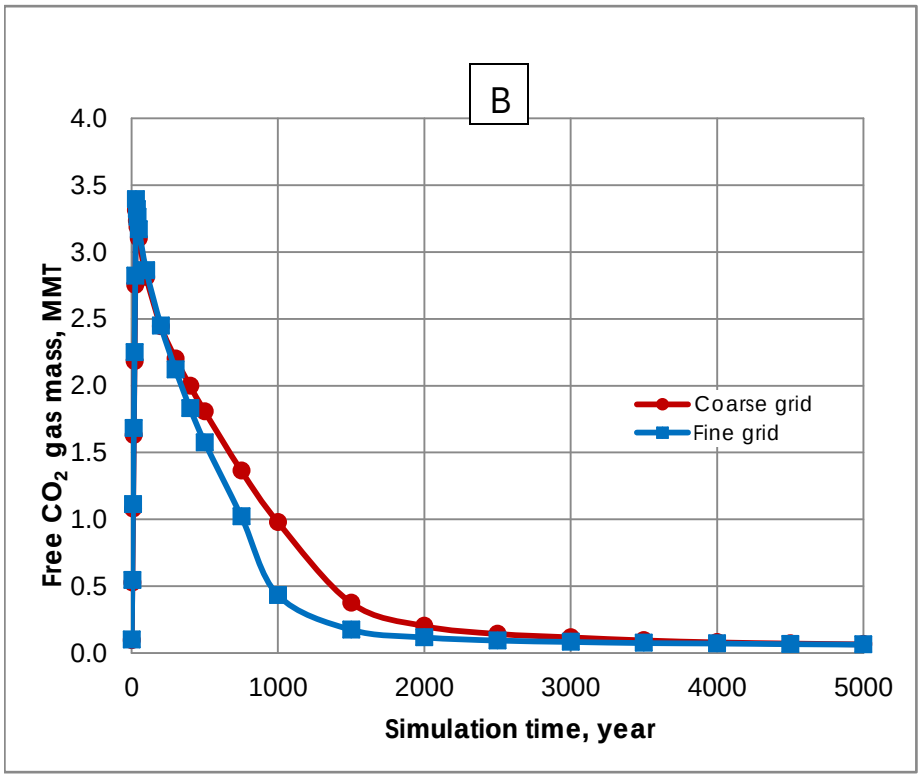

Figure 6.30. Effect of grid resolution on; (A) dissolved CO_2 (B) free-gas CO_2 in a homogeneous domain for cases 1 and 6.

Higher values of capillary pressure had also been caught through the finer grid as depicted in Figure 6.31(a), at all values of water saturation. Logically, this is ought to reflect greater entrapment of CO_2 in smaller pores, however, unexpectedly this wasn't the case because the results plotted in Figure 6.31(b) revealed higher gas entrapment in the coarse grid. This can be due to that by using larger blocks in the computational domain, part of the dissolved CO_2 might have been logged either as a free or trapped gas which can be explained from the relatively larger amounts of the latter two forms of the content gas in the case of coarse refinement. In spite of this significant overestimation of the netted values of the trapped gas in the coarse grid, the amount of the free gas was found to be less in the finer grid by ~ 3.2% as displayed in Table 6.4. However, the increase in the storage efficiency factor was only ~ 0.1% using a finer grid as shown in Figure 6.32. This further clarifies that the grid refinement has only a small impact on the simulation results. The amount of the illustrated residually trapped gas was much smaller than the amount of the dissolved CO_2 shown in Figure 6.31(a) and moreover, this small amount of the trapped gas itself is subject to dissolve in medium and long time frames.

Some preceding publications concluded only slight or no impact of grid resolution on the simulation results. Conversely, ranking our simulation cases according to the attribute of safer storage of the disposed gas in Table 6.4, the finer grid case was found to be laying on the top of the list. Therefore and despite the excessive execution time required to conduct simulation runs with finer grids, it is imposing to magnify focus on the behaviour of the injected gas in different phases (i. e. dissolved, residually trapped and free-gas) within in situ pores network by using reasonably refined grids. Results from the finer mesh (see case 6 in Table 6.4) detected only about 0.497 MMT of free gas at the end of the simulation lifetime compared to about 0.514 MMT for the coarse grid in case 1, which reflects about 3.2% safer storage by the means of deploying the finer grid. This should be motivating for the researchers to refine their modelling grids for further focused and more credible accurate results. Nevertheless, it is recommended that sensible balance between the grid refinement and the computational time required for calculations be embraced. For the cylindrical domain modelled in this research work (3 km radius and 96 m thickness), it was found that discretizing it to 176 by 48 nodes in the lateral and vertical direction respectively, was found to provide reasonably effective level of refinement in terms of balancing between the accuracy of the achieved results and, the computational time and requirements.

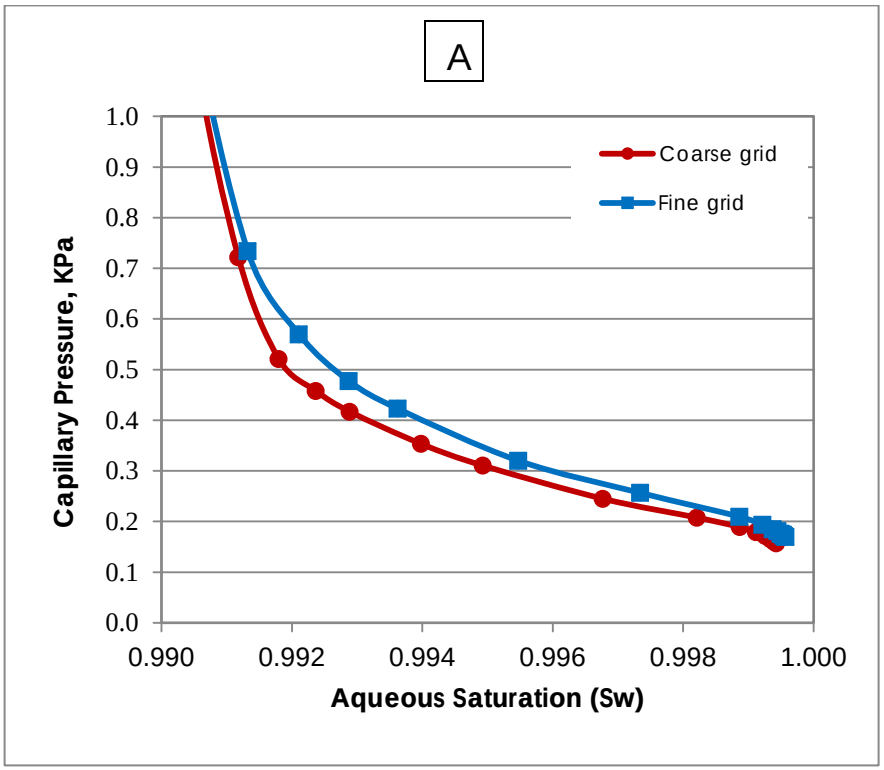

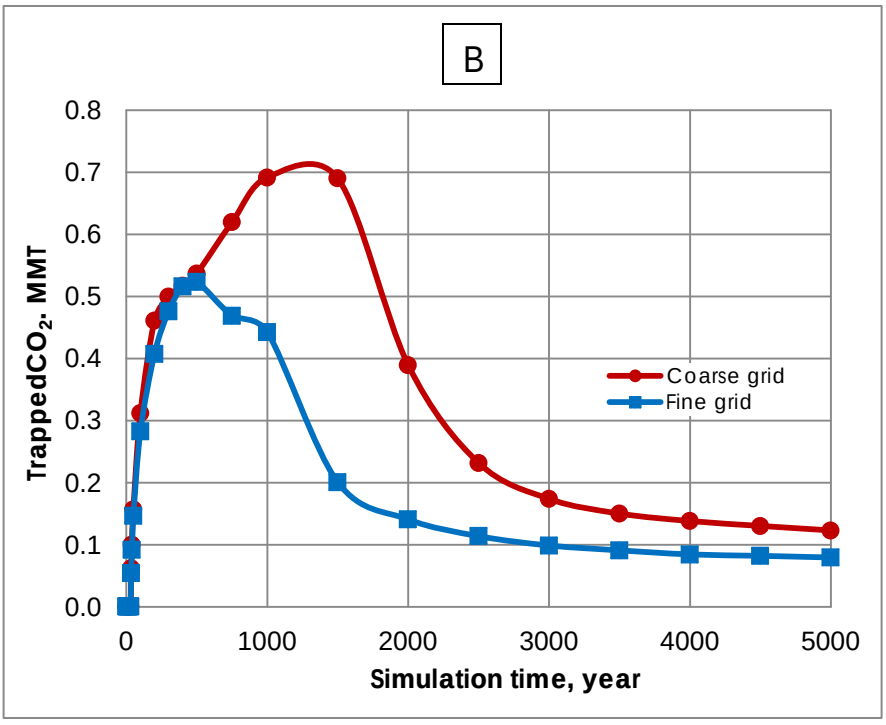

Figure 6.31. Impact of grid resolution on (A) capillary pressure profiles.

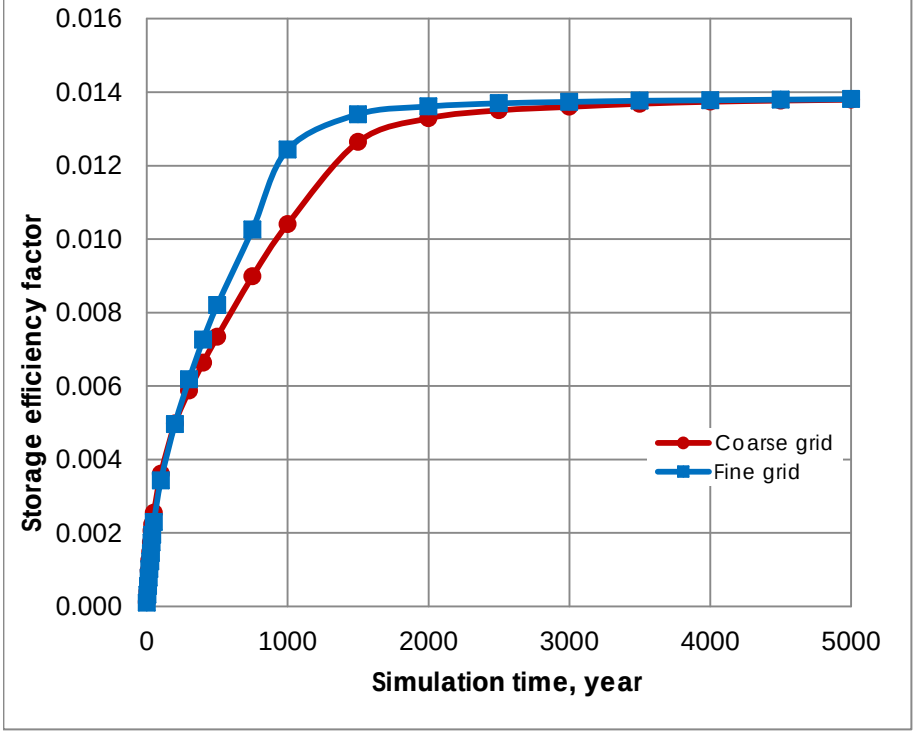

Figure 6.32. Grid refinement effect on CO_2 storage efficiency in a homogeneous domain for cases 1 and 6.

6.5. Chapter Summary

A set of numerical simulation cases were developed and conducted using STOMP-CO_2 numerical simulation code to investigate the influence of various types of heterogeneity, injection schemes, grid resolution, anisotropy, and injection orientation on the CO_2-water flow system behaviour and storage efficiency in saline aquifers.

The findings from this study work can be concluded as follows:

1- Heterogeneity has significant impact on saturation-capillary pressure relationship because simulation results demonstrated greater values of capillary pressure at any specific saturations in heterogeneous domains compared to the homogeneous one. Consequently, this increase contributes in amplifying the residual trapping of the injected gas in heterogeneous geological formations.

2- CO_2 dissolution (i.e. solubility trapping mechanism) show higher trends in homogeneous formations because they facilitate both lateral and vertical transfer of the injected gas however, overall, heterogeneous media are found to be more effective in storing CO_2 safely over long-time frames. This is referred to the presence of intermingled layers of shales in sand rocks, which endorses the gas passage through more pores that significantly increases the residual trapping mechanism compared to the solubility one.

3- Compared to the homogeneous media, cyclic injection methodology has shown more influence on the heterogeneous domains through which the injected gas spreads out further leading to greater interfacial area with brine and consequently escalates CO_2 dissolution. According to the attained results, it is evident that the injection methodology has influence on the storage efficiency of CO_2 in geological formations. However, more research work is required to investigate more details about optimizing the injection times and pausing intervals in long-term sequestration projects where mineralization trapping plays an important role.

4- Injecting $scCO_2$ through the whole thickness of the domain has shown no significant influence on the storage efficiency compared to injecting the gas through the lower segment of the domain, however, it has been noticed that about 3.2% less amount of free-gas was left off in the former case by the end of the simulation timeline.

5- While gas plume extends further at higher (k_v/k_h) values, lower ratios enhance the solubility trapping of CO_2 at early stages of simulation. Additionally stronger hysteresis at higher permeability ratios enhances the residual trapping mechanism. Overall, storage efficiency increases proportionally with the permeability ratio of geological formations because higher ratios facilitate further extent of the gas plume and increases solubility trapping of the integrated gas. Additionally, it encourages the upward movement of the injected gas and the convectional movement of the CO_2-saturated water, which tends to sink down towards the bottom of the domain.

6- Using the maximum length of the gas plume in equation 6.21 to calculate the available porous volume in open-boundary domains requires more investigation because it has produced some unrealistic results. Therefore, an optimization is suggested to setup the domain length according to the employed injection rate or pressure so that the extended gas

plume just reach but does not pass. This length can be called the effective length and used to calculate the volume available to host the potential injected gas.

7- Implementing horizontal injection methodology significantly influences the fluid flow in geological formations and gas distribution maps by magnifying the average capillary pressure in the domain and enhances both permanent trapping mechanisms (solubility and residual). It has been found that employing longer horizontal wells does not increase storage efficiency however, more research work is recommended to optimize the length of the horizontal wells and the injection techniques including injecting chase brine along with $scCO_2$.

8- Simulated domain discretization has minor consequences on the CO_2 plumes shape and extent because finer grids produce smoother-edged plumes that extend further from the injection well compared to the coarse grids. Moreover about 2.5 times higher values of trapped CO_2 were determined in coarse grids while greater amount of dissolved CO_2 was found in the finer grid.

9- Despite the excessive execution time required to run simulations on finer-grid domains, it is imposing to magnify focus on the behaviour of the injected gas in order to increase the accuracy of the logged results. Finer- resolution grids can slightly increase the calculated values of the storage efficiency factor specifically in the medium-terms of sequestration; however, practical balance should be maintained between the refinement level and the computational requirements along with the execution time needed.

Chapter 7

Conclusions and Recommendations for Future Work

7.1. Conclusions

One of the promising measures used to mitigate the emission of CO_2 into the atmosphere is injecting it into deep saline aquifers as this has a vast feasibility and potential for CO_2 sequestration. Trapping CO_2 in aquifers is governed by different trapping mechanisms (i.e., structural, residual, solubility and mineral), therefore the scope of this model framework is to optimize the influential parameters while aimed at enhancing such trapping methods and immobilizing CO_2 underground to reduce the risk of any future leakage.

As the time scales of CO_2 sequestration vary widely, a series of well-defined numerical simulations have been conducted for supercritical CO_2-water flow in homogeneous and heterogeneous core-scale, large-scale and field-scale porous media to determine dynamic and quasi-static P_c-S relationships. STOMP-CO_2 computer code has been utilized in this study to determine CO_2 gas saturation changes at various time scales through different injection scenarios taking into consideration the effects of porosity/permeability, heterogeneity, anisotropy, injection scope and scenario, and capillarity for CO_2-water system.

This research work has concluded the following:

- Not considering the dynamic capillary pressure effect for scCO_2-water flow in porous media (i.e., assuming $(\tau = 0)$) entails that dynamic and quasi-static P_c-S relationships are the same which contravene the findings of this work which demonstrate that $\tau \neq 0$ but varies with both water saturation and the desaturation rate $(\partial S/\partial \mathrm{t})$. It has been affirmed that simulating CO_2-water flow in porous media may return some errors that are likely to increase should one chooses to use a traditional modelling scheme based on quasi-static P_c-S relation to account for the capillary pressures in the modelling calculations.

- To implement the results of this research work in the field scale, firstly, the simulation results need to be validated against an in-house experimental set up results under similar operating conditions to establish a robust credibility and reliability of their accuracy. Following this validation, the results can be upscaled and implemented in the field setting. Accordingly, the obtained results of the simulation code (STOMP-CO_2) employed in this study have been validated against experimental ones (from the literature) and shown good agreement, which has established a robust credibility of the computer code in simulating the

injection of CO_2 into geological formation to assess the storage efficiency and ultimate fate of the injected gas.

- It has been evidenced form this study that fluids flow faster in homogeneous domains and the least permeable medium dominates in heterogeneous media. It has also been found out that injecting the supercritical gas into lower segments is more efficient than upper ones or even through the whole thickness. This is owing to more mixing with the ambient brine is promoted, which enhances the solubility trapping supported by the less amount of free-gas left off by about 3.2% in the case of lower segment injection by the end of the simulation timeline.

- The results from this work have depicted that the higher the injection pressure, the higher the capillary forces are (i. e. more residual trapping), however, the maximum sustainable pressure has to be taken into consideration to avoid any geomechanical fracture to the overlaying formation rock.

- Low-permeability formations have shown higher storage capacity and efficiency of CO_2 due to the higher capillary forces that amplify the residual trapping mechanism during the imbibition process. Similarly, solubility trapping has been found to be more efficient in low-permeability formation because they tend to retard CO_2 migration maintaining more contact with the accommodated brine, which leads to more CO_2 dissolution.

- Warm aquifers are more effective in sequestering CO_2 because higher temperatures increase capillary forces and consequently heighten the residual trapping of CO_2.

- Heterogeneity in geological formations has shown significant impact on capillary pressure – saturation relationship and amplifies the residual trapping of CO_2 because the simulation results in this research work have demonstrated greater values of capillary pressure at any specific saturation value in the heterogeneous domains compared to the homogeneous one. Moreover, despite the higher trends of solubility trapping of CO_2 in homogeneous formations, heterogeneous media have shown greater efficiency in storing CO_2 safely over long-time frames.

- It has been illustrated that the heterogeneity patterns of fine sand embedded in coarse sands are more effective in sequestering CO_2 over long time frames, however more research is required to clarify how the field distribution of heterogeneity and injection scenarios of CO_2 affect the efficiency of sequestration.

- Cyclic injection methodology has shown more influence on the storage efficiency of CO_2 in heterogeneous domains compared to the homogeneous ones due to the further extent of the gas plume that leads to greater interfacial area with brine and consequently escalates CO_2 dissolution.

- The results from this work suggest imposing finer-grid discretisation to magnify focus on the behaviour of the injected gas in order to increase the accuracy of the logged data. However, practical balance should be maintained between such refinement level and the computational requirements along with the execution time needed.

- The results from this study have demonstrated that CO_2 storage efficiency increases proportionally with the vertical to horizontal permeability ratio (heterogeneity anisotropy) of geological formations because higher ratios facilitate more vertical flow of the injected gas and increases both residual and solubility trapping of the integrated gas.

- Implementing horizontal injection methodology significantly influences the behaviour of fluid flow in geological formations and gas distribution maps by magnifying the average capillary pressure in the domain and enhances both permanent trapping mechanisms (solubility and residual). It has also been found that employing longer horizontal wells does not increase storage efficiency; however, more research work is recommended to investigate the impact of the length of the horizontal wells and the deployed injection techniques including injecting chase brine along with the injected $scCO_2$.

7.2. Recommendations for Future Work

Carbon storage (CS) in saline aquifers is relatively a new technology that encounters high level of uncertainty due to the lack of geological data about theses formations.

Despite a growing number of research works and studies in the field of injecting CO_2 into geological formations and from the experience gained from this current research work, there are

still several significant knowledge gaps that have not been addressed and are recommended for further investigation. These concluded gap areas are listed below:

- More experimental work should be conducted at natural geological formation conditions to determine the influence of various parameter on the ultimate fate of the injected CO_2 more realistically. Furthermore, these empirical results and more from literature are to be used to validate the numerical results attained by different employed computer codes to evaluate their efficiency in assessing the storage capacity and efficiency of geological sites for sequestering CO_2.
- To enrich this area of research, more simulations are needed to be conducted to quantify the effects of salinity in CO_2 sequestration in saline aquifers by including the equation of mass for NaCl in the simulation code because brine is the actual existing fluid rather than pure water in deep aquifers.
- According to the attained results, it is evident that the injection methodology has significant influence on the storage efficiency of CO_2 in geological formations; however, more research work is required to investigate more details about optimizing the injection times and pausing intervals in long-term sequestration projects where mineralization trapping plays an important role.
- To assess the storage capacity and efficiency in geological formations, many methodologies have been developed including the one by (Szulczewski, 2013) which has been deployed in this work and presented in Equation 6.21. The maximum length of the gas plume used in this equation to calculate the available porous volume in open-boundary domains requires more investigation because it has produced some unrealistic results. Therefore, an optimization is suggested to setup the domain length according to the employed injection rate or pressure so that the extended gas plume just reach but does not pass. This length can be named the effective length, which can be used to calculate the volume available to host the potential gas.
- It has been illustrated from this research work that the heterogeneity patterns of fine sand embedded in coarse bed are more efficient in sequestering CO_2 over long periods. However, more research is required to clarify the extent of the field distribution of heterogeneity effect and injection scenarios of CO_2 influence on the efficiency of the sequestration.

- It has been clarified from the current results that employing longer horizontal wells to some extent does not increase storage efficiency; however, more research work is recommended to investigate the influence of the length of the horizontal wells and the injection techniques including injecting chase brine along with scCO_2.
- In spite of some experience gained from the enhanced oil recovery (EOR) operations, more research work is required to evaluate the usage of multi-injection well techniques aiming at increasing the productivity of CO_2 disposal into the subsurface taking into account the means to control the expected over-pressure and water displacement rate.
- More research is required to explore the effect of dynamic coefficient which is dependent not only on the dynamic flow of existing fluids but many other parameters, like the geometry of the domain and the pore size distribution index on CO_2 sequestration in details. This may include how changes in the injection pressure and hydrostatic conditions influence the equilibrium curves which need to be compared with the dynamic ones. The impact of dynamic capillary pressure effect is crucial particularly in upscaling from core-scale to larger-scale domains with different geometry and heterogeneity, which affects the effective permeability values in porous domains because as claimed by Mirzaei and Das (2007) ”the soil grains have preferred orientation depending on depositional environments, which create anisotropy in the media permeability”. Future works should include determining the capacity of various CO_2 sequestration mechanisms over wide range of time scales and optimising the influential factors on each of them to enhance storage capacity and maintain safer and more secure sequestration of the injected gas.
- More numerical simulations need to be conducted to highlight some significant aspects of various trapping mechanisms, including CO_2 dissolution rate, precipitation kinetics, interpreting the influence of solubility on a resistivity log for monitoring processes and upscaling the simulation results from lab to field-scale.

REFERENCES

Abidoye, L. K., Khudaida, K. J., & Das, D. B. (2015). Geological carbon sequestration in the context of two-phase flow in porous media: A review. *Critical Reviews in Environmental Science and Technology*, 45(11), 1105-1147.

Abidoye, L. K., (2014). Dynamic two-phase flow in porous media and its implications in geologic carbon sequestration (*Doctoral thesis, Chemical Eng. Dep., Loughborough University, UK*).

Abu-Khader, M. M. (2006). Recent progress in CO_2 capture/sequestration: a review. *Energy Sources*, Part A, 28(14), 1261-1279.

Adams, J. J., & Bachu, S. (2002). Equations of state for basin geofluids: algorithm review and intercomparison for brines. *Geofluids*, *2*(4), 257-271.

Alabi, O. O. (2011). Fluid flow in homogeneous and heterogeneous porous media. *Electronic Journal of Geotechnical Engineering*, *16*, 61-70.

Alkan, H., Cinar Y., & Ülker E. B. (2010). Impact of Capillary Pressure, Salinity and In situ Conditions on CO_2 Injection into Saline Aquifers. *Transp. Porous Media*, 84(3), 799-819.

Allen, M. R., & Stocker, T. F. (2014). Impact of delay in reducing carbon dioxide emissions. *Nature Climate Change*, *4*(1), 23-26.

Assteerawatt, A., Bastian, P., Bielinski, A., Breiting, T., Class, H., Ebigbo, A., ... & Niessner, J. (2005). MUFTE-UG: structure, applications and numerical methods. *Newsletter, International Groundwater Modeling Centre, Colorado School of Mines*, *23*(2), 10.

Ataie-Ashtiani, B., Hassanizadeh, S.M., Oostrom, M., Celia, M.A., & White, M.D. (2001). Effective parameters for two-phase flow in a porous medium with periodic heterogeneities. *Journal of Contaminant Hydrology* 49, 87–109.

Azdarpour, A., Asadullah, M., Mohammadian, E., Hamidi, H., Junin, R., & Karaei, M. A. (2015). A review on carbon dioxide mineral carbonation through pH-swing process. *Chemical Engineering Journal*, *279*, 615-630.

Bachu, S. (2015). Review of CO_2 storage efficiency in deep saline aquifers. *International Journal of Greenhouse Gas Control*.

Bachu, S., & Bennion, D. B. (2009). Dependence of CO_2-brine interfacial tension on aquifer pressure, temperature and water salinity. *Energy Procedia*, *1*(1), 3157-3164.

Bachu, S. (2008). CO_2 storage in geologic media: role, means, status and barriers to deployment. *Progress in Energy and Combustion Science*, 34.254-273.

Bachu, S., & Bennion B. (2008). Experimental assessment of brine and/or CO_2 leakage through well cements at reservoir conditions, *"International Journal of Greenhouse Gas Control*, 3: 494-501.

REFERENCES

Bachu, S., Bonijoly, D., Bradshaw, J., Burruss, R., Holloway, S., Christensen, N.P. & Mathiassen, O.M. (2007). CO_2 storage capacity estimation: Methodology and gaps. *International Journal of Greenhouse Gas Control*, 1(4), pp. 430-443.

Bachu, S., Haug, K., Michael, K., Buschkuehle, B. E., & Adams, J. J. (2005). Deep injection of acid gas in Western Canada. *Developments in Water Science*, 52, 623-635.

Bachu, S. (2003). Screening and ranking of sedimentary basins for sequestration of CO_2 in geological media in response to climate change. *Environmental Geology*, 44(3), 277-289.

Bachu, S., & Adams, J. J. (2003). Sequestration of CO_2 in geological media in response to climate change: capacity of deep saline aquifers to sequester CO_2 in solution. *Energy Conversion and management*, *44*(20), 3151-3175.

Bachu, S., Gunter, W.D., & Perkins, E.H. (1994). Aquifer disposal of CO_2. Hydrodynamic and mineral trapping. *Energy Convers. Manage.* 35, 269–279.

Battistelli, A., Claudio, C., & Pruess, K. (1997). The simulator TOUGH2/EWASG for modelling geothermal reservoirs with brines and gas. *Geothermics* 26 (4), 437–464.

Batzle M & Wang Z. (1992). Seismic properties of pore fluids. *Geophysics*, 57, 1396–1408.

Bear, J. (2013). Dynamics of fluids in porous media. *Courier Corporation*.

Bear, J., Verruijt, A. (1987). Modelling Groundwater Flow and Pollution. *D. Reidel Publishers Company*, Dordrecht, The Netherlands. 414pp.

Beliaev, A.Y., & Schotting, R.J. (2002). Analysis of a new model for unsaturated flow in porous media including hysteresis and dynamic effects. *Computational Geosciences* 5, 345–368.

Beni A. N., Michael Kühn, Robert Meyer, & Christoph Clauser (2012). Numerical Modeling of a Potential Geological CO_2 Sequestration Site at Minden (Germany). *Environmental Modeling & Assessment*, August (2012), Volume 17, Issue 4, pp 337-351.

Bennion DB, & Bachu S. (2008). Drainage and imbibition relative permeability relationships for supercritical CO_2 /brine and H2S/brine systems in intergranular sandstone, carbonate, shale and anhydrite rocks. *SPE. Res.Eval. & Eng.*; 11, 487-96.

Benson, S.M., Li, B., Krause, M., Krevor, S., Kuo, C., & Pini, R. (2011). Investigations in Geologic Carbon Sequestration: Multiphase Flow of CO_2 and water in reservoir rocks. *Department of Energy Resources Engineering, School of Earth Sciences, Stanford University*, 1, 19-20.

Benson, S., Pini, R., Reynolds, C., & Krevor, S. (2012). Relative permeability analyses to describe multi-phase flow in CO_2 storage reservoirs. *Stanford: Global CCS Institute*.

Bentham, M., Mallows, T., Lowndes, J., & Green, A. (2014). CO_2 Storage Evaluation Database (CO_2 Stored). The UK's online storage atlas. *Energy Procedia*, 63, 5103-5113.

REFERENCES

Bergman, P. D., & Winter, E. M. (1995). Disposal of carbon dioxide in aquifers in the US. *Energy Conversion and Management*, *36*(6), 523-526.

Bethke, C.M., 1996. Geochemical Reaction Modeling. University Press, New York.

Bickle, M., Chadwick, A., Huppert, H. E., Hallworth, M., & Lyle, S. (2007). Modelling carbon dioxide accumulation at Sleipner: Implications for underground carbon storage. *Earth and planetary science letters*, 255(1), 164-176.

Bielinski, A. (2007). Numerical simulation of CO_2 sequestration in geological formations, *PhD thesis, University of Stuttgart.*

Birkholzer, J.T., Zhou, Q., Tsang, C.F. (2009). Large-scale impact of CO_2 storage in deep saline aquifers: a sensitivity study on the pressure response in stratified systems. *Int. J. Greenhouse Gas Control* 3 (2), 181–194.

Birkholzer, J.T., Zhou, Q., Rutqvist, J., Jordan, P., Zhang, K. & Tsang, C. (2007). Research project on CO_2 geological storage and groundwater resources: large-scale hydrogeological evaluation and impact on groundwater systems. Report LBNL-63544, *Lawrence Berkeley National Laboratory*, Berkeley, CA, USA.

Bobicki, E. R., Liu, Q., Xu, Z., & Zeng, H. (2012). Carbon capture and storage using alkaline industrial wastes. *Progress in Energy and Combustion Science*, *38*(2), 302-320.

Bondor, P. L. (1992). Applications of carbon dioxide in enhanced oil recovery. *Energy Conversion and Management*, 33(5), 579-586.

Bottero, S., Hassanizadeh, S. M., Kleingeld, P. J., & Heimovaara, T. J. (2011b). Nonequilibrium capillarity effects in two-phase flow through porous media at different scales. *Water Resources Research*, 47(10).

Bottero, S., Hassanizadeh, S.M., & Kleingeld, P.J. (2011;a). From Local Measurement to an Upscaled Capillary Pressure-Saturation Curve. *Trans Porous Med* (2011) 88:271-291.

Bottero, S., Hassanizadeh, S.M., Kleingeld, P.J., & Bezuijen, A. (2006). Experimental study of dynamic capillary pressure effect in two-phase flow in porous media. In: Proceedings of the XVI *International Conference on Computational Methods in Water Resources* (CMWR), Copenhagen, Denmark.

Brooks, A., Corey, A. (1964). Hydraulic Properties of Porous Media. Colorado State University *Hydrology Paper No.3*, For Collins, CO: Colorado, U.S.A.

Burdine, N. T. (1953). Relative permeability calculations from pore-size distribution data. *Petroleum Trans.,* . 1953; 198:71-77.

Camps-Roach, G., O'Carroll, D.M., Newson, T.A., Sakaki, T., & Illangasekare, T.H., (2010): Experimental investigation of dynamic effects in capillary pressure: grain size dependency and upscaling. *Water Resources Research*, 46(8), 1-13.

Chadwick, A., Arts, R., Bernstone, C., May, F., Thibeau, S., & Zweigel, P. (2008). Best practice for the storage of CO_2 in saline aquifers. *British Geological Survey Occasional Publication*, 14, 267.

Chang, Y. (1990). Development of a three-dimensional, equation-of-state compositional reservoir simulator for miscible gas flooding (*Doctoral dissertation, Ph. D. Dissertation, The University of Texas at Austin*).

Chasset, C., Jarsjö, J., Erlström, M., Cvetkovic, V., & Destouni, G. (2011). Scenario simulations of CO_2 injection feasibility, plume migration and storage in a saline aquifer, Scania, Sweden. *International Journal of Greenhouse Gas Control*, *5*(5), 1303-1318.

Chiquet, P., Daridon, J. L., Broseta, D., & Thibeau, S. (2007). CO_2/water interfacial tensions under pressure and temperature conditions of CO_2 geological storage. *Energy Conversion and Management*, 48, 736-744.

Civan, F. (2012). Temperature Dependency of Dynamic Coefficient for Nonequilibrium Capillary Pressure-Saturation Relationships. *American Institute of Chemical Engineers*, 58 (7), 2282-2285.

Civan, F. (2007). Critical Modification to the Vogel-Tammann-Fulcher Equation for Temperature Effect on the Density of Water. *Industrial Engineering and Chemistry Research Journal*, 46 (17), 5810 -5814.

Collins, R.E. (1961). Flow of Fluids through Porous Material. *Reinhold Publishing Corporation*, New York.

Comerlati, A., Pini, G., & Gambolati, G. (2005). Projection and partitioned solution for two-phase flow problems. *International Journal for numerical methods in fluids*, *49*(12), 1329-1346.

Computer Modeling Group (2012). User's Guide GEM, Advanced Compositional Reservoir Simulator (version 2012).

Computer Modeling Group (1990). STARS Technical Manual Version 4.0. Calgary.

Corey, A. T. (1977). Mechanics of heterogeneous fluids in porous media. *Water Resources Publications*.

Cormack, A.M. (1963). Representation of a function by its line integrals, with some radiological applications. *Journal of applied physics*, *34*(9), pp.2722-2727.

Cormack, A.M. (1964). Representation of a function by its line integrals, with some radiological applications. II. *Journal of Applied Physics*, *35*(10), pp.2908-2913.

Dahle, H.K., Celia, M.A., & Hassanizadeh, S.M. (2005). Bundle-of-tubes model for calculating dynamic effects in the capillary pressure–saturation relationship. *Transport in Porous Media* 58 (1–2), 5–22.

REFERENCES

Daneshfar, J., Hughes, R.G., & Civan, F. (2009). Feasibility Investigation and Modeling Analysis of CO_2 Sequestration in Arbuckle Formation Utilizing Salt Water Disposal Wells. *Journal of Energy Resources Technology*, 131(2), Article Number: 023301, pp. 1-10.

Das, D. B., Gill, B. S., Abidoye, L. K., & Khudaida, K. J. (2014). A numerical study of dynamic capillary pressure effect for supercritical carbon dioxide-water flow in porous domain. *AIChE Journal*, *60*(12), 4266-4278.

Das, DB & Mirzaei, M. (2013). Experimental measurement of dynamic effect in capillary pressure relationship for two-phase flow in weakly layered porous media. *AIChE Journal*, 59(5), 1723–1734.

Das, D. B., & Mirzaei, M. (2012). Dynamic effects in capillary pressure relationships for two-phase flow in porous media: Experiments and numerical analyses. *AIChE Journal*, *58*(12), 3891-3903.

Das, D., Gauldie, R., & Mirzaei, M. (2007). Dynamic Effects for Two-Phase Flow in Porous Media: Fluid Property Effects. *American Institute of Chemical Engineers*, 53(10), 2505-2520.

Das, D.B., Mirzaei, M., & Widdows, N. (2006). Non-uniqueness in capillary pressure–saturation–relative permeability relationships for two-phase flow in porous media: interplay between intensity and distribution of random microheterogeneities. *Chem. Eng. Sci.* 61, 6786–6803.

De Silva, P.N.K. & Ranjith, P.G. (2012). A study of methodologies for CO_2 storage capacity estimation of saline aquifers. *Fuel*, **93**(0), pp. 13-27.

Domenico, P. A., & Schwartz, F. W. (1998). *Physical and chemical hydrogeology* (Vol. 44). New York: Wiley.

Doughty, C. (2007). Modeling geologic storage of carbon dioxide: comparison of non-hysteretic and hysteretic characteristic curves. *Energy Conversion and Management*, 48(6), 1768-1781.

Doughty, C., & Pruess, K. (2004). Modeling supercritical carbon dioxide injection in heterogeneous porous media. *Vadose Zone Journal*, 3(3), 837-847.

Doughty, C., & Pruess, K. (1990). A similarity solution for two-phase fluid and heat flow near high-level nuclear waste packages emplaced in porous media. *International Journal of Heat and Mass Transfer*, 33(6), 1205-1222.

Dullien F. A. L., & G. K. Dhawan (1973): Photographic Size Determination of non-spherical objects. *Powder Technol.* 7, 305.

Dullien F. A. L., & P. N. Mehta (1971-1972): Particle Size and Pore (Void) Size Determination by Photomicrographic Methods. *Powder Technol*. 5, 179

REFERENCES

Edenhofer, O., Pichs-Madruga, R., Sokona, Y., Farahani, E., Kadner, S., Seyboth, K., & Minx, J. C. (2014). Climate change (2014): mitigation of climate change. *Contribution of Working Group III to the Fifth Assessment Report of the Intergovernmental Panel on Climate Change*, 511-597.

Ehlig-Economides, C. and Economides, M.J. (2010). Sequestering carbon dioxide in a closed underground volume. *Journal of Petroleum Science and Engineering*, 70(1), pp. 123-130.

Ennis-King, J., & L. Paterson (2003). Role of Convective Mixing in the Long-Term Storage of Carbon Dioxide in Deep Saline Formations, paper *SPE*-84344, presented at Society of Petroleum Engineers Annual Fall Technical Conference and Exhibition, Denver, CO, October.

Enick**,** R.M. & S.M. Klara (1990): CO_2 solubility in water and brine under reservoir conditions. *Chem. Eng. Comm*., 90, pp 23−33.

Fanchi, J. R., & Christiansen, R. L. (2015). PEH: Relative Permeability and Capillary Pressure. Accessed online at (http://petrowiki.org/Relative_permeability_and_capillary_pressure) on 21 August 2015,

Farber, L., Tardos, G., & Michaels, J. N. (2003). Use of X-ray tomography to study the porosity and morphology of granules. Powder Technology, 132(1), 57-63.

Fenghour, A., Wakeham, W.A., & Vesovic, V. (1998). The Viscosity of Carbon Dioxide. *Journal of Physical and Chemical Reference Data*, 27, 31-44.

Fitch, P.J.R. 2011. Heterogeneity in the Petrophysical Properties of Carbonate Reservoirs (*Doctoral dissertation, University of Leicester*).

Flannery, B. P., Deckman, H. W., Roberge, W. G., & D'AMICO, K. L. (1987). Three-dimensional X-ray microtomography. *Science*, *237*(4821), 1439-1444.

Flett, M. A., Gurton, R. M., & Taggart, I. J. (2005). Heterogeneous saline formations: Long-term benefits for geo-sequestration of greenhouse gases. In *Proceedings of the 7. international conference on greenhouse gas control technologies*.

Fučík, R., Mikyška, J., Sakaki, T., Beneš, M., & Illangasekare TH. (2010). Significance of Dynamic Effect in Capillarity during Drainage Experiments in Layered Porous Media, *Vadose Zone Journal*, *9*(3), pp.697-708.

FRAILEY, S.M. (2009). Methods for estimating CO_2 storage in saline reservoirs. *Energy Procedia*, 1(1), pp. 2769-2776.

Fučík Radek, Jiří Mikyška, Toshihiro Sakaki, Michal Beneš, & Tissa H. (2010). Illangasekare. Significance of dynamic effect in capillarity during drainage experiments in layered porous media. *Vadose Zone J.* 9:697–708, Aug. (2010).

Fujii, T., Sato, Y., Lin, H., Sasaki, K., Takahashi, T., Inomata, H., & Hashida, T. (2007). Evaluation of CO_2 Sorption Capacity of Granite for CO_2 Geological Sequestration. In

WATER DYANMICS: *4th International Workshop on Water Dynamics* (Vol. 898, No. 1, pp. 79-83). AIP Publishing.

Fujii, T., Gautier, S., Gland, N., Boulin, P., Norden, B., & Schmidt-Hattenberger, C. (2010). Sorption characteristics of CO_2 on rocks and minerals in storing CO_2 processes. *Natural Resources (2158-706X)*, 1(1), 1–10.

GeoQuest, S. (2003). ECLIPSE 100 Technical Description.

Ghaderi, S., Keith, D. & Leonenko, Y. (2009). Feasibility of injecting large volumes of CO_2 into aquifers. *Energy Procedia*, 1(1), pp. 3113-3120.

Giljarhus, K. E. T., Munkejord, S. T., & Skaugen, G. (2011). Solution of the Span–Wagner equation of state using a density–energy state function for fluid-dynamic simulation of carbon dioxide. *Industrial & Engineering Chemistry Research*, *51*(2), 1006-1014.

Giorgis, T., Carpita, M., & Battistelli, A. (2007). 2D modeling of salt precipitation during the injection of dry CO_2 in a depleted gas reservoir.*Energy Conversion and Management*, *48*(6), 1816-1826.

Goel, G & O'Carroll, DM (2011). Experimental investigation of nonequilibrium capillarity effects: Fluid viscosity effects. *Water Resources Research*, VOL. 47, W09507, doi:10.1029/2010WR009861, 2011.

Gonzalez-Nicolas, A., Cody, B. & Bau, D. (2011). Numerical simulation of CO_2 injection into deep saline aquifers. *Proceedings AGU Hydrology Days*.

Goodman, A., Bromhal, G., Strazisar, B., Rodosta, T., Guthrie, W.F., Allen, D. & Guthrie, G., (2013). Comparison of methods for geologic storage of carbon dioxide in saline formations. *International Journal of Greenhouse Gas Control*, 18, pp. 329-342.

Goodman, A., Hakala, A., Bromhal, G., Deel, D. Rodosta, T., Frailey, S., & Guthrie, G., (2011). US-DOE methodology for the development of geologic storage potential for carbon dioxide at the national and regional scale. *International Journal of Greenhouse Gas Control*, 5(4), 952-965.

Gorke U. J, Park C. H., Taron J., Wang W., & Olaf K. (2010). Modeling of Multiphase Transport and Deformation Process in Saline Aquifers During CO_2 Sequestration. *XVIII International Conference on Water Resources, Barcelona*, (2010).

Gough, C., Shackley, S., Holloway, S., Bentham, M., Bulatov, I., Mclachlan, C., Klemes, J., Purdt, R. & Cockerill, T. (2006). An integrated assessment of carbon dioxide capture and storage in the UK, In: 8th International Conference on greenhouse gas control technologies [proceedings]/[edited by Greenhouse Gas Control Technologies. Trondheim, Norway: GHGT8 2006, *Greenhouse Gas Control Technologies*.

Greenkorn, R. A. (1983). Flow phenomena in porous media: fundamentals and applications in petroleum, water and food production.

Gunter, W. D., Perkins, E. H., & Hutcheon, I. (2000). Aquifer disposal of acid gases: modelling of water–rock reactions for trapping of acid wastes. *Applied geochemistry*, *15*(8), 1085-1095.

Gunter, W. D., Perkins, E. H., & McCann, T. J. (1993). Aquifer disposal of CO_2-rich gases: reaction design for added capacity. *Energy Conversion and management*, *34*(9-11), 941-948.

Gunter, W. D., Bachu, S., Law, D. S., Marwaha, V., Drysdale, D. L., MacDonald, D. E., & McCann, T. J. (1996). Technical and economic feasibility of CO_2 disposal in aquifers within the Alberta sedimentary basin, Canada. *Energy Conversion and Management*, *37*(6), 1135-1142.

Gunter, W. D., Wiwehar, B., & Perkins, E. H. (1997). Aquifer disposal of CO_2-rich greenhouse gases: extension of the time scale of experiment for CO_2-sequestering reactions by geochemical modelling. *Mineralogy and Petrology*, *59*(1-2), 121-140.

Haas, J. L. (1976). Physical properties of the coexisting phases and thermochemical properties of the H_2O component in boiling NaCl solutions: 1421-A. *United States Government Printing Office, Washington, DC, 20402*.

Hammond, G. E., Lichtner, P. C., Lu, C., & Mills, R. T. (2012). PFLOTRAN: Reactive flow & transport code for use on laptops to leadership-class supercomputers. *Groundwater Reactive Transport Models*, 142-160.

Hanspal, N. S., Allison, B. A., Deka, L., & Das, D. B. (2013). Artificial neural network (ANN) modeling of dynamic effects on two-phase flow in homogenous porous media. *Journal of Hydroinformatics*, *15*(2), 540-554.

Hanspal, N. S., & Das, D. B. (2012). Dynamic effects on capillary pressure–Saturation relationships for two-phase porous flow: Implications of temperature. *AIChE Journal*, *58*(6), 1951-1965.

Hanyga, A., & Seredynska, M. (2005). A dynamic model of capillary hysteresis in immiscible fluid displacement. *Transport in Porous Media* 59, 249–265.

Hassanzadeh, H., Pooladi-Darvish, M. & Keith, D. (2009). Accelerating CO_2 Dissolution in Saline Aquifers for Geological Storage — Mechanistic and Sensitivity Studies. *Energy & Fuels*, **23**(6), pp. 3328-3336.

Hassanizadeh, S. M., Celia, M. A. & Dahle, H. K. (2002). Dynamic Effect in the Capillary Pressure-Saturation Relationship and its Impacts on Unsaturated Flow. *Vadose Zone Journal*, 1: p. 38-57.

Hassanizadeh, S. M., & Gray, W. G. (1993:a). Thermodynamic basis of capillary pressure in porous media. *Water Resources Research*, 29(10), 3389-3405.

Hassanizadeh, S. M., & Gray, W. G. (1993:b). Toward an improved description of the physics of two-phase flow. Advances in *Water Research*, 16, 53-67.

Hassanizadeh, S.M., & Gray, W.G. (1990). Mechanics and thermodynamics of multiphase flow in porous media including interphase boundaries. *Adv. Water Resour.* 13, 169–186.

Helmig, R., Weiss, A. & Wohlmuth, B. I. (2007). Dynamic Capillary Effects in Heterogeneous Porous Media. *Computers & Geosciences*, 11: p. 261-274.

Helmig, R. (1997). Multiphase Flow and Transport Processes in the Subsurface. *Springer*, Berlin. 367pp.

Holtz, M. H. (2002). Residual gas saturation to aquifer influx: A calculation method for 3-D computer reservoir model construction. In *SPE Gas Technology Symposium*. Society of Petroleum Engineers.

Hsu, S. Y., & Hilpert, M. (2011). Incorporation of dynamic capillary pressure into the Green–Ampt model for infiltration. *Vadose Zone Journal*, *10*(2), 642-653.

Huh, C., Kang, S. G., Hong, S., Choi, J. S., Baek, J. H., Lee, C. S., & Lee, J. S. (2009). CO_2 storage in marine geological structure: A review of latest progress and its application in Korea. *Energy Procedia*, *1*(1), 3993-4000.

Ide S. K., Jessen K., & Orr Jr. F. M. (2007). Storage of CO_2 in saline aquifers: Effects of gravity, viscous, and capillary forces on amount and timing of trapping. *International Journal of Greenhouse Gas Control* 1 (2007) 481 – 491.

IPCC *Intergovernmental Panel on Climate Change* (2001): Climate Change 2001: Synthesis Report. A Contribution of Working Groups I, II, and III to the Third Assessment Report of the Integovernmental Panel on Climate Change [Watson, R.T. and the Core Writing Team (eds.)]. Cambridge University Press, Cambridge, United Kingdom, and New York, NY, USA, 398 pp. Accessed online at (http://www.grida.no/publications/other/ipcc_tar/) on 11 August 2015.

IPCC *Intergovernmental Panel on Climate Change* 2005. Carbon dioxide capture and storage. IPCC Special Report. Cambridge University Press: Prepared by Working Group III of the *Intergovernmental Panel on Climate Change*.

IPCC, *Intergovernmental Panel on Climate Change* (2013). Climate Change 2013: The Physical Science Basis. Contribution of Working Group I to the Fifth Assessment Report of the Intergovernmental Panel on Climate Change [Stocker, T.F., D. Qin, G.-K. Plattner, M. Tignor, S.K. Allen, J. Boschung, A. Nauels, Y. Xia, V. Bex and P.M. Midgley (eds.)]. Cambridge University Press, Cambridge, United Kingdom and New York, NY, USA, 1535 pp.

Jikich, S. A., Sams, W. N., Bromhal, G., Pope, G., Gupta, N., & Smith, D. H. (2003). Carbon dioxide injectivity in brine reservoirs using horizontal wells. In *Second Annual Conference on Carbon Sequestration, Pittsburgh, PA* (pp. 5-8), May 2003.

Juanes, R. (2008). Nonequilibrium effects in models of three-phase flow in porous media. *Advances in Water Resources*, *31*(4), 661-673.

Juanes, R., Spiteri, E. J., Orr, F. M., & Blunt, M. J. (2006). Impact of relative permeability hysteresis on geological CO2 storage. Water Resources Research, 42(12).

Kaluarachchi, J.J. & Parker, J.C. 1992. Multiphase flow with a simplified model for oil entrapment. *Transport in Porous Media*, **7**, pp. 1-14.

Kalaydjian, F. (1992). Effect of the Flow Rate on an Imbibition Capillary Pressure Curve-Theory versus Experiment. In SCA European Core Analysis Symposium, *Institute Francais du Petrole, Rueil-Malmaison*, France, 175-194.

Kestin J, Khalifa HE, & Correia RJ (1981). Tables of dynamic and kinematic viscosity of aqueous KCl solutions in the temperature range 25–150 8C and the pressure range 0.1–35 MPa. *Journal of Physical Chemistry Reference Data*, 10, 57–70.

Khudaida, K.J. & Das, D.B. (2014). A numerical study of capillary pressure–saturation relationship for supercritical carbon dioxide (CO_2) injection in deep saline aquifer. *Chemical Engineering Research and Design*, *92*(12), 3017-3030.

Knauss K.G., Johnson J.W., & Steefel C. I. (2005). Evaluation of the impact of CO_2, co-contaminant gas, aqueous fluid and reservoir rock interactions on the geologic sequestration of CO_2. *Chem. Geol*, 217:339-350.

Kopp A., Class H., & Helmig R. (2009). Investigations on CO_2 storage capacity in saline aquifers Part 1. Dimensional analysis of flow processes and reservoir characteristics. *International Journal of Greenhouse Gas Control*, 3: 263-276.

Kopp, A., Class, H. & Helmig, R. (2009). Investigations on CO_2 storage capacity in saline aquifers—Part 2: Estimation of storage capacity coefficients. *International Journal of Greenhouse Gas Control*, **3**(3), pp. 277-287.

Kopp, A., Probst, P., Class, H., Hurter, S. & Helmig, R. (2009). Estimation of CO_2 storage capacity coefficients in geologic formations. *Energy Procedia*, **1**(1), pp. 2863-2870.

Kovscek, A. R. (2002). Screening criteria for CO_2 storage in oil reservoirs. *Petroleum Science and Technology*, 20(7-8), 841-866.

Kumar A., Noh M., Pope G. A., Sepehrnoori K., Bryant S. & Lake L. W. (2005). Reservoir Simulation of CO_2 Storage in Deep Saline Aquifers. *SPEJ*, 10 (3): 336-348.

Land, C.S. (1968). Calculation of imbibition relative permeability for two- and three-phase flow from rock properties. *Trans. Am. Inst. Min. Metall. Pet. Eng*, **243**, pp. 149-156.

Lasaga, A. C. (1984). Chemical kinetics of water-rock interactions. *Journal of Geophysical Research: Solid Earth*, *89*(B6), 4009-4025.

Lauffer, D. E. (1981). *U.S. Patent No. 4,291,271*. Washington, DC: U.S. Patent and Trademark Office.

Law, D. H. S., & Bachu, S. (1996). Hydrogeological and numerical analysis of CO_2 disposal in deep aquifers in the Alberta sedimentary basin. *Energy Conversion and Management*, *37*(6), 1167-1174.

Lokhorst, A., & Wildenborg, T. (2005). Introduction on CO_2 Geological storage-classification of storage options. *Oil & gas science and technology*, *60*(3), 513-515.

Lopez, O., Idowu, N., Rueslatten, H., Boassen, T., Leary, S., & Ringrose, P. (2011). Pore-scale modelling of CO_2 -brine flow properties at In Salah, Algeria. *Energy Procedia,* **4,** 3762-3769.

Lyle, S., Huppert, H. E., Hallworth, M., Bickle, M., & Chadwick, A. (2005). Axisymmetric gravity currents in a porous medium. *Journal of Fluid Mechanics*, *543*, 293-302.

Macminn, C.W. & Juanes, R. (2009). A mathematical model of the footprint of the CO_2 plume during and after injection in deep saline aquifer systems. *Energy Procedia*, **1**(1), pp. 3429-3436.

Manthey, S., Hassanizadeh, S.M., & Helmig R. (2005). Macro-scale dynamic effects in homogeneous and heterogeneous porous media. *Transport in Porous Media* 58 (1–2), 121–145.

May, F., Krull, P., & Gerling, P. (2004): CO_2 Storage Scenarios in North Germany. *GESTCO Project Case Studies.* – Bundesanstalt für Geowissenschaften und Rohstoffe, 50 p.

McCain Jr, W. D. (1991). Reservoir· Fluid Property Correlations-State of the Art. *SPE Reservoir Engineering*.

Mehnert, E., Damico, J., Frailey, S., Leetaru, H., Lin, Y. F., Okwen, R., & Valocchi, A. (2013). Development of a Basin-scale Model for CO_2 Sequestration in the Basal Sandstone Reservoir of the Illinois Basin-Issues, Approach and Preliminary Results. *Energy Procedia*, 37, 3850-3858.

Mercer, J. W., Pinder, G. F., & Donaldson, I. G. (1975). A Galerkin-finite element analysis of the hydrothermal system at Wairakei, New Zealand. *Journal of Geophysical Research*, 80(17), 2608-2621.

Metz, B., Davidson, O., De Coninck, H. C., Loos, M., & Meyer, L. A. (2005). IPCC special report on carbon dioxide capture and storage. Prepared by Working Group III of the Intergovernmental Panel on Climate Change. *IPCC, Cambridge University Press: Cambridge, United Kingdom and New York, USA*, *4*.

Meyer, C.A., R.B. McClintock, G.J. Silvestri, and R.C. Spencer. (1993). ASME Steam Tables, The American Society of Mechanical Engineers, New York.

Meyer CA, Mclintock RB, Silvestri GJ, & Spencer RC (1967). ASME Steam Tables: Thermodynamic and Transport for Steam and Water. 6th Ed. 1967:13–30, *American Society of Mechanical Engineers*, New York.

Michael, K., Golab, A., Shulakova, V., Ennis-King, J., Allinson, G., Sharma, S., & Aiken, T. (2010). Geological Storage of CO_2 in Saline Aquifers – A Review of the Experience from Existing Storage Operations. *International Journal of Greenhouse Gas Control*, **4**, 659-667.

Mirzaei, M., & Das, D.B. (2013). Experimental investigation of hysteretic dynamic effect in capillary pressure–saturation relationship for two-phase flow in porous media. *AIChE Journal*, 59(10), 3958–3974.

Mirzaei M, & Das D. B. (2007). Dynamic effects in capillary pressure saturations relationships for two-phase flow in 3D porous media: implications of micro-heterogeneities. *Chem Eng Sci.* (2007); 62:1927–1947.

Mitiku, A. B., Li, D., Bauer, S., & Beyer, C. (2013). Geochemical modelling of CO_2–water–rock interactions in a potential storage formation of the North German sedimentary basin. *Applied geochemistry*, *36*, 168-186.

Morrow, N. R. (1970). Physics and thermodynamics of capillary action in porous media. *Industrial & Engineering Chemistry*, 62(6), 32-56.

Mualem, Y. (1976). A new model for predicting the hydraulic conductivity of unsaturated porous media. *Water Resources Research*, **12**(3), pp. 513-522.

Müller, N. (2011). Supercritical CO_2-brine relative permeability experiments in reservoir rocks—Literature review and recommendations. *Transport in porous media*, 87(2), 367-383.

Neufeld, J. A., & Huppert, H. E. (2009). Modelling carbon dioxide sequestration in layered strata. *Journal of Fluid Mechanics*, 625, 353-370.

Nitao, J.J. (1988). Numerical Modeling of the Thermal and Hydrological Environment around a Nuclear Waste Package Using the Equivalent Continuum Approximation: Horizontal Emplacement. UCID-2144, *Lawrence Livermore National Laboratory*, Livermore, California.

Nordbotten, J. M., J. P. Nogues, & M. A. Celia. (2010), Appropriate Choice of Average Pressure for Upscaling Relative Permeability in Dynamic Flow Conditions, *SPE*, 228-237.

Nordbotten, J. M., Celia, M. A., Dahle, H. K., & Hassanizadeh, S. M. (2008). On the definition of macroscale pressure for multiphase flow in porous media. *Water Resources Research*, 44(6).

Nordbotten, J. M., Celia, M. A., Dahle, H. K., & Hassanizadeh, S. M. (2007). Interpretation of macroscale variables in Darcy's law. *Water resources research*, 43(8).

Nordbotten, J. M., Celia, M. A., & Bachu, S. (2005). Injection and storage of CO_2 in deep saline aquifers: Analytical solution for CO2 plume evolution during injection. *Transport in Porous media*, 58(3), 339-360.

Nordbotten, J.M., Celia, M.A., & Bachu, S. (2004a). Injection and Storage of CO_2 in Deep Saline Aquifers: Analytical Solution for CO_2 Plume Evolution During Injection. *Transport in Porous Media*, 58, 339-343.

Nordbotten, J. M., Celia, M. A. & Bachu, S (2004b). Analytical solutions for leakage rates through abandoned wells. *Water Resources Research*, 40(4).

OKWEN, R., STEWART, M., & CUNNINGHAM, J. (2011). Effect of well orientation (vertical vs. horizontal) and well length on the injection of CO_2 in deep saline aquifers. *Transport in porous media*, 90(1), 219-232.

OKWEN, R.T., STEWART, M.T. & CUNNINGHAM, J.A. (2010). Analytical solution for estimating storage efficiency of geologic sequestration of CO_2. *International Journal of Greenhouse Gas Control*, 4(1), pp. 102-107.

Orsini, P., Cantucci, B., & Quattrocchi, F. (2014). Large-scale Numerical Modelling of CO_2 Injection and Containment Phases for an Italian Near-coast Reservoir Using PFLOTRAN. *Energy Procedia*, *51*, 334-343.

O'Sullivan, M. J. (1981). A similarity method for geothermal well test analysis. *Water Resources Research*, 17(2), 390-398.

Oung, O., Hassanizadeh, S.M., & Bezuijen, A. (2005). Two-phase flow experiments in a geocentrifuge and the significance of dynamic capillary pressure effect. *Journal of Porous Media* 8 (3), 247–257.

Ozgur, E. & Gumrah, F. (2009). Diffusive and Convective Mechanisms during CO_2 Sequestration in Aquifers. Energy Sources, Part A: Recovery. *Utilization and Environmental Effects*, 31 (8), 698-709.

Perkins, E. H., Gunter, W. D., Nesbitt, H. W., & St-Arnaud, L. C. (1997). Critical review of classes of geochemical computer models adaptable for prediction of acidic drainage from mine waste rock. In *Proceedings of the 4th International Conference on Acid Rock Drainage* (pp. 587-601).

Perrin, J., Krause, M., Kuo, C., Miljkovic, L., Charoba, E., & Benson, S. (2009). Core-scale experimental study of relative permeability properties of CO_2 and brine in reservoir rocks. *Energy Procedia*, 1**,** 3515-3522.

Peszynska, M., & Yi, S. Y. (2008). Numerical methods for unsaturated flow with dynamic capillary pressure in heterogeneous porous media. *Int J Numer Anal Model*, *5*(Special Issue), 126-149.

Phillips, S. L., Igbene, A., Fair, J. A., Ozbek, H., & Tanana, M. (1981). *Technical databook for geothermal energy utilization* (No. LBL-12810). Lawrence Berkeley Lab., CA (USA).

Plug W. J. & Bruining J. (2007). Capillary pressure for the sand- CO_2 –Water system under various pressure conditions. Application to CO_2 sequestration. *Advances in Water Resources* 30- 2339 -2353.

Prausnitz J. M., R. N. Lichtenthaller, and E. G. De Azedevo. (1986). Molecular Thermodynamics of Fluid Phase Equilibria. Prentice Hall, New York.

Prevost J., Fuller R., Altevogt A. S., Bruant R., & Scherer G. (2005). Numerical Modelling of Carbon Dioxide Injection and Transport in Deep Saline Aquifers. *Greenhouse Gas Control Technologies*, 2: 2189-2193.

Pruess, K. (2011). ECO2M: a TOUGH2 fluid property module for mixtures of water, NaCl, and CO_2, including super-and sub-critical conditions, and phase change between liquid and gaseous CO_2. *Lawrence Berkeley National Laboratory*.

Pruess, K., & K. Zhang (2008), Numerical Modeling Studies of the Dissolution-Diffusion-Convective Process during CO_2 Storage in Saline Aquifers, Paper LBNL-1243E, *Lawrence Berkeley National Laboratory*, Berkeley, Calif.,

Pruess, K., Xu, T., Apps, J., & Garcı a, J. (2003). Numerical modeling of aquifer disposal of CO_2. Paper *SPE*-83695. SPE J. 49–60.

Pruess, K. & Garcia, J. (2002). Multiphase flow dynamics during CO_2 disposal into saline aquifers. *Environmental Geology*, 42(2-3), pp. 282-295.

Ranganathan, P., van Hemert, P., Rudolph, E. S. J., & Zitha, P. Z. (2011). Numerical modeling of CO_2 mineralisation during storage in deep saline aquifers. *Energy Procedia*, *4*, 4538-4545.

Redlich, O. & Kwong, J. N. S. (1949). On the thermodynamics of solutions. V. An equation of state. Fugacities of gaseous solutions. *Chemical Reviews* (44), 233–244.

Riaz, A., H. A. Tchelepi, & F. M. Orr (2006). Onset of Convection in a Gravitationally Unstable Diffusive Boundary Layer in Porous Media. *Journal of Fluid Mechanics*, 548:87–111.

Rochelle, C. A., Czernichowski-Lauriol, I., & Milodowski, A. E. (2004). The impact of chemical reactions on CO_2 storage in geological formations: a brief review. *Geological Society, London, Special Publications*, *233*(1), 87-106.

Rosenbauer, R. J., Koksalan, T., & Palandri, J. L. (2005). Experimental investigation of CO_2–brine–rock interactions at elevated temperature and pressure: implications for CO_2 sequestration in deep-saline aquifers. *Fuel processing technology*, *86*(14), 1581-1597.

Rowe Jr, A. M., & Chou, J. C. (1970). Pressure-volume-temperature-concentration relation of aqueous sodium chloride solutions. *Journal of Chemical and Engineering Data*, *15*(1), 61-66.

Sadras, V. & Bongiovanni, R. 2004. Use of Lorenz curves and Gini coefficients to assess yield inequality within paddocks. *Field Crops Research*, 90, 303-310.

Sakaki, T, O'Carroll, DM, & Illangasekare, TH. (2010). Direct Quantification of Dynamic Effects in Capillary Pressure for Drainage-Wetting Cycles. Vadose Zone Journal, 9(2): 424-437.

Scheidegger, A.E. (1974). Physics of Flow Through Porous Media. *University of Toronto Press*, Toronto.

Schnaar G., & Digiulio D. C. (2009). Computational Modeling of the Geologic Sequestration of Carbon Dioxide. *Vadose Zone Journal*, 8 (2): 389-403.

Shafrin, E. G., & Zisman, W. A. (1960). Constitutive relations in the wetting of low energy surfaces and the theory of the retraction method of preparing monolayers. *The Journal of Physical Chemistry*, 64(5), 519-524.

Shubao, T. I. A. N., Gang, L. E. I., Shunli, H. E., & Limin, Y. A. N. G. (2012). Dynamic effect of capillary pressure in low permeability reservoirs. *Petroleum Exploration and Development*, 39(3), 405-411.

Shukla, R., Ranjith, P., Haque, A. and Choi, X. 2010. A review of studies on CO_2 sequestration and caprock integrity. *Fuel*, 89, 2651-2664.

Silin D., Patzek T., & Benson S.M. (2009). A Model of Buoyancy-Driven Two-Phase Countercurrent Fluid Flow. *Transp Porous Med*, 76:449-469.

Sipilä, J., Teir, S., & Zevenhoven, R. (2008). Carbon dioxide sequestration by mineral carbonation Literature review update 2005–2007. *Report VT*, *1*, 2008.

Smith, M., Campbell, D., Mackay, E., & Polson, D. (2011). CO_2 aquifer storage site evaluation and monitoring. *Heriot Watt University, Edinburgh, ISBN*, 978-0.

Soldal, M. (2008). Caprock interaction with CO_2: Geomechanical and geochemical effects. Master Thesis in Geosciences, Faculty of Mathematics and Natural Sciences, University of Oslo.

Sonnenthale, E. (2001). Drift-Scale coupled processes *(DST and THC seepage)* models (No. MDL-NBS-HS-000001, REV 01, ICN 01). Yucca Mountain Project, Las Vegas, Nevada (US).

Span, R. & Wagner, W. (1996). A new equation of state for carbon dioxide covering the fluid region from the triple-point temperature to 1100 K at pressures up to 800 MPa. *Journal of physical and chemical reference data,* 25(6), pp. 1509-1596.

Spycher, N. & Pruess, K. (2010). A Phase-Partitioning Model for CO_2 –Brine Mixtures at Elevated Temperatures and Pressures: Application to CO_2 –Enhanced Geothermal Systems. Transport in Porous Media, doi:10.1007/s11242-009-9425-y, 82, pp. 173-196.

Spycher, N., Pruess, K. & ENNIS-KING, J. (2003). CO_2 -H_2O mixtures in the geological sequestration of CO_2. I. Assessment and calculation of mutual solubilities from 12 to 100°C and up to 600 bar. *Geochimica et Cosmochimica Acta*, 67(16), pp. 3015-3031.

Stanmore, B.R., & Gilot, P. (2005). Review - Calcination and Carbonation of Limestone During Thermal Cycling For CO_2 Sequestration. Fuel Processing Technology 86 (2005): 1707-1743.

Stauffer, P. H., Viswanathan, H. S., Pawar, R. J., & Guthrie, G. D. (2008). A system model for geologic sequestration of carbon dioxide. *Environmental science & technology*, *43*(3), 565-570.

Steefel, C. I., & Lasaga, A. C. (1994). A coupled model for transport of multiple chemical species and kinetic precipitation/dissolution reactions with application to reactive flow in single phase hydrothermal systems. *American Journal of science*, *294*(5), 529-592.

SZULCZEWSKI, M. L. (2013). The subsurface fluid mechanics of geologic carbon dioxide storage (*Doctoral dissertation, Massachusetts Institute of Technology*).

Szulczewski, M.L., Macminn, C.W., Herzog, H.J. & Juanes, R. (2011). How pressure buildup and CO_2 migration can both constrain storage capacity in deep saline aquifers. *Energy Procedia*, 4, pp. 4889–4896.

Szulczewski, M.L. (2009). Storage capacity and injection rate estimates for CO_2 sequestration in deep saline aquifers in the conterminous United States. *MSC dissertation, Massachusetts Institute of Technology*.

Topp, G. C., Klute, A., & Peters, D. B. (1967). Comparison of water content-pressure head data obtained by equilibrium, steady-state, and unsteady-state methods. *Soil Science Society of America Journal*, *31*(3), 312-314.

Tsang Chin-Fu, Birkholzer E. J., Rutqvist E. J. (2008). A comparative review of hydrologic issues involved in geologic storage of CO_2 and injection disposal of liquid waste. *Environ. Geol*. 54:1723–1737.

Van Genuchten, M.T. (1980). A closed-form equation for predicting the hydraulic conductivity of unsaturated soils. Soil Science Society of America Journal, 44(5), pp. 892-898.

Vilarrasa, V. (2014). Impact of CO_2 injection through horizontal and vertical wells on the caprock mechanical stability. *International Journal of Rock Mechanics and Mining Sciences*, 66, 151-159.

Viswanath, D. S., Ghosh, T. K., Prasad, D. H. L., Dutt, N. V. K., & Rani, K. Y (2007). Viscosity of liquids: theory, estimation, experiment, and data.

Wagner, W., Cooper, J. R., Dittmann, A., Kijima, J., Kretzschmar, H. J., Kruse, A., & Willkommen, T. (2000). The IAPWS industrial formulation 1997 for the thermodynamic properties of water and steam. *Journal of Engineering for Gas Turbines and Power*, 122(1), 150-184.

Wang, Y., Zhang, K. & Wu, N. (2013). Numerical Investigation of the Storage Efficiency Factor for CO_2 Geological Sequestration in Saline Formations. *Energy Procedia*, 37(0), pp. 5267-5274.

Wellington, S.L. & Vinegar, H.J. (1987). X-ray computerized tomography. *Journal of Petroleum Technology*, *39*(08), pp.885-898.

White, M.D., Watson, D.J., Bacon, D.H., White, S.K., Mcgrail, B.P. and Zhang, Z.F. (2013). STOMP- Subsurface Transport Over Multiple Phases- STOMP- CO_2 and - CO_2 e Guide, Version 1.1. *Pacific Northwest National Laboratory*, Prepared for the U.S. Department of Energy under Contract DE-AC05-76RL01830.

White, M.D., & Oostrom, M. (2006). STOMP, Subsurface Transport Over Multiple Phases, Version 4.0, User's Guide. Pacific Northwest National Laboratory, pp.13,14, 63-93.

White, M.D., Oostrom, M. & Lenhard, R.J. (2004). A Practical Model for Mobile, Residual, and Entrapped NAPL in Water-Wet Porous Media. Ground Water, 42(5), pp. 734-746.

White, M. D. & M. Oostrom (2003). STOMP subsurface transport over multiple phases, Version 3.0, An Introductory Short Course. *PNNL 1440, Pacific Northwest National Laboratory*, Richland, Washington. In Press.

Widarsono, Bambang; Muladi, Ari; Jaya, Indra. (2007). Vertical–Horizontal Permeability Ratio in Indonesian Sandstone and Carbonate Reservoirs. *Proceeding Simposium Nasional IATMI, 25 - 28 Juli 2007*, UPN "Veteran" Yogyakarta.

Xu, T., Apps, J. A., Pruess, K., & Yamamoto, H. (2007). Numerical modeling of injection and mineral trapping of CO_2 with H_2S and SO_2 in a sandstone formation. *Chemical Geology*, *242*(3), 319-346.

Xu, T., E. Sonnenthal, N. Spycher, & K. Pruess (2006). TOUGHREACT: A simulation program for non-isothermal multiphase reactive geochemical transport in variably saturated geologic media: Applications to geothermal injectivity and CO_2 geological sequestration. *Comput. Geosci*. 32:145–165.

Xu, T., Apps, J. A., & Pruess, K. (2004). Numerical simulation of CO_2 disposal by mineral trapping in deep aquifers. *Applied geochemistry*, *19*(6), 917-936.

Yang, F., Bai, B., Tang, D., Shari, D. & David, W. (2010). Characteristics of CO_2 sequestration in saline aquifers. *Petroleum Science*, **7**(1), *pp. 83-92.*

Zahid, U., Lim, Y., Jung, J. & Han, C. (2011). CO_2 geological storage: A review on present and future prospects. *Korean Journal of Chemical Engineering*, 28 (3), 674-685.

Zakkour, P., & Haines, M. (2007). Permitting issues for CO_2 capture, transport and geological storage: a review of Europe, USA, Canada and Australia. *International Journal of Greenhouse Gas Control*, 1(1), 94-100.

Zerai, B., Saylor, B. Z., & Matisoff, G. (2006). Computer simulation of CO_2 trapped through mineral precipitation in the Rose Run Sandstone, Ohio. *Applied Geochemistry*, 21(2), 223-240.

Zhang, K., Wu, Y. S., & Pruess, K. (2008). User's guide for TOUGH2-MP-a massively parallel version of the TOUGH2 code. *Report LBNL-315E, Lawrence Berkeley National Laboratory, Berkeley, CA.*

Zhao, X., Liao, X., Wang, W., Chen, C., Rui, Z. & Wang, H. (2014). The CO_2 storage capacity evaluation: Methodology and determination of key factors. *Journal of the Energy Institute,* **87**(4), pp. 297-305.

Zhou, Q., Birkholzer, J.T., Tsang, C. and Rutqvist, J. (2008). A method for quick assessment of CO_2 storage capacity in closed and semi-closed saline formations. I*nternational Journal of Greenhouse Gas Control*, 2(4), pp. 626-639.

Appendices

APPENDIX A-1:

Stomp-CO_2 Algorithmic Flow Chart

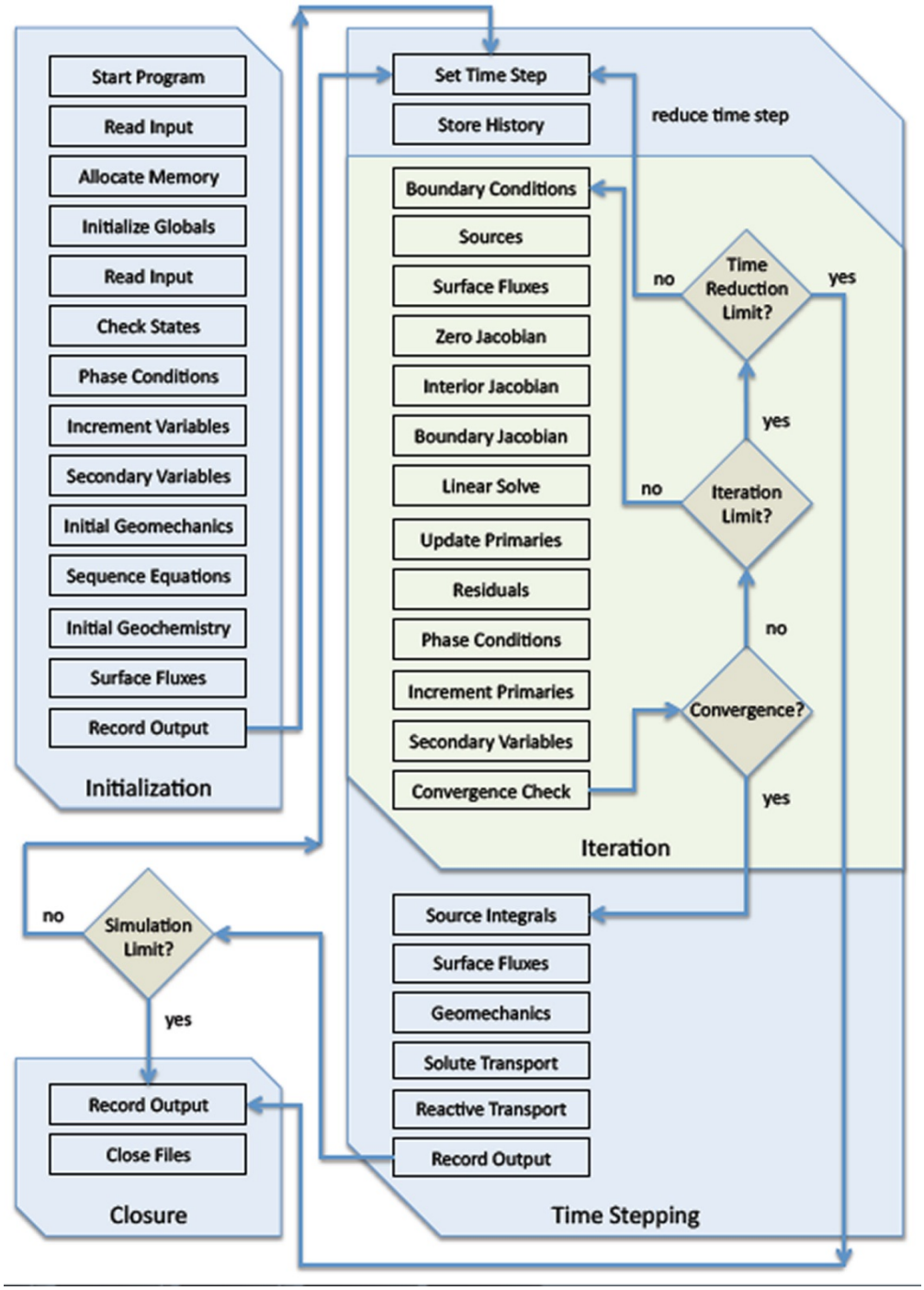

Figure A.1. STOMP-CO_2 and -CO_2e Algorithmic Flow Chart (after White et al., 2013)

APPENDIX A-2

STOMP-CO_2 Coordination System

```
Cylindrical Coordinate System

Coordinate System Dimensions
  Number of I-indexed Nodes:          75
  Number of J-indexed Nodes:           4
  Number of K-indexed Nodes:          24

Coordinate System Physical Dimensions

R-Direction Coordinates
  Rad(   1), m:  3.0000E-01  Rad(   2), m:  1.0300E+01  Rad(   3), m:
2.0300E+01  Rad(   4), m:  3.0300E+01  Rad(   5), m:  4.0300E+01
  Rad(   6), m:  5.0300E+01  Rad(   7), m:  7.0300E+01  Rad(   8), m:
9.0300E+01  Rad(   9), m:  1.1030E+02  Rad(  10), m:  1.3030E+02
  Rad(  11), m:  1.5030E+02  Rad(  12), m:  1.7030E+02  Rad(  13), m:
1.9030E+02  Rad(  14), m:  2.1030E+02  Rad(  15), m:  2.3030E+02
  Rad(  16), m:  2.5030E+02  Rad(  17), m:  2.8030E+02  Rad(  18), m:
3.1030E+02  Rad(  19), m:  3.4030E+02  Rad(  20), m:  3.7030E+02
  Rad(  21), m:  4.0030E+02  Rad(  22), m:  4.3030E+02  Rad(  23), m:
4.6030E+02  Rad(  24), m:  4.9030E+02  Rad(  25), m:  5.2030E+02
  Rad(  26), m:  5.5030E+02  Rad(  27), m:  5.8030E+02  Rad(  28), m:
6.1030E+02  Rad(  29), m:  6.4030E+02  Rad(  30), m:  6.7030E+02
  Rad(  31), m:  7.0030E+02  Rad(  32), m:  7.4030E+02  Rad(  33), m:
7.8030E+02  Rad(  34), m:  8.2030E+02  Rad(  35), m:  8.6030E+02
  Rad(  36), m:  9.0030E+02  Rad(  37), m:  9.4030E+02  Rad(  38), m:
9.8030E+02  Rad(  39), m:  1.0203E+03  Rad(  40), m:  1.0603E+03
  Rad(  41), m:  1.1003E+03  Rad(  42), m:  1.1403E+03  Rad(  43), m:
1.1803E+03  Rad(  44), m:  1.2203E+03  Rad(  45), m:  1.2603E+03
  Rad(  46), m:  1.3003E+03  Rad(  47), m:  1.3403E+03  Rad(  48), m:
1.3803E+03  Rad(  49), m:  1.4203E+03  Rad(  50), m:  1.4603E+03
  Rad(  51), m:  1.5003E+03  Rad(  52), m:  1.5503E+03  Rad(  53), m:
1.6003E+03  Rad(  54), m:  1.6503E+03  Rad(  55), m:  1.7003E+03
  Rad(  56), m:  1.7503E+03  Rad(  57), m:  1.8003E+03  Rad(  58), m:
1.8503E+03  Rad(  59), m:  1.9003E+03  Rad(  60), m:  1.9503E+03
  Rad(  61), m:  2.0003E+03  Rad(  62), m:  2.0503E+03  Rad(  63), m:
2.1003E+03  Rad(  64), m:  2.1503E+03  Rad(  65), m:  2.2003E+03
  Rad(  66), m:  2.2503E+03  Rad(  67), m:  2.3003E+03  Rad(  68), m:
2.3503E+03  Rad(  69), m:  2.4003E+03  Rad(  70), m:  2.4503E+03
  Rad(  71), m:  2.5003E+03  Rad(  72), m:  2.5503E+03  Rad(  73), m:
2.6003E+03  Rad(  74), m:  2.6503E+03  Rad(  75), m:  2.7003E+03
  Rad(  76), m:  2.7503E+03

Azimuthal-Direction Coordinates
  Azim(   1), deg:  0.0000E+00  Azim(   2), deg:  9.0000E+01
Azim(   3), deg:  1.8000E+02  Azim(   4), deg:  2.7000E+02  Azim(   5),
deg:  3.6000E+02
```

```
Vertical-Direction Coordinates
  Vert(   1), m:  0.0000E+00  Vert(   2), m:  4.0000E+00  Vert(   3),
m:  8.0000E+00  Vert(   4), m:  1.2000E+01  Vert(   5), m:  1.6000E+01
  Vert(   6), m:  2.0000E+01  Vert(   7), m:  2.4000E+01  Vert(   8),
m:  2.8000E+01  Vert(   9), m:  3.2000E+01  Vert(  10), m:  3.6000E+01
  Vert(  11), m:  4.0000E+01  Vert(  12), m:  4.4000E+01  Vert(  13),
m:  4.8000E+01  Vert(  14), m:  5.2000E+01  Vert(  15), m:  5.6000E+01
  Vert(  16), m:  6.0000E+01  Vert(  17), m:  6.4000E+01  Vert(  18),
m:  6.8000E+01  Vert(  19), m:  7.2000E+01  Vert(  20), m:  7.6000E+01
  Vert(  21), m:  8.0000E+01  Vert(  22), m:  8.4000E+01  Vert(  23),
m:  8.8000E+01  Vert(  24), m:  9.2000E+01  Vert(  25), m:  9.6000E+01
```

APPENDIX B : Grid Refinement Optimization

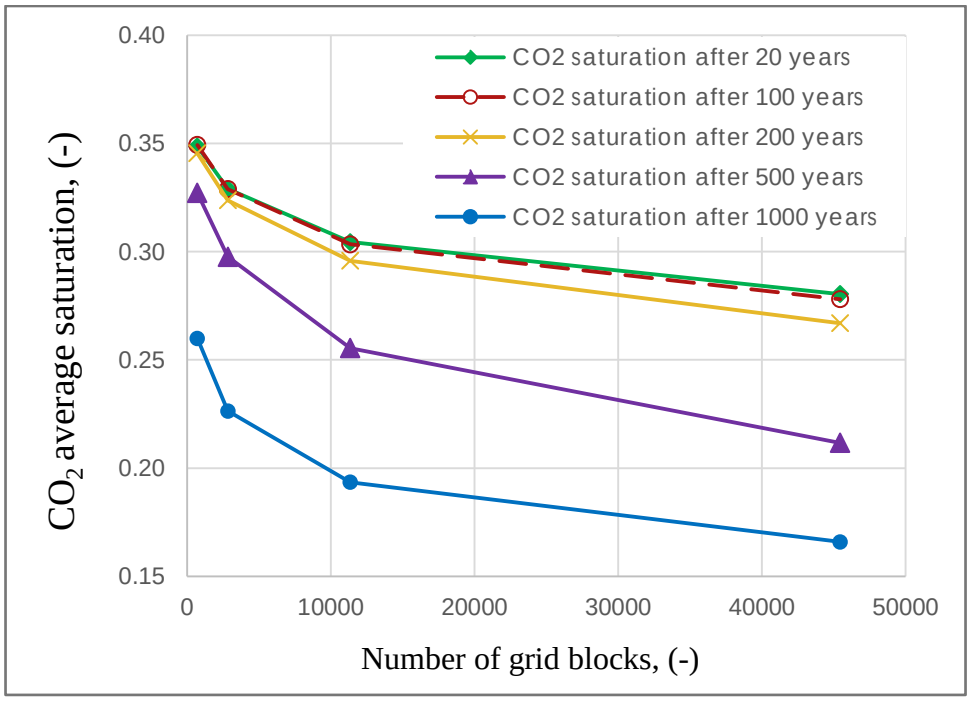

Figure B.1. The impact of grid refinement on the CO_2 saturation results.

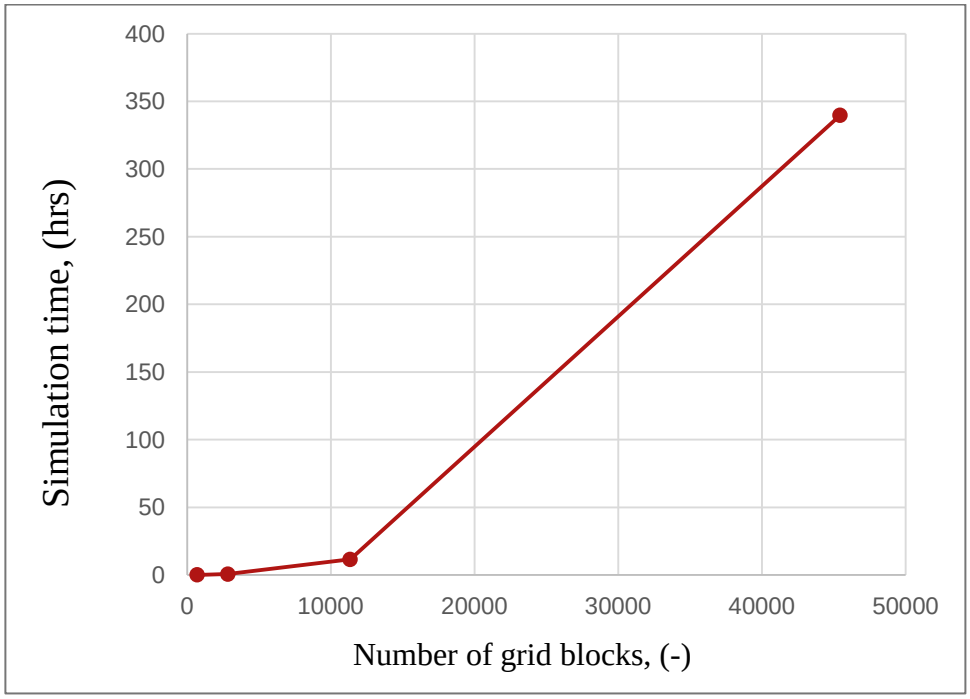

Figure B.2. Dependence of simulation execution time on grid refinement for 2D simulated domain.

APPENDIX: C-1

Homogeneous coarse sand 3D – vertical injection

#Y5, base case-small - Homogeneous Medium Permeability sands - 3D Coarse-grid, continueous injection in to lower section, Total Simulation Time=5000 yrs

~Simulation Title Card
1,
Simulation of CO2 Sequestration in Deep Saline Aquifers,
Kamal Khudaida,
Chemical Eng. Dep.,Loughborough University,
31 October 2014,
11:00 PM UK,
23,
CC**********
CC BRIEF DESCRIPTION OF PROJECT
CC**********
CC Cylindrical geometry
CC 3D Full scale, radial model
CC (phase 1=inactive water, phase 2 = water/co2, phase 3=co2/gas
CC Radius(m):2750 INJECTION FLUID: CO2
CC HEIGHT(m):96 INJECTION RATE:2.0 kg/s(each of the 16 nodes) INJECTION TIME (Total)=30 YEARS
CC WIDTH(m):
CC POROSITY: 0.35
CC ABS. PERM(MD): Vertical=304 md Horizontal=304 md 3-PHASE REL. PERM: water endpt.=1.0
CC TEMP(C): 37 WETTIBILITY:
CC INJECTION PRESSURE(MPa):Variable HYDROSTATIC PRESSURE (MPa)=11.2
CC SOR: G/O CAP. PRESSURE: *
CC SWC: DISPLACEMENT TYPE: HORIZONTAL
CC inject 30 yrs (continuously) and monitor for 4970 yrs, h2o k endpoint=1
CC ****NON-IDEAL MIXING, NO GRAVITY, WITH Pc, WITH X-FLOW
CC FILE NAME: Homogeneous 3D Coarse-grid intermingled sands and shales
CC CREATED BY Kamal Khudaida
CC MODIFIED ON 11/07/2015,
CC**********

~Solution Control Card
#excution mode to read initial conditions (normal, restart, initial conditions) Normal
normal,
#operational mode
H2O-NaCl-CO2,
#excution time periods

1,
#initial time,final time (injection time 30 yrs with lockup time 4970 yrs),init. time step, max. t. s.,t. s. accel. factor,Iteration,convergence
0,year,5000,year,1.e-3,s,20,year,1.125,32,1.e-06,
#max num. of time steps
100000,
#aqueous diffusion option,dissolved CO2 diffusion Coefficient,Dissolved Salt Diffusion Coefficient
Variable Aqueous Diffusion,
Variable Gas Diffusion,
#Number of Interfacial Averaging Variables
0,

~Grid Card
Cylindrical,
75,4,24,
#for grids with non-uniform spacing one plus the number of nodes entries are required for each grid #direction.Domain Radius=3200 m.
0.3,m,5@10.0,m,10@20.0,m,15@30.0,m,20@40.0,m,25@50.0,m,
0.0,deg,4@90.0,deg,
0.0,m,24@4.0,m,

~Rock/Soil Zonation Card
#number of zonation domains
1,
#rock or soil group with start and end indeces in each direction
Sands1,1,75,1,4,1,24,

~Mechanical Properties Card
#rock grouping name,density,total porosity,diffusive porosity,specific storativity,
#aq. tortuosity,gas tortuosity,tortuosity function,
Sands1,2650,kg/m^3,0.35,0.35,Pore Compressibility,4.5e-10,1/Pa,,,Millington and Quirk,

~Hydraulic Properties Card
#rock grouping name,intrinsic permeability in r,theta and z-directions, Pore-body Fractional Length, Fractional Critical Porosity (NaCl precipitation is NOT considered)
Sands1,3.0e-13,m^2,3.0e-13,m^2,3.0e-13,m^2,

~Saturation Function Card
#rock grouping name,Saturation Function option,alpha Parameter,units,n Parameter,minumum saturation,m Parameter,Maximum residual gas saturation (Sgrm)=-0.9696*0.35+0.5473 (after Holts 2002)
Sands1,Entrapment van Genuchten,2.735,1/m,1.667,0.2,0.4,0.208,

~Aqueous Relative Permeability Card

#rock grouping name,Permeability Function Option,van Genuchten m parameter,Irreducible Aqueous Saturation
Sands1,Mualem Irreducible,0.4,0.2,

~Gas Relative Permeability Card
#rock grouping name,Permeability Function Option,van Genuchten m parameter
Sands1,Mualem,0.4,

~Salt Transport Card
#rock grouping name,Longitudinal Dispersivity (equal zero for homogeneous),
Units,Transverse Dispersivity, Units
Sands1,0.0,m,0.0,m,

~Initial Conditions Card
#initial saturation option,initial saturation option,
Aqueous Pressure,Gas Pressure,
#number of initial conditions domains
4,
#Variable Name Option,pressure,unit,X,y,z,-Dir. Gradient, Units (1/m),I,j,k-Start Index, I,j,k-End Index,
Aqueous Pressure,11.2e+6,Pa,,,,,-10.012e+3,1/m,1,75,1,4,1,24,
Gas Pressure,11.2e+6,Pa,,,,,-10.012e+3,1/m,1,75,1,4,1,24,
Temperature,37.0,C,,,,,,,1,75,1,4,1,24,
Salt Mass Fraction,0.032,,,,,,,,1,75,1,4,1,24,

~Source Card
1,
Gas Mass Rate,Water-Vapor Mass Fraction,1,1,1,4,2,5,2,
#injection of 2.0 kg/s of CO2 over 4 nodes at 4 of 90 degrees angles for cylindrical shape (i.e. 4 x 4 = 16 nodes) represents 1 MMT/year for the whole cylindrical domain
0,s,,,2.0,kg/s,0.0,
30,year,,,2.0,kg/s,0.0,

~Boundary Conditions Card
1,
#Boundary Surface Direction Option,Aqueous-Phase Boundary Type Option,Gas-Phase Boundary Type Option,Salt Boundary Type Option
East,Aqueous Initial Condition,Gas Initial Condition,Salt Initial Condition,
75,75,1,4,1,24,1,
0,s,,,,,,,,
#West,Aqu. Zero Flux,Gas Hydraulic Gradient,Aqueous Mass Fraction,
#Boundary Time, Units (s),Aqueous Pressure, Units (Pa),Aqueous Dissolved- CO2-Relative Saturation,Gas Pressure, Units(Pa),Water-Vapor Relative Humidity,Salt Mass Fraction, Null,
#1,1,1,4,2,5,2,
#0,day,,,0.0,18.e+6,Pa,1.0,0.2,,
#7300,day,,,0.0,18.e+6,Pa,1.0,0.2,,

~Output Options Card
#Number of Reference Nodes
3,
#I Index, J Index, K Index
#R=150 m Z= 16, 48, 84 Ref Nodes=
10,1,4,
10,1,12,
10,1,21,
#Reference Node Screen Output Frequency,Reference Node Output File Frequency,Output Time Units(s),
#Output Length Units (m),Screen Significant Digits,Output File Significant Digits,Plot File Significant Digits
1,1,year,m,deg,6,6,6,
#Number of Reference Node Variables
17,
#Reference Node Variable Option, Reference Node Variable Units,
Aqueous Saturation,,
Gas Saturation,,
Aqueous Pressure,Pa,
Gas Pressure,Pa,
CO2 Aqueous Mass Fraction,,
CO2 Gas Mass Fraction,,
trapped gas saturation,,
#total CO2 mass in the computational domain
Integrated CO2 Mass,MMT,
Integrated Aqueous CO2 Mass,MMT,
#total CO2 mass in the gas phase in the computational domain
Integrated Gas CO2 Mass,MMT,
Integrated CO2 Trapped-Gas Mass,MMT,
Aqueous Density,kg/m^3,
Gas Density,kg/m^3,
Aqueous Relative Permeability,,
Gas Relative Permeability,,
Salt Aqueous Mass Fraction,,
Diffusive Porosity,,
#Number of Plot File Ouput Times
13,
10,year,
20,year,
30,year,
40,year,
50,year,
100,year,
200,year,
500,year,
1000,year,

2000,year,
3000,year,
4000,year,
5000,year,
#Number of Plot File Variables
13,
#Plot File Variable Option, Plot File Variable Units
Aqueous Saturation,,
Gas Saturation,,
Aqueous Pressure,Pa,
Gas Pressure,Pa,
CO2 Aqueous Mass Fraction,,
CO2 Gas Mass Fraction,,
Trapped Gas Saturation,,
Aqueous Density,kg/m^3,
Gas Density,kg/m^3,
Aqueous Relative Permeability,,
Gas Relative Permeability,,
Salt Aqueous Mass Fraction,,
Diffusive Porosity,,
~Surface Flux Card
2,
Total CO2 Flux,kg/s,kg,West,1,1,1,4,2,5,
Aqueous Mass Flux,kg/s,kg,East,75,75,1,4,1,24,

APPENDIX: C-2

Homogeneous coarse sand 2D – vertical injection

```
#Y5, base case-small - Homogeneous Medium Permeability sands - 2D Coarse-grid,
continueous injection in to lower section, Total Simulation Time=5000 yrs

~Simulation Title Card
1,
Simulation of CO2 Sequestration in Deep Saline Aquifers,
Kamal Khudaida,
Chemical Eng. Dep.,Loughborough University,
31 October 2014,
11:00 PM UK,
23,
CC*************************************************************************
CC BRIEF DESCRIPTION OF PROJECT
CC*************************************************************************
CC Cylindrical geometry
CC 2D Full scale, radial model
CC (phase 1=inactive water, phase 2 = water/co2, phase 3=co2/gas
CC Radius(m):2750  INJECTION FLUID: CO2
CC HEIGHT(m):96 INJECTION RATE:2.0 kg/s(each of the 16 nodes)      INJECTION TIME
(Total)=30 YEARS
CC WIDTH(m):
CC POROSITY: 0.35
CC ABS. PERM(MD): Vertical=304 md   Horizontal=304 md        3-PHASE REL. PERM:
        water endpt.=1.0
CC TEMP(C): 37                  WETTIBILITY:
CC INJECTION PRESSURE(MPa):Variable    HYDROSTATIC PRESSURE (MPa)=11.2
CC SOR: G/O CAP. PRESSURE: *
CC SWC: DISPLACEMENT TYPE: HORIZONTAL
CC inject 30 yrs (continuously) and monitor for 4970 yrs,    h2o k endpoint=1
CC ****NON-IDEAL MIXING, NO GRAVITY, WITH Pc, WITH X-FLOW
CC FILE NAME: Homogeneous 2D Coarse-grid intermingled sands and shales
CC CREATED BY Kamal Khudaida
CC MODIFIED ON 11/07/2015,
CC*************************************************************************

~Solution Control Card
#excution mode to read initial conditions (normal, restart, initial conditions) Normal
normal,
#operational mode
H2O-NaCl-CO2,
#excution time periods
```

1,
#initial time,final time (injection time 30 yrs with lockup time 4970 yrs),init. time step, max. t. s.,t. s. accel. factor,Iteration,convergence
0,year,5000,year,1.e-3,s,20,year,1.125,32,1.e-06,
#max num. of time steps
100000,
#aqueous diffusion option,dissolved CO2 diffusion Coefficient,Dissolved Salt Diffusion Coefficient
Variable Aqueous Diffusion,
Variable Gas Diffusion,
#Number of Interfacial Averaging Variables
0,

~Grid Card
Cylindrical,
75,1,24,
#for grids with non-uniform spacing one plus the number of nodes entries are required for each grid #direction.Domain Radius=3200 m.
0.3,m,5@10.0,m,10@20.0,m,15@30.0,m,20@40.0,m,25@50.0,m,
0.0,deg,90.0,deg,
0.0,m,24@4.0,m,

~Rock/Soil Zonation Card
#number of zonation domains
1,
#rock or soil group with start and end indeces in each direction
Sands1,1,75,1,1,1,24,

~Mechanical Properties Card
#rock grouping name,density,total porosity,diffusive porosity,specific storativity,
#aq. tortuosity,gas tortuosity,tortuosity function,
Sands1,2650,kg/m^3,0.35,0.35,Pore Compressibility,4.5e-10,1/Pa,,,Millington and Quirk,

~Hydraulic Properties Card
#rock grouping name,intrinsic permeability in r,theta and z-directions, Pore-body Fractional Length, Fractional Critical Porosity (NaCl precipitation is NOT considered)
Sands1,3.0e-13,m^2,3.0e-13,m^2,3.0e-13,m^2,

~Saturation Function Card
#rock grouping name,Saturation Function option,alpha Parameter,units,n Parameter,minumum saturation,m Parameter,Maximum residual gas saturation (Sgrm)=-0.9696*0.35+0.5473 (after Holts 2002)
Sands1,Entrapment van Genuchten,2.735,1/m,1.667,0.2,0.4,0.208,

~Aqueous Relative Permeability Card

#rock grouping name,Permeability Function Option,van Genuchten m parameter,Irreducible Aqueous Saturation
Sands1,Mualem Irreducible,0.4,0.2,

~Gas Relative Permeability Card
#rock grouping name,Permeability Function Option,van Genuchten m parameter
Sands1,Mualem,0.4,

~Salt Transport Card
#rock grouping name,Longitudinal Dispersivity (equal zero for homogeneous),
Units,Transverse Dispersivity, Units
Sands1,0.0,m,0.0,m,

~Initial Conditions Card
#initial saturation option,initial saturation option,
Aqueous Pressure,Gas Pressure,
#number of initial conditions domains
4,
#Variable Name Option,pressure,unit,X,y,z,-Dir. Gradient, Units (1/m),I,j,k-Start Index, I,j,k-End Index,
Aqueous Pressure,11.2e+6,Pa,,,,,-10.012e+3,1/m,1,75,1,1,1,24,
Gas Pressure,11.2e+6,Pa,,,,,-10.012e+3,1/m,1,75,1,1,1,24,
Temperature,37.0,C,,,,,,,1,75,1,1,1,24,
Salt Mass Fraction,0.032,,,,,,,,1,75,1,1,1,24,

~Source Card
1,
Gas Mass Rate,Water-Vapor Mass Fraction,1,1,1,1,2,5,2,
#injection of 2.0 kg/s of CO2 over 4 nodes at 90 degrees angles for cylindrical shape (i.e. 4 x 4 = 16 nodes) represents 1 MMT/year for the whole cylindrical domain
0,s,,,2.0,kg/s,0.0,
30,year,,,2.0,kg/s,0.0,

~Boundary Conditions Card
1,
#Boundary Surface Direction Option,Aqueous-Phase Boundary Type Option,Gas-Phase Boundary Type Option,Salt Boundary Type Option
East,Aqueous Initial Condition,Gas Initial Condition,Salt Initial Condition,
75,75,1,1,1,24,1,
0,s,,,,,,,,
#West,Aqu. Zero Flux,Gas Hydraulic Gradient,Aqueous Mass Fraction,
#Boundary Time, Units (s),Aqueous Pressure, Units (Pa),Aqueous Dissolved- CO2-Relative Saturation,Gas Pressure, Units(Pa),Water-Vapor Relative Humidity,Salt Mass Fraction, Null,
#1,1,1,1,2,5,2,
#0,day,,,0.0,18.e+6,Pa,1.0,0.2,,
#7300,day,,,0.0,18.e+6,Pa,1.0,0.2,,

```
~Output Options Card
#Number of Reference Nodes
3,
#I Index, J Index, K Index
#R=150 m Z=16, 48, 84 Ref Nodes=
10,1,4,
10,1,12,
10,1,21,
#Reference Node Screen Output Frequency,Reference Node Output File Frequency,Output Time Units(s),
#Output Length Units (m),Screen Significant Digits,Output File Significant Digits,Plot File Significant Digits
1,1,year,m,deg,6,6,6,
#Number of Reference Node Variables
17,
#Reference Node Variable Option, Reference Node Variable Units,
Aqueous Saturation,,
Gas Saturation,,
Aqueous Pressure,Pa,
Gas Pressure,Pa,
CO2 Aqueous Mass Fraction,,
CO2 Gas Mass Fraction,,
trapped gas saturation,,
#total CO2 mass in the computational domain
Integrated CO2 Mass,MMT,
Integrated Aqueous CO2 Mass,MMT,
#total CO2 mass in the gas phase in the computational domain
Integrated Gas CO2 Mass,MMT,
Integrated CO2 Trapped-Gas Mass,MMT,
Aqueous Density,kg/m^3,
Gas Density,kg/m^3,
Aqueous Relative Permeability,,
Gas Relative Permeability,,
Salt Aqueous Mass Fraction,,
Diffusive Porosity,,
#Number of Plot File Ouput Times
13,
10,year,
20,year,
30,year,
40,year,
50,year,
100,year,
200,year,
500,year,
1000,year,
```

2000,year,
3000,year,
4000,year,
5000,year,
#Number of Plot File Variables
13,
#Plot File Variable Option, Plot File Variable Units
Aqueous Saturation,,
Gas Saturation,,
Aqueous Pressure,Pa,
Gas Pressure,Pa,
CO2 Aqueous Mass Fraction,,
CO2 Gas Mass Fraction,,
Trapped Gas Saturation,,
Aqueous Density,kg/m^3,
Gas Density,kg/m^3,
Aqueous Relative Permeability,,
Gas Relative Permeability,,
Salt Aqueous Mass Fraction,,
Diffusive Porosity,,
~Surface Flux Card
2,
Total CO2 Flux,kg/s,kg,West,1,1,1,1,2,5,
Aqueous Mass Flux,kg/s,kg,East,75,75,1,1,1,24,

APPENDIX: C-3

homogeneous coarse sand – vertical injection

```
#Y5, case001- Homogeneous Medium Permeability sands - 2D Coarse-grid, continueous injection in to lower section, Total Simulation Time=5000 yrs

~Simulation Title Card
1,
Simulation of CO2 Sequestration in Deep Saline Aquifers,
Kamal Khudaida,
Chemical Eng. Dep.,Loughborough University,
31 October 2014,
11:00 PM UK,
23,
CC*************************************************************************
CC BRIEF DESCRIPTION OF PROJECT
CC*************************************************************************
CC Cylindrical geometry
CC 2D Full scale,radial model
CC (phase 1=inactive water, phase 2 = water/co2, phase 3=co2/gas
CC Radius(m):6000  INJECTION FLUID: CO2
CC HEIGHT(m):96 INJECTION RATE:1.0 kg/s(each of 32 nodes)          INJECTION TIME (Total)=30 YEARS
CC WIDTH(m):
CC POROSITY: 0.35
CC ABS. PERM(MD): Vertical=304 md   Horizontal=304 md       3-PHASE REL. PERM:
        water endpt.=1.0
CC TEMP(C): 37                WETTIBILITY:
CC INJECTION PRESSURE(MPa):Variable    HYDROSTATIC PRESSURE (MPa)=11.2
CC SOR: G/O CAP. PRESSURE: *
CC SWC: DISPLACEMENT TYPE: HORIZONTAL
CC inject 30 yrs (continuously) and monitor for 4970 yrs,    h2o k endpoint=1
CC ****NON-IDEAL MIXING, NO GRAVITY, WITH Pc, WITH X-FLOW
CC FILE NAME: Homogeneous 2D Coarse-grid intermingled sands and shales
CC CREATED BY Kamal Khudaida
CC MODIFIED ON 04/03/2015,
CC*************************************************************************

~Solution Control Card
#excution mode to read initial conditions (normal, restart, initial conditions) Normal
normal,
#operational mode
H2O-NaCl-CO2,
#excution time periods
```

1,
#initial time,final time (injection time 30 yrs with lockup time 4970 yrs),init. time step, max. t. s.,t. s. accel. factor,Iteration,convergence
0,year,5000,year,1.e-3,s,20,year,1.125,32,1.e-06,
#max num. of time steps
100000,
#aqueous diffusion option,dissolved CO2 diffusion Coefficient,Dissolved Salt Diffusion Coefficient
Variable Aqueous Diffusion,
Variable Gas Diffusion,
#Number of Interfacial Averaging Variables
0,

~Grid Card
Cylindrical,
88,1,24,
#for grids with non-uniform spacing one plus the number of nodes entries are required for each grid #direction.Domain Radius=6000 m.
0.3,m,10@20.0,m,14@40.0,m,18@60.0,m,22@80.0,m,24@100.0,m,
0.0,deg,45.0,deg,
0.0,m,6@5.0,m,3@1.0,m,6@5.0,m,3@1.0,m,6@5.0,m,

~Rock/Soil Zonation Card
#number of zonation domains
1,
#rock or soil group with start and end indeces in each direction
Sands1,1,88,1,1,1,24,

~Mechanical Properties Card
#rock grouping name,density,total porosity,diffusive porosity,specific storativity,
#aq. tortuosity,gas tortuosity,tortuosity function,
Sands1,2650,kg/m^3,0.35,0.35,Pore Compressibility,4.5e-10,1/Pa,,,Millington and Quirk,

~Hydraulic Properties Card
#rock grouping name,intrinsic permeability in r,theta and z-directions, Pore-body Fractional Length, Fractional Critical Porosity (NaCl precipitation is NOT considered)
Sands1,3.0e-13,m^2,3.0e-13,m^2,3.0e-13,m^2,

~Saturation Function Card
#rock grouping name,Saturation Function option,alpha Parameter,units,n Parameter,minumum saturation,m Parameter,Maximum residual gas saturation (Sgrm)=-0.9696*0.35+0.5473 (after Holts 2002)
Sands1,Entrapment van Genuchten,2.735,1/m,1.667,0.2,0.4,0.208,

~Aqueous Relative Permeability Card

#rock grouping name,Permeability Function Option,van Genuchten m parameter,Irreducible Aqueous Saturation
Sands1,Mualem Irreducible,0.4,0.2,

~Gas Relative Permeability Card
#rock grouping name,Permeability Function Option,van Genuchten m parameter
Sands1,Mualem,0.4,

~Salt Transport Card
#rock grouping name,Longitudinal Dispersivity (equal zero for homogeneous),
Units,Transverse Dispersivity, Units
Sands1,0.0,m,0.0,m,

~Initial Conditions Card
#initial saturation option,initial saturation option,
Aqueous Pressure,Gas Pressure,
#number of initial conditions domains
4,
#Variable Name Option,pressure,unit,X,y,z,-Dir. Gradient, Units (1/m),I,j,k-Start Index, I,j,k-End Index,
Aqueous Pressure,11.2e+6,Pa,,,,,-10.012e+3,1/m,1,88,1,1,1,24,
Gas Pressure,11.2e+6,Pa,,,,,-10.012e+3,1/m,1,88,1,1,1,24,
Temperature,37.0,C,,,,,,,1,88,1,1,1,24,
Salt Mass Fraction,0.032,,,,,,,,1,88,1,1,1,24,

~Source Card
1,
Gas Mass Rate,Water-Vapor Mass Fraction,1,1,1,1,2,5,2,
#injection of 1.0 kg/s of CO2 over 4 nodes at 8 of 45 degrees angles for cylindrical shape (i.e. 8 x 4 = 32 nodes) represents 1 MMT/year for the whole cylindrical domain
0,s,,,1.0,kg/s,0.0,
30,year,,,1.0,kg/s,0.0,

~Boundary Conditions Card
1,
#Boundary Surface Direction Option,Aqueous-Phase Boundary Type Option,Gas-Phase Boundary Type Option,Salt Boundary Type Option
East,Aqueous Initial Condition,Gas Initial Condition,Salt Initial Condition,
88,88,1,1,1,24,1,
0,s,,,,,,,,
#West,Aqu. Zero Flux,Gas Hydraulic Gradient,Aqueous Mass Fraction,
#Boundary Time, Units (s),Aqueous Pressure, Units (Pa),Aqueous Dissolved- CO2-Relative Saturation,Gas Pressure, Units(Pa),Water-Vapor Relative Humidity,Salt Mass Fraction, Null,
#1,1,1,1,2,5,2,
#0,day,,,0.0,18.e+6,Pa,1.0,0.2,,
#7300,day,,,0.0,18.e+6,Pa,1.0,0.2,,

~Output Options Card
#Number of Reference Nodes
3,
#I Index, J Index, K Index
#R=0 m Z=15,48,81 Ref Nodes=265,1057,1849
#R=200 m Z=48 Ref Nodes=
11,1,4,
11,1,13,
11,1,22,
#R=590m Z=15,48,81 Ref Nodes=296,1088,1880
#R=500 m Z=15,48,81 Ref Nodes=309,1101,1893
#R=1000 m Z=15,48,81 Ref Nodes=333,1125,1917
#Reference Node Screen Output Frequency,Reference Node Output File Frequency,Output Time Units(s),
#Output Length Units (m),Screen Significant Digits,Output File Significant Digits,Plot File Significant Digits
1,1,year,m,deg,6,6,6,
#Number of Reference Node Variables
17,
#Reference Node Variable Option, Reference Node Variable Units,
Aqueous Saturation,,
Gas Saturation,,
Aqueous Pressure,Pa,
Gas Pressure,Pa,
CO2 Aqueous Mass Fraction,,
CO2 Gas Mass Fraction,,
trapped gas saturation,,
#total CO2 mass in the computational domain
Integrated CO2 Mass,MMT,
Integrated Aqueous CO2 Mass,MMT,
#total CO2 mass in the gas phase in the computational domain
Integrated Gas CO2 Mass,MMT,
Integrated CO2 Trapped-Gas Mass,MMT,
Aqueous Density,kg/m^3,
Gas Density,kg/m^3,
Aqueous Relative Permeability,,
Gas Relative Permeability,,
Salt Aqueous Mass Fraction,,
Diffusive Porosity,,
#Number of Plot File Ouput Times
25,
1,year,
5,year,
10,year,
15,year,
20,year,

25,year,
30,year,
35,year,
40,year,
50,year,
100,year,
200,year,
300,year,
400,year,
500,year,
750,year,
1000,year,
1500,year,
2000,year,
2500,year,
3000,year,
3500,year,
4000,year,
4500,year,
5000,year,
#Number of Plot File Variables
13,
#Plot File Variable Option, Plot File Variable Units
Aqueous Saturation,,
Gas Saturation,,
Aqueous Pressure,Pa,
Gas Pressure,Pa,
CO2 Aqueous Mass Fraction,,
CO2 Gas Mass Fraction,,
Trapped Gas Saturation,,
Aqueous Density,kg/m^3,
Gas Density,kg/m^3,
Aqueous Relative Permeability,,
Gas Relative Permeability,,
Salt Aqueous Mass Fraction,,
Diffusive Porosity,,
~Surface Flux Card
2,
Total CO2 Flux,kg/s,kg,West,1,1,1,1,2,5,
Aqueous Mass Flux,kg/s,kg,East,88,88,1,1,1,24,

APPENDIX: C-4

Uniform Heterogeneous coarse sand – vertical continuous injection

```
#Y5, case002- Uniform-heterogeneous Medium Permeability intermingled sands and shales -
2D Coarse-grid Domain, Total Simulation Time=5000 yrs, investigation of heterogeniety effect

~Simulation Title Card
1,
Simulation of CO2 Sequestration in Deep Saline Aquifers,
Kamal Khudaida,
Chemical Eng. Dep.,Loughborough University,
16 January 2015,
11:30 PM UK,
23,
CC**********************************************************************
CC BRIEF DESCRIPTION OF PROJECT
CC**********************************************************************
CC Cylindrical geometry
CC 2D Full scale,radial model
CC (phase 1=inactive water, phase 2 = water/co2, phase 3=co2/gas
CC Radius(m):6000  INJECTION FLUID: CO2
CC HEIGHT(m):96 INJECTION RATE:1.0 kg/s (each of the 32 nodes)     INJECTION TIME
(Total)=30 YEARS
CC WIDTH(m):
CC POROSITY: 0.35, 0.1025
CC ABS. PERM(MD): 10.13-304 md          3-PHASE REL. PERM:         water endpt.=1.0
CC TEMP(C): 37                  WETTIBILITY:
CC INJECTION PRESSURE(MPa):Variable    HYDROSTATIC PRESSURE (MPa)=11.2
CC SOR: G/O CAP. PRESSURE: *
CC SWC: DISPLACEMENT TYPE: HORIZONTAL
CC inject 30 yrs (continuously) and monitor for 4970 yrs, h2o k endpoint=1
CC ****NON-IDEAL MIXING, NO GRAVITY, WITH Pc, WITH X-FLOW
CC FILE NAME: Uniform Heterogeneous 2D Coarse-grid intermingled sands and shales
CC CREATED BY Kamal Khudaida
CC MODIFIED ON 04/03/2015,
CC**********************************************************************

~Solution Control Card
#excution mode to read initial conditions (normal, restart, initial conditions)Normal
normal,
#operational mode
H2O-NaCl-CO2,
#excution time periods
1,
```

#initial time,final time (injection time 30 yrs + lockup time 4970 yrs),init. time step, max. t. s.,t. s. accel. factor,Iteration,convergence
0,year,5000,year,1.e-3,s,20,year,1.125,32,1.e-06,
#max num. of time steps
100000,
#aqueous diffusion option,dissolved CO2 diffusion Coefficient,Dissolved Salt Diffusion Coefficient
Variable Aqueous Diffusion,
Variable Gas Diffusion,
#Number of Interfacial Averaging Variables
0,

~Grid Card
Cylindrical,
88,1,24,
#for grids with non-uniform spacing one plus the number of nodes entries are required for each grid #direction.Domain Radius=6000 m.
0.3,m,10@20.0,m,14@40.0,m,18@60.0,m,22@80.0,m,24@100.0,m,
0.0,deg,45.0,deg,
0.0,m,6@5.0,m,3@1.0,m,6@5.0,m,3@1.0,m,6@5.0,m,

~Rock/Soil Zonation Card
#number of zonation domains
5,
#rock or soil group with start and end indeces in each direction
Sands1,1,88,1,1,1,6,
Shale1,1,88,1,1,7,9,
Sands2,1,88,1,1,10,15,
Shale2,1,88,1,1,16,18,
Sands3,1,88,1,1,19,24,

~Mechanical Properties Card
#rock grouping name,density,total porosity,diffusive porosity,specific storativity,
#aq. tortuosity,gas tortuosity,tortuosity function,
Sands1,2650,kg/m^3,0.35,0.35,Pore Compressibility,4.5e-10,1/Pa,,,Millington and Quirk,
Shale1,2650,kg/m^3,0.1025,0.1025,Pore Compressibility,4.5e-10,1/Pa,,,Millington and Quirk,
Sands2,2650,kg/m^3,0.35,0.35,Pore Compressibility,4.5e-10,1/Pa,,,Millington and Quirk,
Shale2,2650,kg/m^3,0.1025,0.1025,Pore Compressibility,4.5e-10,1/Pa,,,Millington and Quirk,
Sands3,2650,kg/m^3,0.35,0.35,Pore Compressibility,4.5e-10,1/Pa,,,Millington and Quirk,

~Hydraulic Properties Card
#rock grouping name,intrinsic permeability in r,theta and z-directions, Pore-body Fractional Length, Fractional Critical Porosity (NaCl precipitation is NOT considered)
Sands1,3.0e-13,m^2,3.0e-13,m^2,3.0e-13,m^2,
Shale1,1.0e-14,m^2,1.0e-14,m^2,1.0e-14,m^2,
Sands2,3.0e-13,m^2,3.0e-13,m^2,3.0e-13,m^2,
Shale2,1.0e-14,m^2,1.0e-14,m^2,1.0e-14,m^2,

Sands3,3.0e-13,m^2,3.0e-13,m^2,3.0e-13,m^2,

~Saturation Function Card
#rock grouping name,Saturation Function option,alpha Parameter,units,n Parameter,minumum saturation,m Parameter,Maximum residual gas saturation (Sgrm)=-0.9696*0.35+0.5473 (after Holts 2002)
Sands1,Entrapment van Genuchten,2.735,1/m,1.667,0.2,0.4,0.208,
Shale1,Entrapment van Genuchten,0.158,1/m,1.667,0.2,0.4,0.448,
Sands2,Entrapment van Genuchten,2.735,1/m,1.667,0.2,0.4,0.208,
Shale2,Entrapment van Genuchten,0.158,1/m,1.667,0.2,0.4,0.448,
Sands3,Entrapment van Genuchten,2.735,1/m,1.667,0.2,0.4,0.208,

~Aqueous Relative Permeability Card
#rock grouping name,Permeability Function Option,van Genuchten m parameter,Irreducible Aqueous Saturation
Sands1,Mualem Irreducible,0.4,0.2,
Shale1,Mualem Irreducible,0.4,0.2,
Sands2,Mualem Irreducible,0.4,0.2,
Shale2,Mualem Irreducible,0.4,0.2,
Sands3,Mualem Irreducible,0.4,0.2,

~Gas Relative Permeability Card
#rock grouping name,Permeability Function Option,van Genuchten m parameter
Sands1,Mualem,0.4,
Shale1,Mualem,0.4,
Sands2,Mualem,0.4,
Shale2,Mualem,0.4,
Sands3,Mualem,0.4,

~Salt Transport Card
#rock grouping name,Longitudinal Dispersivity (equal zero for homogeneous),
Units,Transverse Dispersivity, Units
Sands1,0.0,m,0.0,m,
Shale1,0.0,m,0.0,m,
Sands2,0.0,m,0.0,m,
Shale2,0.0,m,0.0,m,
Sands3,0.0,m,0.0,m,

~Initial Conditions Card
#initial saturation option,initial saturation option,
Aqueous Pressure,Gas Pressure,
#number of initial conditions domains
4,
#Variable Name Option,pressure,unit,X,y,z,-Dir. Gradient, Units (1/m),I,j,k-Start Index, I,j,k-End Index,
Aqueous Pressure,11.2e+6,Pa,,,,,-10.012e+3,1/m,1,88,1,1,1,24,
Gas Pressure,11.2e+6,Pa,,,,,-10.012e+3,1/m,1,88,1,1,1,24,

Temperature,37.0,C,,,,,,,1,88,1,1,1,24,
Salt Mass Fraction,0.032,,,,,,,,1,88,1,1,1,24,

~Source Card
1,
Gas Mass Rate,Water-Vapor Mass Fraction,1,1,1,1,2,5,2,
#injection of 1.0 kg/s of CO2 over 4 nodes at 8 of 45 degrees angles for cylindrical shape (i.e. 8 x 4 = 32 nodes) represents 1 MMT/year for the whole cylindrical domain
0,s,,,1.0,kg/s,0.0,
30,year,,,1.0,kg/s,0.0,

~Boundary Conditions Card
1,
#Boundary Surface Direction Option,Aqueous-Phase Boundary Type Option,Gas-Phase Boundary Type Option,Salt Boundary Type Option
East,Aqueous Initial Condition,Gas Initial Condition,Salt Initial Condition,
88,88,1,1,1,24,1,
0,s,,,,,,,,
#West,Aqu. Zero Flux,Gas Hydraulic Gradient,Aqueous Mass Fraction,
#Boundary Time, Units (s),Aqueous Pressure, Units (Pa),Aqueous Dissolved- CO2-Relative Saturation,Gas Pressure, Units(Pa),Water-Vapor Relative Humidity,Salt Mass Fraction, Null,
#1,1,1,1,2,5,2,
#0,day,,,0.0,18.e+6,Pa,1.0,0.2,,
#7300,day,,,0.0,18.e+6,Pa,1.0,0.2,,

~Output Options Card
#Number of Reference Nodes
3,
#I Index, J Index, K Index
#R=0 m Z=15,48,81 Ref Nodes=265,1057,1849
#R=200 m Z=15,48,81 Ref Nodes=275,1067,1859
11,1,4,
11,1,13,
11,1,22,
#R=200 m Z=15,48,81 Ref Nodes=280,1072,1864
#R=590m Z=15,48,81 Ref Nodes=296,1088,1880
#R=500 m Z=15,48,81 Ref Nodes=309,1101,1893
#R=1000 m Z=15,48,81 Ref Nodes=333,1125,1917
#Reference Node Screen Output Frequency,Reference Node Output File Frequency,Output Time Units(s),
#Output Length Units (m),Screen Significant Digits,Output File Significant Digits,Plot File Significant Digits
1,1,year,m,deg,6,6,6,
#Number of Reference Node Variables
17,
#Reference Node Variable Option, Reference Node Variable Units,
Aqueous Saturation,,

Gas Saturation,,
Aqueous Pressure,Pa,
Gas Pressure,Pa,
CO2 Aqueous Mass Fraction,,
CO2 Gas Mass Fraction,,
trapped gas saturation,,
#total CO2 mass in the computational domain
Integrated CO2 Mass,MMT,
Integrated Aqueous CO2 Mass,MMT,
#total CO2 mass in the gas phase in the computational domain
Integrated Gas CO2 Mass,MMT,
Integrated CO2 Trapped-Gas Mass,MMT,
Aqueous Density,kg/m^3,
Gas Density,kg/m^3,
Aqueous Relative Permeability,,
Gas Relative Permeability,,
Salt Aqueous Mass Fraction,,
Diffusive Porosity,,
#Number of Plot File Ouput Times
25,
1,year,
5,year,
10,year,
15,year,
20,year,
25,year,
30,year,
35,year,
40,year,
50,year,
100,year,
200,year,
300,year,
400,year,
500,year,
750,year,
1000,year,
1500,year,
2000,year,
2500,year,
3000,year,
3500,year,
4000,year,
4500,year,
5000,year,
#Number of Plot File Variables
13,

#Plot File Variable Option, Plot File Variable Units
Aqueous Saturation,,
Gas Saturation,,
Aqueous Pressure,Pa,
Gas Pressure,Pa,
CO2 Aqueous Mass Fraction,,
CO2 Gas Mass Fraction,,
Trapped Gas Saturation,,
Aqueous Density,kg/m^3,
Gas Density,kg/m^3,
Aqueous Relative Permeability,,
Gas Relative Permeability,,
Salt Aqueous Mass Fraction,,
Diffusive Porosity,,
~Surface Flux Card
4,
Total CO2 Flux,kg/s,kg,West,1,1,1,1,1,24,
Aqueous Mass Flux,kg/s,kg,East,88,88,1,1,1,24,
Total CO2 Flux,kg/s,kg,Top,1,88,1,1,7,9,
Total CO2 Flux,kg/s,kg,Top,1,88,1,1,16,18,

APPENDIX: C-5

Non-Uniform Heterogeneous coarse sand – vertical continuous injection

```
#Y5, case003- Nonuniform-heterogeneous Medium Permeability intermingled sands and shales
- 2D Coarse-grid Total Simulation Time=5000 yrs, investigation of heterogeniety effect

~Simulation Title Card
1,
Simulation of CO2 Sequestration in Deep Saline Aquifers,
Kamal Khudaida,
Chemical Eng. Dep.,Loughborough University,
03 November 2014,
01:00 PM UK,
23,
CC**********************************************************************
CC BRIEF DESCRIPTION OF PROJECT
CC**********************************************************************
CC Cylindrical geometry
CC 2D Full scale,radial model
CC (phase 1=inactive water, phase 2 = water/co2, phase 3=co2/gas
CC Radius(m):6000  INJECTION FLUID: CO2
CC HEIGHT(m):96 INJECTION RATE:1.0 kg/s (each of the 32 nodes)     INJECTION TIME
(Total)=30 YEARS
CC WIDTH(m):
CC POROSITY: 0.35, 0.1025
CC ABS. PERM(MD): 10.13-304 md          3-PHASE REL. PERM:         water endpt.=1.0
CC TEMP(C): 37                  WETTIBILITY:
CC INJECTION PRESSURE(MPa):Variable    HYDROSTATIC PRESSURE (MPa)=11.2
CC SOR: G/O CAP. PRESSURE: *
CC SWC: DISPLACEMENT TYPE: HORIZONTAL
CC inject 30 yrs (continuously) and monitor for 4970 yrs, h2o k endpoint=1
CC ****NON-IDEAL MIXING, NO GRAVITY, WITH Pc, WITH X-FLOW
CC FILE NAME: Nonuniform Heterogeneous Coarse-grid Medium Permeability intermingled
sands and shales
CC CREATED BY Kamal Khudaida
CC MODIFIED ON 05/03/2015,
CC**********************************************************************

~Solution Control Card
#excution mode to read initial conditions (normal, restart, initial conditions)Normal
normal,
#operational mode
H2O-NaCl-CO2,
#excution time periods
```

1,
#initial time,final time (injection time 30 yrs + lockup time 4970 yrs),init. time step, max. t. s.,t. s. accel. factor,Iteration,convergence
0,year,5000,year,1.e-3,s,20,year,1.125,32,1.e-06,
#max num. of time steps
100000,
#aqueous diffusion option,dissolved CO2 diffusion Coefficient,Dissolved Salt Diffusion Coefficient
Variable Aqueous Diffusion,
Variable Gas Diffusion,
#Number of Interfacial Averaging Variables
0,

~Grid Card
Cylindrical,
88,1,24,
#for grids with non-uniform spacing one plus the number of nodes entries are required for each grid #direction.Domain Radius=6000 m.
0.3,m,10@20.0,m,14@40.0,m,18@60.0,m,22@80.0,m,24@100.0,m,
0.0,deg,45.0,deg,
0.0,m,6@5.0,m,3@1.0,m,6@5.0,m,3@1.0,m,6@5.0,m,

~Rock/Soil Zonation Card
#number of zonation domains
97,
#rock or soil group with start and end indeces in each direction
Sands1,1,88,1,1,1,4,
Sands1,1,75,1,1,5,5,
Shale1,76,79,1,1,5,5,
Sands1,80,88,1,1,5,5,
Sands1,1,13,1,1,6,6,
Shale1,14,19,1,1,6,6,
Sands1,20,32,1,1,6,6,
Shale1,33,37,1,1,6,6,
Sands1,38,74,1,1,6,6,
Shale1,75,75,1,1,6,6,
Sands2,76,78,1,1,6,6,
Shale1,79,79,1,1,6,6,
Sands1,80,88,1,1,6,6,
Shale1,1,13,1,1,7,9,
Sands2,14,19,1,1,7,9,
Shale1,20,22,1,1,7,9,
Sands1,23,31,1,1,7,9,
Shale1,32,33,1,1,7,9,
Sands2,34,37,1,1,7,9,
Shale1,38,38,1,1,7,9,
Sands1,39,44,1,1,7,9,

Shale1,45,57,1,1,7,9,
Sands1,58,64,1,1,7,9,
Shale1,65,75,1,1,7,9,
Sands2,76,78,1,1,7,9,
Shale1,79,88,1,1,7,9,
Sands2,1,21,1,1,10,10,
Shale1,22,22,1,1,10,10,
Sands1,23,31,1,1,10,10,
Shale1,32,33,1,1,10,10,
Sands2,34,37,1,1,10,10,
Shale1,38,45,1,1,10,10,
Sands2,46,56,1,1,10,10,
Shale1,57,57,1,1,10,10,
Sands1,58,64,1,1,10,10,
Shale1,65,65,1,1,10,10,
Sands2,66,88,1,1,10,10,
Sands2,1,22,1,1,11,11,
Shale1,23,33,1,1,11,11,
Sands2,34,57,1,1,11,11,
Shale1,58,64,1,1,11,11,
Sands2,65,88,1,1,11,11,
Sands2,1,88,1,1,12,13,
Sands2,1,51,1,1,14,14,
Shale2,52,60,1,1,14,14,
Sands2,61,76,1,1,14,14,
Shale2,77,81,1,1,14,14,
Sands2,82,88,1,1,14,14,
Sands2,1,30,1,1,15,15,
Shale2,31,32,1,1,15,15,
Sands2,33,50,1,1,15,15,
Shale2,51,51,1,1,15,15,
Sands3,52,58,1,1,15,15,
Shale2,59,60,1,1,15,15,
Sands2,61,76,1,1,15,15,
Shale2,77,77,1,1,15,15,
Sands3,78,80,1,1,15,15,
Shale2,81,81,1,1,15,15,
Sands2,82,88,1,1,15,15,
Shale2,1,23,1,1,16,18,
Sands2,24,28,1,1,16,18,
Shale2,29,30,1,1,16,18,
Sands3,31,32,1,1,16,18,
Shale2,33,39,1,1,16,18,
Sands2,40,41,1,1,16,18,
Shale2,42,51,1,1,16,18,
Sands3,52,58,1,1,16,18,
Shale2,59,60,1,1,16,18,

Sands2,61,65,1,1,16,18,
Shale2,66,75,1,1,16,18,
Sands2,76,76,1,1,16,18,
Shale2,77,77,1,1,16,18,
Sands3,78,80,1,1,16,18,
Shale2,81,88,1,1,16,18,
Sands3,1,20,1,1,19,19,
Shale2,21,23,1,1,19,19,
Sands2,24,28,1,1,19,19,
Shale2,29,29,1,1,19,19,
Sands3,30,38,1,1,19,19,
Shale2,39,39,1,1,19,19,
Sands2,40,41,1,1,19,19,
Shale2,42,42,1,1,19,19,
Sands3,43,60,1,1,19,19,
Shale2,61,65,1,1,19,19,
Sands3,66,74,1,1,19,19,
Shale2,75,75,1,1,19,19,
Sands2,76,76,1,1,19,19,
Shale2,77,77,1,1,19,19,
Sands3,78,88,1,1,19,19,
Sands3,1,23,1,1,20,20,
Shale2,24,28,1,1,20,20,
Sands3,29,39,1,1,20,20,
Shale2,40,41,1,1,20,20,
Sands3,42,75,1,1,20,20,
Shale2,76,76,1,1,20,20,
Sands3,77,88,1,1,20,20,
Sands3,1,88,1,1,21,24,

~Mechanical Properties Card
#rock grouping name,density,total porosity,diffusive porosity,specific storativity,
#aq. tortuosity,gas tortuosity,tortuosity function,
Sands1,2650,kg/m^3,0.35,0.35,Pore Compressibility,4.5e-10,1/Pa,,,Millington and Quirk,
Shale1,2650,kg/m^3,0.1025,0.1025,Pore Compressibility,4.5e-10,1/Pa,,,Millington and Quirk,
Sands2,2650,kg/m^3,0.35,0.35,Pore Compressibility,4.5e-10,1/Pa,,,Millington and Quirk,
Shale2,2650,kg/m^3,0.1025,0.1025,Pore Compressibility,4.5e-10,1/Pa,,,Millington and Quirk,
Sands3,2650,kg/m^3,0.35,0.35,Pore Compressibility,4.5e-10,1/Pa,,,Millington and Quirk,

~Hydraulic Properties Card
#rock grouping name,intrinsic permeability in r,theta and z-directions, Pore-body Fractional Length, Fractional Critical Porosity (NaCl precipitation is NOT considered)
Sands1,3.0e-13,m^2,3.0e-13,m^2,3.0e-13,m^2,
Shale1,1.0e-14,m^2,1.0e-14,m^2,1.0e-14,m^2,
Sands2,3.0e-13,m^2,3.0e-13,m^2,3.0e-13,m^2,
Shale2,1.0e-14,m^2,1.0e-14,m^2,1.0e-14,m^2,
Sands3,3.0e-13,m^2,3.0e-13,m^2,3.0e-13,m^2,

~Saturation Function Card
#rock grouping name,Saturation Function option,alpha Parameter,units,n Parameter,minumum saturation,m Parameter,Maximum residual gas saturation (Sgrm)=-0.9696*0.35+0.5473 (after Holts 2002)
Sands1,Entrapment van Genuchten,2.735,1/m,1.667,0.2,0.4,0.208,
Shale1,Entrapment van Genuchten,0.158,1/m,1.667,0.2,0.4,0.448,
Sands2,Entrapment van Genuchten,2.735,1/m,1.667,0.2,0.4,0.208,
Shale2,Entrapment van Genuchten,0.158,1/m,1.667,0.2,0.4,0.448,
Sands3,Entrapment van Genuchten,2.735,1/m,1.667,0.2,0.4,0.208,

~Aqueous Relative Permeability Card
#rock grouping name,Permeability Function Option,van Genuchten m parameter,Irreducible Aqueous Saturation
Sands1,Mualem Irreducible,0.4,0.2,
Shale1,Mualem Irreducible,0.4,0.2,
Sands2,Mualem Irreducible,0.4,0.2,
Shale2,Mualem Irreducible,0.4,0.2,
Sands3,Mualem Irreducible,0.4,0.2,

~Gas Relative Permeability Card
#rock grouping name,Permeability Function Option,Irreducible Gas Saturation, Irreducible Aqueous Saturation
Sands1,Mualem,0.4,
Shale1,Mualem,0.4,
Sands2,Mualem,0.4,
Shale2,Mualem,0.4,
Sands3,Mualem,0.4,

~Salt Transport Card
#rock grouping name,Longitudinal Dispersivity (equal zero for homogeneous), Units,Transverse Dispersivity, Units
Sands1,0.0,m,0.0,m,
Shale1,0.0,m,0.0,m,
Sands2,0.0,m,0.0,m,
Shale2,0.0,m,0.0,m,
Sands3,0.0,m,0.0,m,

~Initial Conditions Card
#initial saturation option,initial saturation option,
Aqueous Pressure,Gas Pressure,
#number of initial conditions domains
4,
#Variable Name Option,pressure,unit,X,y,z,-Dir. Gradient, Units (1/m),I,j,k-Start Index, I,j,k-End Index,
Aqueous Pressure,11.2e+6,Pa,,,,,-10.012e+3,1/m,1,88,1,1,1,24,
Gas Pressure,11.2e+6,Pa,,,,,-10.012e+3,1/m,1,88,1,1,1,24,

Temperature,37.0,C,,,,,,,1,88,1,1,1,24,
Salt Mass Fraction,0.032,,,,,,,,1,88,1,1,1,24,

~Source Card
1,
Gas Mass Rate,Water-Vapor Mass Fraction,1,1,1,1,2,5,2,
#injection of 1.0 kg/s of CO2 over 4 nodes at 8 of 45 degrees angles for cylindrical shape (i.e. 8 x 4 = 32 nodes) represents 1 MMT/year for the whole cylindrical domain
0,s,,,1.0,kg/s,0.0,
30,year,,,1.0,kg/s,0.0,

~Boundary Conditions Card
1,
#Boundary Surface Direction Option,Aqueous-Phase Boundary Type Option,Gas-Phase Boundary Type Option,Salt Boundary Type Option
East,Aqueous Initial Condition,Gas Initial Condition,Salt Initial Condition,
88,88,1,1,1,24,1,
0,s,,,,,,,,
#West,Aqu. Zero Flux,Gas Hydraulic Gradient,Aqueous Mass Fraction,
#Boundary Time, Units (s),Aqueous Pressure, Units (Pa),Aqueous Dissolved- CO2-Relative Saturation,Gas Pressure, Units(Pa),Water-Vapor Relative Humidity,Salt Mass Fraction, Null,
#1,1,1,1,1,6,2,
#0,day,,,0.0,32.e+6,Pa,1.0,0.2,,
#7300,day,,,0.0,36.e+6,Pa,1.0,0.2,,

~Output Options Card
#Number of Reference Nodes
3,
#I Index, J Index, K Index
#R=0 m Z=15,48,81 Ref Nodes=265,1057,1849
#R=200 m Z=15,48,81 Ref Nodes=275,1067,1859
11,1,4,
11,1,13,
11,1,22,
#R=200 m Z=15,48,81 Ref Nodes=280,1072,1864
#R=590m Z=15,48,81 Ref Nodes=296,1088,1880
#R=500 m Z=15,48,81 Ref Nodes=309,1101,1893
#R=1000 m Z=15,48,81 Ref Nodes=333,1125,1917
#Reference Node Screen Output Frequency,Reference Node Output File Frequency,Output Time Units(s),
#Output Length Units (m),Screen Significant Digits,Output File Significant Digits,Plot File Significant Digits
1,1,year,m,deg,6,6,6,
#Number of Reference Node Variables
17,
#Reference Node Variable Option, Reference Node Variable Units,
Aqueous Saturation,,

Gas Saturation,,
Aqueous Pressure,Pa,
Gas Pressure,Pa,
CO2 Aqueous Mass Fraction,,
CO2 Gas Mass Fraction,,
trapped gas saturation,,
#total CO2 mass in the computational domain
Integrated CO2 Mass,MMT,
Integrated Aqueous CO2 Mass,MMT,
#total CO2 mass in the gas phase in the computational domain
Integrated Gas CO2 Mass,MMT,
Integrated CO2 Trapped-Gas Mass,MMT,
Aqueous Density,kg/m^3,
Gas Density,kg/m^3,
Aqueous Relative Permeability,,
Gas Relative Permeability,,
Salt Aqueous Mass Fraction,,
Diffusive Porosity,,
#Number of Plot File Ouput Times
25,
1,year,
5,year,
10,year,
15,year,
20,year,
25,year,
30,year,
35,year,
40,year,
50,year,
100,year,
200,year,
300,year,
400,year,
500,year,
750,year,
1000,year,
1500,year,
2000,year,
2500,year,
3000,year,
3500,year,
4000,year,
4500,year,
5000,year,
#Number of Plot File Variables
13,

```
#Plot File Variable Option, Plot File Variable Units
Aqueous Saturation,,
Gas Saturation,,
Aqueous Pressure,Pa,
Gas Pressure,Pa,
CO2 Aqueous Mass Fraction,,
CO2 Gas Mass Fraction,,
Trapped Gas Saturation,,
Aqueous Density,kg/m^3,
Gas Density,kg/m^3,
Aqueous Relative Permeability,,
Gas Relative Permeability,,
Salt Aqueous Mass Fraction,,
Diffusive Porosity,,
~Surface Flux Card
4,
Total CO2 Flux,kg/s,kg,West,1,1,1,1,1,24,
Aqueous Mass Flux,kg/s,kg,East,88,88,1,1,1,24,
Total CO2 Flux,kg/s,kg,Top,1,88,1,1,7,9,
Total CO2 Flux,kg/s,kg,Top,1,88,1,1,16,18,
```

APPENDIX: C-6

Homogeneous coarse sand – vertical cyclic injection

```
#Y5, case005- Homogeneous Medium Permeability sands - 2D Coarse-grid, Total Simulation Time=5000 yrs

~Simulation Title Card
1,
Simulation of CO2 Sequestration in Deep Saline Aquifers,
Kamal Khudaida,
Chemical Eng. Dep.,Loughborough University,
31 October 2014,
11:00 PM UK,
23,
CC**********************************************************************
CC BRIEF DESCRIPTION OF PROJECT
CC**********************************************************************
CC Cylindrical geometry
CC 2D Full scale,radial model
CC (phase 1=inactive water, phase 2 = water/co2, phase 3=co2/gas
CC Radius(m):6000  INJECTION FLUID: CO2
CC HEIGHT(m):96 INJECTION RATE:1.0 kg/s(each of the 32 nodes)      INJECTION TIME (Total)=30 YEARS
CC WIDTH(m):
CC POROSITY: 0.35
CC ABS. PERM(MD): 304 md         3-PHASE REL. PERM:         water endpt.=1.0
CC TEMP(C): 37                   WETTIBILITY:
CC INJECTION PRESSURE(MPa):Variable    HYDROSTATIC PRESSURE (MPa)=11.2
CC SOR: G/O CAP. PRESSURE: *
CC SWC: DISPLACEMENT TYPE: HORIZONTAL
CC inject 30 yrs (batch injection: 10-5-10-5-10 yrs) and monitor for 4960 yrs,       h2o k endpoint=1
CC ****NON-IDEAL MIXING, NO GRAVITY, WITH Pc, WITH X-FLOW
CC FILE NAME: Homogeneous 2D Coarse-grid intermingled sands and shales
CC CREATED BY Kamal Khudaida
CC MODIFIED ON 04/03/2015,
CC**********************************************************************

~Solution Control Card
#excution mode to read initial conditions (normal, restart, initial conditions)Normal
normal,
#operational mode
H2O-NaCl-CO2,
```

#excution time periods
1,
#initial time,final time (injection time 30 yrs + 10 yrs stopping with lockup time 4960 yrs),init. time step, max. t. s.,t. s. accel. factor,Iteration,convergence
0,year,5000,year,1.e-3,s,20,year,1.125,32,1.e-06,
#max num. of time steps
100000,
#aqueous diffusion option,dissolved CO2 diffusion Coefficient,Dissolved Salt Diffusion Coefficient
Variable Aqueous Diffusion,
Variable Gas Diffusion,
#Number of Interfacial Averaging Variables
0,

~Grid Card
Cylindrical,
88,1,24,
#for grids with non-uniform spacing one plus the number of nodes entries are required for each grid #direction.Domain Radius=6000 m.
0.3,m,10@20.0,m,14@40.0,m,18@60.0,m,22@80.0,m,24@100.0,m,
0.0,deg,45.0,deg,
0.0,m,6@5.0,m,3@1.0,m,6@5.0,m,3@1.0,m,6@5.0,m,

~Rock/Soil Zonation Card
#number of zonation domains
1,
#rock or soil group with start and end indeces in each direction
Sands1,1,88,1,1,1,24,

~Mechanical Properties Card
#rock grouping name,density,total porosity,diffusive porosity,specific storativity,
#aq. tortuosity,gas tortuosity,tortuosity function,
Sands1,2650,kg/m^3,0.35,0.35,Pore Compressibility,4.5e-10,1/Pa,,,Millington and Quirk,

~Hydraulic Properties Card
#rock grouping name,intrinsic permeability in r,theta and z-directions, Pore-body Fractional Length, Fractional Critical Porosity (NaCl precipitation is NOT considered)
Sands1,3.0e-13,m^2,3.0e-13,m^2,3.0e-13,m^2,

~Saturation Function Card
#rock grouping name,Saturation Function option,alpha Parameter,units,n Parameter,minumum saturation,m Parameter,Maximum residual gas saturation (Sgrm)=-0.9696*0.35+0.5473 (after Holts 2002)
Sands1,Entrapment van Genuchten,2.735,1/m,1.667,0.2,0.4,0.208,

~Aqueous Relative Permeability Card
#rock grouping name,Permeability Function Option,van Genuchten m parameter,Irreducible Aqueous Saturation
Sands1,Mualem Irreducible,0.4,0.2,

~Gas Relative Permeability Card
#rock grouping name,Permeability Function Option,van Genuchten m parameter
Sands1,Mualem,0.4,

~Salt Transport Card
#rock grouping name,Longitudinal Dispersivity (equal zero for homogeneous),
Units,Transverse Dispersivity, Units
Sands1,0.0,m,0.0,m,

~Initial Conditions Card
#initial saturation option,initial saturation option,
Aqueous Pressure,Gas Pressure,
#number of initial conditions domains
4,
#Variable Name Option,pressure,unit,X,y,z,-Dir. Gradient, Units (1/m),I,j,k-Start Index, I,j,k-End Index,
Aqueous Pressure,11.2e+6,Pa,,,,,-10.012e+3,1/m,1,88,1,1,1,24,
Gas Pressure,11.2e+6,Pa,,,,,-10.012e+3,1/m,1,88,1,1,1,24,
Temperature,37.0,C,,,,,,,1,88,1,1,1,24,
Salt Mass Fraction,0.032,,,,,,,,1,88,1,1,1,24,

~Source Card
1,
Gas Mass Rate,Water-Vapor Mass Fraction,1,1,1,1,2,5,12,
#injection of 1.0 kg/s of CO2 over each nodes at a one 45 degree arc (i.e. for cylindrical shape 4 x 8 = 32 nodes) represents 1 MMT/year for the whole domain.
0,s,,,1.0,kg/s,0.0,
10,year,,,1.0,kg/s,0.0,
10,year,,,0.0,kg/s,0.0,
15,year,,,0.0,kg/s,0.0,
15,year,,,1.0,kg/s,0.0,
25,year,,,1.0,kg/s,0.0,
25,year,,,0.0,kg/s,0.0,
30,year,,,0.0,kg/s,0.0,
30,year,,,1.0,kg/s,0.0,
40,year,,,1.0,kg/s,0.0,
40,year,,,0.0,kg/s,0.0,
5000,year,,,0.0,kg/s,0.0,

~Boundary Conditions Card
1,

#Boundary Surface Direction Option,Aqueous-Phase Boundary Type Option,Gas-Phase Boundary Type Option,Salt Boundary Type Option
East,Aqueous Initial Condition,Gas Initial Condition,Salt Initial Condition,
88,88,1,1,1,24,1,
0,s,,,,,,,,
#West,Aqu. Zero Flux,Gas Hydraulic Gradient,Aqueous Mass Fraction,
#Boundary Time, Units (s),Aqueous Pressure, Units (Pa),Aqueous Dissolved- CO2-Relative Saturation,Gas Pressure, Units(Pa),Water-Vapor Relative Humidity,Salt Mass Fraction, Null,
#1,1,1,1,2,5,2,
#0,day,,,0.0,18.e+6,Pa,1.0,0.2,,
#7300,day,,,0.0,18.e+6,Pa,1.0,0.2,,

~Output Options Card
#Number of Reference Nodes
3,
#I Index, J Index, K Index
#R=0 m Z=15,48,81 Ref Nodes=265,1057,1849
#R=200 m Z=48 Ref Nodes=
11,1,4,
11,1,13,
11,1,22,
#R=590m Z=15,48,81 Ref Nodes=296,1088,1880
#R=500 m Z=15,48,81 Ref Nodes=309,1101,1893
#R=1000 m Z=15,48,81 Ref Nodes=333,1125,1917
#Reference Node Screen Output Frequency,Reference Node Output File Frequency,Output Time Units(s),
#Output Length Units (m),Screen Significant Digits,Output File Significant Digits,Plot File Significant Digits
1,1,year,m,deg,6,6,6,
#Number of Reference Node Variables
17,
#Reference Node Variable Option, Reference Node Variable Units,
Aqueous Saturation,,
Gas Saturation,,
Aqueous Pressure,Pa,
Gas Pressure,Pa,
CO2 Aqueous Mass Fraction,,
CO2 Gas Mass Fraction,,
trapped gas saturation,,
#total CO2 mass in the computational domain
Integrated CO2 Mass,MMT,
Integrated Aqueous CO2 Mass,MMT,
#total CO2 mass in the gas phase in the computational domain
Integrated Gas CO2 Mass,MMT,
Integrated CO2 Trapped-Gas Mass,MMT,
Aqueous Density,kg/m^3,
Gas Density,kg/m^3,

Aqueous Relative Permeability,,
Gas Relative Permeability,,
Salt Aqueous Mass Fraction,,
Diffusive Porosity,,
#Number of Plot File Ouput Times
25,
1,year,
5,year,
10,year,
15,year,
20,year,
25,year,
30,year,
35,year,
40,year,
50,year,
100,year,
200,year,
300,year,
400,year,
500,year,
750,year,
1000,year,
1500,year,
2000,year,
2500,year,
3000,year,
3500,year,
4000,year,
4500,year,
5000,year,
#Number of Plot File Variables
13,
#Plot File Variable Option, Plot File Variable Units
Aqueous Saturation,,
Gas Saturation,,
Aqueous Pressure,Pa,
Gas Pressure,Pa,
CO2 Aqueous Mass Fraction,,
CO2 Gas Mass Fraction,,
Trapped Gas Saturation,,
Aqueous Density,kg/m^3,
Gas Density,kg/m^3,
Aqueous Relative Permeability,,
Gas Relative Permeability,,
Salt Aqueous Mass Fraction,,
Diffusive Porosity,,

```
~Surface Flux Card
4,
Total CO2 Flux,kg/s,kg,West,1,1,1,1,2,5,
Aqueous Mass Flux,kg/s,kg,East,88,88,1,1,1,24,
Total CO2 Flux,kg/s,kg,Top,1,88,1,1,7,9,
Total CO2 Flux,kg/s,kg,Top,1,88,1,1,16,18,
```

APPENDIX: C-7

Homogeneous coarse sand - finer grid-mesh

#Y5, case006- Homogeneous Medium Permeability sands - 2D Fine- grid (100% finer), Total Simulation Time=5000 yrs, investigation of grid resolution effect

```
~Simulation Title Card
1,
Simulation of CO2 Sequestration in Deep Saline Aquifers,
Kamal Khudaida,
Chemical Eng. Dep.,Loughborough University,
31 October 2014,
11:00 PM UK,
23,
CC*************************************************************************
CC BRIEF DESCRIPTION OF PROJECT
CC*************************************************************************
CC Cylindrical geometry
CC 2D Full scale,radial model
CC (phase 1=inactive water, phase 2 = water/co2, phase 3=co2/gas
CC Radius(m):6000  INJECTION FLUID: CO2
CC HEIGHT(m):96 INJECTION RATE:0.5kg/s(each of 64 nodes)  INJECTION TIME
(Total)=30 YEARS
CC WIDTH(m):
CC POROSITY: 0.35
CC ABS. PERM(MD): 304 md        3-PHASE REL. PERM:        water endpt.=1.0
CC TEMP(C): 37                  WETTIBILITY:
CC INJECTION PRESSURE(MPa):Variable    HYDROSTATIC PRESSURE (MPa)=11.2
CC SOR: G/O CAP. PRESSURE: *
CC SWC: DISPLACEMENT TYPE: HORIZONTAL
CC inject 30 yrs (continuously) and monitor for 4970 yrs,    h2o k endpoint=1
CC ****NON-IDEAL MIXING, NO GRAVITY, WITH Pc, WITH X-FLOW
CC FILE NAME: Homogeneous 2D Coarse-grid intermingled sands and shales
CC CREATED BY Kamal Khudaida
CC MODIFIED ON 05/03/2015,
CC*************************************************************************

~Solution Control Card
#excution mode to read initial conditions (normal, restart, initial conditions)Normal
normal,
#operational mode
H2O-NaCl-CO2,
#excution time periods
```

1,
#initial time,final time (injection time 30 yrs with lockup time 4970 yrs),init. time step, max. t. s.,t. s. accel. factor,Iteration,convergence
0,year,5000,year,1.e-3,s,20,year,1.125,32,1.e-06,
#max num. of time steps
100000,
#aqueous diffusion option,dissolved CO2 diffusion Coefficient,Dissolved Salt Diffusion Coefficient
Variable Aqueous Diffusion,
Variable Gas Diffusion,
#Number of Interfacial Averaging Variables
0,

~Grid Card
Cylindrical,
176,1,48,
#for grids with non-uniform spacing one plus the number of nodes entries are required for each grid #direction.Domain Radius=6000 m.
0.3,m,20@10.0,m,28@20.0,m,36@30.0,m,44@40.0,m,48@50.0,m,
0.0,deg,45.0,deg,
0.0,m,12@2.5,m,6@0.5,m,12@2.5,m,6@0.5,m,12@2.5,m,

~Rock/Soil Zonation Card
#number of zonation domains
1,
#rock or soil group with start and end indeces in each direction
Sands1,1,176,1,1,1,48,

~Mechanical Properties Card
#rock grouping name,density,total porosity,diffusive porosity,specific storativity,
#aq. tortuosity,gas tortuosity,tortuosity function,
Sands1,2650,kg/m^3,0.35,0.35,Pore Compressibility,4.5e-10,1/Pa,,,Millington and Quirk,

~Hydraulic Properties Card
#rock grouping name,intrinsic permeability in r,theta and z-directions, Pore-body Fractional Length, Fractional Critical Porosity (NaCl precipitation is NOT considered)
Sands1,3.0e-13,m^2,3.0e-13,m^2,3.0e-13,m^2,

~Saturation Function Card
#rock grouping name,Saturation Function option,alpha Parameter,units,n Parameter,minumum saturation,m Parameter,Maximum residual gas saturation (Sgrm)=-0.9696*0.35+0.5473
Sands1,Entrapment van Genuchten,2.735,1/m,1.667,0.2,0.4,0.208,

~Aqueous Relative Permeability Card

#rock grouping name,Permeability Function Option,van Genuchten m parameter,Irreducible Aqueous Saturation
Sands1,Mualem Irreducible,0.4,0.2,

~Gas Relative Permeability Card
#rock grouping name,Permeability Function Option,van Genuchten m parameter
Sands1,Mualem,0.4,

~Salt Transport Card
#rock grouping name,Longitudinal Dispersivity (equal zero for homogeneous),
Units,Transverse Dispersivity, Units
Sands1,0.0,m,0.0,m,

~Initial Conditions Card
#initial saturation option,initial saturation option,
Aqueous Pressure,Gas Pressure,
#number of initial conditions domains
4,
#Variable Name Option,pressure,unit,X,y,z,-Dir. Gradient, Units (1/m),I,j,k-Start Index, I,j,k-End Index,
Aqueous Pressure,11.2e+6,Pa,,,,,-10.012e+3,1/m,1,176,1,1,1,48,
Gas Pressure,11.2e+6,Pa,,,,,-10.012e+3,1/m,1,176,1,1,1,48,
Temperature,37.0,C,,,,,,,1,176,1,1,1,48,
Salt Mass Fraction,0.032,,,,,,,,1,176,1,1,1,48,

~Source Card
1,
Gas Mass Rate,Water-Vapor Mass Fraction,1,1,1,1,3,10,2,
#injection of 0.5 kg/s of CO2 over each nodes at a one 45 degree arc (i.e. for cylindrical shape 8 x 8 = 64 nodes) represents 1 MMT/year for the whole domain.
0,s,,,0.5,kg/s,0.0,
30,year,,,0.5,kg/s,0.0,

~Boundary Conditions Card
1,
#Boundary Surface Direction Option,Aqueous-Phase Boundary Type Option,Gas-Phase Boundary Type Option,Salt Boundary Type Option
East,Aqueous Initial Condition,Gas Initial Condition,Salt Initial Condition,
176,176,1,1,1,48,1,
0,s,,,,,,,,
#West,Aqu. Zero Flux,Gas Hydraulic Gradient,Aqueous Mass Fraction,
#Boundary Time, Units (s),Aqueous Pressure, Units (Pa),Aqueous Dissolved- CO2-Relative Saturation,Gas Pressure, Units(Pa),Water-Vapor Relative Humidity,Salt Mass Fraction, Null,
#1,1,1,1,2,5,2,
#0,day,,,0.0,18.e+6,Pa,1.0,0.2,,
#7300,day,,,0.0,18.e+6,Pa,1.0,0.2,,

```
~Output Options Card
#Number of Reference Nodes
3,
#I Index, J Index, K Index
#R=0 m Z=15,48,81 Ref Nodes=265,1057,1849
#R=200 m Z=15, 48, 81m Ref Nodes=
21,1,7,
21,1,25,
21,1,43,
#R=200 m Z=15,48,81 Ref Nodes=280,1072,1864
#R=590m Z=15,48,81 Ref Nodes=296,1088,1880
#R=500 m Z=15,48,81 Ref Nodes=309,1101,1893
#R=1000 m Z=15,48,81 Ref Nodes=333,1125,1917
#Reference Node Screen Output Frequency,Reference Node Output File Frequency,Output Time Units(s),
#Output Length Units (m),Screen Significant Digits,Output File Significant Digits,Plot File Significant Digits
1,1,year,m,deg,6,6,6,
#Number of Reference Node Variables
17,
#Reference Node Variable Option, Reference Node Variable Units,
Aqueous Saturation,,
Gas Saturation,,
Aqueous Pressure,Pa,
Gas Pressure,Pa,
CO2 Aqueous Mass Fraction,,
CO2 Gas Mass Fraction,,
trapped gas saturation,,
#total CO2 mass in the computational domain
Integrated CO2 Mass,MMT,
Integrated Aqueous CO2 Mass,MMT,
#total CO2 mass in the gas phase in the computational domain
Integrated Gas CO2 Mass,MMT,
Integrated CO2 Trapped-Gas Mass,MMT,
Aqueous Density,kg/m^3,
Gas Density,kg/m^3,
Aqueous Relative Permeability,,
Gas Relative Permeability,,
Salt Aqueous Mass Fraction,,
Diffusive Porosity,,
#Number of Plot File Ouput Times
25,
1,year,
5,year,
10,year,
15,year,
```

20,year,
25,year,
30,year,
35,year,
40,year,
50,year,
100,year,
200,year,
300,year,
400,year,
500,year,
750,year,
1000,year,
1500,year,
2000,year,
2500,year,
3000,year,
3500,year,
4000,year,
4500,year,
5000,year,
#Number of Plot File Variables
13,
#Plot File Variable Option, Plot File Variable Units
Aqueous Saturation,,
Gas Saturation,,
Aqueous Pressure,Pa,
Gas Pressure,Pa,
CO2 Aqueous Mass Fraction,,
CO2 Gas Mass Fraction,,
Trapped Gas Saturation,,
Aqueous Density,kg/m^3,
Gas Density,kg/m^3,
Aqueous Relative Permeability,,
Gas Relative Permeability,,
Salt Aqueous Mass Fraction,,
Diffusive Porosity,,
~Surface Flux Card
4,
Total CO2 Flux,kg/s,kg,West,1,1,1,1,3,10,
Aqueous Mass Flux,kg/s,kg,East,176,176,1,1,1,48,
Total CO2 Flux,kg/s,kg,Top,1,176,1,1,13,18,
Total CO2 Flux,kg/s,kg,Top,1,176,1,1,31,36,

APPENDIX: C-8

Homogeneous coarse sand – horizontal injection

```
#Y5, case012- Homogeneous Medium Permeability sands - 2D Coarse-grid, Horizontal continueous injection into a section equivalent to two times of the whole aquifer thickness, Vertica Perm./Horizantal Perm. ration=0.01 Total Simulation Time=5000 yrs

~Simulation Title Card
1,
Simulation of CO2 Sequestration in Deep Saline Aquifers,
Kamal Khudaida,
Chemical Eng. Dep.,Loughborough University,
31 October 2014,
11:00 PM UK,
23,
CC*************************************************************************
CC BRIEF DESCRIPTION OF PROJECT
CC*************************************************************************
CC Cylindrical geometry
CC 2D Full scale, radial model
CC (phase 1 = inactive water, phase 2 = water/CO2, phase 3 = CO2/gas
CC Radius(m):6000  INJECTION FLUID: CO2
CC HEIGHT(m):96 INJECTION RATE:0.083335 kg/s(each one of 384 horizontal nodes)
         INJECTION TIME (Total)=30 YEARS
CC WIDTH(m):
CC POROSITY: 0.35
CC ABS. PERM(MD): Vertical=3.04 md   Horizontal=304 md (Pv/Hp=0.1)         3-PHASE REL. PERM:   water endpt.=1.0
CC TEMP(C): 37                WETTIBILITY:
CC INJECTION PRESSURE(MPa):Variable    HYDROSTATIC PRESSURE (MPa)=11.2
CC SOR: G/O CAP. PRESSURE: *
CC SWC: DISPLACEMENT TYPE: HORIZONTAL
CC inject 30 yrs (continuously) and monitor for 4970 yrs,    H2O k endpoint=1
CC ****NON-IDEAL MIXING, NO GRAVITY, WITH Pc, WITH X-FLOW
CC FILE NAME: Homogeneous 2D Coarse-grid intermingled sands and shales
CC CREATED BY Kamal Khudaida
CC MODIFIED ON 24/07/2015,
CC*************************************************************************

~Solution Control Card
#excution mode to read initial conditions (normal, restart, initial conditions)Normal
normal,
#operational mode
```

H2O-NaCl-CO2,
#excution time periods
1,
#initial time,final time (injection time 30 yrs with lockup time 4970 yrs),init. time step, max. t. s.,t. s. accel. factor,Iteration,convergence
0,year,5000,year,1.e-3,s,20,year,1.125,32,1.e-06,
#max num. of time steps
100000,
#aqueous diffusion option,dissolved CO2 diffusion Coefficient,Dissolved Salt Diffusion Coefficient
Variable Aqueous Diffusion,
Variable Gas Diffusion,
#Number of Interfacial Averaging Variables
0,

~Grid Card
Cylindrical,
88,1,24,
#for grids with non-uniform spacing one plus the number of nodes entries are required for each grid #direction.Domain Radius=6000 m.
0.3,m,50@4.0,m,20@50.0,m,14@100.0,m,4@850.0,m,
0.0,deg,45.0,deg,
0.0,m,24@4.0,m,

~Rock/Soil Zonation Card
#number of zonation domains
1,
#rock or soil group with start and end indeces in each direction
Sands1,1,88,1,1,1,24,

~Mechanical Properties Card
#rock grouping name,density,total porosity,diffusive porosity,specific storativity,
#aq. tortuosity,gas tortuosity,tortuosity function,
Sands1,2650,kg/m^3,0.35,0.35,Pore Compressibility,4.5e-10,1/Pa,,,Millington and Quirk,

~Hydraulic Properties Card
#rock grouping name,intrinsic permeability in r,theta and z-directions, Pore-body Fractional Length, Fractional Critical Porosity (NaCl precipitation is NOT considered)
Sands1,3.0e-13,m^2,3.0e-13,m^2,0.03e-13,m^2,

~Saturation Function Card
#rock grouping name,Saturation Function option,alpha Parameter,units,n Parameter,minumum saturation,m Parameter,Maximum residual gas saturation (Sgrm)=-0.9696*0.35+0.5473 (after Holts 2002)
Sands1,Entrapment van Genuchten,2.735,1/m,1.667,0.2,0.4,0.208,

~Aqueous Relative Permeability Card
#rock grouping name,Permeability Function Option,van Genuchten m parameter,Irreducible Aqueous Saturation
Sands1,Mualem Irreducible,0.4,0.2,

~Gas Relative Permeability Card
#rock grouping name,Permeability Function Option,van Genuchten m parameter
Sands1,Mualem,0.4,

~Salt Transport Card
#rock grouping name,Longitudinal Dispersivity (equal zero for homogeneous), Units,Transverse Dispersivity, Units
Sands1,0.0,m,0.0,m,

~Initial Conditions Card
#initial saturation option,initial saturation option,
Aqueous Pressure,Gas Pressure,
#number of initial conditions domains
4,
#Variable Name Option,pressure,unit,X,y,z,-Dir. Gradient, Units (1/m),I,j,k-Start Index, I,j,k-End Index,
Aqueous Pressure,11.2e+6,Pa,,,,,-10.012e+3,1/m,1,88,1,1,1,24,
Gas Pressure,11.2e+6,Pa,,,,,-10.012e+3,1/m,1,88,1,1,1,24,
Temperature,37.0,C,,,,,,,1,88,1,1,1,24,
Salt Mass Fraction,0.032,,,,,,,,1,88,1,1,1,24,

~Source Card
1,
Gas Mass Rate,Water-Vapor Mass Fraction,1,48,1,1,1,1,2,
#injection of 0.083335 kg/s of CO2 over 384 nodes at 8 of 45 degrees angles for cylindrical shape (i.e. 8 x 48 = 384 nodes) represents 1 MMT/year for the whole cylindrical domain
0,s,,,0.083335,kg/s,0.0,
30,year,,,0.083335,kg/s,0.0,

~Boundary Conditions Card
1,
#Boundary Surface Direction Option,Aqueous-Phase Boundary Type Option,Gas-Phase Boundary Type Option,Salt Boundary Type Option
East,Aqueous Initial Condition,Gas Initial Condition,Salt Initial Condition,
88,88,1,1,1,24,1,
0,s,,,,,,,,,
#West,Aqu. Zero Flux,Gas Hydraulic Gradient,Aqueous Mass Fraction,
#Boundary Time, Units (s),Aqueous Pressure, Units (Pa),Aqueous Dissolved- CO2-Relative Saturation,Gas Pressure, Units(Pa),Water-Vapor Relative Humidity,Salt Mass Fraction, Null,
#1,1,1,1,1,24,2,

#0,day,,,,,1.0,0.2,,
#7300,day,,,,,1.0,0.2,,

~Output Options Card
#Number of Reference Nodes
4,
#I Index, J Index, K Index
#R=200 m Z=24,48,72,96 Ref Nodes=
50,1,6,
50,1,12,
50,1,18,
50,1,24,
#Reference Node Screen Output Frequency,Reference Node Output File Frequency,Output Time Units(s),
#Output Length Units (m),Screen Significant Digits,Output File Significant Digits,Plot File Significant Digits
1,1,year,m,deg,6,6,6,
#Number of Reference Node Variables
17,
#Reference Node Variable Option, Reference Node Variable Units,
Aqueous Saturation,,
Gas Saturation,,
Aqueous Pressure,Pa,
Gas Pressure,Pa,
CO2 Aqueous Mass Fraction,,
CO2 Gas Mass Fraction,,
trapped gas saturation,,
#total CO2 mass in the computational domain
Integrated CO2 Mass,MMT,
Integrated Aqueous CO2 Mass,MMT,
#total CO2 mass in the gas phase in the computational domain
Integrated Gas CO2 Mass,MMT,
Integrated CO2 Trapped-Gas Mass,MMT,
Aqueous Density,kg/m^3,
Gas Density,kg/m^3,
Aqueous Relative Permeability,,
Gas Relative Permeability,,
Salt Aqueous Mass Fraction,,
Diffusive Porosity,,
#Number of Plot File Ouput Times
25,
1,year,
5,year,
10,year,
15,year,
20,year,
25,year,

30,year,
35,year,
40,year,
50,year,
100,year,
200,year,
300,year,
400,year,
500,year,
750,year,
1000,year,
1500,year,
2000,year,
2500,year,
3000,year,
3500,year,
4000,year,
4500,year,
5000,year,
#Number of Plot File Variables
13,
#Plot File Variable Option, Plot File Variable Units
Aqueous Saturation,,
Gas Saturation,,
Aqueous Pressure,Pa,
Gas Pressure,Pa,
CO2 Aqueous Mass Fraction,,
CO2 Gas Mass Fraction,,
Trapped Gas Saturation,,
Aqueous Density,kg/m^3,
Gas Density,kg/m^3,
Aqueous Relative Permeability,,
Gas Relative Permeability,,
Salt Aqueous Mass Fraction,,
Diffusive Porosity,,
~Surface Flux Card
2,
Total CO2 Flux,kg/s,kg,Bottom,1,48,1,1,1,1,
Aqueous Mass Flux,kg/s,kg,East,88,88,1,1,1,24,

APPENDIX: C-9

Homogeneous coarse sand – dynamic flow

#Y4 homc-3D case2 - Sandstone -Coarse 3D Simulation Time=1000 yrs initial cond. changed to Aqueous Press., Aqu. Sat. with Sw=0.9999

~Simulation Title Card
1,
Simulation of CO2 Sequestration in Deep Saline Aquifers,
Kamal Khudaida,
Chemical Eng. Dep.,Loughborough University,
21 January 2014,
11:30 AM UK,
23,
CC**********
CC BRIEF DESCRIPTION OF PROJECT
CC**********
CC Cylindrical geometry
CC 3D Full scale,radial model
CC (phase 1=inactive water, phase 2 = water/co2, phase 3=co2/gas
CC Radius(m):2500 INJECTION FLUID: CO2
CC HEIGHT(m):100 INJECTION RATE:40.0 kg/s (i. e. 4 arcs * 4 nodes * 2.5 kg/s)
INJECTION TIME=20 YEARS
CC WIDTH(m):
CC POROSITY: 0.25
CC ABS. PERM(MD): variable 3-PHASE REL. PERM: water endpt.=1.0
CC TEMP(C): 58 WETTIBILITY:
CC INJECTION PRESSURE(MPa):36 HYDROSTATIC PRESSURE (MPa)=32
CC SOR: G/O CAP. PRESSURE: *
CC SWC: DISPLACEMENT TYPE: HORIZONTAL
CC stop injection after 20 years run for 1000 yrs,h2o k endpoint=1
CC ****NON-IDEAL MIXING, NO GRAVITY, WITH Pc, WITH X-FLOW
CC FILE NAME: Homogeneous Low Permeability Sandstone
CC CREATED BY Kamal Khudaida
CC MODIFIED ON 21/01/2014,
CC**********

~Solution Control Card
#excution mode to read initial conditions (normal, restart, initial conditions)Normal
normal,
#operational mode
H2O-NaCl-CO2,
#excution time periods

1,
#initial time,final time (injection time 50 yrs with lockup time 1000 yrs),init. time step, max. t. s.,t. s. accel. factor,Iteration,convergence
0,year,1000,year,1.e-3,s,20,year,1.125,64,1.e-06,
#max num. of time steps
200000,
#aqueous diffusion option,dissolved CO2 diffusion Coefficient,Dissolved Salt Diffusion Coefficient
Variable Aqueous Diffusion,
Variable Gas Diffusion,
#Number of Interfacial Averaging Variables
0,

~Grid Card
Cylindrical,
71,4,10,
#for grids with non-uniform spacing one plus the number of nodes entries are required for each grid direction. Domain Radius=2500 m.
0.2,m,25@20,m,15@30,m,31@50,m,
0.0,deg,4@90.0,deg,
0.0,m,10@10,m,

~Rock/Soil Zonation Card
#number of zonation domains
1,
#rock or soil group with start and end indeces in each direction
Delfurth Sandstone,1,71,1,4,1,10,

~Mechanical Properties Card
#rock grouping name,density,total porosity,diffusive porosity,specific storativity,
#aq. tortuosity,gas tortuosity,tortuosity function,
Delfurth Sandstone,2430,kg/m^3,0.25,0.25,Pore Compressibility,1.0e-9,1/Pa,100.0,bar,Millington and Quirk,

~Hydraulic Properties Card
#rock grouping name,intrinsic permeability in r,theta and z-directions, Pore-body Fractional Length, Fractional Critical Porosity (NaCl precipitation is NOT considered)
Delfurth Sandstone,5.625e-13,m^2,5.625e-13,m^2,1.688e-13,m^2,

~Saturation Function Card
#rock grouping name,Saturation Function option,alpha Parameter,units,n Parameter,minumum saturation,m Parameter,
Delfurth Sandstone,van Genuchten,0.5,1/m,1.84,0.0,0.457,,

~Aqueous Relative Permeability Card
#rock grouping name,Permeability Function Option,van Genuchten m parameter,Irreducible Aqueous Saturation

Delfurth Sandstone,Mualem Irreducible,0.457,0.1,

~Gas Relative Permeability Card
#rock grouping name,Permeability Function Option,Irreducible Gas Saturation ,Irreducible Aqueous Saturation
Delfurth Sandstone,Corey,0.05,0.1,

~Salt Transport Card
#rock grouping name,Longitudinal Dispersivity (equal zero for homogeneous),
Units,Transverse Dispersivity, Units
Delfurth Sandstone,0.0,m,0.0,m,

~Initial Conditions Card
#initial saturation option,initial saturation option,
Aqueous Pressure,Aqueous Saturation,
#number of initial conditions domains
4,
#Variable Name Option,pressure,unit,X,y,z,-Dir. Gradient, Units (1/m),I,j,k-Start Index, I,j,k-End Index,
Aqueous Pressure,32.e+6,Pa,,,,,-10.5e+3,1/m,1,71,1,4,1,10,
#Gas Pressure,32.e+6,pa,,,,,-10.5e+3,1/m,1,71,1,4,1,10,
Aqueous Saturation,0.9999,,,,,,,,1,71,1,4,1,10,
Temperature,58.0,C,,,,,,,1,71,1,4,1,10,
Salt Mass Fraction,0.2,,,,,,,,1,71,1,4,1,10,

~Source Card
#Number of Source Domains
1,
#Source Type Option,Water Vapor Source Option,I,j,k-Start Index, I,j,k-End Index,
Gas Mass Rate,Water-Vapor Mass Fraction,1,1,1,4,1,4,2,
#Source (injection) Start Time,Units(s),Pressure,Units (Pa),Gas Mass Rate,Units(kg/s),Water Vapor Mass Fraction
0,s,36.e+6,Pa,2.5,kg/s,0.0,
#Source End Time,Units(s),Pressure,Units (Pa),Gas Mass Rate,Units(kg/s),Water Vapor Mass Fraction
7300,day,36.e+6,Pa,40.0,kg/s,0.0,

~Boundary Conditions Card
2,
#Boundary Surface Direction Option,Aqueous-Phase Boundary Type Option,Gas-Phase Boundary Type Option,Salt Boundary Type Option
East,Aqueous Initial Condition,Gas Initial Condition,Salt Initial Condition,
71,71,1,4,1,10,1,
0,s,,,,,,,,
#Boundary Time, Units (s),Aqueous Pressure, Units (Pa),Aqueous Dissolved- CO2-Relative Saturation,Gas Pressure, Units(Pa),Water-Vapor Relative Humidity,Salt Mass Fraction, Null,

West,Aqu. Zero Flux,Gas Dirichlet,Aqueous Mass Fraction,
1,1,1,4,1,4,1,
0,s,,,0.0,,,1.0,0.2,,

~Output Options Card
#Number of Reference Nodes
15,
#I Index, J Index, K Index
#R=100 m
6,1,3,
6,1,5,
6,1,8,
#R=200 m
11,1,3,
11,1,5,
11,1,8,
#R=500 m
26,1,3,
26,1,5,
26,1,8,
#R=800 m
36,1,3,
36,1,5,
36,1,8,
#R=1000 m
42,1,3,
42,1,5,
42,1,8,
#Reference Node Screen Output Frequency,Reference Node Output File Frequency,Output Time Units(s),
#Output Length Units (m),Screen Significant Digits,Output File Significant Digits,Plot File Significant Digits
1,1,year,m,deg,6,6,6,
#Number of Reference Node Variables
13,
#Reference Node Variable Option, Reference Node Variable Units,
Aqueous Saturation,,
Gas Saturation,,
Aqueous Pressure,Pa,
Gas Pressure,Pa,
#total CO2 mass in the computational domain
Integrated CO2 Mass,kg,
Integrated Aqueous CO2 Mass,kg,
#total CO2 mass in the gas phase in the computational domain
Integrated Gas CO2 Mass,kg,
Aqueous relative permeability,,
Gas relative permeability,,

Aqueous Density,kg/m^3,
Gas Density,kg/m^3,
Salt Aqueous Mass Fraction,,
Diffusive Porosity,,
#Number of Plot File Ouput Times
12,
1,year,
5,year,
10,year,
20,year,
50,year,
100,year,
200,year,
300,year,
400,year,
500,year,
750,year,
1000,year,
#Number of Plot File Variables
11,
#Plot File Variable Option, Plot File Variable Units
Aqueous Saturation,,
Gas Saturation,,
Aqueous Pressure,Pa,
Gas Pressure,Pa,
CO2 Aqueous Mass Fraction,,
CO2 Gas Mass Fraction,,
Aqueous relative permeability,,
Gas relative permeability,,
Aqueous Density,kg/m^3,
Gas Density,kg/m^3,
Salt Aqueous Mass Fraction,,
Diffusive Porosity,,
~Surface Flux Card
2,
Total CO2 Mass Flux,kg/s,kg,West,71,71,1,4,1,10,
Aqueous Mass Flux,kg/s,kg,East,71,71,1,4,1,10,

APPENDIX: C-10

Homogeneous coarse sand – Quasi-static flow

#Y4 homc-3D case10 - Sandstone -Coarse 3D Simulation Time=1000 yrs initial cond. changed to Aqueous Press., Aqu. Sat. with Sw=0.9999

~Simulation Title Card
1,
Simulation of CO2 Sequestration in Deep Saline Aquifers,
Kamal Khudaida,
Chemical Eng. Dep.,Loughborough University,
28 January 2014,
11:30 AM UK,
23,
CC**********
CC BRIEF DESCRIPTION OF PROJECT
CC**********
CC Cylindrical geometry
CC 3D Full scale,radial model
CC (phase 1=inactive water, phase 2 = water/co2, phase 3=co2/gas
CC Radius(m):2500 INJECTION FLUID: CO2
CC HEIGHT(m):100 INJECTION RATE:40.0 kg/s (i. e. 4 arcs * 4 nodes * 2.5 kg/s)
INJECTION TIME=20 YEARS
CC WIDTH(m):
CC POROSITY: 0.25
CC ABS. PERM(MD): variable 3-PHASE REL. PERM: water endpt.=1.0
CC TEMP(C): 58 WETTIBILITY:
CC INJECTION PRESSURE(MPa):36 HYDROSTATIC PRESSURE (MPa)=32
CC SOR: G/O CAP. PRESSURE: *
CC SWC: DISPLACEMENT TYPE: HORIZONTAL
CC stop injection after 20 years run for 1000 yrs,h2o k endpoint=1
CC ****NON-IDEAL MIXING, NO GRAVITY, WITH Pc, WITH X-FLOW
CC FILE NAME: Homogeneous Low Permeability Sandstone
CC CREATED BY Kamal Khudaida
CC MODIFIED ON 28/01/2014,
CC**********

~Solution Control Card
#excution mode to read initial conditions (normal, restart, initial conditions)Normal
normal,
#operational mode
H2O-NaCl-CO2,
#excution time periods

1,
#initial time,final time (injection time 50 yrs with lockup time 1000 yrs),init. time step, max. t. s.,t. s. accel. factor,Iteration,convergence
0,year,1000,year,1.e-3,s,20,year,1.125,64,1.e-06,
#max num. of time steps
200000,
#aqueous diffusion option,dissolved CO2 diffusion Coefficient,Dissolved Salt Diffusion Coefficient
Variable Aqueous Diffusion,
Variable Gas Diffusion,
#Number of Interfacial Averaging Variables
0,

~Grid Card
Cylindrical,
71,4,10,
#for grids with non-uniform spacing one plus the number of nodes entries are required for each grid direction. Domain Radius=2500 m.
0.2,m,25@20,m,15@30,m,31@50,m,
0.0,deg,4@90.0,deg,
0.0,m,10@10,m,

~Rock/Soil Zonation Card
#number of zonation domains
1,
#rock or soil group with start and end indeces in each direction
Delfurth Sandstone,1,71,1,4,1,10,

~Mechanical Properties Card
#rock grouping name,density,total porosity,diffusive porosity,specific storativity,
#aq. tortuosity,gas tortuosity,tortuosity function,
Delfurth Sandstone,2430,kg/m^3,0.25,0.25,Pore Compressibility,1.0e-9,1/Pa,100.0,bar,Millington and Quirk,

~Hydraulic Properties Card
#rock grouping name,intrinsic permeability in r,theta and z-directions, Pore-body Fractional Length, Fractional Critical Porosity (NaCl precipitation is NOT considered)
Delfurth Sandstone,5.625e-13,m^2,5.625e-13,m^2,1.688e-13,m^2,

~Saturation Function Card
#rock grouping name,Saturation Function option,alpha Parameter,units,n Parameter,minumum saturation,m Parameter,
Delfurth Sandstone,van Genuchten,0.5,1/m,1.84,0.0,0.457,,

~Aqueous Relative Permeability Card
#rock grouping name,Permeability Function Option,van Genuchten m parameter,Irreducible Aqueous Saturation

Delfurth Sandstone,Mualem Irreducible,0.457,0.1,

~Gas Relative Permeability Card
#rock grouping name,Permeability Function Option,Irreducible Gas Saturation ,Irreducible Aqueous Saturation
Delfurth Sandstone,Corey,0.05,0.1,

~Salt Transport Card
#rock grouping name,Longitudinal Dispersivity (equal zero for homogeneous),
Units,Transverse Dispersivity, Units
Delfurth Sandstone,0.0,m,0.0,m,

~Initial Conditions Card
#initial saturation option,initial saturation option,
Aqueous Pressure,Aqueous Saturation,
#number of initial conditions domains
4,
#Variable Name Option,pressure,unit,X,y,z,-Dir. Gradient, Units (1/m),I,j,k-Start Index, I,j,k-End Index,
Aqueous Pressure,32.e+6,Pa,,,,,-10.5e+3,1/m,1,71,1,4,1,10,
#Gas Pressure,32.e+6,pa,,,,,-10.5e+3,1/m,1,71,1,4,1,10,
Aqueous Saturation,0.9999,,,,,,,,1,71,1,4,1,10,
Temperature,58.0,C,,,,,,,1,71,1,4,1,10,
Salt Mass Fraction,0.2,,,,,,,,1,71,1,4,1,10,

~Source Card
#Number of Source Domains
1,
#Source Type Option,Water Vapor Source Option,I,j,k-Start Index, I,j,k-End Index,
Gas Mass Rate,Water-Vapor Mass Fraction,1,1,1,4,1,4,74,
#Source (injection) Start Time,Units(s),Pressure,Units (Pa),Gas Mass Rate,Units(kg/s),Water Vapor Mass Fraction
0,s,10.0000e+6,Pa,2.5,kg/s,0.0,
#Source Step Time,Units(s),Pressure,Units (Pa),Gas Mass Rate,Units(kg/s),Water Vapor Mass Fraction
100,day,10.3464e+6,Pa,40.0,kg/s,0.0,
200,day,10.7027e+6,Pa,40.0,kg/s,0.0,
300,day,11.0590e+6,Pa,40.0,kg/s,0.0,
400,day,11.0590e+6,Pa,40.0,kg/s,0.0,
500,day,11.7716e+6,Pa,40.0,kg/s,0.0,
600,day,12.1279e+6,Pa,40.0,kg/s,0.0,
700,day,12.4842e+6,Pa,40.0,kg/s,0.0,
800,day,12.8405e+6,Pa,40.0,kg/s,0.0,
900,day,13.1968e+6,Pa,40.0,kg/s,0.0,
1000,day,13.5531e+6,Pa,40.0,kg/s,0.0,
1100,day,13.9094e+6,Pa,40.0,kg/s,0.0,

1200,day,14.2657e+6,Pa,40.0,kg/s,0.0,
1300,day,14.6220e+6,Pa,40.0,kg/s,0.0,
1400,day,14.9783e+6,Pa,40.0,kg/s,0.0,
1500,day,15.3346e+6,Pa,40.0,kg/s,0.0,
1600,day,15.6909e+6,Pa,40.0,kg/s,0.0,
1700,day,16.0472e+6,Pa,40.0,kg/s,0.0,
1800,day,16.4035e+6,Pa,40.0,kg/s,0.0,
1900,day,16.7598e+6,Pa,40.0,kg/s,0.0,
2000,day,17.1161e+6,Pa,40.0,kg/s,0.0,
2100,day,17.4724e+6,Pa,40.0,kg/s,0.0,
2200,day,17.8287e+6,Pa,40.0,kg/s,0.0,
2300,day,18.1850e+6,Pa,40.0,kg/s,0.0,
2400,day,18.5413e+6,Pa,40.0,kg/s,0.0,
2500,day,18.8976e+6,Pa,40.0,kg/s,0.0,
2600,day,19.2539e+6,Pa,40.0,kg/s,0.0,
2700,day,19.6102e+6,Pa,40.0,kg/s,0.0,
2800,day,19.9665e+6,Pa,40.0,kg/s,0.0,
2900,day,20.3228e+6,Pa,40.0,kg/s,0.0,
3000,day,20.6791e+6,Pa,40.0,kg/s,0.0,
3100,day,21.0354e+6,Pa,40.0,kg/s,0.0,
3200,day,21.3917e+6,Pa,40.0,kg/s,0.0,
3300,day,21.7480e+6,Pa,40.0,kg/s,0.0,
3400,day,22.1043e+6,Pa,40.0,kg/s,0.0,
3500,day,22.4606e+6,Pa,40.0,kg/s,0.0,
3600,day,22.8169e+6,Pa,40.0,kg/s,0.0,
3700,day,23.1732e+6,Pa,40.0,kg/s,0.0,
3800,day,23.5295e+6,Pa,40.0,kg/s,0.0,
3900,day,23.8858e+6,Pa,40.0,kg/s,0.0,
4000,day,24.2421e+6,Pa,40.0,kg/s,0.0,
4100,day,24.5984e+6,Pa,40.0,kg/s,0.0,
4200,day,24.9547e+6,Pa,40.0,kg/s,0.0,
4300,day,25.3110e+6,Pa,40.0,kg/s,0.0,
4400,day,25.6673e+6,Pa,40.0,kg/s,0.0,
4500,day,26.0236e+6,Pa,40.0,kg/s,0.0,
4600,day,26.3799e+6,Pa,40.0,kg/s,0.0,
4700,day,26.7362e+6,Pa,40.0,kg/s,0.0,
4800,day,27.0925e+6,Pa,40.0,kg/s,0.0,
4900,day,27.4488e+6,Pa,40.0,kg/s,0.0,
5000,day,27.8051e+6,Pa,40.0,kg/s,0.0,
5100,day,28.1614e+6,Pa,40.0,kg/s,0.0,
5200,day,28.5177e+6,Pa,40.0,kg/s,0.0,
5300,day,28.8740e+6,Pa,40.0,kg/s,0.0,
5400,day,29.2303e+6,Pa,40.0,kg/s,0.0,
5500,day,29.5866e+6,Pa,40.0,kg/s,0.0,
5600,day,29.9429e+6,Pa,40.0,kg/s,0.0,
5700,day,30.2992e+6,Pa,40.0,kg/s,0.0,
5800,day,30.6555e+6,Pa,40.0,kg/s,0.0,

5900,day,31.0118e+6,Pa,40.0,kg/s,0.0,
6000,day,31.3681e+6,Pa,40.0,kg/s,0.0,
6100,day,31.7244e+6,Pa,40.0,kg/s,0.0,
6200,day,32.0807e+6,Pa,40.0,kg/s,0.0,
6300,day,32.4370e+6,Pa,40.0,kg/s,0.0,
6400,day,32.7933e+6,Pa,40.0,kg/s,0.0,
6500,day,33.1496e+6,Pa,40.0,kg/s,0.0,
6600,day,33.5059e+6,Pa,40.0,kg/s,0.0,
6700,day,33.8622e+6,Pa,40.0,kg/s,0.0,
6800,day,34.2185e+6,Pa,40.0,kg/s,0.0,
6900,day,34.5748e+6,Pa,40.0,kg/s,0.0,
7000,day,34.9311e+6,Pa,40.0,kg/s,0.0,
7100,day,35.2874e+6,Pa,40.0,kg/s,0.0,
7200,day,35.6437e+6,Pa,40.0,kg/s,0.0,
7300,day,36.0000e+6,Pa,40.0,kg/s,0.0,

~Boundary Conditions Card
2,
#Boundary Surface Direction Option,Aqueous-Phase Boundary Type Option,Gas-Phase Boundary Type Option,Salt Boundary Type Option
East,Aqueous Initial Condition,Gas Initial Condition,Salt Initial Condition,
71,71,1,4,1,10,1,
0,s,,,,,,,,
#Boundary Time, Units (s),Aqueous Pressure, Units (Pa),Aqueous Dissolved- CO2-Relative Saturation,Gas Pressure, Units(Pa),Water-Vapor Relative Humidity,Salt Mass Fraction, Null,
West,Aqu. Zero Flux,Gas Dirichlet,Aqueous Mass Fraction,
1,1,1,4,1,4,1,
0,s,,,0.0,,,1.0,0.2,,

~Output Options Card
#Number of Reference Nodes
15,
#I Index, J Index, K Index
#R=100 m
6,1,3,
6,1,5,
6,1,8,
#R=200 m
11,1,3,
11,1,5,
11,1,8,
#R=500 m
26,1,3,
26,1,5,
26,1,8,
#R=800 m
36,1,3,

36,1,5,
36,1,8,
#R=1000 m
42,1,3,
42,1,5,
42,1,8,
#Reference Node Screen Output Frequency,Reference Node Output File Frequency,Output Time Units(s),
#Output Length Units (m),Screen Significant Digits,Output File Significant Digits,Plot File Significant Digits
1,1,year,m,deg,6,6,6,
#Number of Reference Node Variables
13,
#Reference Node Variable Option, Reference Node Variable Units,
Aqueous Saturation,,
Gas Saturation,,
Aqueous Pressure,Pa,
Gas Pressure,Pa,
#total CO2 mass in the computational domain
Integrated CO2 Mass,kg,
Integrated Aqueous CO2 Mass,kg,
#total CO2 mass in the gas phase in the computational domain
Integrated Gas CO2 Mass,kg,
Aqueous relative permeability,,
Gas relative permeability,,
Aqueous Density,kg/m^3,
Gas Density,kg/m^3,
Salt Aqueous Mass Fraction,,
Diffusive Porosity,,
#Number of Plot File Ouput Times
12,
1,year,
5,year,
10,year,
20,year,
50,year,
100,year,
200,year,
300,year,
400,year,
500,year,
750,year,
1000,year,
#Number of Plot File Variables
11,
#Plot File Variable Option, Plot File Variable Units
Aqueous Saturation,,

Gas Saturation,,
Aqueous Pressure,Pa,
Gas Pressure,Pa,
CO2 Aqueous Mass Fraction,,
CO2 Gas Mass Fraction,,
Aqueous relative permeability,,
Gas relative permeability,,
Aqueous Density,kg/m^3,
Gas Density,kg/m^3,
Salt Aqueous Mass Fraction,,
Diffusive Porosity,,
~Surface Flux Card
2,
Total CO2 Mass Flux,kg/s,kg,West,71,71,1,4,1,4,
Aqueous Mass Flux,kg/s,kg,East,71,71,1,4,1,10,